ULTRAFILTRATION IN RENAL GLOMERULAR CAPILLARIES: THEORETICAL EFFECTS OF ULTRASTRUCTURE

by

Maria Cláudia Ferreira Drumond de Sousa

Diploma in Chemical Engineering
University of Porto
(1987)

Submitted to the Department of Chemical Engineering
in Partial Fulfillment of the Requirements for the Degree of
DOCTOR OF PHILOSOPHY
in Chemical Engineering

at the

MASSACHUSETTS INSTITUTE OF TECHNOLOGY

February 1994

Signature of Author _____
Department of Chemical Engineering
December 8, 1993

Certified by _____
William M. Deen
Professor of Chemical Engineering
Thesis Supervisor

Accepted by _____
Robert E. Cohen
Chairman, Committee for Graduate Students

ULTRAFILTRATION IN RENAL GLOMERULAR CAPILLARIES: THEORETICAL EFFECTS OF ULTRASTRUCTURE

by

Maria Cláudia Ferreira Drumond de Sousa

Submitted to the Department of Chemical Engineering
on December 8, 1993 in Partial Fulfillment of the
Requirements for the Degree of Doctor of Philosophy in
Chemical Engineering

ABSTRACT

We developed hydrodynamic models for transport of water and macromolecules across the glomerular capillary wall, based on the ultrastructure of its constituent layers. Models were developed for the endothelial fenestrae, basement membrane and epithelial filtration slits with slit diaphragms. The input data included the dimensions of the various structures from previous electron microscopy studies, and the hydraulic permeability recently measured for isolated basement membrane *in vitro*. The model for hindered transport of macromolecules focused on the slit diaphragms and basement membrane.

As a model for flow through the slit diaphragms which connect the epithelial foot processes, we obtained finite element solutions of Stokes' equations for flow perpendicular to a single row of cylinders confined between parallel walls. We computed a dimensionless "additional resistance" (f), defined as the increment in resistance above the Poiseuille flow value, for $L/W \leq 4$ and $0.1 \leq R/L \leq 0.9$, where L is half the distance between cylinder centers, W is half the distance between walls and R is the cylinder radius. Two factors contributed to f: the drag on the cylinders, and the incremental shear stresses on the walls of the channel. Of these two factors, the drag on the cylinders tended to be dominant. We also analyzed another representation of the slit diaphragm suggested in the literature, which consists of a central filament, parallel to the surfaces of the foot processes and connected to the foot processes by alternating cross-bridges on either side.

We computed velocity and pressure profiles within the endothelial fenestrae and the basement membrane, and calculated the hydraulic permeability of these structures. These results were combined with those for the epithelial slits and the resulting values of the overall hydraulic permeability of the capillary wall (k) agreed very well with an experimental range derived from micropuncture measurements in normal rats. Furthermore, the model provided estimates of the relative contribution of each layer to the total water flow resistance. The hydraulic resistance of the endothelium was predicted to be small, while the basement membrane and epithelial slits were each found to contribute roughly half of the total water flow resistance. When applied to a study of

glomerular injury in rats, the model correctly predicted the observed trends in hydraulic permeability.

The hydraulic permeability model was applied also to a study of healthy and nephrotic humans. There was good agreement between the predicted values of hydraulic permeability (based on measurements of basement membrane thickness and filtration slit frequency) and independent estimates based on hemodynamic measurements and measurements of glomerular filtering surface area. Moreover, the model provided an explanation for the fact that reductions of glomerular filtration rate in various human nephropathies tend to be correlated more with reductions in filtration slit frequency than with changes in basement membrane thickness.

To describe the hindered transport of plasma proteins and other macromolecules through the slit diaphragm, we developed an approximate hydrodynamic model for spherical, Brownian particles passing through a row of infinitely long cylinders of macromolecular dimensions. The selectivity of the slit diaphragm was assessed by computing concentration profiles for a wide range of molecular sizes for $Pe \leq 1$, where Pe is a Peclet number based on the cylinder radius. The sieving coefficient for the slit diaphragm was computed as the concentration far downstream (corresponding to Bowman's space) divided by the average concentration at a specified distance upstream from the cylinders (corresponding to the location of the basement membrane). The results of previous experimental sieving studies using rats could be accounted for approximately by postulating a wide distribution of spacings between the fibers of the slit diaphragm. Calculations made by coupling the results for the slit diaphragm with a model of the glomerular basement membrane suggest that the slit diaphragm is by far the most size-restrictive part of the overall barrier.

In addition, we developed a model of glomerular filtration with pulsatile pressures and flows, and used this model as a standard in evaluating the suitability of the usual steady-state formulations. The model included sinusoidal variations in the transcapillary hydraulic pressure and the afferent arteriolar plasma flow rate over each cardiac cycle. The analysis suggested that the previously ignored time derivatives in the luminal mass balances are not negligible, and that the oscillations in pressure are sufficient to cause filtration reversal at the more efferent locations in a capillary. However, the time-averaged values of glomerular filtration rate and sieving coefficients for macromolecules were not significantly different from those for a steady-state formulation. This supports the validity of the steady-state assumption used in previous models of glomerular filtration as well as in the hydrodynamic models described in this thesis.

Thesis Supervisor: William M. Deen
Professor of Chemical Engineering

Aos meus Pais

ACKNOWLEDGMENTS

I would like to thank my thesis supervisor, Professor William M. Deen. Without his expertise and technical guidance, this work would have not been possible. I am deeply grateful for his patience, his kindness and his continuous support.

I would like to thank the members of my thesis committee, Professors Robert C. Armstrong, Howard Brenner, Robert A. Brown and Roger D. Kamm for their insightful comments and suggestions during our meetings.

I am very grateful to Dr. Bryan D. Myers and Dr. Batya Kristal, at the Stanford University Medical Center, who obtained all the experimental data for the study described in Chapter 5. I have greatly appreciated our collaboration in this study.

This work was supported by a grant from the National Institutes of Health. I thankfully acknowledge financial support from Junta Nacional de Investigação Científica e Tecnológica, Escola Superior de Biotecnologia, and Comissão Cultural Luso-Americana (Fulbright).

I would like to thank my past and present lab-mates for making the lab a really friendly place. Thanks to Jennifer Smith, whose help I remember with lots of gratitude. Thanks to Erin Johnson and Aurélie Edwards for their friendship and support.

I would like to thank Ellen Banaghan who has been a really good friend since the time we were roommates.

I would like to thank my portuguese friends, who have been helpful to me in many ways. I am very grateful for the friendship and support of Isabel Rajão and Fátima Branco. Thanks to João Paulo Ferreira, who has helped me keep a positive attitude.

Finally, I would like to thank my parents and my sisters. I would have not been able to keep on going if it were not for their love, encouragement and unfailing support. I just hope one day I can compensate them for all they have given me throughout the years.

CONTENTS

LIST OF FIGURES

LIST OF TABLES

FOREWORD

Following are references for material described in this thesis.

The reference for the material of Chapter 2 is: M. Claudia Drumond and William M. Deen, "Analysis of pulsatile pressures and flows in glomerular filtration", *Am. J. Physiol.* 261 (*Renal Fluid Electrolyte Physiol.* 30): F409-F419, 1991.

Most of the material in Chapter 3 will appear as a paper in *J. Biomech. Eng.* which is still in press as of this writing. The paper, by M. Claudia Drumond and William M. Deen, is entitled "Stokes flow through a row of cylinders between parallel walls: Model for the glomerular slit diaphragm".

Most of the material in Chapter 4 will appear as a paper in the *Am. J. Physiol.* which is also still in press. The paper, by M. Claudia Drumond and William M. Deen, is entitled "Structural determinants of glomerular hydraulic permeability".

A manuscript by M. Claudia Drumond, Batya Kristal, Bryan D. Myers and William M. Deen, based on the work described in Chapter 5, has been submitted to the *J. Clin. Invest.* The manuscript is entitled "Structural basis for reduced glomerular filtration capacity in nephrotic humans".

A manuscript by M. Claudia Drumond and William M. Deen, based on the work described in Chapter 6, has been submitted to the *J. Biomech. Eng.* The manuscript is entitled "Hindered transport of macromolecules through a single row of cylinders: Application to glomerular filtration".

CHAPTER 1
BACKGROUND

1.1 INTRODUCTION

The major function of the kidneys is to maintain the volume and composition of the body fluids within normal limits. The functional subunits of the kidneys are the nephrons, each consisting of a tubular and a vascular structure. There are about one million nephrons in a human kidney and about 30,000 in a rat kidney. The blood reaches a nephron via an afferent arteriole which bifurcates into a network of capillaries, the glomerulus, where an ultrafiltrate of the blood plasma is produced. The capillaries rejoin to form an efferent arteriole (Figure 1.1). The ultrafiltrate, collected in Bowman's space, proceeds through the renal tubules. Both the amount and composition of the tubule fluid change throughout the tubular segments, via reabsorption and secretion processes across the tubule walls. The fluid still remaining at the end of the collecting tubules (usually less than 1% of the glomerular filtrate) becomes urine.

We will focus our attention on glomerular filtration, a process driven by imbalances of hydrostatic and osmotic pressures between the capillary lumen and Bowman's space. The wall of the glomerular capillaries is normally very permeable to water and small solutes but highly selective to macromolecules, such that it permits almost no loss of the major plasma proteins into the urine. Molecular size, configuration and charge, hemodynamic conditions, and structural properties of the capillary wall are all important determinants of glomerular filtration. Functional information on mass transport in the renal microcirculation is provided largely by micropuncture and clearance experiments. Following is a brief summary of the information available from

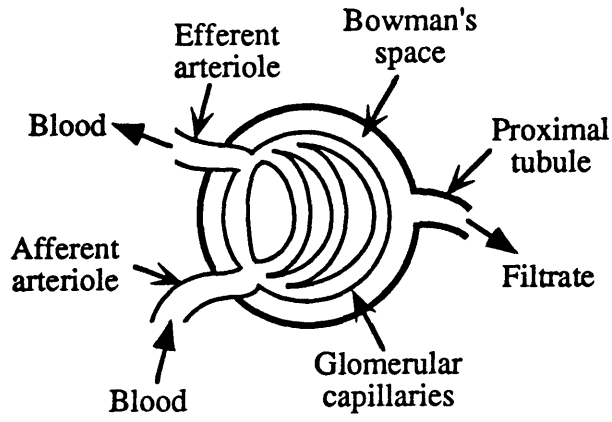

Figure 1.1 - Schematic representation of a glomerulus.

these physiological studies. A more comprehensive review can be found in Maddox et al. (1992).

MICROPUNCTURE. Micropuncture techniques allow measurements at the level of a single nephron and involve a surgical procedure in which one of the kidneys of an anesthetized animal (commonly the rat) is exposed. Sharpened micropipettes are then inserted into portions of some nephrons, allowing collection of fluids and pressure measurements. Quantities such as the "single-nephron glomerular filtration rate" of water (*SNGFR*), afferent plasma flow rate (Q_A), glomerular (P_G) and tubular (P_T) pressures, and solute concentrations can be determined by micropuncture. Typical values found in male euvolemic [1] Munich-Wistar rats are *SNGFR* ~ 40 nl/min, Q_A ~ 150 nl/min, P_G ~ 50 mm Hg, ΔP ~ 35 mm Hg, c_{PA} ~ 6 g/dl, and π_A ~ 20 mm Hg (Maddox et al., 1992), where ΔP is the transmural hydraulic pressure difference ($\Delta P = P_G - P_T$), and c_{PA}

[1] Euvolemic rats are rats in which plasma has been infused to compensate for surgical fluid losses.

and π_A are the concentration of protein and the osmotic pressure, respectively, in the afferent arteriole. We see that the net ultrafiltration pressure at the afferent end of a capillary (ΔP - π_A) is ~ 15 mm Hg. Because of the large volume of fluid crossing the capillary wall, the osmotic pressure rises considerably along the capillary and, thus, the net ultrafiltration pressure decreases. Typical values for the net ultrafiltration pressure at the efferent end are only ~ 2 mm Hg (Maddox et al., 1992). As will be seen below, the results of micropuncture experiments can be used to calculate the glomerular ultrafiltration coefficient, K_f, which is the product of the glomerular filtration area, S, and the hydraulic permeability of the capillary wall, k. For normal male euvolemic Munich-Wistar rats the range for K_f is ~ 4 - 6 nl/min/mm Hg (Maddox et al., 1992). The total glomerular capillary surface area (S) of superficial glomeruli for this strain is about 0.0016 cm^2 (Pinnick and Savin, 1986). Thus, k ~ 3 - 5x10^{-9} m/s/Pa. It is noteworthy that these values of hydraulic permeability are one to two orders of magnitude greater than typical values found in other capillary systems (Maddox et al., 1992).

FRACTIONAL CLEARANCE. The fractional clearance of a given solute is defined as the urinary clearance of that solute ($Q_U c_{SU}/c_{SA}$, where Q_U is the flow rate of urine and c_{SU} and c_{SA} are the solute concentration in the urine and afferent arteriole, respectively) divided by the glomerular filtration rate of water (GFR). Since it is a less invasive technique than micropuncture, requiring only urine and systemic blood samples, clearance measurements can be performed both in humans and experimental animals. If the test solute is neither reabsorbed nor secreted in the renal tubules, the fractional clearance equals the sieving coeficient, θ, defined as the ratio between the solute concentration in Bowman's space and that in the afferent arteriole. Dextran and other exogeneous polymers, such as Ficoll, polyethylene glycol and polyvinylpyrrolidone, fall into this category of solutes and thus are suitable for clearance experiments aimed at measuring θ. Although dextran and its charged derivatives have been the test solutes most frequently used, Oliver et al. (1992) recently concluded that Ficoll (which has a

cross-linked structure and behaves approximately as a rigid sphere) is a better marker than dextran (which is approximately a linear polymer, existing in solution as a random coil) for the glomerular filtration of neutral globular proteins and that it may be preferred over dextran in studies of glomerular size-selectivity. Figure 1.2 shows the sieving curve for Ficoll obtained in this study (Oliver et al., 1992). Molecular charge is another important determinant of glomerular filtration of macromolecules. Because the capillary wall is negatively charged, the filtration of cationic macromolecules is enhanced and the filtration of anionic macromolecules is retarded relative to that of neutral macromolecules (Deen et al., 1980). As will be seen in Section 1.3, under the assumption that the capillary wall is a membrane perforated by a homogeneous population of cylindrical pores, one can estimate the pore radius, r_0, and the concentration of fixed anionic charges, c_m, from sieving curves of neutral and charged macromolecules. Typical values for the rat, obtained from sieving curves for dextran and its charged derivatives, are $r_0 \sim 50$ Å and $c_m \sim 160$ meq/l (Deen et al., 1980; Maddox et al., 1992).

Chronic renal diseases are commonly characterized by reductions in the glomerular filtration rate, and by the appearance of substantial amounts of protein in the urine (proteinuria). These abnormalities have been reported in a number of human diseases (Deen et al., 1985; Guasch et al., 1991, 1992; Myers et al., 1982; Nakamura and Myers, 1987; Shemesh et al., 1986), and studied in more detail in experimental diseases induced in animals (Anderson et al., 1988; Ichikawa et al., 1982; Yoshioka et al., 1987). The functional changes in these diseases are commonly attributed to a decrease in the ultrafiltration coefficient for water (K_f) and, depending on the particular model of the capillary wall (see below), to an increase in the pore radius (r_0), to a shift in the pore size distribution to larger pores, or simply to an increase in the number of very large, non-selective pathways. In some cases, it has also been suggested that there is loss of charge-selectivity of the capillary wall (Bridges et al., 1991; Guasch et al., 1993; Olson et al.,

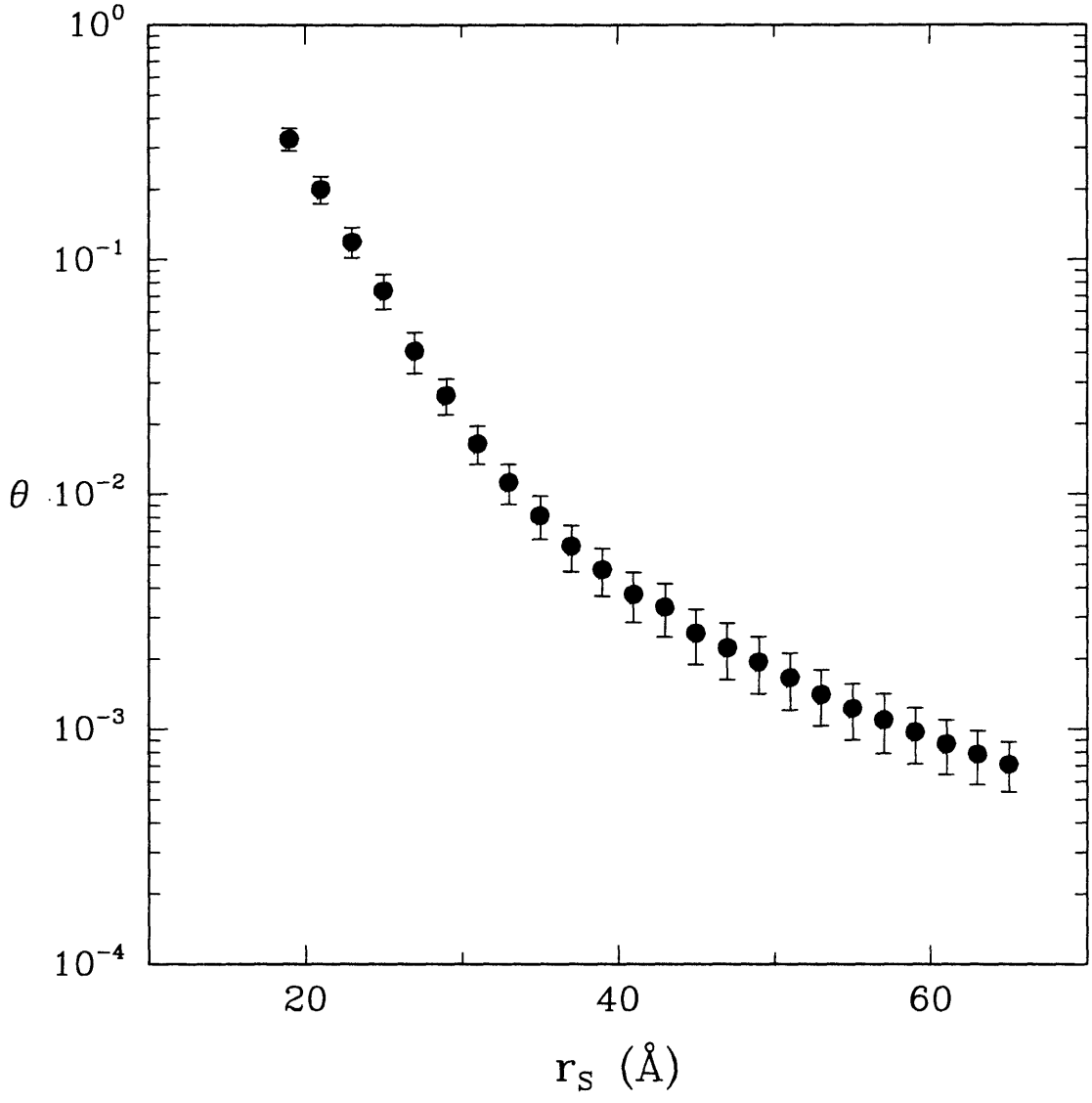

Figure 1.2 - Experimental sieving coefficients (θ) for Ficoll as a function of Stokes-Einstein radius (r_s). (Data from Oliver et al., 1992.)

1981). A finding of numerous studies of altered glomerular permeability, including most of the studies cited above, is that there are significant alterations in the morphology of the capillary wall.

1.2 CHARACTERIZATION OF THE GLOMERULAR CAPILLARY WALL

Figure 1.3 shows a schematic representation of the capillary wall with its constituent layers: the fenestrated endothelium, adjacent to the capillary lumen; the glomerular basement membrane; and the epithelial foot processes, facing Bowman's space. Electron microscopy techniques have allowed a relatively detailed characterization of the capillary wall. Presented next is a brief review of some of the existing studies. Because there is a vast amount of information in this field, some of which is outside the scope of this thesis, the following review will focus mainly on those aspects of the structure that are relevant to the present work. Frequent reference will be made to more extensive reviews on the subject.

1.2.1 FENESTRATED ENDOTHELIAL CELLS

The endothelial cells form the innermost layer of the glomerular capillary wall. The cytoplasm of these cells is perforated by numerous pores (fenestrae), 20 to 100 nm in radius (Kondo, 1990; Koriyama et al., 1992; Larsson and Maunsbach, 1980; Lea et al., 1989; Levick and Smaje, 1987; Maul, 1971; Rhodin; 1962; Ryan, 1986; Takami et al., 1991). Rhodin (1962) observed the existence of a diaphragm (~6 nm thick) covering each fenestra in mouse glomerular capillaries. The existence of one or more diaphragms covering endothelial fenestrae of the rat glomerular capillary wall has also been reported (Larsson and Maunsbach, 1980; Maul, 1971). However, it is usually suggested that the

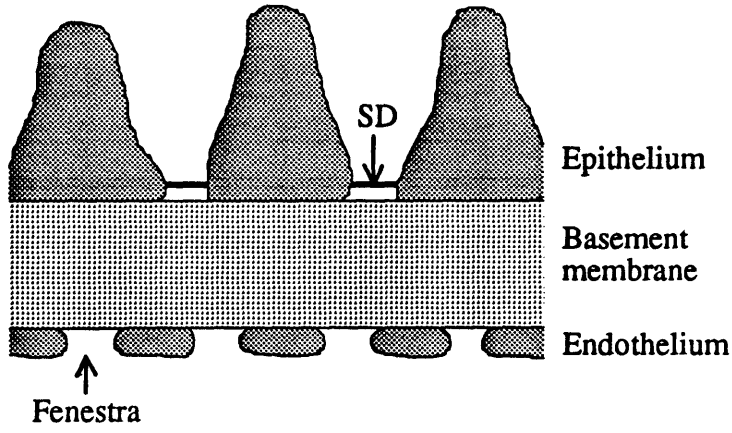

Figure 1.3 - Schematic representation of the glomerular capillary wall. The innermost layer, lining the capillary lumen, is a fenestrated endothelium; the middle layer is a basement membrane; the outermost layer is formed by foot processes of epithelial cells connected by thin slit diaphragms (labeled "SD").

fenestrae have no diaphragm (Abrahamson, 1987; Avasthi and Koshy, 1988; Farquhar, 1981; Levick and Smaje, 1987). In his review, Ryan (1986) states that diaphragms are absent in most species, while Kanwar and Venkatachalam (1992), in their review, state that the diaphragms are present at early age but disappear with further maturation.

The most detailed study of the three-dimensional structure of the endothelial cells seems to be that of Lea et al. (1989), who proposed that the fenestrae are channels of circular cross-section with varying radii (Figure 1.4). The observed frequency of the fenestrae was ~70 per μm^2 of total surface area of the capillary wall. At the luminal or contraluminal surfaces of the endothelial cells about 83% of the surface area of the basement membrane is exposed, whereas in the plane corresponding to the minimum pore diameter (~60 nm), only ~ 20% of the glomerular basement membrane is exposed. Different shapes for the fenestrae have also been suggested (e.g., octagonal (Maul, 1971) and oval (Kondo, 1990)).

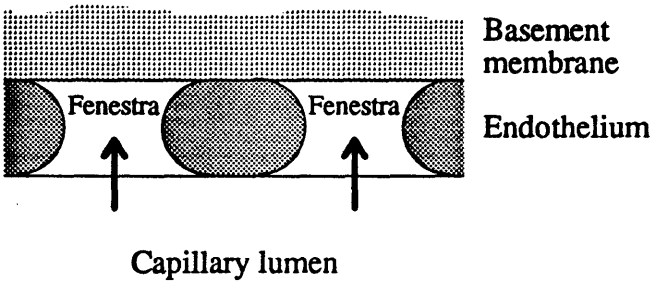

Figure 1.4 - Schematic representation of the endothelium illustrating the shape of the fenestrae proposed by Lea et al. (1989). Each fenestra has a circular cross-section. The direction of filtrate flow is indicated by the arrows.

Although the role of the endothelial layer in glomerular filtration is not known precisely, the possibility of contraction of the fenestrae and consequent changes in pore size has been proposed as a means to control the permeability of the endothelium (Lea et al., 1989). Nonetheless, the large dimension of the fenestrae and the results of tracer studies (see below) suggest that the endothelial resistance to the filtration of water and uncharged macromolecules may not be a significant fraction of the overall resistance of the capillary wall.

It has been observed that the surface of the endothelial cells is covered by a rich polyanionic "coat", forming a sparse fiber matrix lining the capillary lumen and filling the fenestrae (Avasthi and Koshy, 1988). Sialoglycoproteins (namely podocalyxin), heparan sulfate proteoglycans and hyaluronic acid have been identified in this coat (Avasthi and Koshy, 1988; Horvat et al., 1986). Because of its anionic content, it is possible that this fiber matrix is an important resistance to the filtration of negatively charged macromolecules.

1.2.2 GLOMERULAR BASEMENT MEMBRANE

The middle layer of the glomerular capillary wall is the glomerular basement membrane (GBM), which consists of a network of fibers and apparently is divided into three layers of different electron density and composition: the "lamina rara interna" adjacent to the endothelium; a central dense layer (the "lamina densa"); and the "lamina rara externa" adjacent to the epithelial cells. The fibers appear closely packed in the lamina densa and loosely arranged in the lamina rarae, but it has been argued that this three-layered arrangement might be an artifact of the tissue fixation procedure (Goldberg and Escaig-Haye, 1986). Reported values for the diameters of the various "fibrils" (also called "cords") composing each layer range from ~2 to ~10 nm (Farquhar, 1981; Ionue, 1989; Kanwar and Venkatachalam, 1992; Kubosawa and Kondo, 1985; Laurie et al., 1984; Takami et al., 1991). Reported values for the total thickness of the basement membrane range from ~100 nm to ~300 nm (Abrahamson, 1987; Kondo, 1990, Larsson and Maunsbach, 1980; Ryan, 1986, Takami et al., 1991).

There are several reviews on the chemical composition and architecture of basement membranes in general and glomerular basement membrane in particular (Abrahamson, 1987; Farquhar, 1981; Ionue, 1989; Kanwar and Venkatachalam, 1992; Yurchenco and Schittny, 1990). The major components of the glomerular basement membrane identified thus far include type IV collagen, laminin (a sialoglycoprotein) and heparan sulfate proteoglycans (Abrahamson, 1987; Kanwar and Venkatachalam, 1992; Laurie et al., 1984). Other glycoproteins, such as entactin, nidogen and fibronectin, have also been identified in the basement membrane. It has been suggested that the anionic nature of the glomerular basement membrane is mainly due to the presence of proteoglycans, of which heparan sulfate proteoglycan seems to be the most abundant (Abrahamson, 1987), and that the anionic groups of the GBM are important for the charge selectivity of the glomerular capillary wall (Kanwar and Farquhar, 1979).

Smaller amounts of other anionic compounds such as chondroitin sulfates and hyaluronic acid are also present in the basement membrane (Abrahamson, 1987; Rosenzweig and Kanwar, 1982). The precise location of all these components within the glomerular basement membrane is still a matter of debate. While some investigators localize collagen, laminin and proteoglycans in all three layers (Abrahamson, 1987; Ionue, 1989; Laurie et al., 1984) others suggest that some components are present in only one or two layers (Abrahamson, 1987; Farquhar, 1981). The architecture of the various fibrils is also not known precisely. Kubosawa and Kondo (1985) observed that in the lamina rarae the fibrils are interconnected, forming a three-dimensional meshwork, whereas Laurie et al. (1984) and Takami et al. (1991) observed that the fibrils in these layers are oriented approximately perpendicular to the surface of the endothelial and epithelial cells. The lamina densa has been described as being composed of closely packed particles (Kubosawa and Kondo, 1985) or fibrils (Laurie et al., 1984), or composed of fibrils arranged in a polygonal meshwork (Takami et al., 1991).

Methods have been developed that allow the isolation of basement membranes and the subsequent study of their functional properties. Usually, the isolated membranes are placed in ultrafiltration cells and consolidated under pressure to form a layer whose filtration properties are subsequentely studied. These studies have the advantage of eliminating the effects of the endothelial and epithelial layers, but it has been argued that the isolation procedures may destroy some important characteristics of the original membrane (Farquhar, 1981).

It has been observed that films prepared from fragments of tubular and glomerular basement membranes (with > 80% of GBM) behave as compressible ultrafilters and show size-dependent rejection of proteins (Robinson and Walton, 1989). Concentration polarization phenomena were believed to occur when solutions containing large proteins were filtered (Robinson and Cotter, 1979; Robinson and Walton, 1987, 1989). Experimental determination of the solid volume fraction (ϕ) of the isolated films

yielded ϕ = 0.1 (Robinson and Walton, 1987). Estimates of ϕ and fiber radius (r_f) obtained by fitting experimental results to the "fiber matrix model" of Curry and Michel (1980) (see Section 1.3.2), yielded $\phi \sim 0.1 - 0.2$ and $r_f \sim 0.75 - 1.7$ nm (Robinson and Walton, 1987, 1989).

Experiments with films containing > 95% of glomerular basement membrane, albumin solutions at physiological concentrations, and using filtration pressures close to physiological values, have shown that the hydraulic permeability of the basement membrane is ~5 times larger than values reported for *in vivo* glomerulus (Daniels et al., 1992). Furthermore, measured sieving coefficients of albumin ($\theta \sim 0.1$) were much larger than values commonly reported for *in vivo* glomerulus ($\theta < 0.001$; Maddox et al., 1992). Therefore, it was concluded that the cellular components of the capillary wall must represent a major contribution to the resistance to the filtration of water and macromolecules.

1.2.3 EPITHELIAL FOOT PROCESSES AND SLIT DIAPHRAGMS

The third layer of the glomerular capillary wall is formed by the "pedicels" or "foot processes" of the glomerular epithelial cells. Although there are focal regions of contact between adjacent foot processes, in general the narrow gaps between them are spanned by thin, porous diaphragms (the slit diaphragms). Schnabel et al. (1990) identified a tight junction protein known as ZO-1 in the slit diaphragms but the exact composition of the diaphragms is not known yet (Schnabel et al., 1990; Kanwar and Venkatachalam, 1992).

The structural details of the slit diaphragms are still in dispute. Figure 1.5 shows the structure originally proposed by Rodewald and Karnovsky (1974). It consists of a central filament (~110 Å in diameter), parallel to the surfaces of the foot processes, which is connected to the foot processes by alternating cross-bridges (~70 Å in diameter)

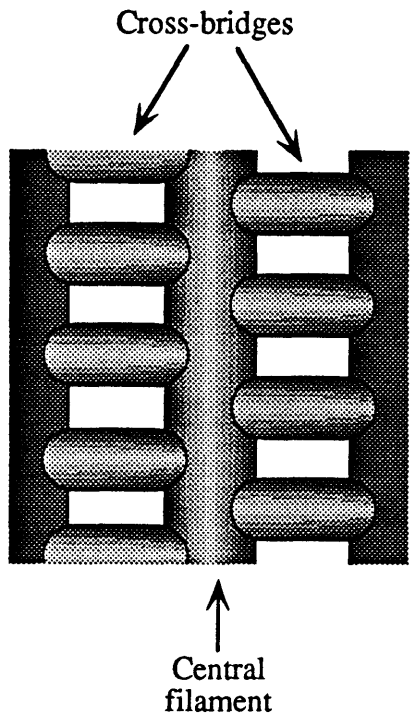

Figure 1.5 - Schematic representation of the epithelial slit diaphragm, as suggested Rodewald and Karnovsky (1974). The reported dimensions of the pores between cross-bridges are 40 x 140 Å.

on either side. Recently, it has been argued that this type of structure (the "zipper" configuration) might be an artifact of tissue fixation. Hora et al. (1990) and Ohno et al. (1992) studied the structure of the slit diaphragm by quick-freezing methods. They argued that when the glomerular tissue is fixed using the method of Rodewald and Karnovsky (1974) (which employs tannic acid, glutaraldehyde and osmium tetroxide), there is contraction of the foot processes which induces artifacts in the structure of the slit diaphragm. They proposed that the slit diaphragm has mainly a non-porous structure, consisting of "sheet-like substructures with the space between the foot processes being occluded by uniform components." (Hora et al., 1990). These structures were the most abundant structures seen in fresh unfixed glomeruli. In glomeruli fixed with paraformaldehyde and glutaraldehyde, Hora et al. (1990) observed these "sheet-like"

structures as well as "ladder-like" structures, "in which cross-bridges were formed between the foot processes". Zipper structures were also seen in parts of the diaphragm. The zipper configuration has also been reported by Kubosawa and Kondo (1985), who used a quick-freeze deep-etch replica method and reported transverse fibrils ~6-8 nm thick, and by Kondo (1990), who used an embedement-free sectioning method and similar fixatives to Rodewald and Karnovsky and saw transverse fibrils ~14-20 nm thick.

Reported values for the width of the slit channels range from ~ 20 to ~ 80 nm (Furukawa et al., 1991; Larsson and Maunsbach, 1980; Ohno et al., 1992; Rodewald and Karnovsky, 1974; Ryan, 1986; Webber and Blackbourne, 1970) comprising ~ 9 - 20% (Furukawa et al., 1991; Rodewald and Karnovsky, 1974; Shea and Morrison, 1975) of the peripheral glomerular capillary surface area.

Although there is still great controversy about the role of the epithelial cells and slit diaphragms, it has been suggested that the filtration slits are likely to be important in controlling the hydraulic permeability of the glomerular capillaries (Ryan, 1986; Shea and Morrison, 1975). In addition, the small dimensions of their pores (see Figure 1.5) suggests that they probably are an important resistance to the transport of plasma proteins (Rodewald and Karnovsky, 1974; Shea and Morrison, 1975).

It has been observed that the epithelial cells can undergo pronounced morphological changes in association with marked alterations in glomerular function, suggesting that this layer is important for the overall performance of the glomerulus. For example, dramatic changes in the foot processes have been reported in proteinuric animals (Bridges et al., 1991; Fries et al., 1989; Messina et al., 1989; Miller et al., 1990; Olson et al., 1981; Ryan et al., 1975) as well as in nephrotic humans (Guasch et al., 1991, 1992, 1993; Shemesh et al., 1986). Specifically, these changes include "fusion" of foot processes, with consequent reduction in the frequency of filtration slits and, in some animal models, displacement of foot processes and diaphragms, and stacking of diaphragms.

The surface of the epithelial cells is covered with a thick anionic coat, the glycocalyx, rich in sialoglycoproteins, the most abundant being podocalyxin (Kerjaschki et al., 1984). Latta et al. (1975) suggested that the glycocalyx also extends over the filtration slits and that it represents an additional size and/or charge selective barrier in glomerular filtration. There is some evidence suggesting that the sialoglycoproteins contribute in part to the charge selectivity properties of the glomerular capillary wall and that the glycocalyx seems to be essential for the maintenance of the normal morphology of the foot processes (Kanwar and Venkatachalam, 1992; Schnabel et al., 1989).

1.2.4 Ultrastructural Tracer Studies

The main purpose of ultrastructural tracer studies is to identify which layer of the glomerular capillary wall is mainly responsible for the retention of plasma proteins (e.g. albumin) in the blood stream. These studies involve the injection of a suitable macromolecular tracer followed by tissue fixation and tracer detection by electron microscopy. If the tracer is held up at a certain level of the glomerular capillary wall, it is concluded that the main barrier to the tracer is present at that level. There is considerable debate over the results of these studies. In general, because uncharged macromolecules are not held up upstream from the fenestrae, no size barrier is attributed to the endothelial cell layer. However, while some investigators attribute the main resistance to the lamina densa of the basement membrane, others consider that the epithelial slits are the principal size barrier (reviews in Farquhar (1981); Kanwar and Venkatachalam (1992) and Ryan (1986)). This controversy might be due to the different nature of the tracers employed and to the different experimental conditions.

There is considerable evidence that the anionic nature of the capillary wall is essential for normal glomerular function. In particular, loss of negative charges is believed to be associated with some forms of proteinuria. There have been efforts to

determine which layer(s) of the wall is(are) mainly responsible for its charge selectivity properties but, once again, no common agreement has been reached. Here there is an additional problem because some cationic tracers may have nephrotoxic effects (Ryan, 1986). It seems reasonable to suppose that the anionic coat of the endothelial cells and/or the anionic groups of the glomerular basement membrane are probably the most important charge barriers of the glomerular capillary wall.

1.2.5 CONCLUDING REMARKS

Although the microstructure of the glomerular capillary wall has been characterized in fairly good detail, it is still a matter of debate which layer(s) is(are) mainly responsible for its water flow resistance as well as its size and charge selectivity. Much of the existing information seems to support the view that the endothelium is not a significant barrier to the filtration of water and uncharged macromolecules, whereas it appears that the epithelial slits and the glomerular basement membrane may both be important barriers.

Mathematical models are needed to critically evaluate current hypotheses on the relationship between glomerular morphology and glomerular barrier function, and to suggest directions for further investigation. The next section reviews the existing mathematical models of glomerular filtration. As will be seen, the existing models are not well suited to the task of relating morphology to function.

1.3 PREVIOUS THEORETICAL MODELS OF GLOMERULAR FILTRATION

In general, mathematical models of glomerular filtration have been used to:

- Characterize the properties of the glomerular capillary wall by computing parameters such as the ultrafiltration coefficient, the pore radius (if the capillary wall is assumed to be perforated by pores), the concentrations of fixed negative charges, etc.
- Predict the outcome of experiments in which one or more variables are changed, in an attempt to find which variables are the most important determinants of glomerular filtration.
- Calculate filtration pressures from sieving or clearance data. This is an attractive application of the theoretical models since in humans it is not possible to perform micropuncture experiments.

A brief review of recent models of glomerular ultrafiltration and glomerular permselectivity is presented next.

1.3.1 MODELS OF GLOMERULAR ULTRAFILTRATION

The water flux (volume flux) across the wall of the glomerular capillaries, J_V, is usually described by the Starling equation

$$J_V = k(\Delta P - \sigma_0 \Delta\pi) \tag{1.1}$$

where ΔP is the hydraulic pressure difference; $\Delta\pi$ is the osmotic pressure difference; k is the hydraulic permeability of the capillary wall; and σ_0 is the osmotic reflection coefficient. The osmotic pressure in the capillary lumen, π_G, is mainly due to the plasma proteins, which are normally retained in the blood stream. Thus, $\sigma_0 \cong 1$ and equation (1.1) can be simplified to

$$J_V = k(\Delta P - \pi_G). \tag{1.2}$$

The osmotic pressure, π_G, can be related to the plasma protein concentration, c_P, by empirical relations (Chang, 1980; Deen et al., 1972; Du Bois et al., 1974; Lambert et al., 1982). An expression which is commonly used is

$$\pi_G = a_1 c_P + a_2 c_P^2 \tag{1.3}$$

where a_1 = 1.629 mm Hg/(g/dl) and a_2 = 0.2935 mm Hg/(g/dl)^2 (Deen et al., 1972).

The water flux, J_V, is a function of position along the capillaries. The filtration of water causes an increase in the plasma protein concentration (and thus in π_G) with axial position, thus leading to a decrease in J_V. A simple steady-state material balance yields

$$\frac{dQ}{dx} = -SJ_V, \tag{1.4}$$

where Q is the plasma flow rate per glomerulus and x is the normalized axial position in the capillaries (x = 0 at the afferent end and x = 1 at the efferent end). Note that implicit in equation (1.4) is the assumption that the glomerular network is made of identical capillaries in parallel, an assumption that has been justified by Remuzzi and Deen (1986). Besides a relationship between π_G and c_P, the integration of equation (1.4) requires the specification of ΔP and a material balance for the plasma proteins. The hydraulic pressure in Bowman's space, P_B, is commonly assumed constant and the pressure drop inside the capillary has been predicted to be small (~3% of pressure at the afferent end (Huss et al., 1975; Lambert et al., 1982)), so that most models assume that ΔP is constant. Neglecting axial diffusion and radial variations of protein concentration - a reasonable assumption, as proved theoretically by Deen et al. (1974) - the material balance for plasma proteins is

$$\frac{d(Qc_P)}{dx} = 0. \tag{1.5}$$

The integration of equations (1.4) and (1.5) leads to mathematical relations that allow the calculation of K_f ($K_f \equiv kS$, where S is the surface area per glomerulus) from micropuncture data (i.e., Q_A, the afferent plasma flow rate; c_{PA} and c_{PE}, the afferent and efferent protein concentrations, and ΔP) (Deen et al., 1972, 1973). Together with estimates of S (Pinnick and Savin, 1986; Maddox et al., 1992), it is then possible to determine the hydraulic permeability of the glomerular capillary wall (k).

1.3.2 Models of Glomerular Permselectivity

There have been considerable advances in the theoretical description of glomerular permselectivity. For a given "test" solute, the steady-state mass balance along a capillary is

$$\frac{d(Qc_S)}{dx} = -SJ_S \tag{1.6}$$

where c_S is the solute concentration in the capillary lumen and J_S is the solute flux across the glomerular capillary wall. Note that, like equation (1.5), equation (1.6) neglects axial diffusion, uses radially averaged concentrations, and treats the capillary network as a set of identical capillaries in parallel. The latter assumption has been justified by Remuzzi and Deen (1989).

To integrate equation (1.6), one needs to find a suitable expression for the solute flux, J_S. A possible approach to calculate J_S for a single solute is based on the principles

of non-equilibrium thermodynamics and makes use of "phenomenological coefficients", as proposed by Kedem and Katchalsky (Chang, 1980; Chang et al., 1975; Kedem and Katchalsky, 1958). While this approach does not require any assumptions about the microstructure of the capillary wall, it has had limited application because the solute reflection coefficient and diffusive permeability need to be determined experimentally for each solute of interest. Alternatively, the solute flux can be calculated by first proposing an idealized model for the glomerular capillary wall. A simple approach that has been widely used consists of assuming that the capillary wall is a membrane perforated by a homogeneous population of cylindrical pores of radius r_0. Since the length of the pores, ℓ, is usually much larger than r_0, it is possible to neglect "end effects" and assume fully developed flow inside the pore. In this "isoporous model", J_S is simply given by

$$J_S = -fK_d D_\infty \frac{dc_S^*}{dz} + K_c J_V c_S^* \tag{1.7}$$

where c_S^* is the radially averaged solute concentration inside the pore; z is the axial distance along the pore; D_∞ is the solute diffusion coefficient in an unbounded medium; f is the fraction of the capillary area occupied by the pores; and K_c and K_d are, respectively, hindrance coefficients for convection and diffusion, both averaged over the cross-section of the pore as described in Deen (1987). Hindrance coefficients quantify the hydrodynamic interactions between the solute particles and the pore walls: hindrance coefficients for diffusion are related to the increased hydrodynamic drag at the particle surface relative to that in an unbounded medium, whereas hindrance coefficients for convection are related to the fact that the *local* velocity of a neutrally buoyant particle inside the pore is smaller than the unperturbed fluid velocity at the same radial position. Most equivalent pore models of glomerular filtration have used "centerline

approximations", in which K_c and K_d are replaced by the local values of the hindrance coefficients at the centerline of the pore (Deen et al., 1980, 1985; Deen and Satvat, 1981; Remuzzi and Deen, 1989).

The function $c_S^* = c_S^*(z)$ in steady-state can be determined by solving a material balance for the solute,

$$\frac{dJ_S}{dz} = 0, \tag{1.8}$$

which, combined with equation (1.7), leads to

$$Pe\frac{dc_S^*}{d\zeta} = \frac{d^2c_S^*}{d\zeta^2}, \tag{1.9}$$

where Pe is a Peclet number defined by

$$Pe = \frac{K_c J_V \ell}{fK_d D_\infty} \tag{1.10}$$

and ζ (= z/ℓ) is a dimensionless pore axial distance. Assuming equilibrium at the entrance and exit of the pore, the boundary conditions can be written as

$$\begin{aligned} c_S^* &= \Phi c_S \quad \text{at } \zeta = 0 \\ c_S^* &= \Phi c_{SB} \quad \text{at } \zeta = 1, \end{aligned} \tag{1.11}$$

where c_{SB} is the solute concentration in Bowman's space and Φ is the equilibrium partitioning coefficient, equal to $(1 - r_s/r_0)^2$ for neutral spherical particles of radius r_s in cylindrical pores of radius r_0. In equilibrium, the "effective" concentration inside the pore is smaller than that in the bulk solution (i.e., $\Phi < 1$) because the center of the particles cannot sample positions closer than r_s from the pore wall (steric exclusion effect).

With regard to the calculation of c_{SB}, different approaches have been used. While some models assume that c_{SB} is independent of x (Chang, 1980; Chang et al., 1975), Deen et al. (1980) argued that Bowman's space is unlikely to be well mixed and that c_{SB} should be calculated at each axial position, x, by (Deen et al., 1980; DuBois et al., 1975)

$$c_{SB} = \frac{J_S}{J_V}. \tag{1.12}$$

In this case, integration of equation (1.9) leads to

$$J_S = \frac{\Phi K_c J_V c_S}{1 - e^{-Pe}(1 - \Phi K_c)}. \tag{1.13}$$

Equation (1.6) can then be integrated, allowing the calculation of the sieving coefficient, θ, which is given by

$$\theta = \frac{\langle c_{SB} \rangle}{c_{SA}} = \frac{\langle J_S \rangle}{c_{SA} \langle J_V \rangle}, \tag{1.14}$$

where c_{SA} is the solute concentration at the afferent end of the capillary and the brackets indicate axially (x) averaged quantities.

The definition of Pe in equation (1.10) involves two parameters, f and ℓ, which can be related to the ultrafiltration coefficient by assuming Poiseuille flow in the pores. With this assumption, the expression for Pe becomes (Deen et al., 1985):

$$Pe = \frac{r_0^2 K_c (\Delta P - \pi_G)}{8 \mu K_d D_\infty} \tag{1.15}$$

where μ is the viscosity of the ultrafiltrate.

Thus, only two parameters, K_f and r_0, are needed to characterize glomerular filtration using this equivalent pore model. It is possible to compute K_f from micropuncture data, as described in the previous section, and to determine r_0 from fractional clearance data for exogeneous test macromolecules. Although this model is attractive because of its simplicity, it is clear from fractional clearance studies using dextrans that this "isoporous" representation of the glomerular capillary wall is inadequate for molecules with r_s > ~45 - 50 Å (Deen et al., 1985, Myers et al., 1982). That is, the fractional clearance results do not show a sharp cut-off in filtration beyond a certain molecular size, as would be expected from an isoporous membrane. As can be inferred from Figure 1.2, the recent results obtained using Ficoll (Oliver et al., 1992) also suggest that an isoporous model of the capillary wall is inadequate.

There have been several attempts to describe the glomerular capillary wall in a more accurate way. One approach involves the assumption of a continuous distribution of pore radii: lognormal, normal and gamma distributions have been used (Deen et al., 1985, Remuzzi and Deen, 1989; Oliver et el., 1992). The existence of two populations of pores of different radii has also been proposed (Deen et al., 1985; Myers et al., 1982).

Another approach was to assume that the capillary wall has a large number of pores of uniform radii and a small number of large, non-selective pathways. This model, referred to as the "isoporous-with-shunt" model, represents an attempt to explain the presence of small amounts of very large macromolecules in Bowman's space (Deen et al., 1985; Remuzzi and Deen, 1989; Oliver et el., 1992). A recent approach, the "lognormal-plus-shunt" model, consisted of adding a shunt to a lognormal distribution of pore sizes (Oliver et al., 1992).

A different approach, suggested by the fibrous nature of the glomerular basement membrane, would be to assume that the glomerular capillary wall is composed of a random network of fibers. Curry and Michel (1980) developed a "fiber matrix model" based on the Carman-Kozeny equation and on the theory of partitioning and diffusion of Ogston and co-workers (Ogston, 1958; Ogston et al., 1973). This model has been applied to the interpretation of filtration data obtained with isolated films of renal basement membranes (Robinson and Walton, 1987, 1989) and basement membranes of Englebreth-Holm-Swarm (EHS) mouse sarcoma (Katz et al., 1992). It has also been used to predict the hydraulic and solute permeabilities of the endothelial glycocalyx (Levick and Smaje, 1986). However, this model completely neglects the hydrodynamic interactions between permeating solutes and fibers and uses a questionable approximation to calculate the filtration reflection coefficient. A more rigorous approach to describe hindered transport in fibrous media has been developed by Phillips et al. (1989), who described the fibers as fixed periodic arrays of spheres and calculated hindered transport coefficients using a detailed hydrodynamic model. For small solid volume fractions ($\phi < \sim 0.1$) the results compared favorably with an "effective medium" approach based on Brinkman's equation (Brinkman, 1947).

There is experimental evidence that the glomerular capillary wall contains fixed anionic charges (Section 1.2) and this fact must be taken into account when modeling transport of charged molecules. There are only a few theoretical models for glomerular

filtration of charged particles. One approach was to assume that the glomerular capillary wall contains a uniform concentration of fixed anionic charges, c_m (Deen and Satvat, 1981; Deen et al., 1980). In an extension of this model, the glomerular capillary wall was modeled as three layers in series (corresponding to the lamina rara interna, lamina densa and lamina rara externa) each characterized by its own pore size and fixed charge concentration (Van Damme and Prevost, 1985). Wolgast and Ötjeg (1988) developed a "gel model" to describe osmotic flow through the capillary wall. However, the physical basis of this model is highly questionable since the integrity of a hydrogel, when in contact with a protein solution, is attributed entirely to a gel swelling pressure generated by the fixed negative charges in the gel. The main objection to this model is that it completely neglects the fact that a gel in solution tends to swell by absorption of the surrounding solvent, leading to the development of forces associated with tension in the fibers (Flory, 1953).

1.3.3 Concluding Remarks

In addition to their theoretical interest, mathematical models of glomerular filtration are important tools in the quantitative analysis of experimental data. Although the existing models have been applied with appreciable success to the interpretation of a variety of experimental results, they are not accurate enough for some important applications (e.g., to estimate filtration pressures from sieving data (Maddox et al., 1992)) and are not capable of simulating a number of experimentally observed situations (e.g., to predict the effects localized changes in the structure of the glomerular capillary wall). To obtain an accurate mathematical representation of the glomerular filtration process, some of the restrictive assumptions of the existing models must be relaxed.

Two important classes of assumptions are common to all models of glomerular filtration. They concern:

- the time-dependent nature of glomerular filtration (i.e., the pulsatility of blood pressure and flow);
- the microstructure of the glomerular capillary wall.

Implicit in all models described above is the use of time-averaged quantities. In other words, the pulsatility of the blood pressure and flows in the glomerulus has always been neglected and steady-state equations used. This assumption, which has never been critically addressed before, is the focus of the analysis described in Chapter 2.

Perhaps the most over-simplified assumptions of the existing models of glomerular filtration concern the structure of the capillary wall. Most models assume that the capillary wall behaves as an equivalent membrane with cylindrical pores. However, it is clear from Section 1.2 that the glomerular capillary wall does not resemble a membrane with straight pores. In fact, its ultrastructure is highly anisotropic. As a result of their lack of structural detail, the existing models are not capable of predicting the effects of local changes in the morphology of the capillary wall. Therefore, a more realistic approach, one considering the ultrastructure of the capillary wall, is clearly needed. This is the focus of Chapters 3 through 6.

CHAPTER 2

ANALYSIS OF PULSATILE PRESSURES AND FLOWS IN GLOMERULAR FILTRATION

2.1 INTRODUCTION

The pulsatility of the glomerular capillary hydraulic pressure (P_G) has been well established for some twenty years, since the first application of the servo-null pressure technique to the Munich-Wistar rat (Brenner et al., 1971). Glomerular pressure tracings are routinely recorded by numerous investigators, although the waveforms are rarely discussed or reproduced in publications. Representative examples of pressure waveforms recently measured in a normal euvolemic rat are shown in Figure 2.1. The tracing for P_G closely resembles that for the systemic arterial pressure (P_F, femoral artery), although of course with a different mean value and amplitude. Now shown in Figure 2.1, but evident in the original simultaneous tracings for P_G and P_F, is that the glomerular capillary and arterial pressure pulses are exactly in phase. The pressure at the venous end of an efferent arteriole (P_E) has greatly attenuated pulses, and the proximal tubule pressure (P_T) is almost constant (on the time scale of a few cardiac cycles). Representative mean values and amplitudes of the various pressures are shown in Table 2.1. Because the amplitude of the pulses in P_T is negligible, the glomerular transcapillary hydraulic pressure difference, $\Delta P = P_G - P_T$, has an amplitude similar to that of P_G, ±10 mm Hg.

Mathematical models for the glomerular filtration of water and macromolecules (Chang, 1980; Chang et al., 1975; Deen et al., 1985; Deen et al., 1972; Deen et al., 1974; Deen et al., 1980; DuBois et al., 1975; Huss et al., 1975; Lambert et al., 1982; Remuzzi and Deen, 1986; Remuzzi and Deen, 1989) have found extensive application in the interpretation of renal micropuncture and clearance data. As mentioned in Chapter 1,

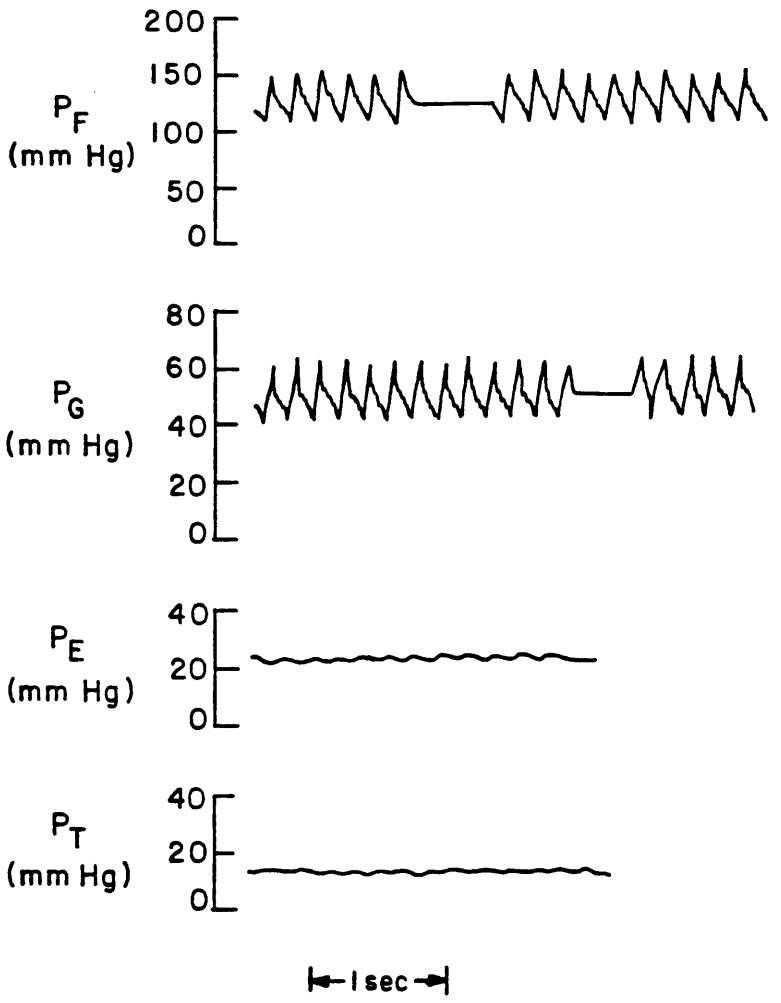

Figure 2.1 - Pressure waveforms measured in the femoral artery (P_F), glomerular capillary (P_G), efferent arteriole (P_E), and proximal tubule (P_T) of a normal euvolemic Munich-Wistar rat (S. Anderson, personal communication). The tracings for P_F and P_G also show time-integrated mean values.

Table 2.1 - Representative Hydraulic Pressures in the Rat

	Mean (mm Hg)	Amplitude (mm Hg)
Femoral artery (P_F)	120	±20
Glomerular capillary (P_G)	48	±10
Efferent arteriole (P_E)	22	±1
Proximal tubule (P_T)	12	≅0

such models are needed to calculate the value of the ultrafiltration coefficient (K_f) from measured pressures and flows, and to obtain pore-size parameters from the fractional clearances of test molecules such as dextran. Accurate models are indispensable in characterizing the effects of a given experimental maneuver or disease state on the intrinsic permeability characteristics of the glomerular capillary wall. All previous models of glomerular filtration use some form of steady state mass balance, and contain only time-averaged pressures, flows, and concentrations. The assumption has been that steady state equations with time-averaged input quantities will accurately simulate the time-averaged behavior of the glomerulus, but this supposition has never been critically examined.

The relatively fast and high amplitude pulses in ΔP provide cause for concern over the validity of steady state models. With a typical afferent oncotic pressure (π_A) of ~20 mm Hg in the rat, the time-averaged net ultrafiltration pressure, $\overline{\Delta P} - \overline{\pi}_G$, declines from ~15 mm Hg at the afferent end of a capillary to at most a few mm Hg at the efferent end. Thus, the ±10 mm Hg variations in ΔP over each cardiac cycle are expected to cause a large percentage change in the net pressure for filtration, enough even to reverse

the transmembrane flux at the more efferent locations along a capillary during part of a cycle. Because the coupled differential equations which describe plasma flow rates, protein concentrations and solute concentrations along a glomerular capillary are nonlinear, the effects of pulsatile pressures (and flows) are not necessarily negligible. That is, the usual steady state equations cannot be obtained from a more accurate set of time-dependent equations by formally averaging all quantities over time. To address these concerns, we describe here a model with pulsatile pressures and flows, and use this model as a standard in evaluating the suitability of previous steady state formulations.

2.2 MATHEMATICAL MODEL

MODEL GEOMETRY. As with most previous models mentioned in Chapter 1, the glomerular capillary network is represented as a number of identical capillaries (of length L) in parallel. As shown in Figure 2.2, the total concentration of impermeant plasma proteins (c_P) and the concentration of some tracer solute (c_S) in the capillary lumen are both assumed to depend on axial position (x) as well as time (t). The effects of a distribution of capillary dimensions in the glomerular network (Remuzzi and Deen, 1986; Remuzzi and Deen, 1989) and of concentration variations over a given lumenal cross-section (Deen et al., 1974) have been shown to be minor. The capillary wall is treated as an equivalent membrane, consisting of a rigid matrix perforated by cylindrical pores of length ℓ. Axial position along a pore is denoted by z, and the solute concentration within a pore is given by c_S^*. The solute concentration at the Bowman's space side of the membrane, c_{SB}, is assumed to be determined by the fluxes of water and solute from nearby pores (Deen et al., 1980), and therefore depends on both x and t.

We will refer frequently to quantities which are averaged over one cardiac cycle (of period t_0), and occasionally to quantities averaged over the length of a capillary. For a given variable X, the time-averaged and length-averaged values are denoted by $\overline{X}$ and

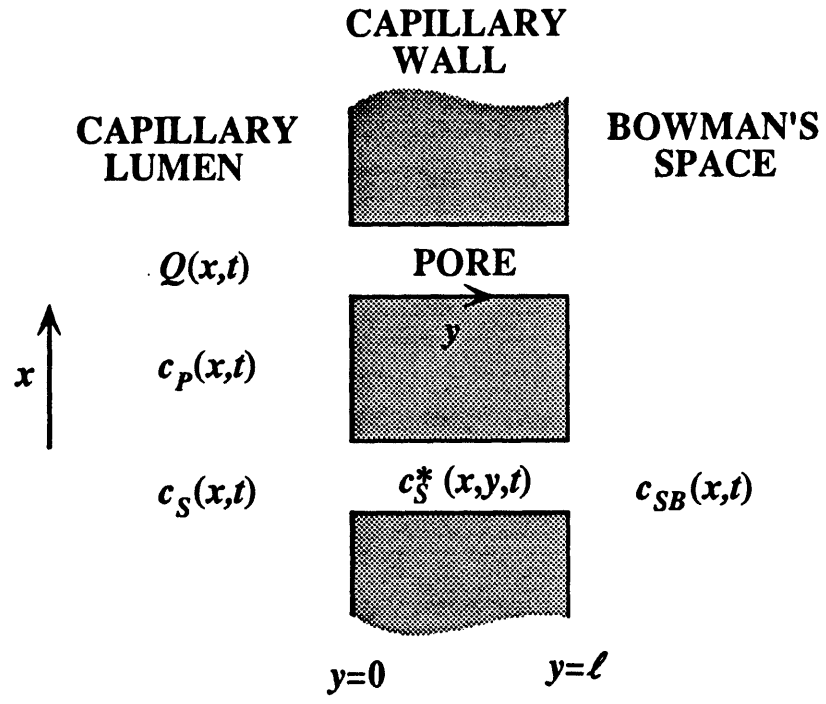

Figure 2.2 - Schematic representation of a portion of the glomerular capillary wall.

$\langle X \rangle$, respectively. The averages were calculated from

$$\overline{X} = \frac{1}{t_0} \int_{t}^{t+t_0} X dt'$$

$$\langle X \rangle = \frac{1}{L} \int_{0}^{L} X dx.$$

In all calculations of $\overline{X}$, t was chosen to be sufficiently large to give a "steady-periodic" variation of X with t (see Section 2.3).

VOLUME FLUX. With the assumption of a rigid membrane, the volume flux J_v from capillary lumen to Bowman's space can be described by the usual Starling relation,

$$J_V = k(\Delta P - \pi_G) \tag{2.1}$$

where k is the effective hydraulic permeability. (Because the final equations to be solved involve only the product SJ_V, where S is the total "membrane" surface area per glomerulus, in this chapter, the important parameter for water filtration is $K_f = kS$.) The local oncotic pressure π_G is related to the plasma protein concentration (c_P) by equation (1.3), that is,

$$\pi_G = a_1 c_P + a_2 c_P^2. \tag{2.2}$$

The oscillations in ΔP, caused by the pulsatility of P_G, are approximated by

$$\Delta P = \overline{\Delta P}(1 + \alpha \cos 2\pi\tau) \tag{2.3}$$

where α is a dimensionless amplitude (fraction of $\overline{\Delta P}$) and the dimensionless time variable is defined as $\tau = t/t_0$. As discussed previously (Brenner et al., 1972), it can be assumed to good approximation that $\overline{\Delta P}$ is independent of x. While the simple harmonic function given by equation (2.3) does not exactly represent the actual P_G waveform in Figure 2.1, it is reasonable to expect that the key elements in pressure pulsatility are the amplitude and frequency, and that waveform details are relatively unimportant.

SOLUTE FLUX. Conservation of solute at any position along a pore requires that

$$\frac{\partial c_S^*}{\partial t} + \frac{\partial J_S^*}{\partial z} = 0 \tag{2.4}$$

where J_S^* is the solute flux based on the cross-sectional area of the pore. Under pulsatile

conditions ($\partial c_s^*/\partial t \neq 0$), J_s^* is not necessarily independent of z, as it would be for a steady state. However, it will be shown that the response time of a pore is sufficiently fast, relative to the pulse time, that the usual steady state expression can be used for the solute flux. That is, the time derivative in equation (2.4) is unimportant, so that the solute concentration and flux in a pore are "quasi-steady."

The instantaneous, local solute flux is given

$$J_s^* = -K_d D_\infty \frac{\partial c_s^*}{\partial z} + K_c J_V^* c_s^* \tag{2.5}$$

where D_∞ is the solute diffusivity in bulk solution, and K_d and K_c are hindrance factors for diffusion and convection, respectively (Deen et al., 1985). The volume flux based on the pore cross-section, J_V^*, is related to J_V by $J_V^* = J_V/f$, where f is the fraction of the capillary surface occupied by pores. Substituting equation (2.5) into equation (2.4), and introducing the dimensionless position variable $\xi = z/\ell$, we obtain

$$\frac{Pe}{Sr}\frac{\partial c_s^*}{\partial \tau} + g\,Pe\frac{\partial c_s^*}{\partial \xi} = \frac{\partial^2 c_s^*}{\partial \xi^2} \tag{2.6}$$

$$Pe = \frac{K_c \bar{J}_V \ell}{f K_d D_\infty} = \frac{r_0^2 K_c \left(\overline{\Delta P} - \overline{\pi}_G\right)}{8\mu K_d D_\infty} \tag{2.7}$$

$$Sr = \frac{K_c \bar{J}_V t_0}{f \ell} = \frac{t_0}{t_c} \tag{2.8}$$

$$g = \frac{J_V}{\bar{J}_V}. \tag{2.9}$$

As described in Section 1.3, the second expression for the Peclet number, Pe, in equation (2.7), involving the pore radius (r_0) and the viscosity of the ultrafiltrate (μ), follows from

the assumption of Poiseuille flow in a pore (Chang et al., 1975; Deen et al., 1985). The "new" dimensionless group is the Strouhal number, *Sr*, which is the ratio of the pulse time (t_0) to the convective transit time for solute in the pore, $t_c = f\ell/(K_c\bar{J}_V)$. Both *Pe* and *Sr* depend on solute size (through K_c, K_d and D_∞) and on position along a capillary (through $\bar{J}_V$).

The magnitude of *Sr* provides an indication of the importance of the time derivative in equation (2.6). In particular, if $Sr >> 1$, the time derivative term will tend to be negligible. When this is true, the solute concentration profile along a pore responds almost instantaneously to changes in c_S or J_V. Under these quasi-steady conditions, the remaining terms in equation (2.6) can be integrated to obtain c_S^*, and then $J_S = J_S^*/f$

$$J_S = \frac{\Phi K_c J_V c_S}{1 - e^{-g\,Pe}(1 - \Phi K_c)} \tag{2.10}$$

where Φ is the equilibrium partition coefficient. As with K_c and K_d, Φ for neutral, spherical macromolecules depends only on the ratio of solute radius to pore radius, r_s/r_0 (Deen et al., 1985). In obtaining equation (2.10) we used the relations

$$c_S^*(x,0,t) = \Phi c_S(x,t) \tag{2.11}$$

$$c_S^*(x,\ell,t) = \Phi c_{SB}(x,t) \tag{2.12}$$

$$c_{SB} = \frac{J_S}{J_V}. \tag{2.13}$$

Equations (2.11) and (2.12) are based on the usual assumption that the pores are sufficiently long to neglect mass transfer resistances associated with the pore ends (Keh, 1986). This is justified by the fact that the thickness of the basement membrane alone (~1000 Å) greatly exceeds typical values of r_0 (~50 Å). The basis for equation (2.13) has

been discussed in Section 1.3.

Equation (2.10) is identical to solute flux expressions in previous steady state models (equation (1.13)), except that J_V, c_S, and the new quantity g are now functions of time. As already mentioned, this quasi-steady result is expected to be valid for $Sr >> 1$. For typical hemodynamic conditions in the rat, Sr declines from ~300 at the afferent end of a capillary to ~30 at the efferent end; the dependence of Sr on solute size is relatively weak for the sizes of main interest, $20 \leq r_s \leq 50$ Å. To test whether $Sr = 30$ is sufficiently large to obtain the quasi-steady result, we compared fluxes calculated from numerical integration of the full time-dependent equation (equation (2.6)) with those obtained from equation (2.10). Equation (2.6) was solved for $c_S^*(\xi,\tau)$ for conditions representative of the efferent end of a capillary, where Sr is smallest. The function $g(\tau)$ and the upstream boundary concentration $c_S^*(0,\tau)$ were assumed to be sinusoidal in time, as determined by the solution to the time-dependent luminal mass balance equations (see below). The other boundary concentration, $c_S^*(1,\tau)$, was assumed constant for the purpose of these tests. The solute flux $J_S^*(\xi,\tau)$ computed from equations (2.5) and (2.6) was found to be practically indistinguishable from that obtained using the quasi-steady approach (equation (2.10)). These results confirmed the validity of equation (2.10) for describing solute fluxes across the glomerular capillary wall under pulsatile conditions.

MASS BALANCES FOR THE CAPILLARY LUMEN. Conservation equations are needed to describe variations in plasma flow rate (Q), c_P, and c_S with time and position along a capillary. Neglecting concentration polarization and axial diffusion (Deen et al., 1974), these equations can be written as

$$\frac{du}{d\eta} = -\frac{SJ_V}{\overline{Q}_A} \tag{2.14}$$

$$\kappa\frac{\partial\phi_P}{\partial\tau} + \frac{\partial(u\phi_P)}{\partial\eta} = 0 \tag{2.15}$$

$$\kappa \frac{\partial \phi_S}{\partial \tau} + \frac{\partial (u \phi_S)}{\partial \eta} = -\frac{S J_S}{\overline{Q}_A c_{SA}}. \tag{2.16}$$

Dimensionless position along a capillary is denoted by $\eta = x/L$. The dimensionless plasma flow rate (u), protein concentration (ϕ_P) and solute concentration (ϕ_S) are all expressed relative to values at the afferent end of a capillary: $u = Q/\overline{Q}_A$, $\phi_P = c_P/c_{PA}$, and $\phi_S = c_S/c_{SA}$. The coefficient κ is defined by

$$\kappa = \frac{t_r}{t_0} \tag{2.17}$$

where t_r is the mean residence time (transit time) for plasma in the capillary lumen. Because κ is not small (see Section 2.3), it is not possible to neglect the time derivatives in equations (2.15) and (2.16), as was done for the analogous conservation equation for a single pore (equation (2.6)). The absence of a time derivative in equation (2.14) depends only on the assumption that the capillaries behave as rigid tubes; for a constant density fluid in a rigid conduit, there is no possibility of any time-dependent accumulation of total mass.

Although technical limitations have prevented measurement of plasma flow oscillations at the single nephron level, the pulsatile pressures undoubtedly result in oscillations of the afferent arteriolar plasma flow rate. We describe these in a manner similar to the oscillations in ΔP (equation (2.3))

$$Q_A = \overline{Q}_A \left[1 + \beta \cos 2\pi (\tau + \tau_0) \right]. \tag{2.18}$$

The new quantities in equation (2.18) are the dimensionless amplitude, β, and the phase

shift (relative to the pressure oscillations), τ_0.

The initial and boundary conditions used to solve equations (2.14) - (2.16) are

$$\eta = 0: \quad u = 1 + \beta \cos 2\pi(\tau + \tau_0)$$
$$\phi_P = 1 \qquad (2.19)$$
$$\phi_S = 1$$

$$\tau = 0: \quad u = 1 + \beta \cos 2\pi\tau_0$$
$$\phi_P = 1 \qquad (2.20)$$
$$\phi_S = 1 \ .$$

Equation (2.19) follows directly from equation (2.18) and the definitions of u, ϕ_P, and ϕ_S. The initial state specified by equation (2.20) is entirely arbitrary, because our objective is to simulate only the "steady-periodic" behavior of the glomerulus, in which all variables experience repetitive cycles. Equation (2.20) serves only as a convenient condition for starting the simulations; as will be shown, the system of equations soon "forgets" the condition imposed at $\tau = 0$.

The equations were solved using a finite difference method adapted from the Lax-Wendroff scheme (Press et al., 1986).

FILTRATION RATES. The single nephron glomerular filtration rate (*SNGFR*), averaged over a cardiac cycle, was calculated from

$$\overline{SNGFR} = \overline{Q}_A \left[1 - \overline{u}(1)\right] . \qquad (2.21)$$

The time-averaged sieving coefficient of a given macromolecule is given by

$$\overline{\theta} = \frac{\langle \bar{J}_S \rangle}{c_{SA} \langle \bar{J}_V \rangle}. \tag{2.22}$$

For a macromolecular tracer which is not secreted or reabsorbed by the tubule, $\overline{\theta}$ would equal the urinary fractional clearance.

FILTRATION REVERSAL. Given the relatively large amplitude of the oscillations in P_G and ΔP (Table 2.1), there are occasions when $\pi_G > \Delta P$, causing the direction of filtration to reverse. Thus, at the more efferent locations along a capillary, there are periods when $J_V < 0$ (equation (2.1)) and, concurrently, $J_S < 0$. For consistency with the underlying physical assumptions, we replaced equation (2.10) during filtration reversal by

$$J_S = \frac{\Phi K_c J_V c_{SB}}{1 - e^{\varepsilon Pe}(1 - \Phi K_c)}. \tag{2.23}$$

Taken together, equations (2.10) and (2.23) yield sieving characteristics of the capillary wall which are independent of the direction of transmembrane flow, as expected for a porous membrane of fixed structure.

The only difficulty in applying equation (2.23) is in evaluating c_{SB}. Because during filtration reversal Bowman's space is no longer "downstream," equation (2.13) for c_{SB} is no longer valid. To develop an alternative approximation for c_{SB}, we note that at each location where filtration reversal occurs, the amount of fluid filtered during the preceding "forward flow" period can be computed. Considering that this fluid forms a layer of thickness ℓ_f, it can be shown that $\ell_f \leq 0.8$ μm, and that the characteristic time for diffusional equilibration within this layer (ℓ_f^2/D_∞) is less than 5% of the pulse period. In other words, concentration variations in this fluid layer, in the direction perpendicular

to the membrane, will tend to be minimal. Accordingly, we replaced c_{SB} in equation (2.23) by $\hat{c}_{SB}$, the average solute concentration computed for the period of forward filtration ($\tau_1 \le \tau \le \tau_2$)

$$\hat{c}_{SB} = \frac{\int_{\tau_1}^{\tau_2} J_S d\tau}{\int_{\tau_1}^{\tau_2} J_V d\tau}. \qquad (2.24)$$

No modifications in the volume flux equation or the mass balance equations are needed to accommodate periods of filtration reversal.

PORE STRUCTURE. For simplicity, most of the calculations assumed a single population of pores of radius r_0. The size-dependent factors Φ , K_d and K_c were calculated as described previously (Deen et al., 1985). For comparison with this "isoporous" model, we considered also an "isoporous with shunt" representation in which, besides small pores of radius r_0, there exists a nonselective pathway which permits free filtration of all sizes of molecules. To account for the contribution of the shunt to the volume flux, J_V, it is necessary to replace equation (2.1) by

$$J_V = k(\Delta P - \pi_G) + \omega J_V \qquad (2.25)$$

where ω is the fraction of the filtrate volume passing through the nonselective pathway.

While the driving pressure for filtration through the shunts, ΔP, is not a function of axial position in the capillary, the driving pressure for filtration through the small pores, ΔP - π_G, changes throughout the capillary. Therefore, ω is not a constant. However, the fraction of the filtrate volume that would pass through the shunts in the hypothetical situation where $\pi_G = 0$ is solely a property of the capillary wall. Denoting this fraction by ω_0, ω can be calculated by

$$\omega = \frac{1}{1 + \frac{1-\omega_0}{\omega_0}\frac{\Delta P - \pi_G}{\Delta P}\frac{\mu_P}{\mu}} \tag{2.26}$$

where μ_P is the viscosity of plasma (Deen et al., 1985). We used $\mu_P/\mu = 1.6$.

The contribution of the shunts to the solute flux, J_S, is $\omega J_V C_S$ and, thus, equation (2.10) must be replaced by

$$J_S = \frac{\Phi K_c (1-\omega) J_V c_S}{1 - e^{-s\,Pe}(1 - \Phi K_c)} + \omega J_V c_S. \tag{2.27}$$

Note that filtration through the shunt does not reverse, because the oncotic pressure is assumed not to act across these large pores.

2.3 RESULTS

Unless noted otherwise, the results presented are for the isoporous representation of the capillary wall. The input parameters used in most of the simulations are summarized in Table 2.2. The values of $\overline{\Delta P}$, $\overline{Q}_A$, c_{PA}, K_f, and r_0 are all representative of normal euvolemic Munich-Wistar rats. The pulse period (t_0) is based on a typical heart rate in the rat of 5 s^{-1} (see Figure 2.1), whereas the lumenal residence time (t_r) is a mean value for the rat glomerulus estimated by Shea (1981). The relative amplitude for ΔP was calculated from the values in Table 2.1: $\alpha = 10/36 = 0.28$.

The relative amplitude and phase for Q_A (β and τ_0) were also estimated from the pressure data, as follows. The instantaneous plasma flow rate is related to the pressure

Table 2.2 - Model Parameters for the Euvolemic Rat

Quantity	Value
$\overline{\Delta P}$	36 mm Hg
$\overline{Q}_A$	140 nl/min
c_{PA}	5.7 g/dl
K_f	5.0 nl/(min.mm Hg)
r_0	50 Å
t_0	0.2 s
t_r	0.4 s
α	0.28
β	0.14
τ_0	0

drop across the afferent arteriole (ΔP_A) and the afferent arteriolar resistance (R_A) by

$$Q_A = \frac{\Delta P_A}{R_A}. \tag{2.28}$$

Assuming that almost all of the pre-glomerular pressure drop occurs in the afferent arteriole, $\Delta P_A \cong P_F - P_G$. As already noted in connection with Figure 2.1, the oscillations in P_F and P_G are in phase. It follows that ΔP_A can be approximated as

$$\Delta P_A = \overline{\Delta P}_A (1 + \gamma \cos 2\pi\tau) \tag{2.29}$$

where γ is a relative amplitude for ΔP_A (analogous to α in equation (2.3)). If it is assumed further that R_A is constant, equations (2.28) and (2.29) can be combined to give

$$Q_A = \overline{Q}_A(1+\gamma\cos 2\pi\tau) \tag{2.30}$$

where $\overline{Q}_A = \overline{\Delta P}_A/R_A$. A comparison of equations (2.18) and (2.30) then suggests that $\beta = \gamma$ and $\tau_0 = 0$. From Table 2.1, $\beta = \gamma = (20 - 10)/(120 - 48) = 0.14$. In support of this approach, we note that the phase shift between pressure and flow in the human renal artery has been found to be approximately zero (Mills et al., 1970). Moreover, for pulsatile blood flow in fine glass tubes, pressure and velocity variations are in phase (Bugliarello and Sevilla, 1970).

Figure 2.3 illustrates the distinction between the "transient" and "steady-periodic" behavior of a variable, in this case the luminal concentration of a solute with $r_S = 30$ Å. The behavior of $\phi_S = c_S/c_{SA}$ is shown for two axial locations, near the afferent end of the capillary ($\eta = 0.2$) and at the efferent end ($\eta = 1$). At either location, ϕ_S evolves from the arbitrary initial value of unity to a pattern which is steady-periodic, or repetitive in time. The evolution occurs more quickly for $\eta = 0.2$ (because there is less change from the initial value), but even for $\eta = 1$ the initial transient is complete after about three pulse periods ($\tau \cong 3$). Plasma flow rates and protein concentrations exhibited similar behavior. Of interest is that varying t_r (over a twenty-five-fold range) caused directionally similar changes in the duration of the transient phase, but had no significant effect on the steady-periodic results. By replacing equation (2.20) by various other initial conditions, we confirmed that the steady-periodic solutions were independent of the flow and concentration profiles specified at $\tau = 0$. Time-averaged values over a cycle were computed only when the root-mean-square difference in each of the variables (u, ϕ_P, ϕ_S) relative to the previous cycle was $< 10^{-5}$.

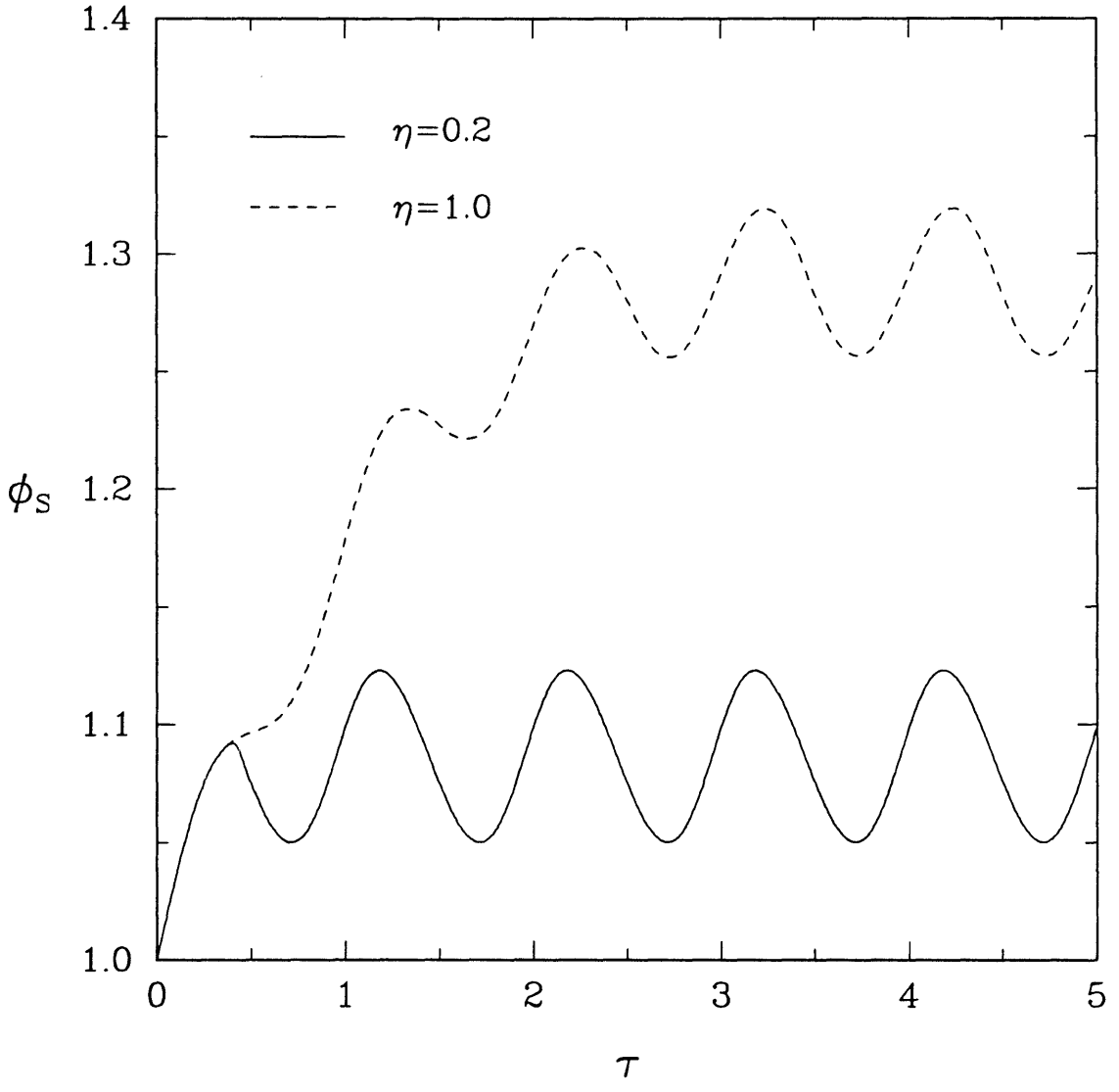

Figure 2.3 - Dimensionless solute concentration in capillary lumen (ϕ_s) as a function of time (τ), at two axial locations (η). The assumed molecular radius is 30 Å, and other quantities are as given in Table 2.2. "Steady-periodic" behavior is achieved for $\tau > 3$.

The time-dependent behavior of the volume flux, expressed in dimensionless form as $SJ_V/\overline{Q}_A$, is illustrated in Figure 2.4. For clarity in this and Figures 2.5 - 2.8, $\tau = 0$ is redefined as the start of any steady-periodic cycle; thus, the complete steady-periodic solution is illustrated for $0 \leq \tau \leq 1$. As shown in Figure 2.4, filtration reversal ($J_V < 0$) is predicted for the efferent end of the capillary over slightly less than half of each cardiac cycle. At either axial position shown, J_V is nearly in phase with ΔP, which peaks at $\tau = 0$ and $\tau = 1$ (equation (2.3)). The reason there is a slight phase difference lies in the behavior of the oncotic pressure term. As shown in Figure 2.5, the protein concentration (expressed as $\phi_P = c_P/c_{P_A}$) lags behind ΔP by about one-quarter cycle. The consequent lag in π_G is responsible for the slight phase shift in J_V.

The plasma flow rate (expressed as $u = Q/\overline{Q}_A$) exhibits more interesting phase behavior, as shown in Figure 2.6. At $\eta = 0.2$ the local plasma flow rate is essentially in phase with Q_A and ΔP, whereas at $\eta = 1$ it is almost fully out of phase. These results may be explained on the basis of two competing effects. Near the afferent end of a capillary the plasma flow rate is controlled largely by conditions in the afferent arteriole, so that it oscillates in phase with Q_A. Opposing this influence is the fact that peaks in J_V (which are almost in phase with those in Q_A), increase the rate at which plasma flow declines along a capillary. Thus, the pressure-induced oscillations in J_V tend to make the plasma flow rate along a capillary completely out of phase with Q_A. As evidenced by the results for $\eta = 1$ in Figure 2.6, the latter effect has become dominant by the efferent end of the capillary, for the parameter values used.

The competing influences of Q_A and ΔP on the efferent arteriolar plasma flow rate (Q_E) can be seen more clearly by integrating equation (2.14) over the length of the capillary. Expressed in terms of $u_E = Q_E/\overline{Q}_A$, the result is

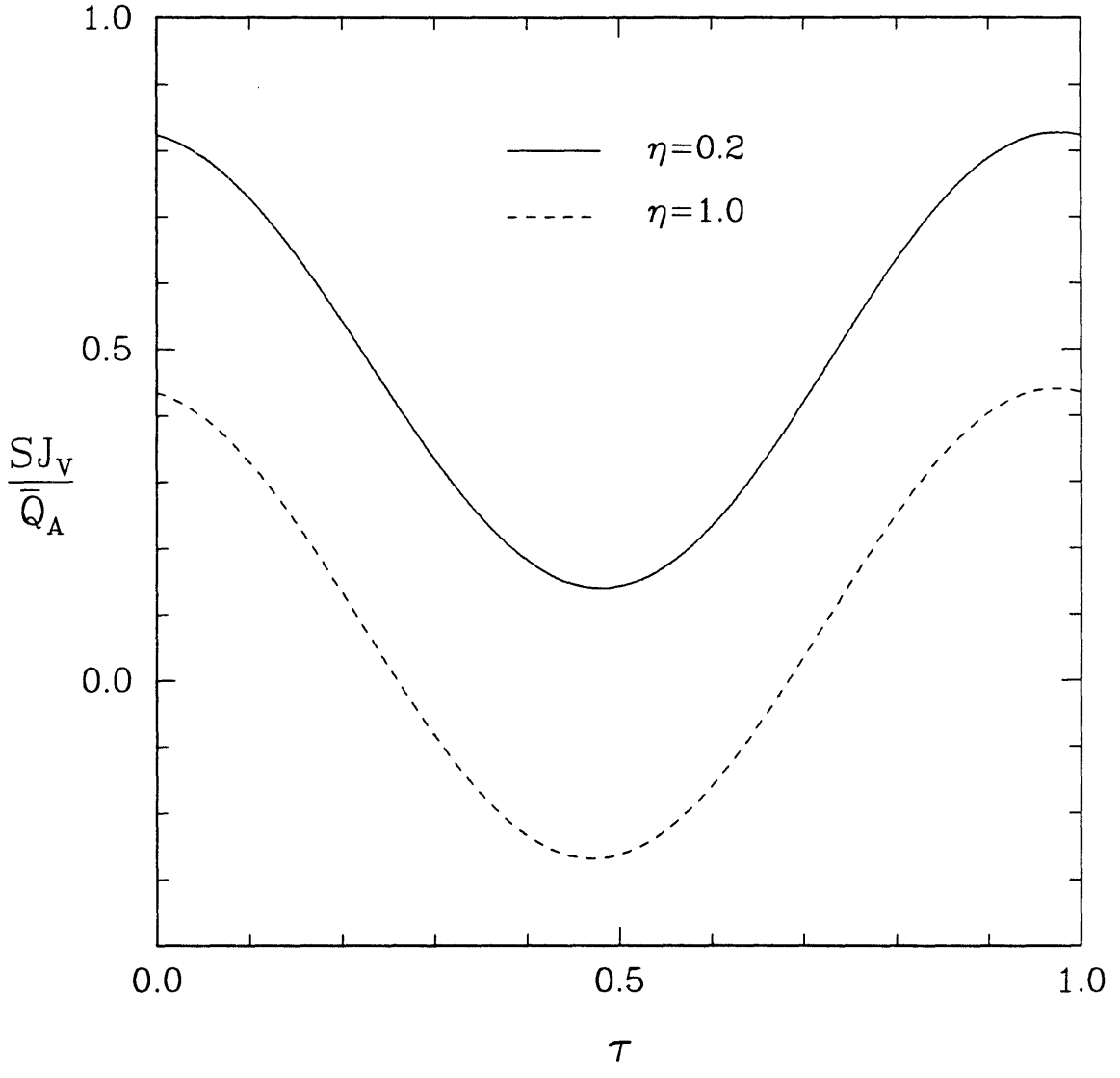

Figure 2.4 - Variations in dimensionless transmural volume flux ($SJ_V/\overline{Q}_A$) over a cardiac cycle, at two axial locations. In this and Figures 2.5 - 2.8, τ = 0 corresponds to the beginning of any cardiac cycle, once steady-periodic behavior has been achieved.

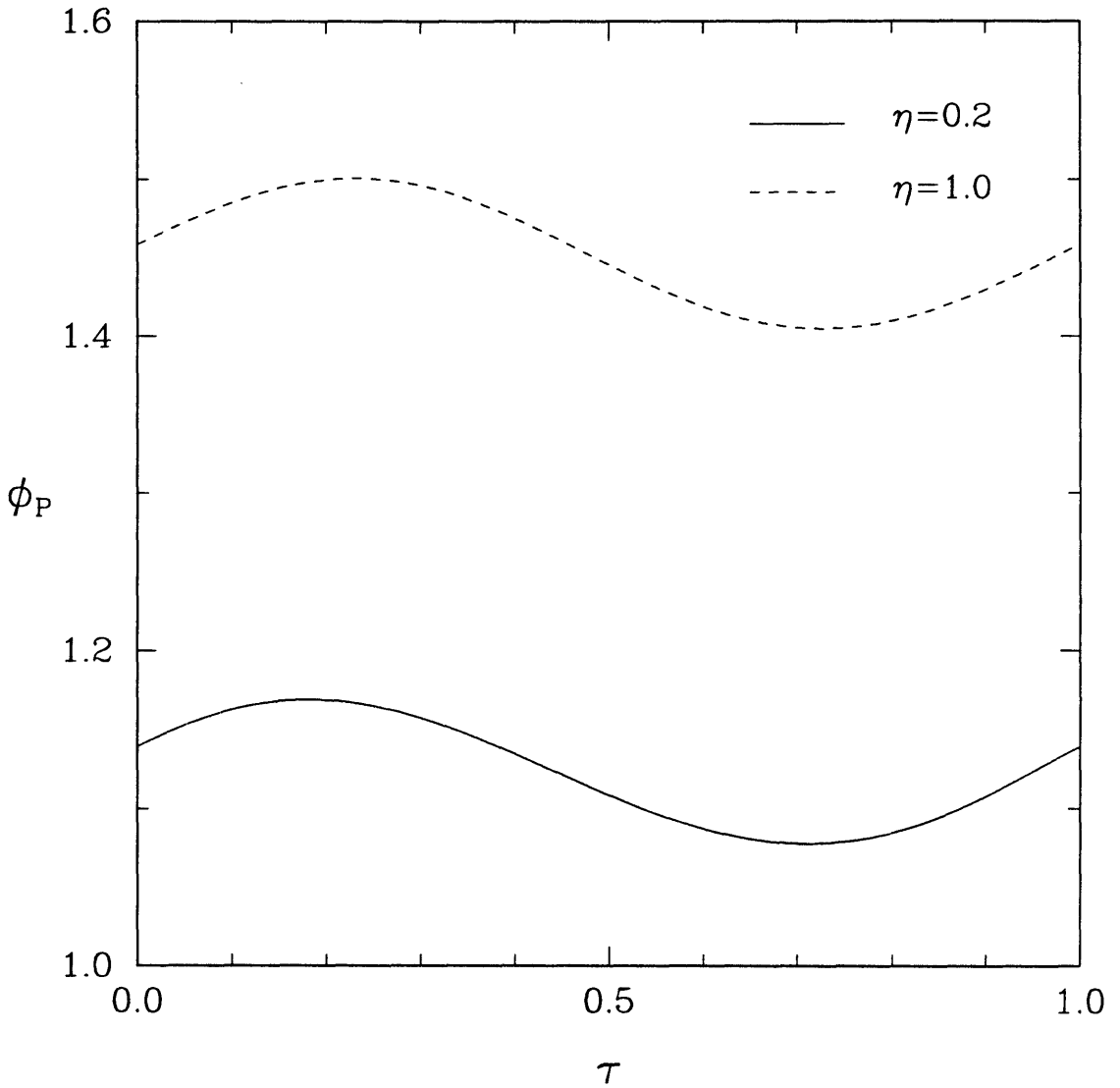

Figure 2.5 - Variations in dimensionless protein concentration (ϕ_P) over a cardiac cycle, at two axial locations.

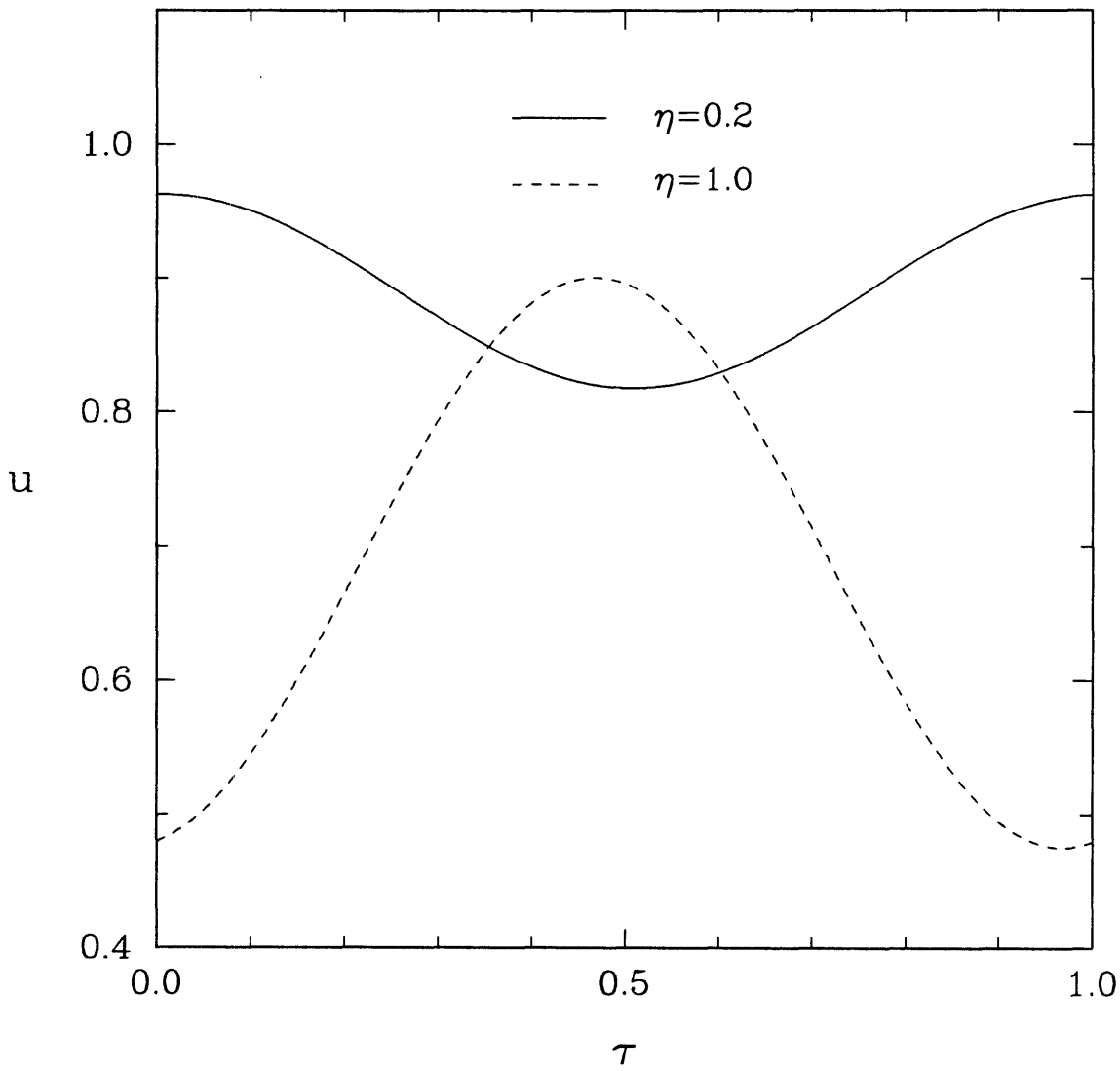

Figure 2.6 - Variations in dimensionless plasma flow rate (u) over a cardiac cycle, at two axial locations.

$$u_E = 1 + F\left(1 - \frac{\langle \pi_G \rangle}{\overline{\Delta P}}\right) + (\beta - \alpha F)\cos 2\pi\tau \qquad (2.31)$$

where $F = K_f \overline{\Delta P}/\overline{Q_A}$. Although $\langle \pi_G \rangle$ also varies with time, the main contribution to the oscillations in u_E comes from the last term in equation (2.31). Thus, Q_E will tend to be in phase with Q_A when β - $\alpha F > 0$, and out of phase when β - $\alpha F < 0$. For the parameter values in Table 2.2, $\beta - \alpha F = -0.22$. Accordingly, u at $\eta = 1$ is out of phase with Q_A, as shown in Figure 2.6.

Instantaneous solute concentrations next to the Bowman's space side of the capillary wall ($\phi_{SB} = c_{SB}/c_{SA}$) are shown in Figure 2.7, again for $r_s = 30$ Å and $\eta = 0.2$ or $\eta = 1$. In interpreting either curve, it is helpful to bear in mind that the instantaneous sieving coefficient (downstream/upstream concentration ratio) varies inversely with $|J_V|$. When volume flow ceases, the transmembrane solute concentrations quickly equilibrate ($c_S = c_{SB}$ for $J_V = 0$). Thus, for $\eta = 0.2$, ϕ_{SB} reaches a maximum for $\tau \cong 0.5$ when J_V is at its minimum (recall Figure 2.4). Likewise, for $\eta = 1$, ϕ_{SB} exhibits similar (although more exaggerated) trends near the beginning and end of a cycle. However, at $\eta = 1$, filtration reversal begins at $\tau = 0.27$ and continues until $\tau = 0.69$, and during this period c_{SB} is assigned the constant value determined by equation (2.24). At the two instants when $J_V = 0$, $c_{SB} = c_S > c_{SA}$, which is why ϕ_{SB} exceeds unity.

Plotted in Figure 2.8 is the transmembrane solute flux computed for the same conditions as in Figure 2.7. As expected from an inspection of equation (2.10), J_S tends to vary in parallel with J_V. The main purpose of Figure 2.8 is to show that the computed value of J_S at $\eta = 1$ varies smoothly with time, despite the discontinuous nature of the approximation used for c_{SB} (recall Figure 2.7). The mass balance equations are very forgiving of possible errors in c_{SB} at times when $J_V \cong 0$, because there is very little transmembrane movement of solute at those moments.

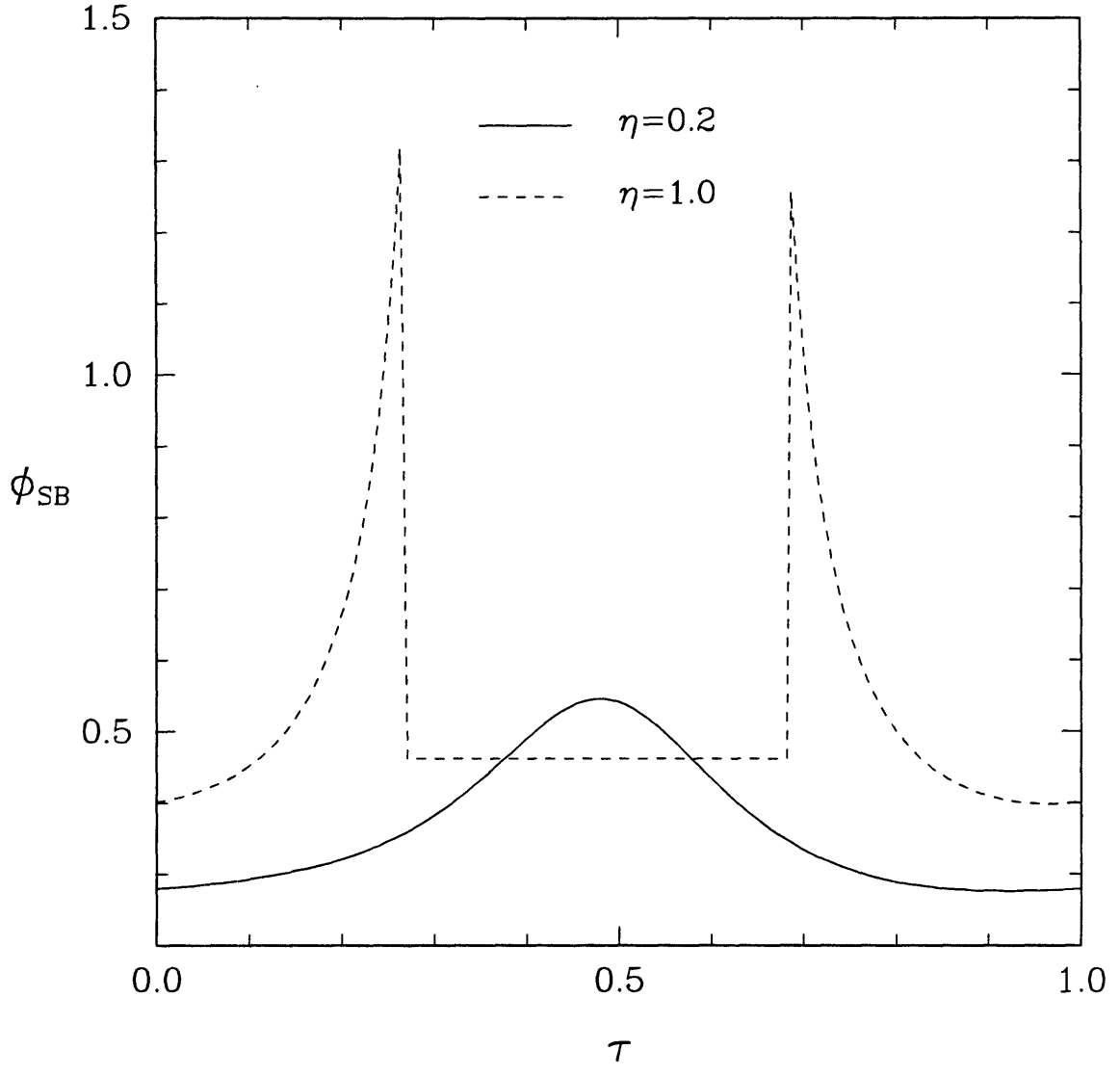

Figure 2.7 - Variations in dimensionless solute concentration in Bowman's space (ϕ_{SB}) over a cardiac cycle, at two axial locations.

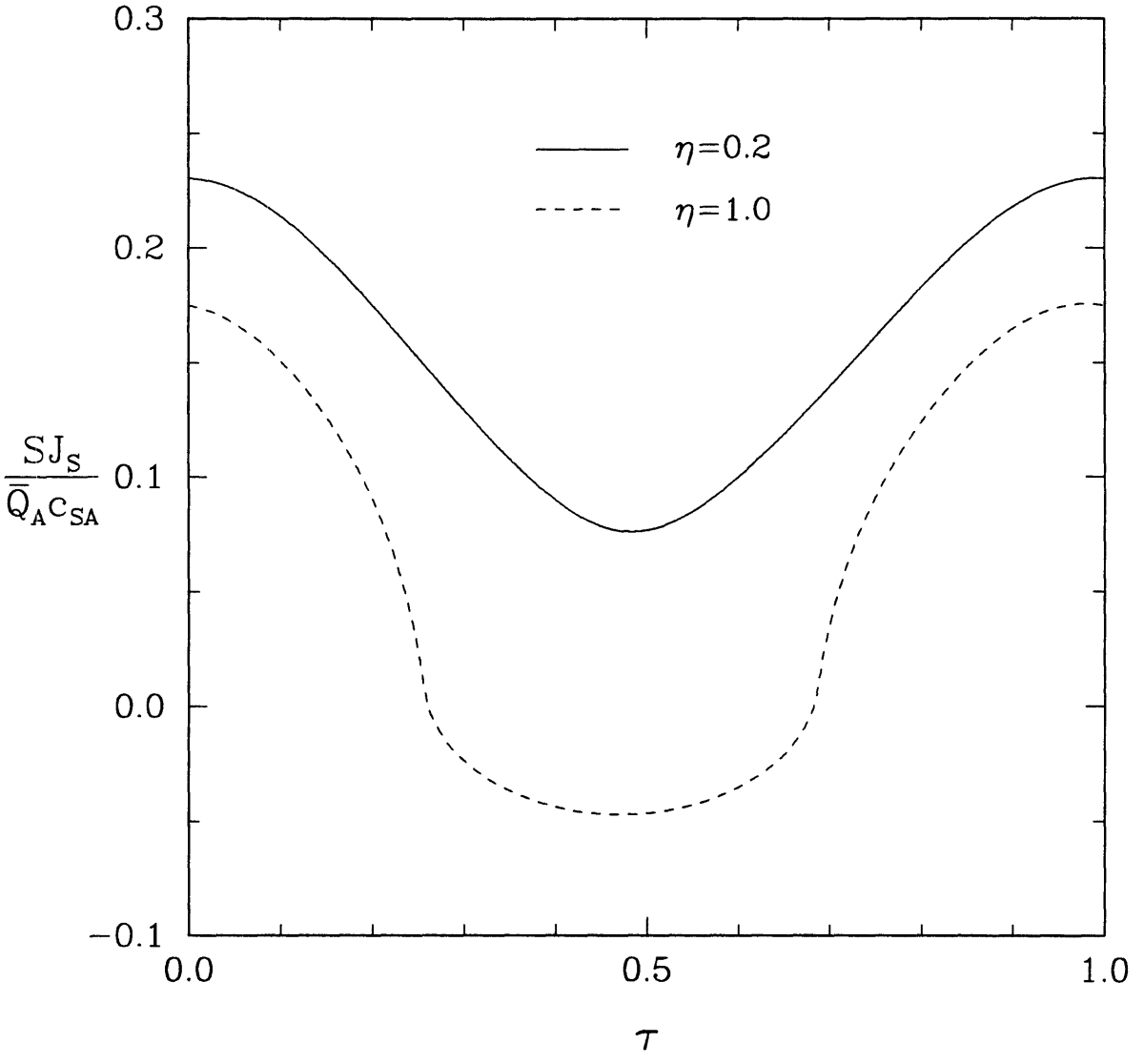

Figure 2.8 - Variations in dimensionless solute flux (30 Å molecular radius) over a cardiac cycle, at two axial locations.

The most significant quantities are the overall measures of the filtration process, $\overline{SNGFR}$ and $\bar{\theta}$. To assess the possible errors in neglecting the pulsatility of ΔP and Q_A, we compared results of the present model with steady state calculations, using the same time-averaged input parameters. A steady state model equivalent to one reported previously (Deen et al., 1985) was obtained by neglecting the time derivatives in equations (2.15) and (2.16), setting $\Delta P = \overline{\Delta P}$ in equation (2.3), and setting $u = 1$ in equation (2.19). For the baseline conditions (Table 2.2), the pulsatile and steady state values of $\overline{SNGFR}$ were identical to four digits (43.63 nl/min). Moreover, $\overline{SNGFR}$ was found to be insensitive to the values chosen for α and β. For example, with $\alpha = 0.28$ and $\tau_0 = 0$, increasing β from 0 to 0.3 caused only a 0.2% change in $\overline{SNGFR}$. Similarly, changes in τ_0 had a negligible effect on $\overline{SNGFR}$. These results imply that there will be negligible error in using a steady state model to calculate K_f from measured values of $\overline{SNGFR}$, $\overline{Q}_A$, $\overline{\Delta P}$, and c_{PA}.

Theoretical sieving curves ($\bar{\theta}$ vs. r_s) computed using the pulsatile and steady state models are compared in Figure 2.9. For the smaller molecules, $\bar{\theta}$ is seen to be lower for the pulsatile model by as much as 10%. The two curves cross at $r_s \cong 35$ Å, but there are only very small differences between the curves for values of r_s larger than that. To assess the magnitude of the error in using the steady-state model to interpret fractional clearance data, we treated the values of $\bar{\theta}$ obtained with the pulsatile model as if they were a set of experimental data, and performed a least-squares fit of the steady state model to these "data" (Remuzzi and Deen, 1989). The pore radius was adjusted to minimize the following sum of squared errors

$$\sum_{i=1}^{n}\left(\frac{\bar{\theta}_i^* - \bar{\theta}_i}{\bar{\theta}_i}\right)^2$$

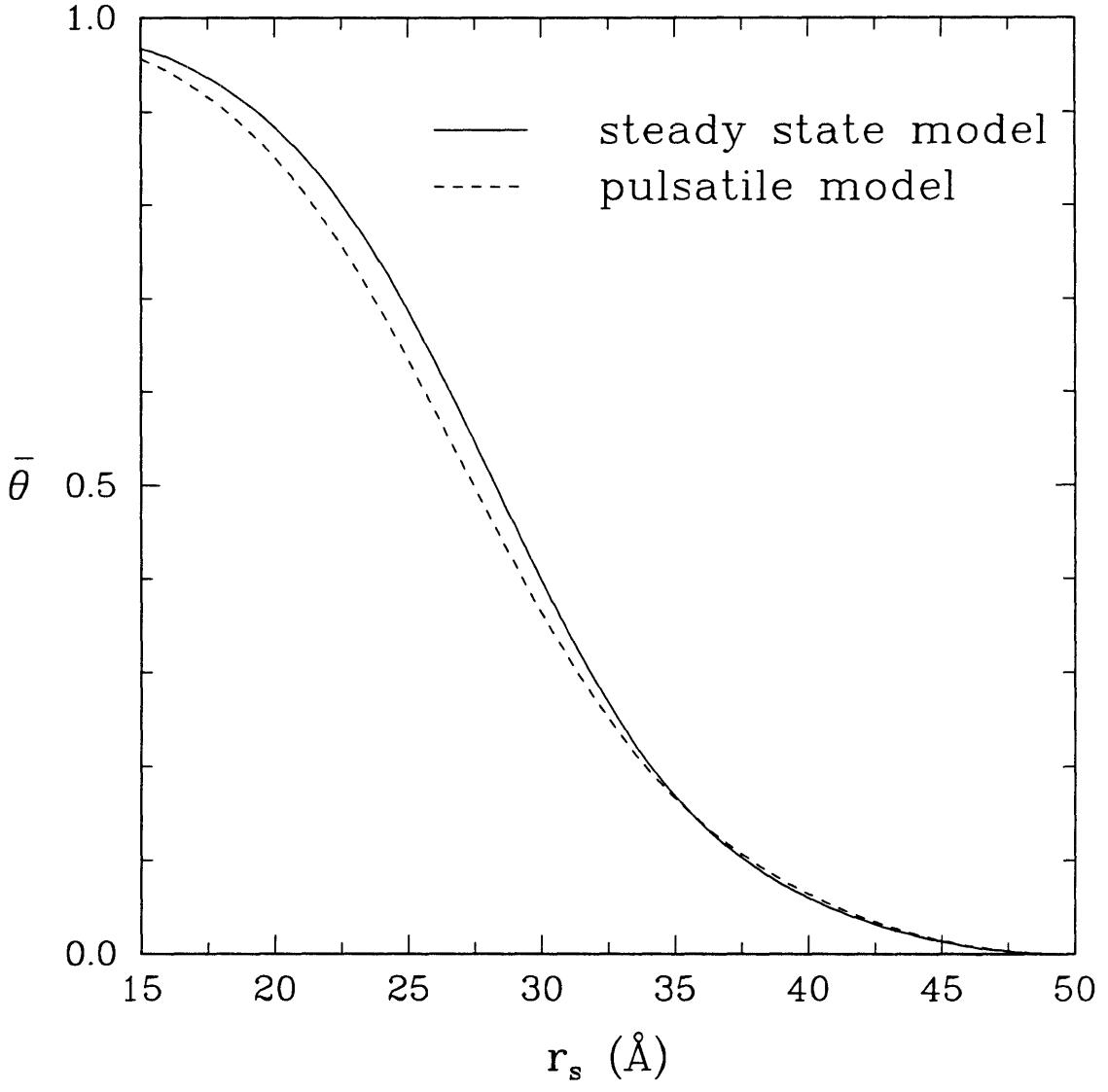

Figure 2.9 - A comparison of sieving curves computed using the pulsatile model and a steady-state model, for an isoporous membrane and input parameters given in Table 2.2.

where n is the number of molecular sizes considered, and $\overline{\theta}_i$ and $\overline{\theta}_i^*$ are the "true" and calculated values of the sieving coefficient, respectively. As shown in Table 2.3, this yielded a pore radius of 50.1 Å. The tendency of the steady-state model to overestimate $\overline{\theta}$ for small molecules was balanced by its tendency to underestimate $\overline{\theta}$ for large molecules, the result being that the best-fit pore radius was virtually identical to the "true" pore radius.

The conclusions reached with the "isoporous with shunt" model were similar to those already described for the isoporous model. The value of $\overline{SNGFR}$ obtained for pulsatile conditions was again indistinguishable from that calculated using steady-state mass balance equations ($\overline{SNGFR}$ = 44.06 nl/min for ω_0 = 0.01). The sieving curves (Figure 2.10) were similar to those obtained with the isoporous approach (Figure 2.9), except that $\overline{\theta}$ with a shunt remains greater than zero for $r_s \geq r_0$. As shown in Table 2.3, when the pulsatile model was used to generate "data", the fitted values of r_0 and ω_0 using the steady state approximation were almost identical to the "true" values, for a wide range of ω_0. The most significant functional characteristic of the shunt is $\overline{\theta}_\infty$, which is the sieving coefficient calculated for the largest molecules (where $r_s \geq r_0$). It is given by

$$\overline{\theta}_\infty = \frac{\left\langle \overline{\omega J_V c_S} \right\rangle}{c_{SA} \left\langle \overline{J}_V \right\rangle} \tag{2.32}$$

where the overbar in the numerator denotes the time-average of the product of the quantities shown (not the product of the individual time-averages). As indicated in Table 2.3, the difference between the pulsatile and best-fit steady state values of $\overline{\theta}_\infty$ was negligible for all cases examined.

Also tested was the ability of the steady state model to accurately describe the response of $\overline{\theta}$ to hemodynamic perturbations. To do this we compared the values of $\overline{\theta}$

Table 2.3 - Effects of the Steady State Assumption on the Values of Fitted Pore-Size Parameters

Membrane Model	Pulsatile Model [a]			Steady-State Model [b]		
	r_0 (Å)	ω_0	$\overline{\theta}_{\infty}$	r_0 (Å)	ω_0	$\overline{\theta}_{\infty}$
Isoporous	50.0	0	0	50.1	0	0
Isoporous	50.0	1.0×10^{-4}	3.3×10^{-4}	50.1	9.9×10^{-5}	3.2×10^{-4}
with	50.0	1.0×10^{-3}	3.3×10^{-3}	50.1	1.0×10^{-3}	3.3×10^{-3}
Shunt	50.0	5.0×10^{-3}	1.6×10^{-2}	50.0	5.1×10^{-3}	1.7×10^{-2}
	50.0	1.0×10^{-2}	3.3×10^{-2}	49.8	1.0×10^{-2}	3.3×10^{-2}

(a) The values of r_0 and ω_0 shown for the pulsatile model were used as inputs in generating "data" to be fitted using the steady state model. Other inputs were as shown in Table 2.2.
(b) The values of r_0 and ω_0 for the steady-state model were obtained via a least-squares fit to the sieving curve generated using the pulsatile model.

obtained with the steady state model with those for the pulsatile model, when either $\overline{\Delta P}$ or $\overline{Q}_A$ were varied above or below their baseline levels given in Table 2.2. The results for the isoporous model are shown in Figures 2.11 and 2.12. In general, the dependence of $\overline{\theta}$ on $\overline{Q}_A$ and $\overline{\Delta P}$ computed with the steady state model was very similar to that obtained using the pulsatile model. The trends obtained with the shunt model were very similar to those illustrated in Figures 2.11 and 2.12. We conclude that the steady state approach is adequate for predicting the effects of hemodynamic perturbations on $\overline{SNGFR}$ and $\overline{\theta}$.

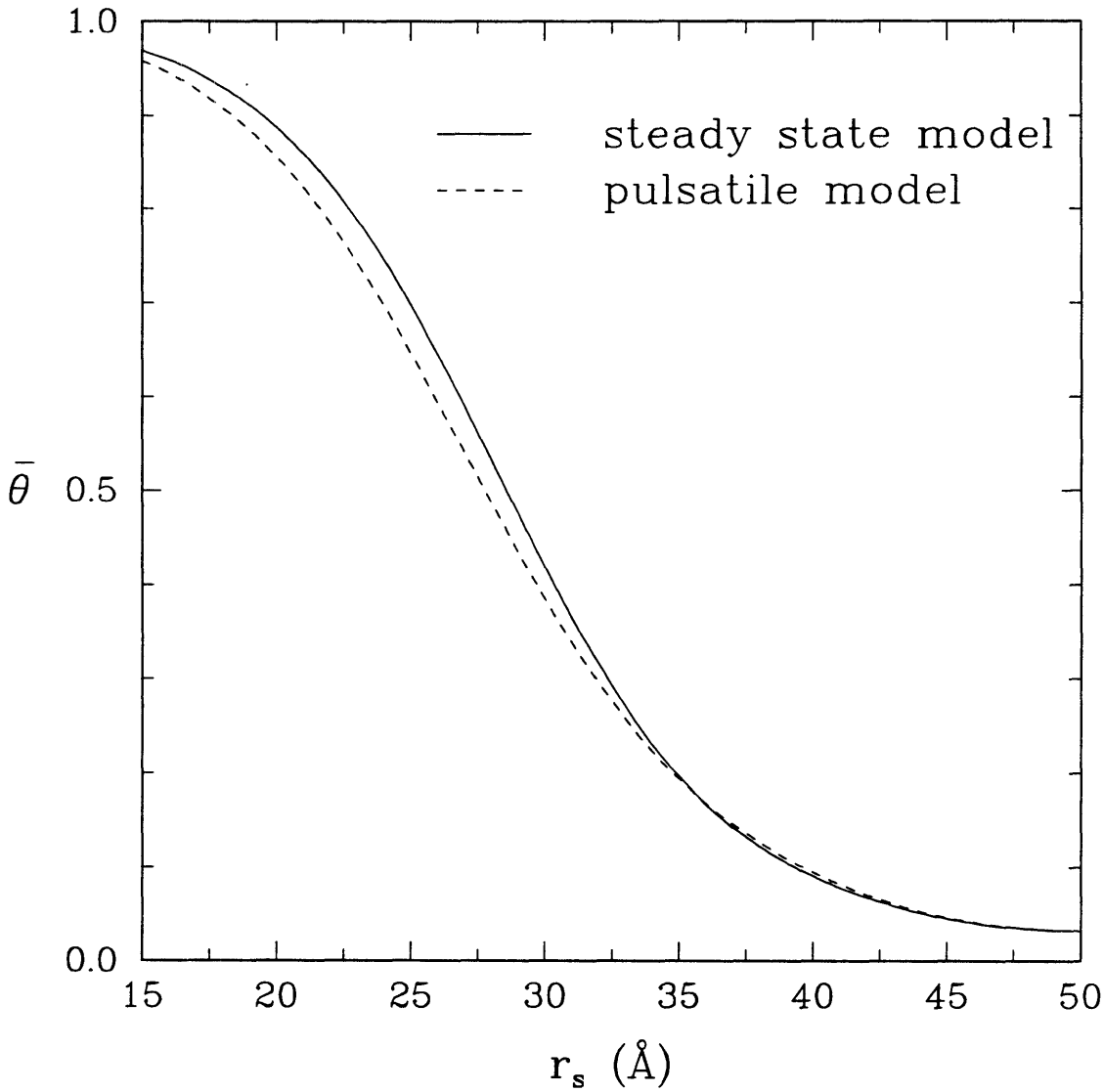

Figure 2.10 - A comparison of sieving curves computed using the pulsatile model and a steady-state model, for an isoporous-with-shunt membrane with $\omega_0 = 0.01$. Other input parameters were as shown in Table 2.2.

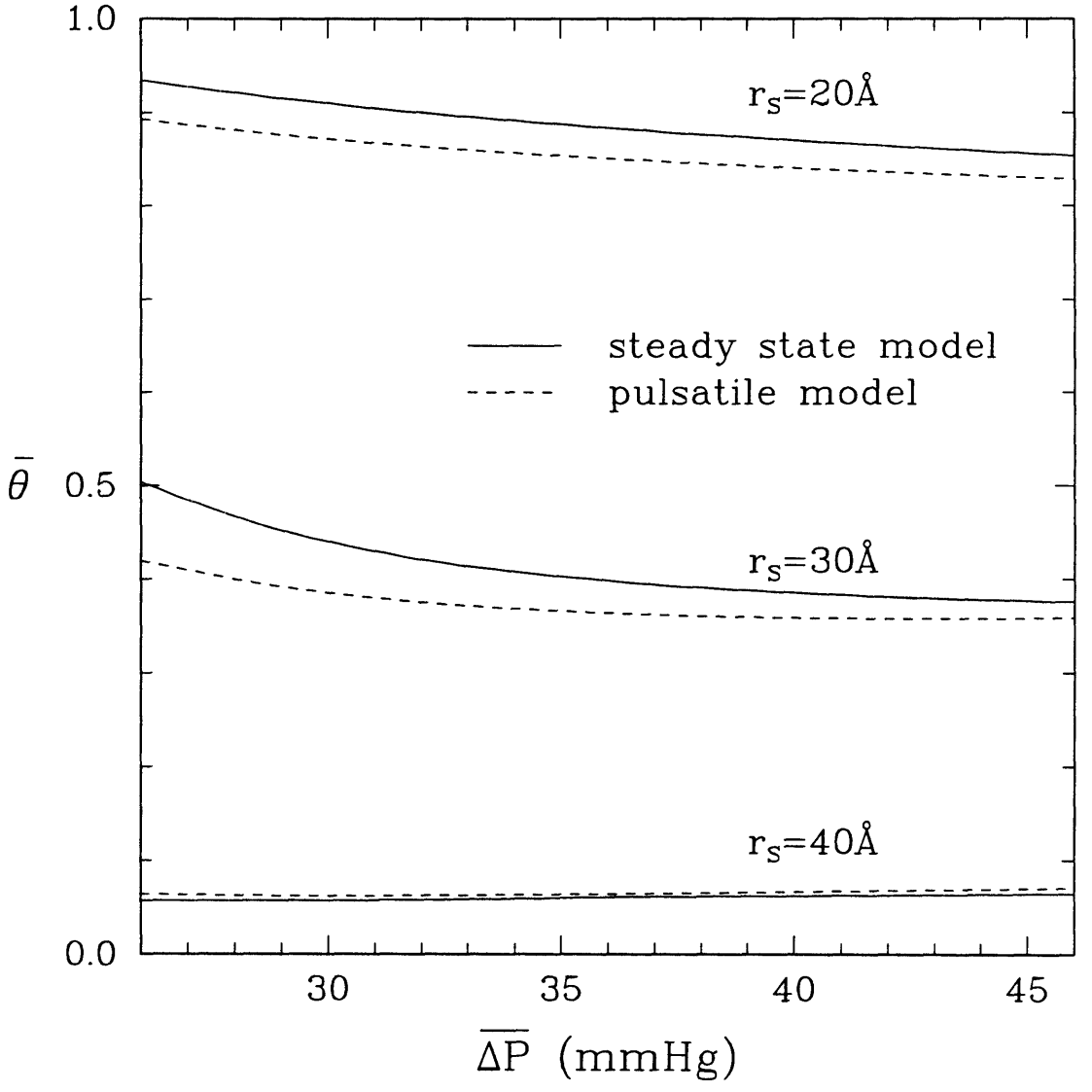

Figure 2.11 - Effects of selective variations in mean transmural pressure ($\overline{\Delta P}$) on sieving coefficient, computed using either the steady-state or pulsatile models. An isoporous membrane was assumed, with effective pore radius of 50 Å. Other parameters were as shown in Table 2.2.

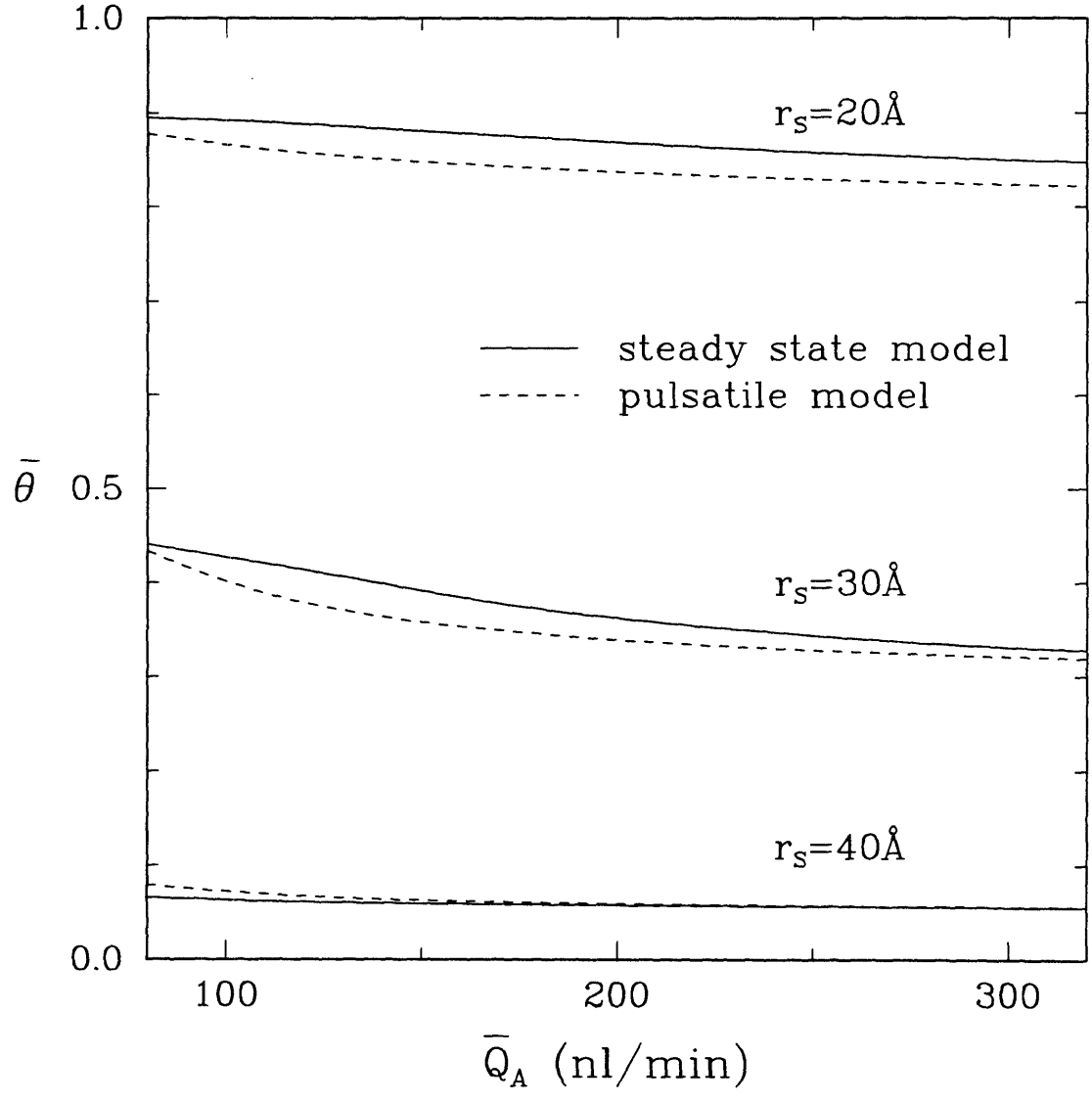

Figure 2.12 - Effects of selective variations in mean afferent arteriolar plasma flow rate ($\bar{Q}_A$) on sieving coefficient, computed as described in Figure 2.11.

2.4 DISCUSSION

The present study represents the first attempt to analyze the effects of pulsatile pressures and flows on glomerular filtration. Previous modeling efforts directed at the filtration of water and/or macromolecules have simply assumed that steady state mass balance and flux equations, employing only time-averaged quantities, accurately describe dynamic events in the glomerulus (Chang, 1980; Chang et al., 1975; Deen et al., 1985; Deen et al., 1972; Deen et al., 1974; Deen et al., 1980; DuBois et al., 1975; Huss et al., 1975; Lambert et al., 1982; Remuzzi and Deen, 1986; Remuzzi and Deen, 1989); no particular justification for this assumption has been offered. The steady state assumption was made especially questionable by the rapid and relatively large oscillations in ΔP ($\pm$ ~30% relative to $\overline{\Delta P}$), and by the nonlinear nature of the equations used to describe the plasma flow rate, the protein concentration, and the concentration of test solutes along a glomerular capillary. Our analysis suggests that solute concentrations within a membrane pore should respond quickly enough to make the usual steady state flux equations applicable, but that the previously ignored time derivatives in the lumenal mass balance equations for protein and test solutes are <u>not</u> negligible.

It is largely fortuitous, then, that the steady state approach works very well. Using the results of the pulsatile model as the standard, the steady state assumption should lead to negligible errors in calculating K_f, r_0, and ω_0 from micropuncture and fractional clearance data. The effects of hemodynamic perturbations on $\overline{SNGFR}$ or $\bar{\theta}$ were also represented accurately by the steady state model. We conclude that the steady state models are still useful tools for extracting membrane properties from micropuncture and clearance data. Given its greater computational complexity, the modest increase in accuracy offered by the pulsatile model would not appear to justify its routine application.

Using the pulsatile model to assess the errors made in the steady state approach

requires, of course, that the assumptions underlying the present formulation be valid. Treating the glomerular capillary network as an array of identical capillaries in parallel, neglecting concentration polarization, and representing the capillary wall as an equivalent porous membrane, are features common to both the steady state and pulsatile formulations. The simplified network representation and the neglect of concentration polarization have been shown previously to cause little error in steady state models (Deen et al., 1974; Remuzzi and Deen, 1986; Remuzzi and Deen, 1989), and we see no reason to believe that these assumptions would be appreciably less accurate under pulsatile conditions. It also seems reasonable to suppose that if we had used a more realistic model of the capillary wall, one based on its ultrastructure (see Chapters 4 - 6), a comparison between steady and pulsatile approaches would yield conclusions similar to those obtained here. One new factor which had to be addressed is the mechanical response of the capillary wall to pulses in ΔP. We assumed that the capillary wall behaves as a rigid structure, so that the filtration surface area and pore structure do not vary over a cardiac cycle. In support of this assumption, it seems likely that the distensibility of a glomerular capillary is determined largely by the elastic properties of the basement membrane. In the absence of specific data for the glomerulus, we used a Young's modulus derived from data for tubular basement membranes (Welling and Grantham, 1972). For oscillations of ± 10 mm Hg in ΔP, the change in capillary radius predicted from this value was $< \pm 1\%$. Thus, it seems unlikely that there would be significant changes in capillary radius during a cardiac cycle.[2]

---

[2] At a given axial position along a capillary, alterations in the transmural pressure difference, which are balanced by changes in the circumferential stress in the capillary wall, may lead to changes in the capillary radius. For thin-wall elastic tubes, the condition of equilibrium between transmural pressure and wall tension can be written as

$$\frac{d\Delta P}{dr} = \frac{E\ell}{R^2}$$

where E is the Young's modulus of the wall material and R is the tube radius (Welling and Grantham, 1972). Applying the integrated form of this equation to a glomerular capillary (with $R \cong 3$ μm and $\ell \cong$

Another new factor in modeling pulsatile pressures and flows was the need to represent filtration reversal (fluid and solute absorption) in the more efferent portions of a capillary during part of each cardiac cycle. This led to difficulty in identifying an equation which governs c_{SB} during filtration reversal. The main source of the difficulty is that the geometric complexity of Bowman's space precludes writing a simple mass balance equation for the test solute, one which would be analogous to equation (2.16). As discussed in connection with equation (2.24), order of magnitude considerations suggest that during filtration reversal c_{SB} can be approximated by its average value during the preceding period of forward filtration. To test the sensitivity of the results to this approximation, we considered also two more extreme situations: Case A, setting c_{SB} (during reversal) equal to its maximum value during forward filtration; and Case B, setting c_{SB} (during reversal) equal to its minimum value during forward filtration. In all cases the predicted fluxes qualitatively resembled those shown in Figure 2.8. The sieving curve for Case B was visually indistinguishable from that shown for the pulsatile model in Figure 2.9, while that for Case A was slightly lower, with a maximum difference of 8% for intermediate molecular sizes. We conclude that possible errors in the approximation used for c_{SB} are unlikely to have a material effect on our results.

Of the various input parameters, the only quantities which could not be derived fairly directly from micropuncture or clearance data were the lumenal residence time (t_T) and the amplitude (β) and phase shift (τ_0) of the oscillations in Q_A. As already noted in connection with Figure 2.3, variations in the assumed value of t_T affected primarily the duration of the initial transient period in the simulations, the time required to achieve the desired steady-periodic behavior of the solutions. The length of this transient period has

---

0.1 μm), and using an average of the values of E reported by Welling and Grantham (1972) for tubular basement membranes ($E = 8 \times 10^6$ dyne/cm^2), it can be shown that for changes in ΔP of ±10 mmHg, the relative changes in capillary radius, $\Delta R/R$, are ±0.005. In other words, the calculated change in R is only ±0.5%.

little or no physiological significance, because of the artificial nature of the initial conditions. The values chosen for τ_0 and β were also found to be relatively unimportant. Varying τ_0 and β in various combinations over the ranges $0 \leq \tau_0 \leq 1$ and $0 \leq \beta \leq 0.3$ affected $\overline{SNGFR}$ and $\bar{\theta}$ by ≤1% and <0.5%, respectively. The effects of oscillations in ΔP, considered alone, tended to be larger than the effects of selective oscillations in Q_A.

While our main results were insensitive to β and τ_0, it is interesting to note that for the baseline conditions of $\beta = 0.14$ and $\tau_0 = 0$ in the afferent arteriole, the analogous amplitude ratio and phase shift computed for Q_E were 0.31 and 0.45, respectively. The predicted amplitude ratio for Q_E may be compared with an independent estimate from the pressures in Table 2.1. Assuming relations analogous to equations (2.28) - (2.30), the amplitude ratio for the efferent flow is (10 - 1)/(48 - 22) = 0.35, in good agreement with the value computed in the simulations. However, the original pressure tracings show that there is no phase shift between the pressure pulses in the efferent arteriole and in the glomerular capillaries. A possible explanation for this inconsistency is that the arteriolar resistances may not be time-independent, as had been assumed in applying equation (2.28).

CHAPTER 3

STOKES FLOW THROUGH A SINGLE ROW OF CYLINDERS BETWEEN WALLS: MODEL FOR THE GLOMERULAR SLIT DIAPHRAGM

3.1 INTRODUCTION

During the ultrafiltration of blood in renal glomerular capillaries, the filtrate must cross the slit diaphragm, which spans the slits between the epithelial foot processes of the capillary wall. As was described in Chapter 1, the structural details of the slit diaphragm are still in dispute. Figure 3.1 shows two possible configurations for the slit diaphragm. The "zipper configuration" is the structure originally proposed by Rodewald and Karnovsky (1974) (see Figure 1.5) and the "ladder configuration" is a simpler structure based on observations of Hora et al. (1990). The main objective of the analysis presented in this chapter was to determine the hydraulic permeability of the ladder and zipper configurations of the slit diaphragm.

The study of viscous flow past cylindrical objects confined between parallel walls has a long history. Hele-Shaw (1898) observed that, for flow around a single cylinder with axis perpendicular to closely spaced walls, the streamlines resemble those for inviscid flow around an infinite cylinder of the same radius. As described by Lamb (1945), Stokes proved that when inertia is negligible and the channel width ($2W$) is small compared with the cylinder diameter ($2R$) the equations of motion indeed reduce to a potential flow equation. He neglected the component of the velocity perpendicular to the walls (v_x) and assumed that $\partial^2 v_i / \partial x^2 >> \partial^2 v_i / \partial y^2$ or $\partial^2 v_i / \partial z^2$ for $i = y, z$. His solution is valid except near the cylinder, in a region of thickness O(W). In particular, his

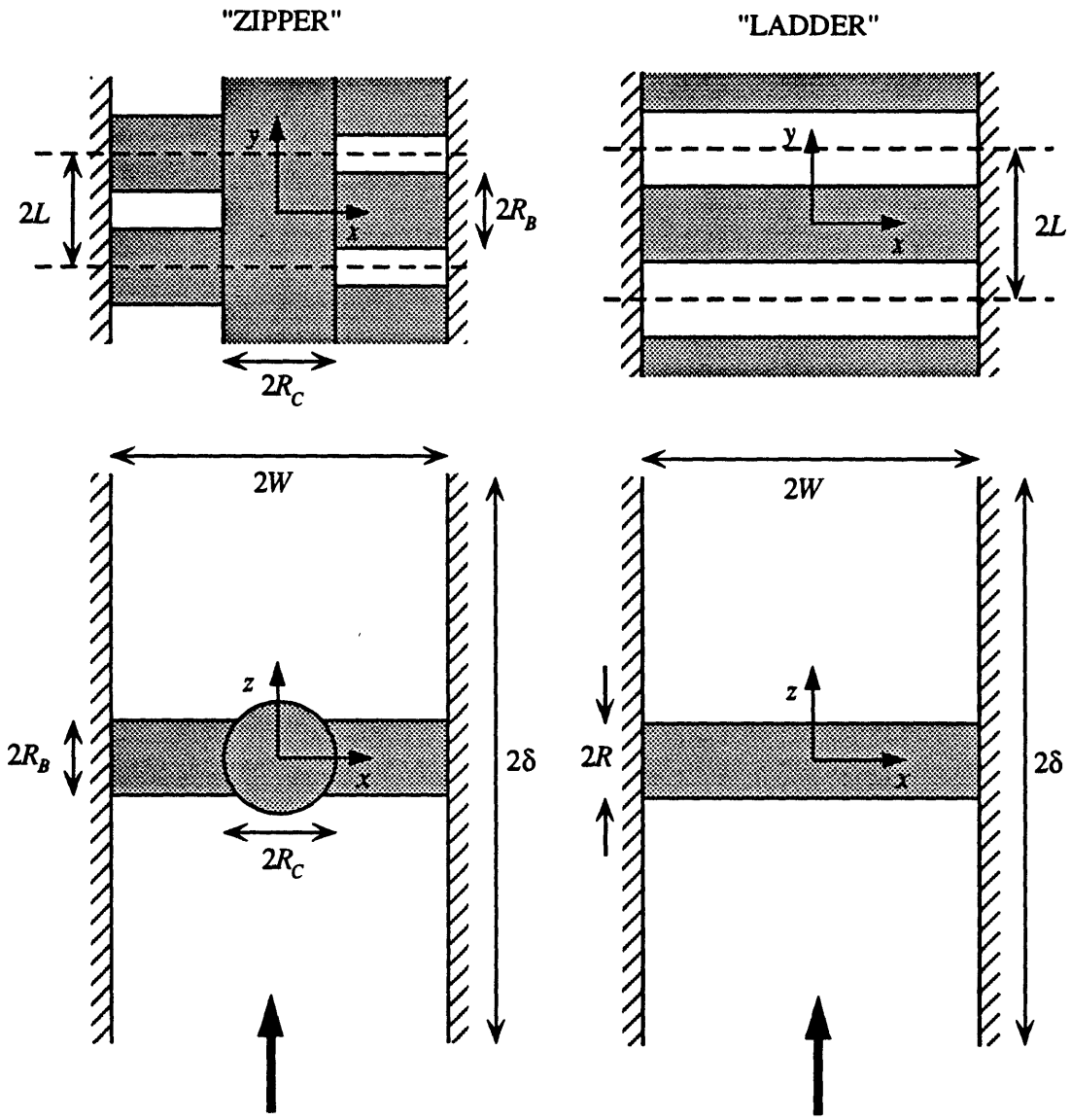

Figure 3.1 - Schematic representations of two possible configurations of the epithelial slit diaphragm of renal glomerular capillaries. The "zipper" structure is based on the observations of Rodewald and Karnovsky (1974), whereas the "ladder" structure is motivated by the work of Hora et al. (1990). The approaching flow is along the *z* axis, as indicated by the arrows at the bottom.

solution does not satisfy the no-slip boundary conditions at the cylinder surface. Improvements on Stokes solution for $W/R << 1$ were made by Thompson (1968), who used a singular perturbation method to obtain inner and outer expansions for the velocity and pressure fields up to $O[(W/R)^2]$. Considering a single cylinder between walls which are not so closely spaced, Lee and Fung (1969) obtained a uniformly valid series solution, each term of which satisfies the equations of motion and the boundary conditions at the channel walls. The coefficients of the (truncated) series had to be determined numerically so as to satisfy the no-slip boundary conditions at the surface of the cylinder. This approach was found to be adequate for practical computations only when $W/R \leq 5$. An approximate two-term solution was also developed by retaining only the first terms of the infinite series. This solution, which neglects v_x, is accurate only for $W/R < \sim 1$. Recently, Vrahopoulou (1992) obtained finite element solutions of the velocity field around a single cylinder between walls for $W/R = 0.1$ and 2. For $W/R = 0.1$ the velocity field in the midplane between cylinders resembled the limiting Hele-Shaw solution, while for $W/R = 2$ there were significant differences between the numerical results and the Hele-Shaw solution.

Lee (1969) used the approximate two-term approach of Lee and Fung (1969) to model flow through a doubly periodic array of cylinders between parallel walls. In addition to the limitations of Lee and Fung's (1969) two-term approximation, the solution obtained by Lee (1969) is accurate only when the volume fraction of cylinders is small. Recently, Tsay and Weinbaum (1991) constructed a more general solution to the problem addressed by Lee (1969). They obtained a doubly-periodic infinite series solution which is an extension of Lee and Fung's (1969) solution for one cylinder. As in the latter, the series identically satisfies the no-slip condition at the channel walls, and the coefficients of the (truncated) series were determined numerically so as to satisfy the no-slip boundary condition at the surfaces of the cylinders.

3.2 PROBLEM FORMULATION

Due to the extremely low Reynolds number in the physiological system of interest (Re ~ 10^{-6}) the local fluid velocity in the periodic unit cells shown by the dashed lines in Figure 3.1 can be obtained from Stokes and continuity equations:

$$\nabla P = \mu \nabla^2 \mathbf{v} \tag{3.1}$$

$$\nabla \cdot \mathbf{v} = 0 \tag{3.2}$$

where P is the pressure, $\mathbf{v}$ the local fluid velocity, and μ the fluid viscosity.

The appropriate boundary condition at all solid surfaces (Ω_S) is zero velocity,

$$v_x = v_y = v_z = 0 \text{ on } \Omega_S. \tag{3.3}$$

Because of symmetry considerations,

$$v_x = 0 \text{ at } x = 0 \tag{3.4}$$

for the ladder configuration and

$$v_y = 0 \text{ at } y = 0 \text{ and } y = L \tag{3.5}$$

for both ladder and zipper configurations.

Restricting the analysis to long channels, the upstream and downstream boundary conditions (representing unperturbed plane Poiseuille flow) are

$$v_z = \frac{3}{2}V\left[1-\left(\frac{x}{W}\right)^2\right], \quad v_x = v_y = 0 \ \text{ at } z = \pm\delta \tag{3.6}$$

where V is the mean fluid velocity. The length δ was chosen to be sufficiently long so as not to affect the flow in the vicinity of the cylinders. Finally, due to symmetry,

$$v_x = v_y = 0 \text{ at } z = 0. \tag{3.7}$$

The hydraulic permeability of each unit cell is defined by:

$$k \equiv \frac{V}{\Delta P} \tag{3.8}$$

where ΔP is the pressure drop between z = -δ and z = δ. Due to symmetry, $\Delta P = 2(P_{-\delta} - P_0)$ where $P_{-\delta}$ and P_0 are the (constant) pressures at z = -δ and z = 0, respectively. It can be shown that, for the ladder configuration, the dimensionless total resistance,

$$f_T \equiv \frac{L\Delta P}{\mu V} \tag{3.9}$$

is a function of three length ratios, which may be chosen as R/L, L/W and δ/L. For the zipper configuration there are four length ratios, R_C/L, R_B/L, L/W and δ/L. In a long channel of length 2δ with no cylinders, the dimensionless resistance would be that for Poiseuille flow,

$$f_P = \frac{6\delta L}{W^2}. \tag{3.10}$$

For large enough $|z|/L$, the disturbances in the velocity field caused by the presence of the cylinders become negligible, as indicated by equation (3.6). Therefore, for large δ/L, the increment in resistance above the Poiseuille flow value will become independent of δ/L. Accordingly, we employ the "additional resistance" (f), where

$$f \equiv f_T - f_P. \tag{3.11}$$

The additional resistance, f, depends only on R/L and L/W for the ladder, and on R_C/L, R_B/L, and L/W for the zipper configurations.

3.3 SOLUTION METHODS

A Galerkin finite element solution of equations (3.1) and (3.2), with boundary conditions (3.3) - (3.7), was obtained with the software package FIDAP (Fluid Dynamics International, Evanston, Illinois) on a Cray X-MP EA/464 supercomputer. We chose a consistent penalty formulation which, relative to alternative mixed formulations, has the advantage of eliminating the pressure unknowns from the discretized finite element equations. This is done by replacing equation (3.2), the continuity equation for an incompressible fluid, by

$$\nabla^* \cdot \mathbf{v}^* = -\varepsilon P^* \tag{3.12}$$

where the dimensionless quantities are

$$\mathbf{v}^* \equiv \frac{\mathbf{v}}{V} \; ; \; P^* \equiv \frac{PL}{\mu V} \; ; \; \nabla^* \equiv L\nabla \; . \tag{3.13}$$

This approach therefore introduces a "compressibility error" which motivates the choice of a small value for the penalty parameter, ε. There is, however, a practical lower bound for ε because very small values of this parameter lead to ill-conditioned matrices and large truncation errors (Kheshgi and Scriven, 1982). Commonly used values of ε range from 10^{-6} to 10^{-9}. The results presented here were obtained with $\varepsilon = 10^{-7}$ or 10^{-8}. We used three-dimensional brick elements with triquadratic basis functions for $\mathbf{v}$ (27 nodes/element) and linear basis functions for P (4 nodes/element). In the preliminary two-dimensional calculations (see below) we used quadrilateral elements with biquadratic basis functions for $\mathbf{v}$ (9 nodes/element) and linear basis functions for P (3 nodes/element). These choices guarantee the absence of spurious pressure modes and, in addition, it has been shown that they lead to optimal rates of convergence in the finite element solution of equations (3.1) and (3.2) in a rectangular domain with uniform mesh and Dirichlet boundary conditions, using a penalty formulation (Oden, 1982).

Typical meshes used in our three-dimensional calculations are shown in Figure 3.2. Due to the symmetry of the velocity and pressure fields, only 1/4 and 1/8 of the unit cells of the zipper and ladder configurations, respectively, needed to be used in the simulations.

3.4 RESULTS

3.4.1 VERIFICATION OF THE NUMERICAL METHOD

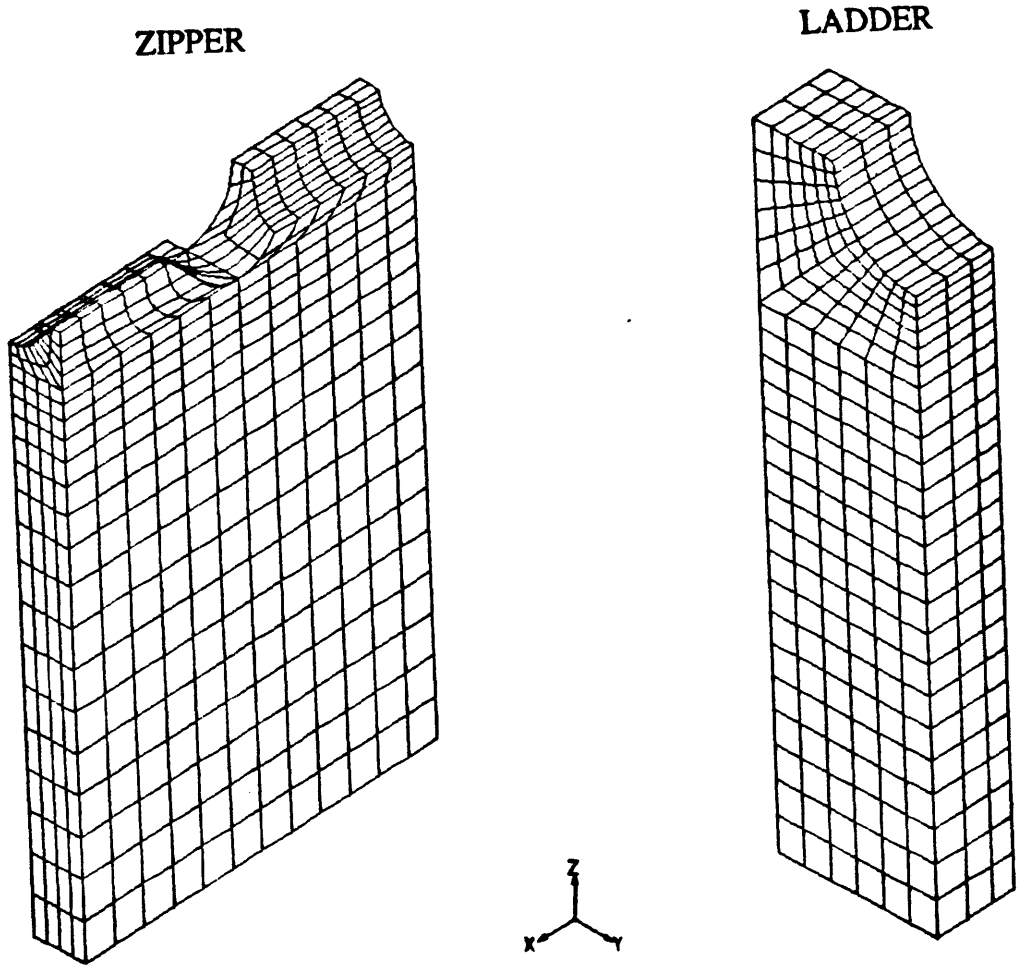

Figure 3.2 - Typical finite element meshes for 1/4 of a unit cell of the zipper configuration (L/W = 0.284; R_B/L = 0.625; R_C/W = 0.277) and 1/8 of a unit cell of the ladder configuration (L/W = 2, R/L = 0.5). Each element has 27 nodes for **v** and 4 nodes for P.

We checked the accuracy of the finite element method against existing solutions for two-dimensional flow perpendicular to a row of cylinders (no walls), or for flow around a single cylinder between parallel walls.

TWO-DIMENSIONAL FLOW THROUGH A SINGLE ROW OF CYLINDERS. Tamada and Fujikawa (1957) used Oseen's technique to obtain an analytical solution for Stokes flow perpendicular to a row of infinitely long cylinders, which is valid when the diameter of the cylinders is small compared with the distance between cylinders ($R/L \ll 1$). Sangani and Acrivos (1982) analysed two-dimensional flow through a square array of infinite cylinders. In particular, they obtained an asymptotic solution for the case of small gaps between cylinders. This lubrication limit also applies to flow through a single row of closely spaced cylinders ($R/L \rightarrow 1$). Edwards et al. (1990) used finite element methods in the analysis of flow through various spatially periodic two-dimensional arrays of cylinders.

We obtained finite element solutions for flow perpendicular to a row of infinitely long cylinders over a range of R/L encompassing both limits. Our meshes were composed of ~750 to ~1200 nodes (~170 to ~280 elements) and the CPU time on the Cray X-MP EA/464 was in all cases < 5 seconds. We analyzed the effect of the penalty parameter on the computed drag on a cylinder. (A force balance shows that the drag on one cylinder per unit length, F, is given by $F = 2L\Delta P$.) Changes in the penalty parameter from 10^{-6} to 10^{-9} produced negligible changes (< 1%) in the drag.

Figure 3.3 shows streamlines and isobars for $R/L = 0.5$. This simulation was done with a mesh containing 949 nodes (216 elements). The CPU time on the Cray X-MP EA/464 was around 3 seconds. It can be seen that the disturbances in the flow field caused by the cylinders decay relatively fast. In fact, as shown in Figure 3.4, the disturbances in v_z become negligible for $|z|/L > 2 - 3$. (It was verified that, when $(|z|-R)/L > 3$, $|v_z^* - 1| < 0.001$) Furthermore, the computed values of P at $z = -\delta$ were independent of

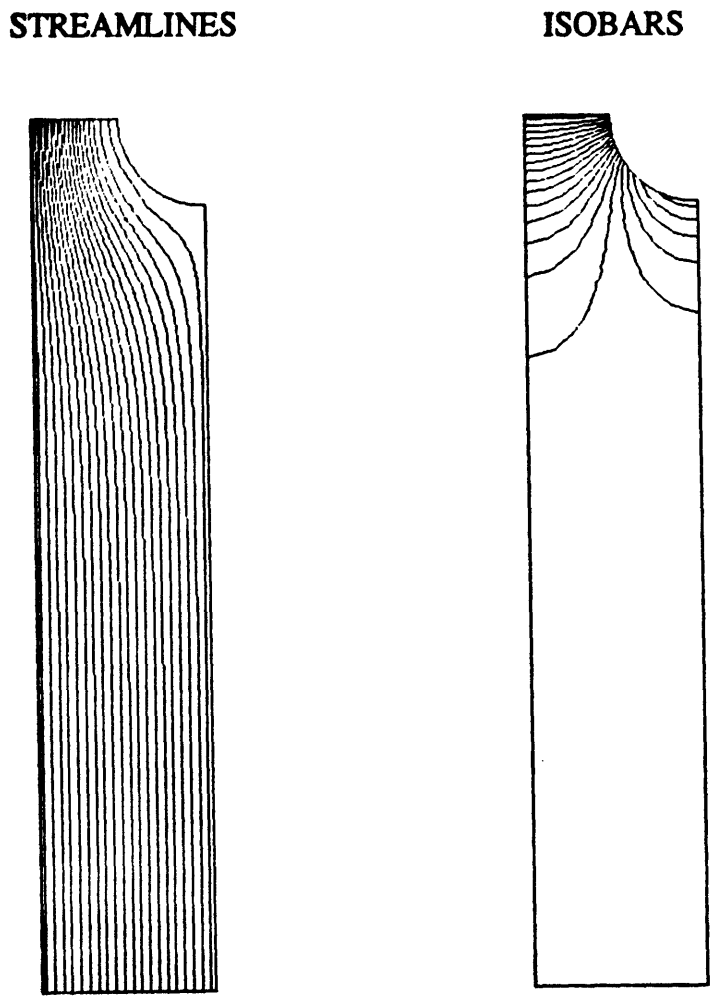

Figure 3.3 - Streamlines and isobars for flow through a row of infinitely long cylinders with $R/L = 0.5$.

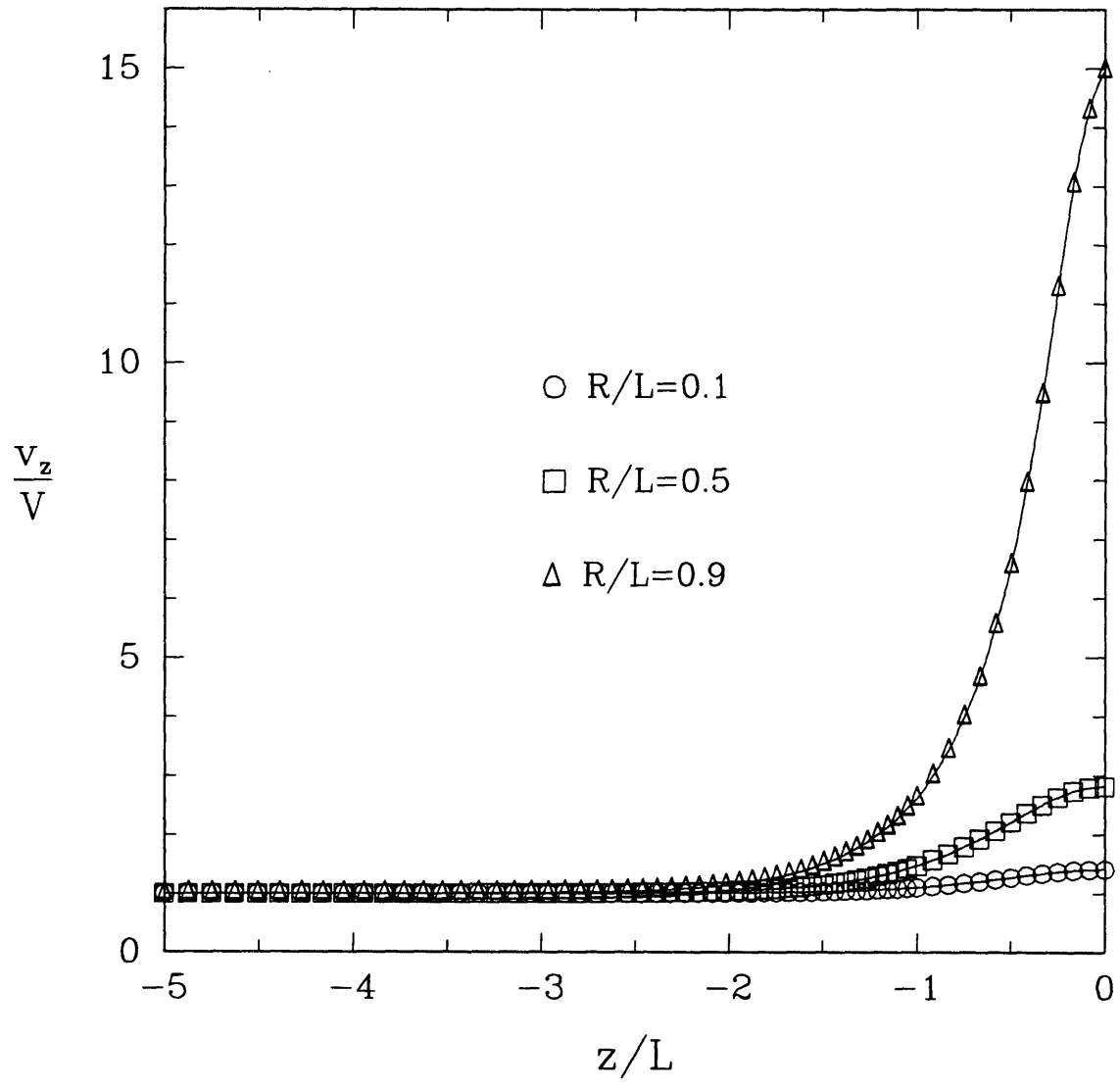

Figure 3.4 - Velocity component v_z at $y/L = 1$ as a function of z/L for flow through a row of infinitely long cylinders with $R/L = 0.1$, 0.5 and 0.9.

y to 5 digits. The results presented in this section were obtained with a conservative value of $\delta/L = 5$.

Figure 3.5 shows the dimensionless drag as a function of the dimensionless gap between cylinders. There is excellent agreement between our results and those of Tamada and Fujikawa (1957) for large gaps ($\leq 0.2\%$ difference for $0.1 \leq R/L \leq 0.5$), and between our results and those of Sangani and Acrivos (1982) for small gaps ($\leq 0.3\%$ difference for $0.8 \leq R/L \leq 0.95$ and 1.1% difference for $R/L = 0.7$). Our numerical values and corresponding analytical results are given in Table 3.1. Also shown in Table 3.1 are values of the dimensionless drag per cylinder for flow through a square array of cylinders, calculated using an asymptotic result for small R/L (Sangani and Acrivos, 1982). Interestingly, these values are similar to those for flow through a single row of cylinders (2, 4 and 6% difference for R/L = 0.1, 0.3 and 0.5, respectively, when compared with our numerical results).

FLOW AROUND A SINGLE CYLINDER BETWEEN PARALLEL WALLS. We also obtained finite element solutions to the three-dimensional problem addressed by Lee and Fung (1969), namely Stokes flow around a single cylinder between parallel walls. To approximate the behavior of a single cylinder in a channel of infinite extent, we had to make both L and δ in our ladder configuration large compared with R and W. (We used $L = \delta$ in these comparisons.) The largest finite element meshes considered had ~10,000 nodes and the CPU time was ~10 minutes.

The numerical values of dimensionless drag on the cylinder, f_D ($f_D \equiv F_D/(\mu VW)$, where F_D is the drag on the cylinder), were compared with the approximate two-term solution of Lee and Fung (1969) which is accurate to within 0.5% for $W/R \leq 1$. For W/R = 0.5, the differences were smaller than 3%. In addition to f_D, we also computed f_T and f. Since, for finite δ, P is not constant at $z = -\delta$, we replaced ΔP in equation (3.9) by $\Delta\overline{P}$, where $\overline{P}$ is the pressure averaged over the cross section of the channel. Using the two-

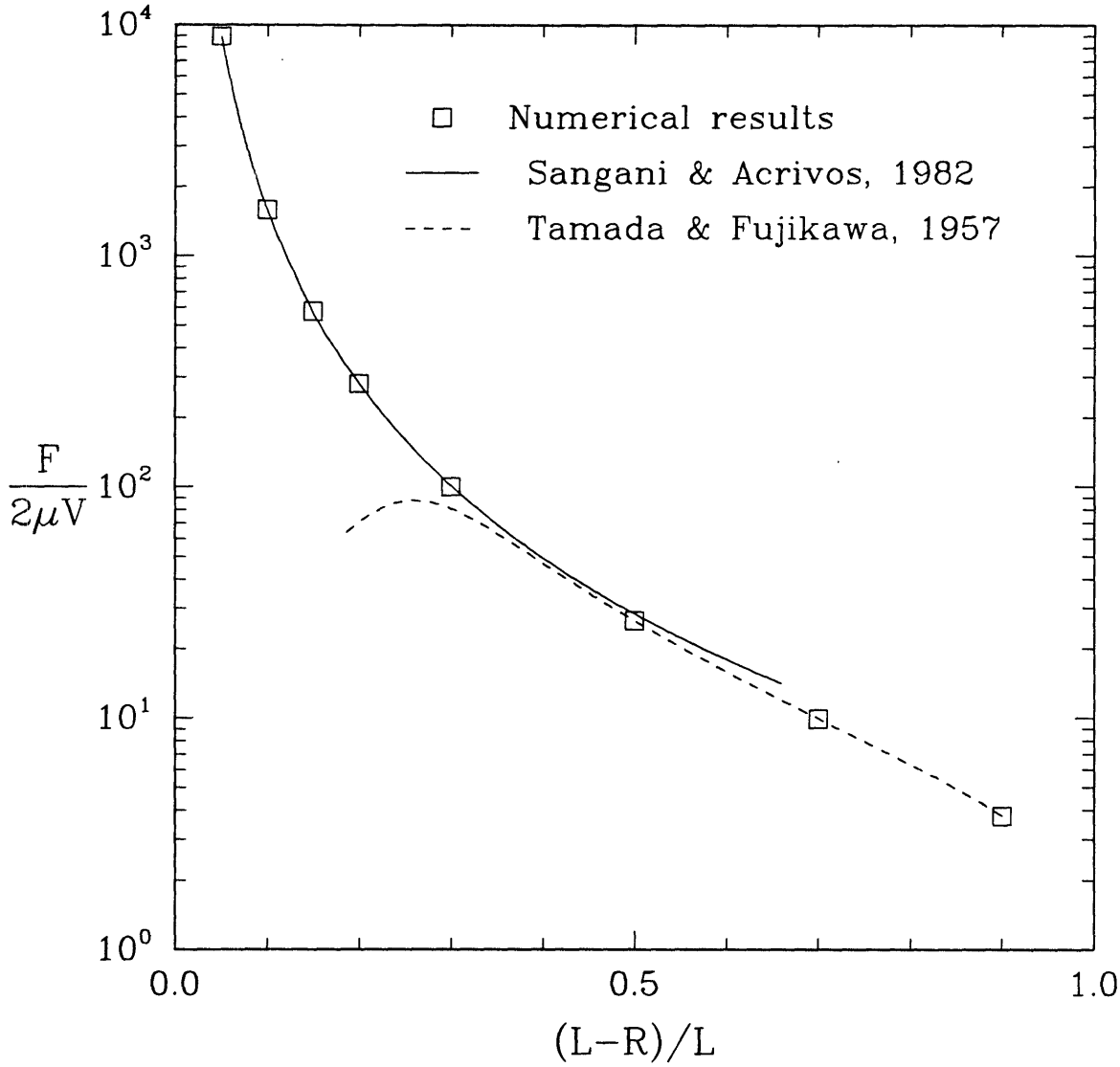

Figure 3.5 - Dimensionless drag as a function of the dimensionless gap between cylinders, for flow through a row of infinitely long cylinders.

Table 3.1 - Dimensionless drag on a cylinder for flow through a single row and square array of cylinders

	$F/(2\mu V)$			
	Single Row		Square Array	
R/L	Numerical	T & F (Small R/L)	S & A (Small R/L)	S & A (Large R/L)
0.1	3.78	3.77	3.71	
0.3	9.96	9.96	9.61	12.2
0.5	26.4	26.4	24.8	28.3
0.7	100	80.6	57.6	101
0.8	280	70.4	43.8	279
0.85	575			574
0.9	$1.59\text{x}10^3$			$1.58\text{x}10^3$
0.95	$8.95\text{x}10^3$			$8.94\text{x}10^3$

T & F: Results of Tamada and Fujikawa (1957)
S & A: Results of Sangani and Acrivos (1982)

term approximation of Lee and Fung (1969) to estimate $\Delta\overline{P}$ and substituting the result in equation (3.9), yields

$$f_T \cong 6\left(\frac{\delta}{W}\right)^2 + \frac{3\pi}{2}\left(\frac{R}{W}\right)^2 \frac{K_2(\kappa R)}{K_0(\kappa R)} \tag{3.14}$$

where K_0 and K_2 are modified Bessel functions of order 0 and 2, respectively, and $\kappa = \pi / 2W$. The first term on the right hand side of equation (3.14) is f_P and the second

term is f (both with $\delta = L$). The second term is equivalent to that derived by Lee and Fung (1969). Comparing the results of numerical simulations for $W/R = 0.5$ with the estimates of equation (3.14), it was verified that while differences in f_T were < 2%, the numerical values of f were as much as twice the analytical estimate given by the second term of equation (3.14). In connection with the discrepancies in f, it should be noted that *both* δ and L had to be large compared with R and, even for large values of δ/R (and L/R), an increase in this parameter resulted in a non-negligible decrease in f. The maximum value of δ/R (= L/R) used was 20, since larger values would have required excessive computational times. The large size of the computational domains required relatively large elements (contributing to the inaccuracies in f_T and f_D), and also caused most of the flow resistance to be due to the viscous stresses at the channel walls ($f_T \sim f_P >> f$). As a consequence of f being one to two orders of magnitude smaller than f_T, small errors in f_T led to large percentage errors in f. Similar difficulties arose in numerical simulations of Hele-Shaw flow ($W/R << 1$). In that case the governing equations reduce to a two-dimensional Laplace equation for P and the analytical solution yields $f = (3\pi/2)(R/W)^2$.

In summary, we conclude that the finite element method gives excellent results for flow through a row of cylinders, but is not well suited for computing f in unbounded domains where the disturbances are of small magnitude. In particular, it is not appropriate for cases where the disturbances are caused by a single object and where $f_T \sim f_P >> f$, since f is then very sensitive to the approximations involved in the truncation of the infinite domain. However, because of the strong hydrodynamic interactions between cylinders, the domains shown in Figure 3.1 should favor the application of the finite element method. In fact, for the ladder and zipper structures, the interactions between the disturbances of adjacent cylinders will help make P independent of x and y at finite z, as has been implicitly assumed in equation (3.6). For these

structures, it was verified that the pressure at $z = -\delta$ was independent of x and y and the value of f reached a constant.

3.4.2 FLOW THROUGH A SINGLE ROW OF CYLINDERS BETWEEN PARALLEL WALLS

For the ladder configuration, the finite element meshes were composed of ~4500 to ~13,500 nodes and the CPU time was between ~2 and ~15 minutes. Changes in the penalty parameter did not have an important effect on the computed values of f. We used $\varepsilon = 10^{-7}$ as long as the total flow rate at the entrance ($z = -\delta$) and center ($z = 0$) of the channel were equal to at least 4 digits (i.e., "compressibility error" < 0.05%). A smaller ε ($\varepsilon = 10^{-8}$) was usually needed to satisfy this requirement for the largest values of R/L.

VELOCITY AND PRESSURE PROFILES. Shown in Figures 3.6 through 3.10 are velocity and pressure profiles for $L/W = 2$ and $R/L = 0.1$, 0.5 and 0.9. Except in Figure 3.10, all profiles were evaluated at the intersection of the plane halfway between the wall and $x = 0$ with the plane halfway between the cylinder surface and $y = L$, that is, at $x = 0.5W$ and $y = 0.5(L-R)$. As seen in Figure 3.6, $v_x = 0$ far upstream from the cylinders, then reaches a minimum as z is increased, and finally returns to zero at $z = 0$. The distance from the cylinder surface over which v_x differs significantly from zero is ~W in each case, not only for the conditions of Figure 3.6 but for all other geometric parameters examined. In addition, the maximum value of $|v_x|$ is significantly smaller than that of $|v_z|$. That is, except in a region of thickness ~W near the cylinders, the flow field has the properties of a two-dimensional Hele-Shaw flow. Similar results were reported for flow around a single cylinder between walls (Lee and Fung, 1969) and flow past a doubly periodic array of cylinders (Tsay and Weinbaum, 1991). As shown in Figure 3.7, v_y also exhibits a minimum for $z < 0$.

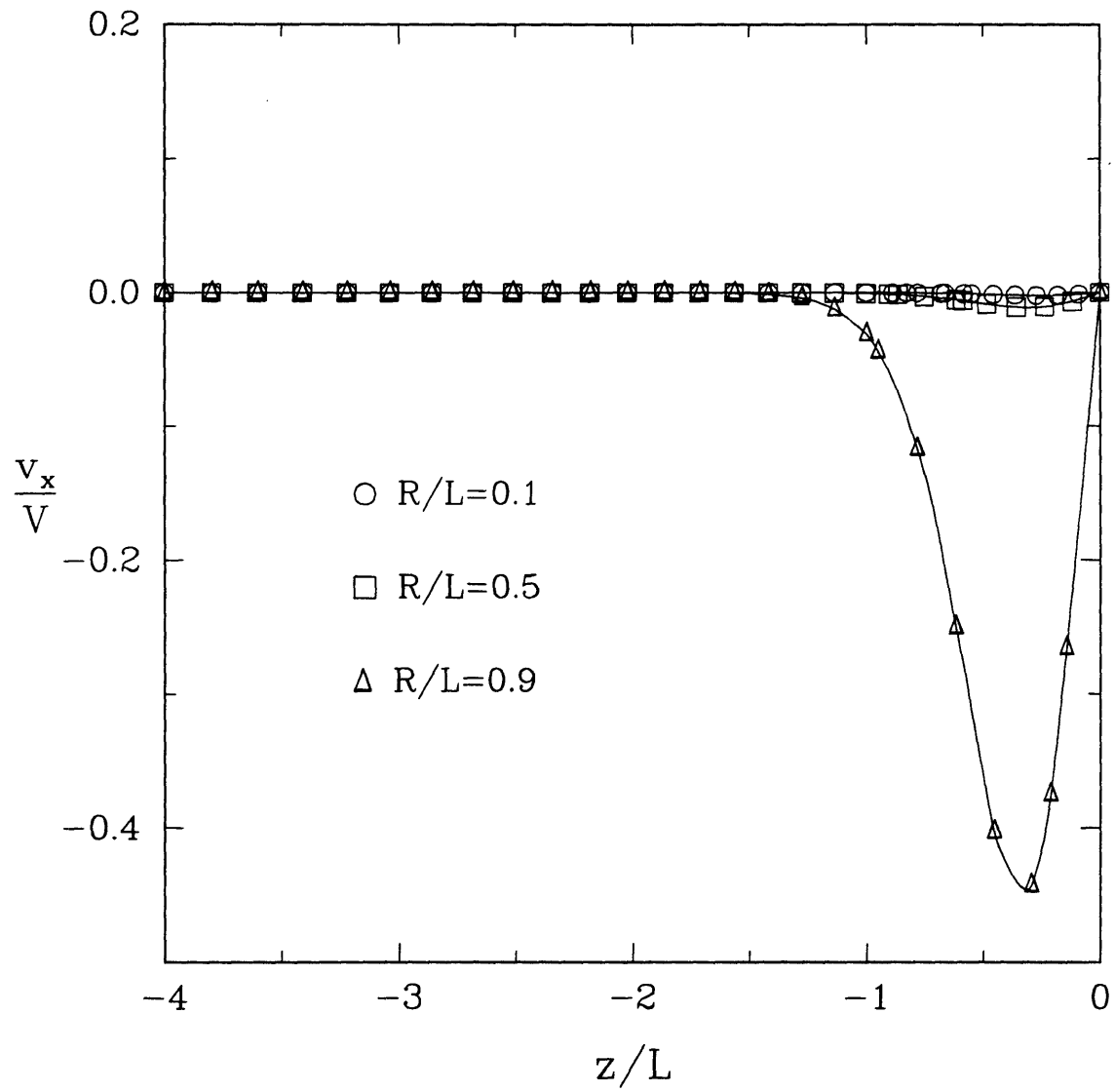

Figure 3.6 - Velocity component v_x for flow through a row of cylinders between walls, with $L/W = 2$ and $R/L = 0.1$, 0.5, and 0.9. v_x is evaluated at $x/W = -0.5$ and $(y-R)/L = -0.5$. This velocity component is anti-symmetric about $x = 0$ or $z = 0$; that is, $v_x(x,y,z) = -v_x(-x,y,z) = -v_x(x,y,-z) = v_x(-x,y,-z)$.

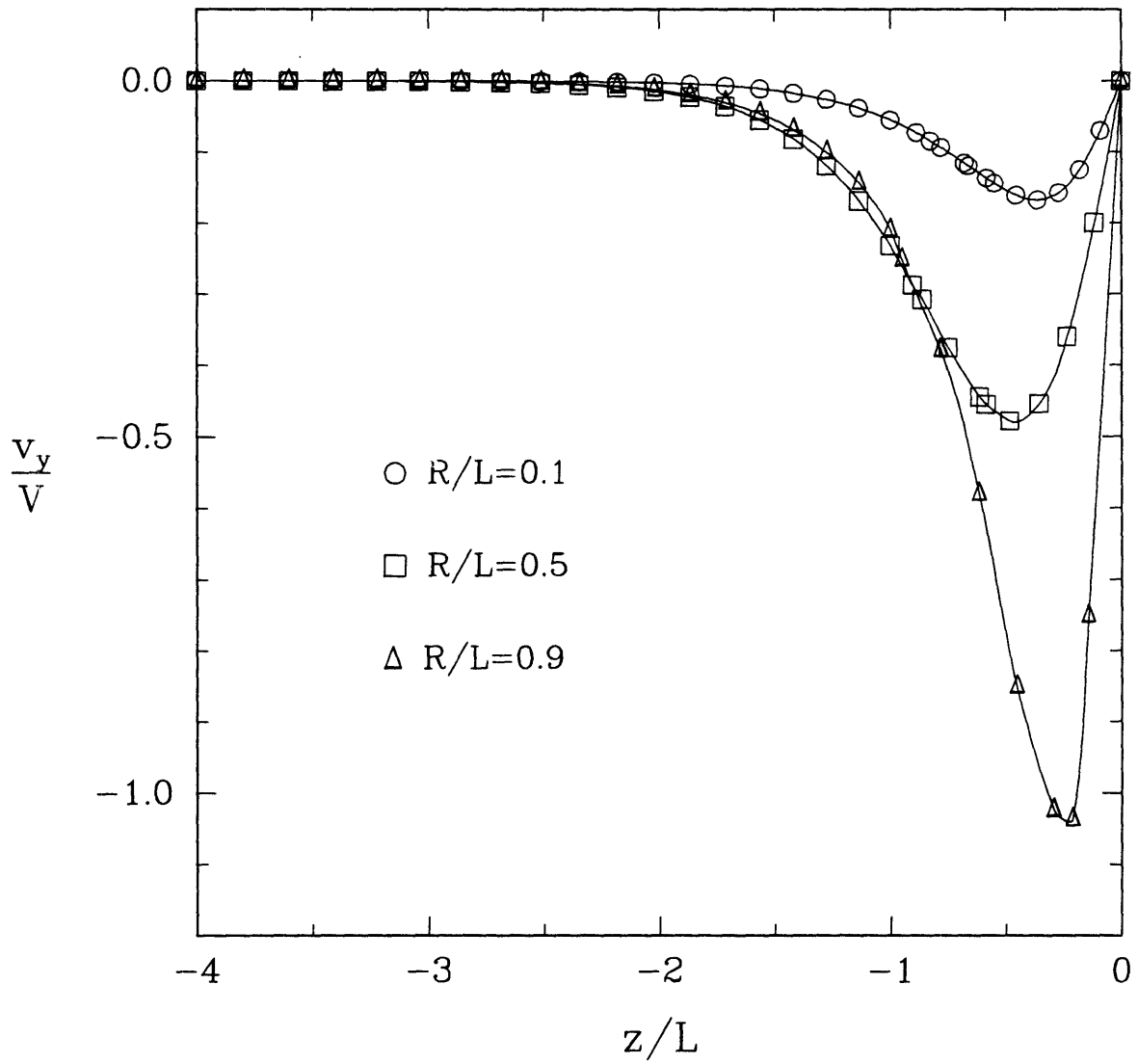

Figure 3.7 - Velocity component v_y for flow through a row of cylinders between walls, with $L/W = 2$ and $R/L = 0.1$, 0.5, and 0.9. v_y is evaluated at $x/W = -0.5$ and $(y-R)/L = -0.5$. This velocity component is anti-symmetric about $y = 0$ or $z = 0$; that is, $v_y(x,y,z) = -v_y(x,-y,z) = -v_y(x,y,-z) = v_x(x,-y,-z)$.

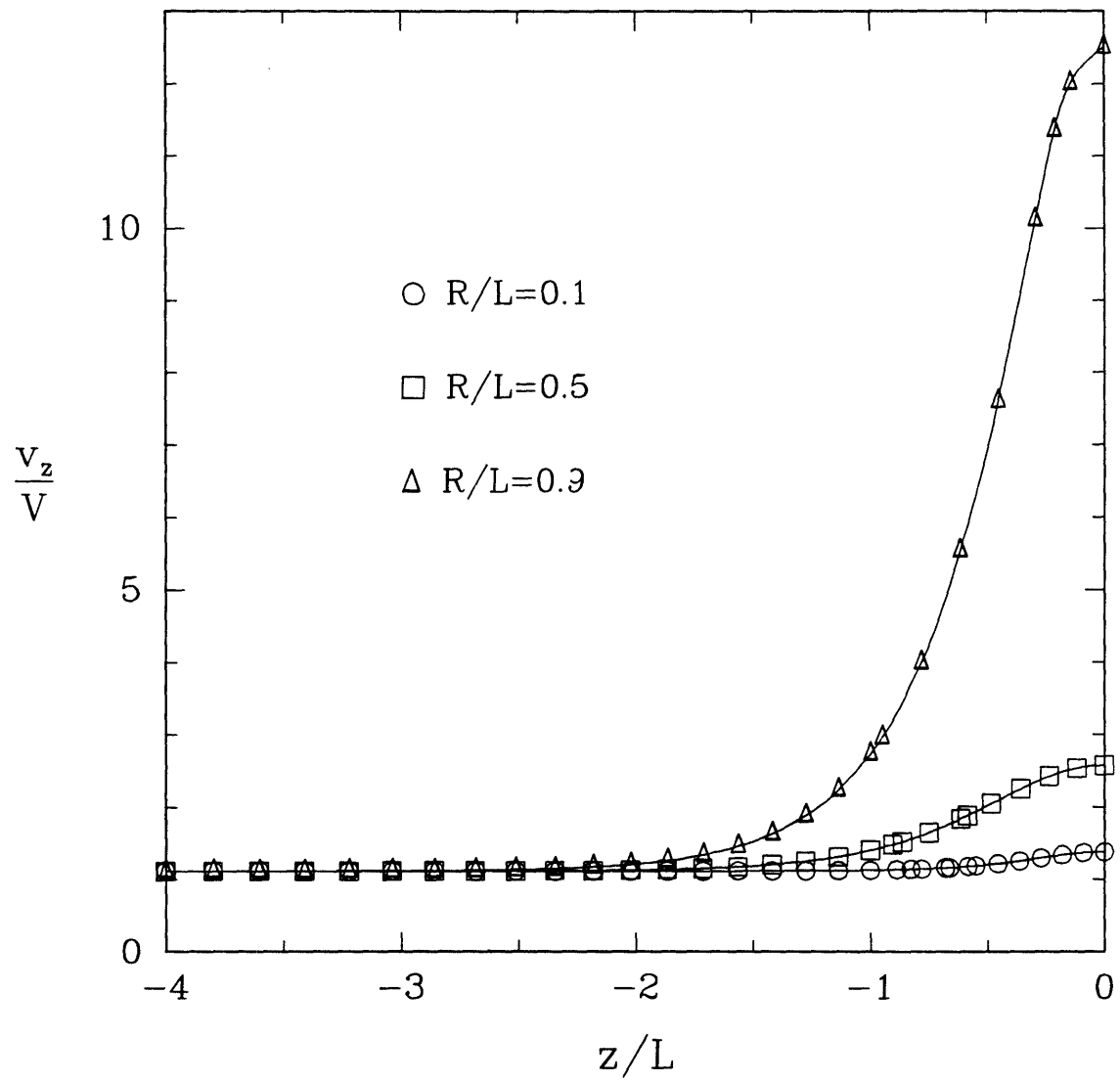

Figure 3.8 - Velocity component v_z for flow through a row of cylinders between walls, with $L/W = 2$ and $R/L = 0.1$, 0.5, and 0.9. v_z is evaluated at $x/W = -0.5$ and $(y-R)/L = -0.5$. The unperturbed value of v_z/V is 1.125. This velocity component is symmetric about $z = 0$.

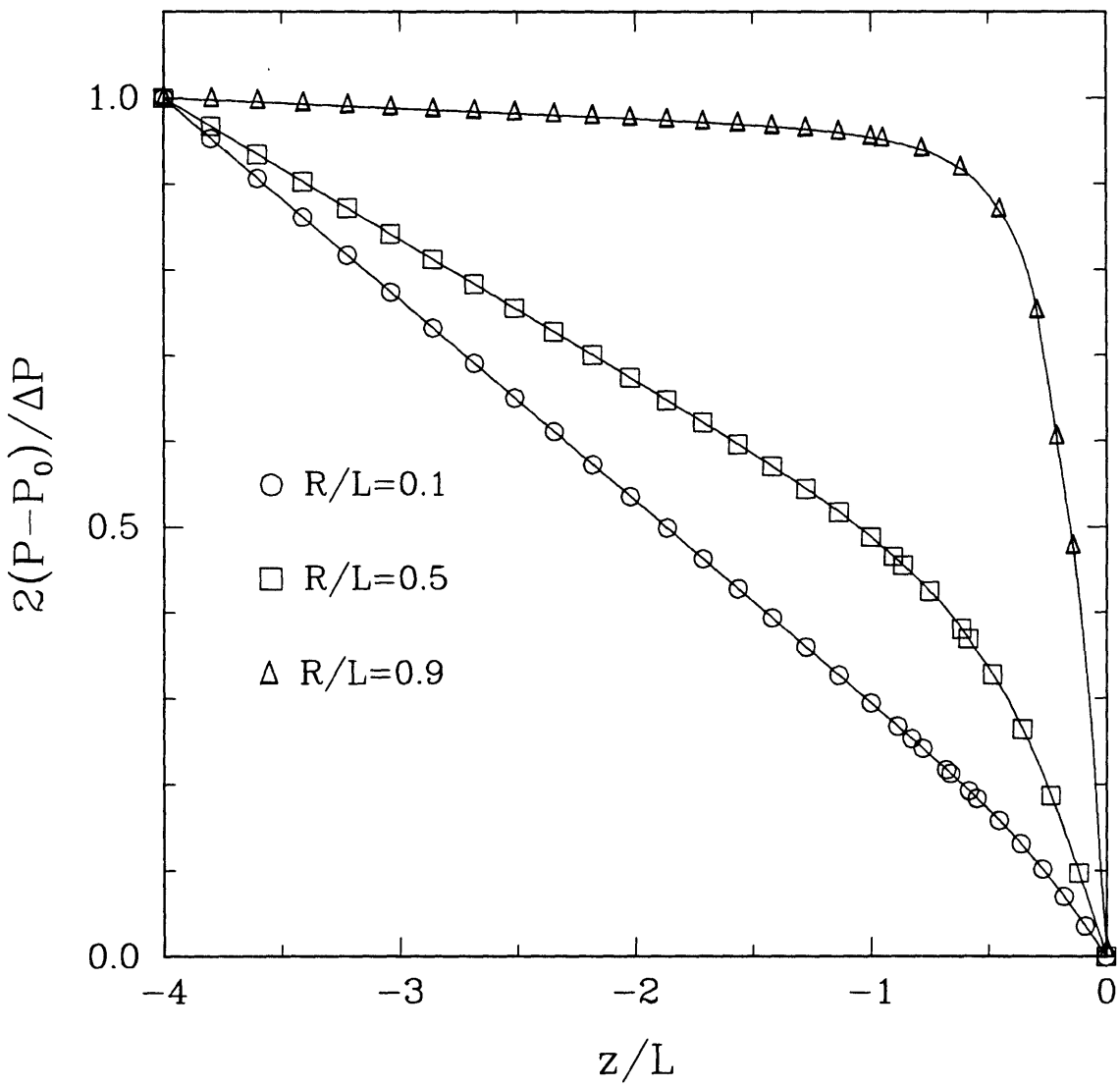

Figure 3.9 - Dimensionless pressure for flow through a row of cylinders between walls, with $L/W = 2$ and $R/L = 0.1$, 0.5, and 0.9. P is evaluated at $x/W = -0.5$ and $(y-R)/L = -0.5$. P_0 is the pressure at $z = 0$. The dimensionless pressure is anti-symmetric about $z = 0$; that is, $[P(x,y,z) - P_0] = -[P(x,y,-z) - P_0]$.

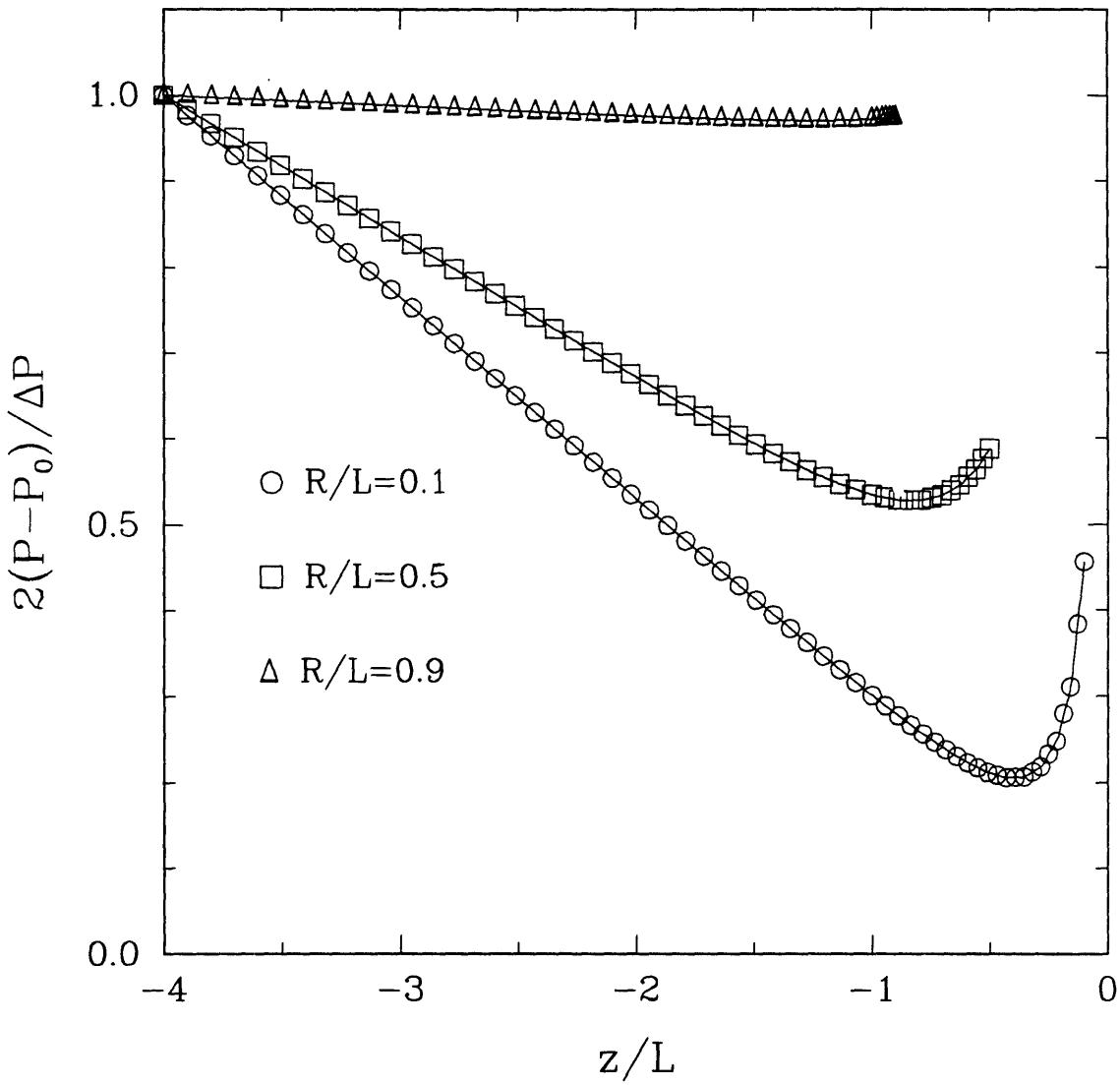

Figure 3.10 - Dimensionless pressure for flow through a row of cylinders between walls, with $L/W = 2$ and $R/L = 0.1$, 0.5, and 0.9. P is evaluated at $x = y = 0$. P_0 is the pressure at $z = 0$. The profiles are interrupted at $z = -R$, which corresponds to the surface of the cylinder.

The profiles of v_z illustrated in Figure 3.8 closely resemble those for the two-dimensional case (Figure 3.4). As R/L increases, that is, as the spacing between cylinders decreases, the decrease in cross-sectional area available for flow causes the magnitude of v_z to increase significantly near $z = 0$. Deviations in v_z/V from the unperturbed Poiseuille flow value are evident in this case only for $|z|/L < \sim 2$. In all cases considered, deviations from the unperturbed value of v_z/V at $x = 0$ were used to help guide the choice of δ; these deviations were required to be < 0.5% at $|z|/L = \delta/L - 0.5$. The additional criterion used was that further increases in δ should produce negligible changes in f.

As seen in Figure 3.9, for the largest values of R/L, most of the pressure drop occurs in the region between cylinders, whereas for the smallest values of R/L, the dimensionless pressure profile resembles the unperturbed (linear) profile. Figure 3.10 shows pressure profiles evaluated at a different location, namely $x = y = 0$. The curves are interrupted at $z = -R$, where the fluid contacts the cylinder. It is noteworthy that the pressure reaches a minimum at $z < 0$. That is, the pressure gradient at that location changes sign in the region upstream from the cylinders. This behavior is also predicted by Lee and Fung's (1969) solution for flow around a single cylinder between walls.

PARAMETRIC STUDIES. Table 3.2 gives the computed values of f as a function of L/W and R/L. The dependence of f on the dimensionless gap between cylinders ($1-R/L$) is illustrated in Figure 3.11. $L/W = 0$ corresponds to the two-dimensional results given in Section 3.4.1 and the solid line is the lubrication limit of Sangani and Acrivos (1982). For $L/W > 0$, there are two contributions to f: the drag on the cylinders and the incremental viscous stresses at the walls. In all cases analyzed, the contribution of the cylinders to the additional resistance was larger than the contribution of the incremental stresses at the walls, both tending to make $f > 0$. This is in contrast to the results of Lee and Fung (1969) for flow around a single cylinder between walls, where the cylinder and wall effects were of opposite algebraic sign. That is, the shear forces at the walls for their single cylinder were smaller than the undisturbed Poiseuille values, while those for

Table 3.2 - Dimensionless additional resistance (f) for flow through a single row of cylinders between parallel walls

	L/W				
R/L	0	1	2	3	4
0.1	3.78	4.95	6.23	7.89	9.79
0.3	9.96	13.7	19.2	27.3	37.6
0.5	26.4	35.6	50.0	71.9	101
0.7	100	125	161	214	286
0.8	280	328	393	482	601
0.85	575	652	747	873	1.04×10^3
0.9	1.59×10^3	1.73×10^3	1.90×10^3	2.10×10^3	2.34×10^3

our row of cylinders were larger. This can be explained as follows. Because of the no slip condition at the cylinder surface, the fluid must decelerate in the immediate vicinity of the cylinders. This decrease in v_z tends to decrease the magnitude of the shear stresses at the channel walls, relative to the undisturbed Poiseuille flow values. On the other hand, in the region between cylinders, the velocity must increase above the undisturbed values in order to satisfy continuity. This increase in v_z tends to increase the stresses at the walls above the undisturbed flow values. In all our simulations with the ladder configuration, the latter factor dominated and, thus, the shear forces at the walls were larger than the undisturbed flow values. For the case of one cylinder (Lee and Fung, 1969), because the domain around the cylinder was infinite in all directions, the decrease in stress caused by the deceleration of the fluid near the cylinder evidentely dominated and thus the shear forces at the walls were smaller than the undisturbed values.

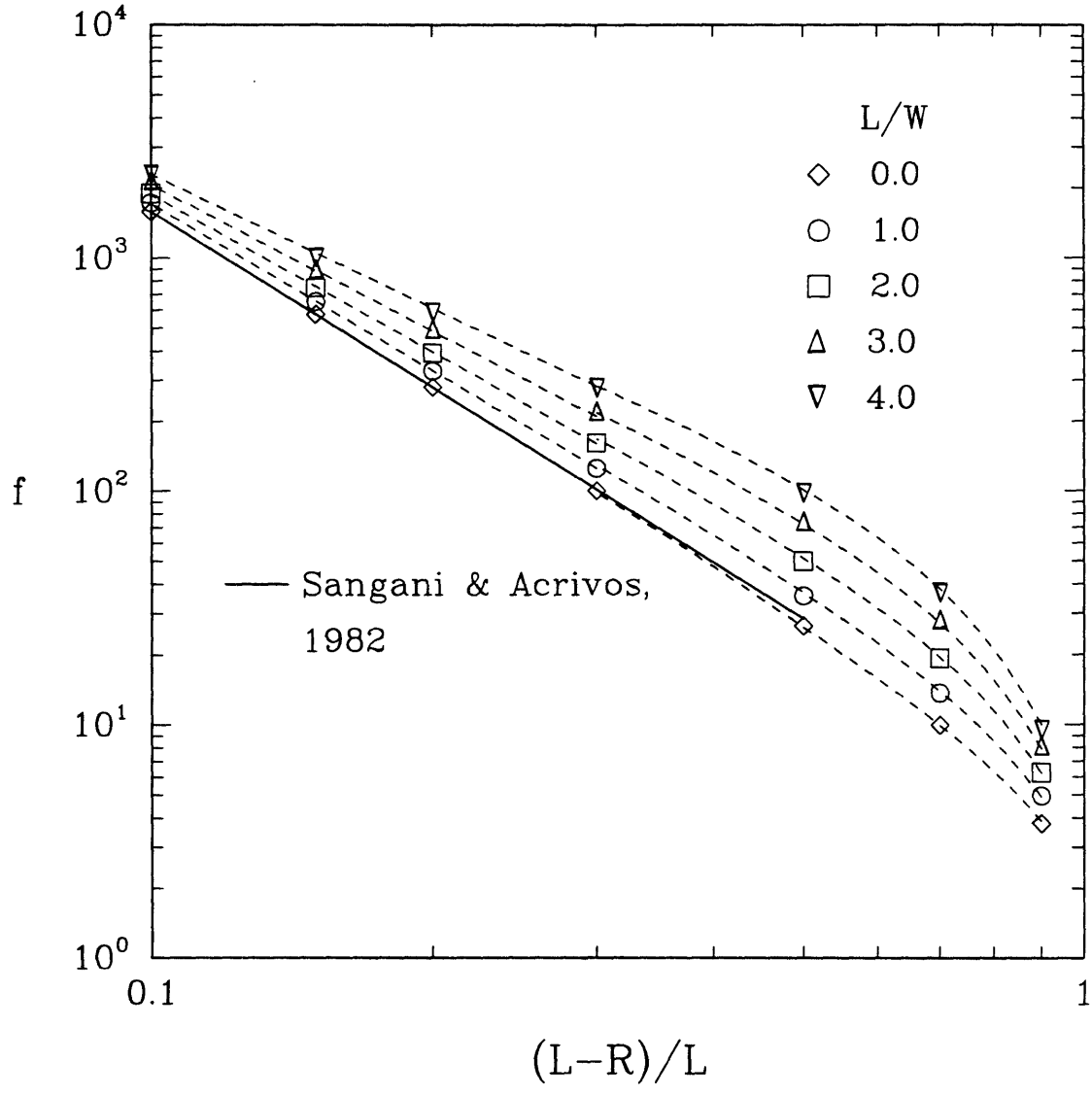

Figure 3.11 - Dimensionless additional resistance as a function of the dimensionless gap between cylinders for flow through a row of cylinders between walls. Symbols are the numerical results; the dashed lines represent the interpolation formulas (equations (3.15) - (3.17) for $R/L \geq 0.7$ and (3.18) - (3.20) for $R/L \leq 0.7$); the solid line is the two-dimensional lubrication solution of Sangani and Acrivos (1982).

For a given aspect ratio L/W, as the gap between cylinders decreases the drag on the cylinders increases and, thus, f increases. Moreover, for fixed L and R, as the spacing between walls decreases (that is, as L/W increases), f increases. It can also be seen that f is more sensitive to changes in R/L than to changes in L/W and, thus, for small gaps, the values of f approach the two-dimensional lubrication limit of Sangani and Acrivos (1982).

Figure 3.12, which is a replot of the results in Figure 3.11, shows the dependence of f on R/W for different values of R/L. The solid line is the two-term approximation of Lee and Fung (1969) for flow around a single cylinder between parallel walls, and corresponds to $R/L = 0$. It can be seen that, as was observed in Figure 3.11, f becomes less dependent on R/W for the larger values of R/L.

Interpolation formulas for f were obtained. When the gap between cylinders is small, f is well approximated by

$$f = A\left(1-\frac{R}{L}\right)^{B} \tag{3.15}$$

where

$$\log A = \log\left(\frac{9\pi}{4\sqrt{2}}\right)+0.144\frac{L}{W}+0.0111\left(\frac{L}{W}\right)^{2} \tag{3.16}$$

and

$$B = -2.5+0.110\left(\frac{L}{W}\right)+0.00957\left(\frac{L}{W}\right)^{2} \tag{3.17}$$

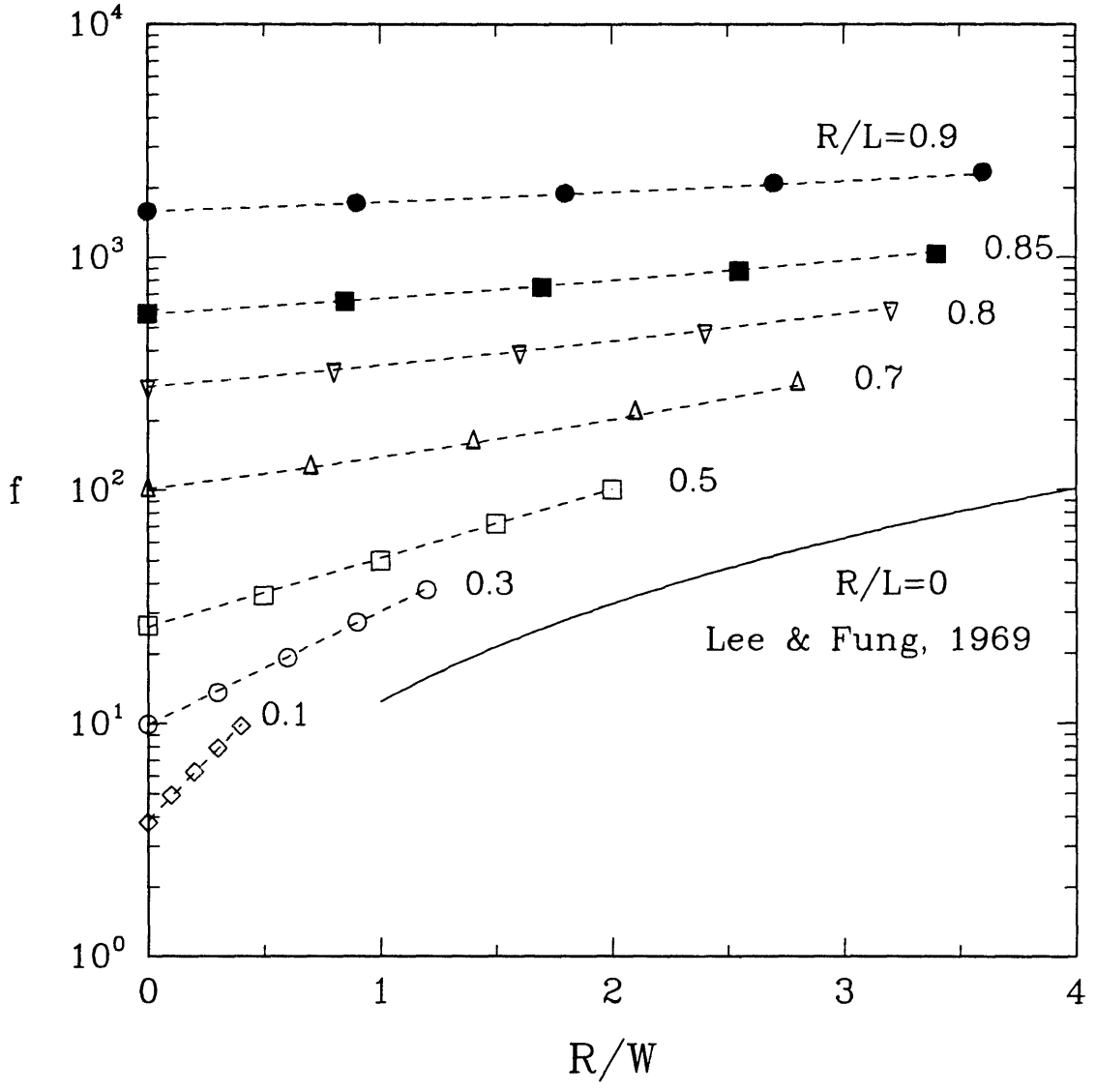

Figure 3.12 - Dimensionless additional resistance as a function of *R/W* for flow through a row of cylinders between walls. Symbols are the numerical results; the dashed lines represent the interpolation formulas (equations (3.15) - (3.17) for $R/L \geq 0.7$ and (3.18) - (3.20) for $R/L < 0.7$); the solid line is the two-term solution of Lee and Fung (1969) for a single cylinder between walls.

These expressions are accurate to within 3% for $0.7 \le R/L \le 0.9$ and $0 \le L/W \le 4$. When $L/W = 0$, equations (3.15) - (3.17) reduce to the two-dimensional lubrication formula of Sangani and Acrivos (1982). For less closely spaced cylinders,

$$\log f = C + D\frac{R}{W} \tag{3.18}$$

where

$$C = 0.336 + 2.74\left(\frac{R}{L}\right) - 2.74\left(\frac{R}{L}\right)^2 + 3.16\left(\frac{R}{L}\right)^3 \tag{3.19}$$

and

$$D = \frac{0.0639}{R/L} + 0.454 - 0.652\left(\frac{R}{L}\right) + 0.152\left(\frac{R}{L}\right)^2 \tag{3.20}$$

which is accurate to within 4% for $0.1 \le R/L \le 0.7$ and $0 \le L/W \le 4$.

It must be emphasized that the relative errors in the numerical values of f are expected to be larger for small R/L and large L/W since in these cases $f_T \sim f_P$. (For the value of δ used in most of the simulations, $f_P = 24$, 96, 216 and 384 for $L/W = 1$, 2, 3 and 4, respectively.)

The fact that, in the two-dimensional limit ($L/W = 0$), the values of f for a single row and for a square (doubly periodic) array of cylinders (with the same R/L) are similar (see Section 3.4.1) suggests that this might also be true when the cylinders are confined between walls. This hypothesis motivates a comparison between our results for the ladder configuration (periodicity in y direction) and those of Tsay and Weinbaum (1991)

for a square array of cylinders between walls (periodicity in y and z directions). Tsay and Weinbaum (1991) assumed that the direction of flow makes an angle of 45° with the z-axis but, as shown in Lee (1969), the drag coefficient for a square array is independent of flow direction. We used the interpolation formula of Tsay and Weinbaum (1991) (accuracy of 20%) to estimate the dimensionless additional resistance for flow perpendicular to a square array of cylinders between walls. The differences between these estimates and our numerical values of f for the ladder geometry were in all cases < 21%.

3.4.3 HYDRAULIC PERMEABILITY OF THE EPITHELIAL SLITS

Here, we consider the zipper configuration of the slit diaphragm, as reported by Rodewald and Karnovsky (1974). According to these authors, the spaces between the central filament (radius R_C) and the membranes of the epithelial foot processes which bound the filtration slit (here represented as a parallel wall channel) are bridged by fibers of radius R_B. The center-to-center spacing of the fibers is $2L$ and width of the slit is $2W$ (Figure 3.1). The average values for the ultrastructural parameters are R_B = 3.5 nm, R_C = 5.45 nm, L = 5.6 nm and W = 19.7 nm (Rodewald and Karnovsky, 1974), giving R_B/L = 0.625, R_C/W = 0.277 and L/W = 0.284. To establish upper and lower bounds for each of these ratios, we used the standard deviations of the slit dimensions given by Rodewald and Karnovsky (1974). We analyzed the sensivitivity of f to changes in the three length ratios by performing a series of six simulations where each of these ratios was independently varied. The finite element meshes used in the simulations were composed of ~7600 to ~10,000 nodes (~750 to ~1000 elements) and the CPU time with a Cray X-MP EA/464 was ~5 to ~11 minutes. The "baseline" results and the results of the six additional simulations are given in Table 3.3. It was verified that f was most sensitive to R_B/L (a change of +22% in R_B/L lead to a change of +180% in f), then to R_C/W (changes

Table 3.3 - Dimensionless additional resistance (f) for flow through the zipper configuration of the slit diaphragm

R_B/L	R_C/W	L/W	f
0.625	0.277	0.284	101
0.516	0.277	0.284	56.7
0.760	0.277	0.284	284
0.625	0.234	0.284	93.0
0.625	0.326	0.284	112
0.625	0.277	0.236	97.6
0.625	0.277	0.340	105

of about ±20% in R_C/W produced changes of about ±10% in f) and finally to L/W (changes of about ±20% in L/W produced changes of about ±4% in f). The high sensitivity of f to R_B/L parallels the high sensitivity of f to R/L in the ladder configuration.

Figure 3.13 shows the dimensionless additional resistance f plotted as a function of A_C/A_T, where $A_T = 4LW$ is the cross-sectional area/unit cell and A_C is the wetted area of the cylinders/unit cell,

$$A_C = 4\pi R_C L - 8R_C \int_0^{\sin^{-1}(R_B/R_C)} \sqrt{R_B^2 - R_C^2 \sin^2\theta}\, d\theta + 4\pi R_B W - 8R_B \int_0^{\pi/2} \sqrt{R_C^2 - R_B^2 \sin^2\theta}\, d\theta \tag{3.21}$$

or, equivalently,

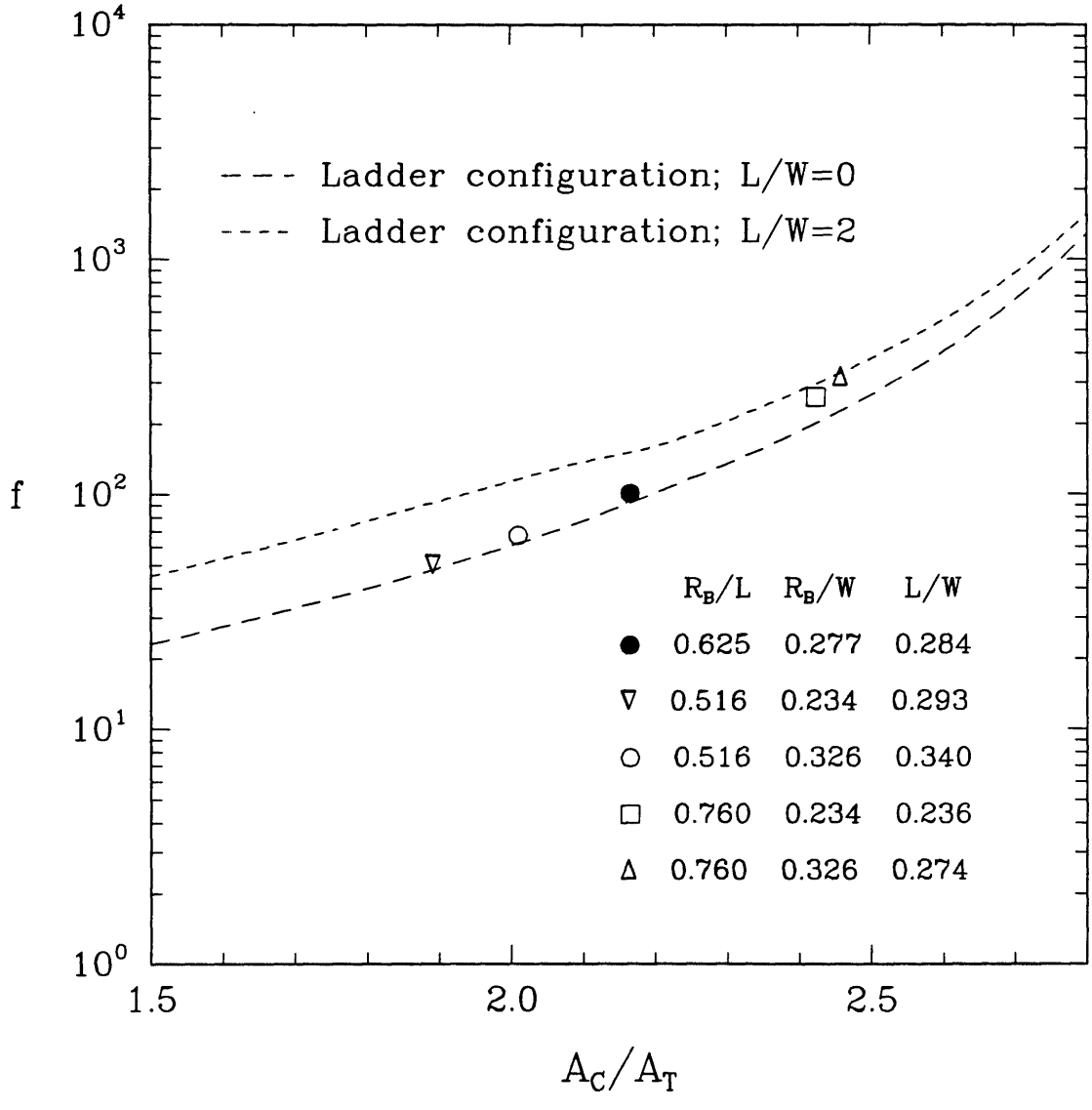

Figure 3.13 - Dimensionless additional resistance as a function of the ratio of wetted cylinder area (A_C) to total cross sectional area (A_T) for the ladder and zipper configurations. The dashed lines are the interpolation formulas for the ladder configuration; symbols are results for the zipper configuration.

$$A_C = 4\pi R_C L - 8R_C^2 E\left(\frac{\pi}{2}, \frac{R_B}{R_C}\right) + 8\left(R_C^2 - R_B^2\right) F\left(\frac{\pi}{2}, \frac{R_B}{R_C}\right) + 4\pi R_B W - 8R_B R_C E\left(\frac{\pi}{2}, \frac{R_B}{R_C}\right) \tag{3.21a}$$

where F and E are elliptic integrals of first and second kinds, respectively. A simple approximate formula which, for the range of parameters studied, is accurate to within 6%, is

$$\frac{A_C}{A_T} \cong \pi\left(\frac{R_C}{W} + \frac{R_B}{L} - 0.5\frac{R_B^2}{LW} - \frac{R_B R_C}{LW}\right) \tag{3.22}$$

The dashed lines in Figure 3.13 correspond to the interpolation formulas for the ladder configuration ($A_C/A_T = \pi R/L$) for the cases of $L/W = 0$ and $L/W = 2$. The symbols are results of numerical simulations with the zipper configuration, for the baseline values of the three length ratios (filled circle) as well as for the combinations of structural parameters that give the largest and smallest values of R_B/L and R_C/W. It can be seen that the values of f for the zipper configuration correlate well with those obtained for the ladder configuration, when plotted in this manner. In particular there is good agreement with the results for the two-dimensional case ($L/W = 0$) (Note that for the zipper configuration, $L/W = 0.24$ - 0.34). This provides a simple way of obtaining a rough estimate of f for the zipper configuration using the results given in Section 3.4.2 for the ladder configuration.

For the average values of the geometric parameters reported by Rodewald and Karnovsky (1974), $A_C/A_T = 2.16$ and, as shown in Table 3.3, $f = 101$ (using a mesh with 9851 nodes, 1008 elements). Neglecting f_p, the hydraulic permeability of the epithelial

slit was computed to be 7.9×10^{-8} m/s/Pa. Typical values for the overall hydraulic permeability of the glomerular capillary wall are ~ 3 - 5×10^{-9} m/s/Pa (see Section 1.1). Since the slits occupy only ~10% of the surface of the glomerular capillary wall, we conclude that the slit diaphragms contribute roughly half of the overall hydraulic resistance of the glomerular capillary wall.

3.5 CONCLUDING REMARKS

As a model for flow through the slit diaphragms, we obtained finite element solutions of Stokes equations for flow perpendicular to a row of cylinders between parallel walls, a geometric model that is referred to as the "ladder configuration". A dimensionless additional resistance (f) of the ladder configuration was computed for $L/W \leq 4$ and $0.1 \leq R/L \leq 0.9$. Two factors contributed to f: the drag on the cylinders, and the incremental shear stresses on the walls of the channel. Of these two factors, the drag on the cylinders tended to be dominant.

We also considered the structure of the slit diaphragm originally proposed by Rodewald and Karnovsky (1974) (the "zipper configuration"). Using the value of f obtained for this structure, the hydraulic permeability of the epithelial slits was estimated to be 7.9×10^{-8} m/s/Pa. In Chapter 4 we develop hydrodynamic models for the other two layers of the capillary wall (the endothelium and the basement membrane) and combine the results of those models with the results obtained in this chapter in order to obtain theoretical estimates of the overall hydraulic permeability of the capillary wall.

CHAPTER 4

STRUCTURAL DETERMINANTS OF GLOMERULAR HYDRAULIC PERMEABILITY

4.1 INTRODUCTION

Under normal conditions the glomerular capillary wall is extremely permeable to water. However, as mentioned in Chapter 1, proteinuric kidney disorders are typically associated with significant reductions in the glomerular filtration rate of water, which are usually atributed to reductions in the glomerular ultrafiltration coefficient (K_f) calculated on a whole kidney and/or single nephron basis (Deen et al., 1985; Maddox et al., 1992; Miller et al., 1990). ($K_f = kS$, where k is the hydraulic permeability of the glomerular capillary wall and S is the total glomerular filtration area.) Frequently, these functional changes are accompanied by considerable alterations in morphology of the capillary wall, such as thickening of the basement membrane and/or broadening of the foot processes. However, there have been no suitable mathematical models to assist in establishing the quantitative relationships between structural and functional properties.

The main objective of the analysis described in this chapter was to elucidate which structures of the capillary wall determine the resistance to the filtration of water. Specifically, our objective was to develop hydrodynamic models for the endothelial fenestrae and basement membrane, and couple those models with the model for the epithelial slits described in the previous chapter in order to predict the hydraulic permeability of the capillary wall and the relative contribution of each layer to the total water flow resistance.

4.2 MODEL FORMULATION

4.2.1 MODEL GEOMETRY AND OVERALL APPROACH

Based on structural information from electron microscopy studies (Chapter 1), it is possible to identify approximate repeating units for the glomerular capillary wall. Figure 4.1 shows the idealized "structural unit" employed here, which is based on a single filtration slit and which is periodic in the x and y directions. Filtration occurs in the positive z-direction. The three layers of the capillary wall (endothelium, basement membrane and epithelium) are illustrated in the top view while the bottom view shows the surface of the fenestrated endothelium as seen from the capillary lumen.

We assumed that the shape of the fenestrae is that suggested by the detailed study of Lea et al. (1989) (see Figure 1.4). Accordingly, the fenestrae were assumed to be channels of circular cross-section (bottom view, Figure 4.1) with varying radii (top view, Figure 4.1). Also, because it has been suggested that the fenestrae are filled with a sparse fiber matrix (glycocalyx), we considered two cases, one for fenestrae containing only fluid and another for fenestrae filled with a glycocalyx. The ultrastructure of the fibers of the basement membrane has not been completely characterized, so that we modeled the basement membrane as an effectively homogeneous medium, without regard for the size, shape and position of individual fibers. The structure of the slit diaphragm was assumed to be that proposed by Rodewald and Karnovsky (1974), that is, the zipper configuration shown in Figure 3.1.

The hydraulic permeability of the glomerular capillary wall (k) is defined by the Starling equation (equation (1.1)),

$$k = \frac{J_V}{P_{UF}} \tag{4.1}$$

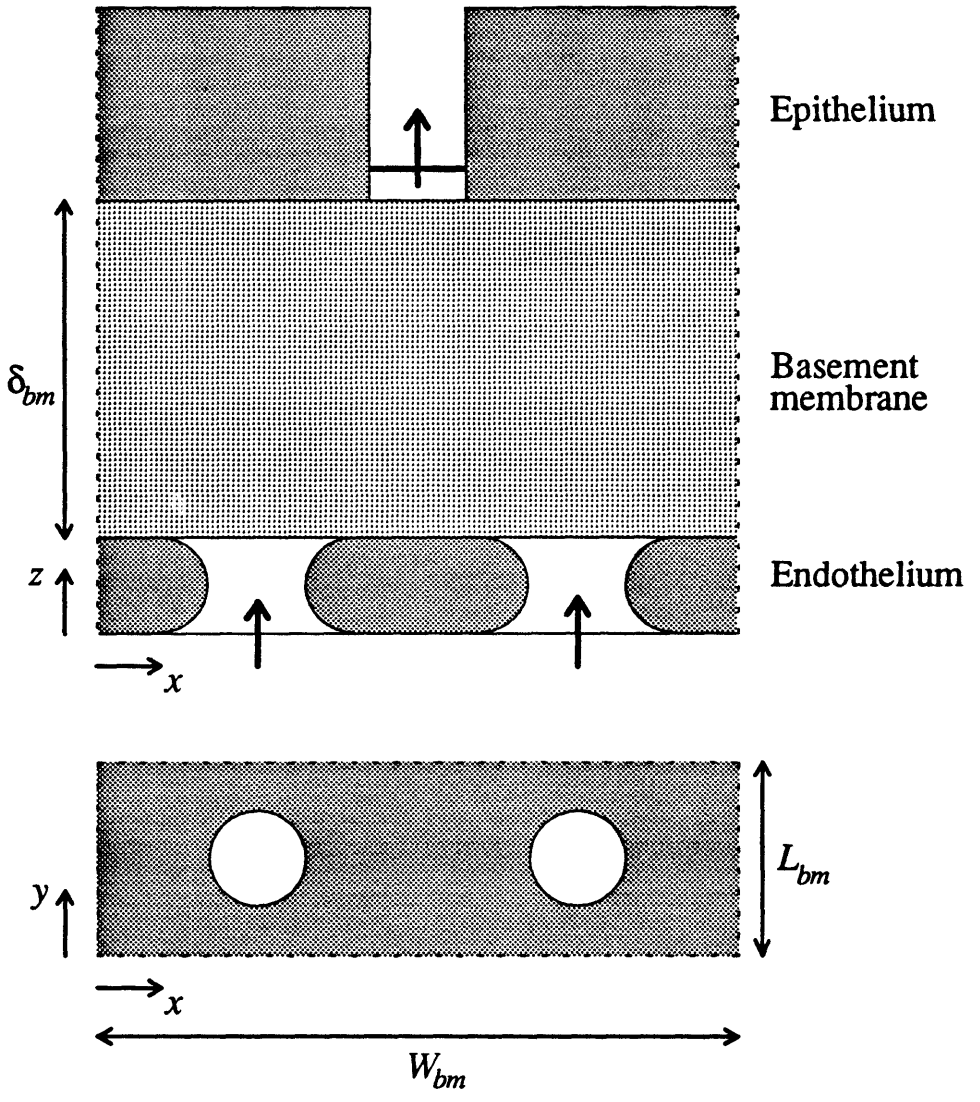

Figure 4.1 - Structural unit for the glomerular capillary wall. The top view shows the three layers of the capillary wall and the bottom view shows the endothelial surface with the circular fenestrae. In this example there are two fenestrae (N_f=2). The direction of filtrate flow is along the z-axis, as indicated by the arrows in the top view.

where J_V and P_{UF} are, respectively, the fluid velocity and net ultrafiltration pressure, both averaged over the full cross-sectional area (x and y directions) in a structural unit. Because the osmotic reflection coefficients of the major plasma proteins are very close to unity, J_V obtained for a Starling or hydraulic-osmotic pressure difference will equal that resulting from an equivalent hydraulic pressure difference. Thus, in calculating k using the structural model it is permissible to replace P_{UF} by a purely hydraulic pressure difference, $\Delta\overline{P}_T$. (In this and other quantities, overbars denote averages in x and y.) Writing $\Delta\overline{P}_T$ as a sum of three terms, one for each layer, and defining

$$k_i = \frac{J_V}{\Delta\overline{P}_i} \quad (i = en,\ bm,\ ep) \tag{4.2}$$

where the subscripts *en*, *bm* and *ep* refer to the endothelium, basement membrane and epithelium, respectively, it follows that

$$\frac{1}{k} = \frac{1}{k_{en}} + \frac{1}{k_{bm}} + \frac{1}{k_{ep}}. \tag{4.3}$$

The modeling approach consisted of computing the velocity and pressure profiles in each layer independently, thereby calculating the three individual permeabilities (equation (4.2)), and then determining k using equation (4.3).

4.2.2 MODEL FOR THE ENDOTHELIUM

Figure 4.2 shows the geometry of a single fenestra, as suggested by the structural findings of Lea et al. (1989). At $z = 0$ the radius of the fenestra is R_f, whereas at $z = -R_f$ and $z = R_f$ the radius is $2R_f$. Water flow is in the positive z-direction. If it is assumed that

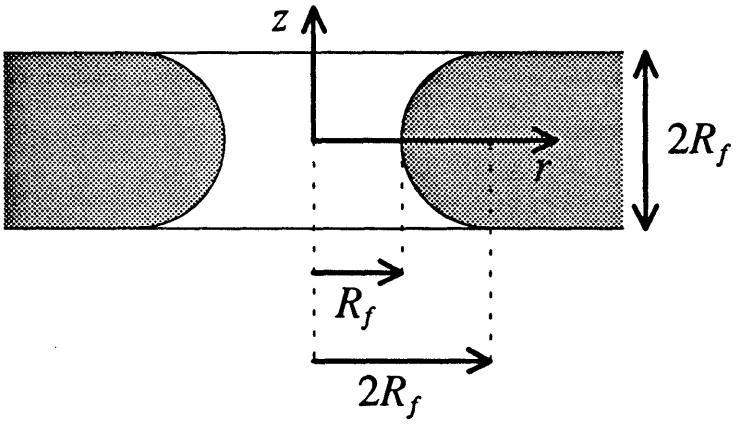

Figure 4.2 - Schematic representation of a single fenestra, as suggested by Lea et al. (1989). The main flow is along the z-axis. The radius of the fenestra at $z = 0$ is R_f, whereas at $z = \pm R_f$ the radius is $2R_f$.

the fenestrae contain only fluid, then the appropriate model equations are the Stokes and continuity equations. The boundary conditions used to solve these equations are given in Appendix A. As mentioned above, we addressed the possibility that the fenestrae might be filled with a fiber matrix (glycocalyx). The alternative mathematical model for this case is also described in Appendix A.

The equations for both modeling approaches were solved numerically using the software package FIDAP (Fluid Dynamics International, Evanston, Illinois) on a Cray X-MP EA/464 supercomputer.

The permeability of a single fenestra was determined from the computed velocity and pressure fields by

$$k_f = \frac{\bar{v}_f}{\Delta \bar{P}_{en}} = \frac{\bar{v}_f}{\left(P_G - \bar{P}_0\right)} \tag{4.4}$$

where $\bar{v}_f$ is an average fluid velocity in the z-direction in the fenestra (based on the cross-sectional area at $z = 0$), P_G is the luminal pressure and $\bar{P}_0$ is the average pressure at

the exit of the fenestra ($z = R_f$). Because $J_V = \varepsilon_f \bar{v}_f$, where ε_f is the fraction of the capillary surface occupied by the fenestrae,

$$k_{en} = \varepsilon_f k_f \ . \tag{4.5}$$

The fractional area was based on the minimum radius of the fenestrae, so that $\varepsilon_f = \pi R_f^2 N_f / (W_{bm} L_{bm})$, where N_f is the number of fenestrae/structural unit, and W_{bm} and L_{bm} are the dimensions of a structural unit in the x and y directions, respectively.

4.2.3 Model for the Basement Membrane

When structural details are not specified, flow through porous media is commonly described using Darcy's law,

$$\mathbf{v}^* = -\frac{K_D}{\mu} \nabla P^* \tag{4.6}$$

where $\mathbf{v}^*$ and P^* are the velocity and pressure averaged over a length scale large enough to represent the microstructure of the porous medium, and K_D is the Darcy permeability of the "effective medium" composed of the solid and fluid phases. This equation could be generalized to a non-isotropic porous medium by replacing the scalar K_D by a tensor, but the basement membrane will be considered here to be isotropic. If there were no cells covering the surfaces of the basement membrane then $k_{bm} = k_{bm}^\circ = K_D / (\mu \delta_{bm})$, where δ_{bm} is the basement membrane thickness. Because much of the basement membrane area *in vivo* is blocked by endothelial cells and foot processes, $k_{bm} < k_{bm}^\circ$. The purpose of the mathematical model described in this section is to predict the effect of partial cell coverage by computing the diverging-converging flow patterns in the

basement membrane. Johnson et al. (1992) developed a similar model to describe the resistance of juxtacanalicular connective tissue in the eye to outflow of aqueous humor.

Combining equation (4.6) with the continuity equation one obtains

$$\nabla^2 P^* = \frac{\partial^2 P^*}{\partial x^2} + \frac{\partial^2 P^*}{\partial y^2} + \frac{\partial^2 P^*}{\partial z^2} = 0. \tag{4.7}$$

To bracket the actual physical situation, we considered two different sets of boundary conditions. One consisted of specifying constant pressure at the openings,

$$\begin{aligned} &P^* = \overline{P}_0^* \text{ at } \Omega_f \\ &P^* = \overline{P}_1^* \text{ at } \Omega_s \\ &\frac{\partial P^*}{\partial z} = 0 \text{ at } \Omega_{en} \text{ and } \Omega_{ep}, \end{aligned} \tag{4.8}$$

where $\overline{P}_0^*$ and $\overline{P}_1^*$ are specified basement membrane pressures at the openings; Ω_f and Ω_s correspond to the endothelial and slit openings, respectively; and Ω_{en} and Ω_{ep} correspond to the surfaces covered by endothelium and epithelium, respectively. The second set of boundary conditions consisted of specifying constant velocity, rather than constant pressure, at the openings

$$\begin{aligned} &\frac{\partial P^*}{\partial z} = -\frac{\mu \overline{v}_{bm}^*}{\varepsilon_f K_D} \text{ at } \Omega_f \\ &\frac{\partial P^*}{\partial z} = -\frac{\mu \overline{v}_{bm}^*}{\varepsilon_s K_D} \text{ at } \Omega_s \\ &\frac{\partial P^*}{\partial z} = 0 \text{ at } \Omega_{en} \text{ and } \Omega_{ep} \end{aligned} \tag{4.9}$$

where ε_s is the fractional area of the slit opening and $\bar{v}^*_{bm}$ is an average basement membrane velocity in the z-direction, based on the area of a structural unit ($\bar{v}^*_{bm} = J_V$). Common to both sets of boundary conditions was that the z-component of the velocity vanishes at the areas covered by the endothelium and epithelium, so that $\partial P^*/\partial z = 0$ at those locations. The remaining boundary conditions in both cases, which incorporate the symmetry in the x and y-directions, were

$$\frac{\partial P^*}{\partial x} = 0 \quad \text{at } x = 0 \text{ and } x = W_{bm}/2 \tag{4.10}$$

and

$$\frac{\partial P^*}{\partial y} = 0 \quad \text{at } y = 0 \text{ and } y = L_{bm}/2 \tag{4.11}$$

where $x = y = 0$ is the center point of the bottom view in Figure 4.1.

Equation (4.7) with either set of boundary conditions was solved using FIDAP. The hydraulic permeability of the basement membrane was then calculated by

$$k_{bm} = \frac{J_V}{\bar{P}_0 - \bar{P}_1} = \frac{-\frac{K_D}{\mu}\frac{\partial \bar{P}^*}{\partial z}}{\bar{P}_0^* - \bar{P}_1^*} \tag{4.12}$$

where $\frac{\partial \bar{P}^*}{\partial z}$ is the z-component of the pressure gradient averaged in x and y, over a structural unit, and $\bar{P}_0^*$ and $\bar{P}_1^*$ are basement membrane pressures averaged over the endothelial and slit openings, respectively.

4.2.4 MODEL FOR THE EPITHELIUM

The hydrodynamic model for the epithelial slits (slit channel with diaphragm) was developed in Chapter 3. In that chapter we analyzed two possible configurations for the slit diaphragm, namely the ladder and zipper configurations shown in Figure 3.1. Here we will consider only the zipper configuration, for which there are reported values of all structural parameters needed.

The hydraulic permeability of the epithelial slits, k_s, is given by

$$k_s = \frac{\bar{v}_s}{\Delta \bar{P}_s} = \frac{\bar{v}_s}{(\bar{P}_1 - P_B)} \tag{4.13}$$

where $\bar{v}_s$ is the average of the z-component of the velocity in the slit channel and P_B is the pressure in Bowman's space. Using equations (3.9) and (3.11) (with $V = \bar{v}_s$ and $\Delta P = \Delta \bar{P}_s$), equation (4.13) becomes

$$k_s = \frac{L}{(f + f_P)\mu} \tag{4.14}$$

where L is half the distance between the centers of the cross-bridges (Figure 3.1), f is the dimensionless additional resistance of the slit diaphragm, and f_P is the dimensionless resistance of the slit channel alone. Because $J_V = \varepsilon_s \bar{v}_s$, the permeability of the epithelium is given by

$$k_{ep} = \varepsilon_s k_s \,. \tag{4.15}$$

4.3 RESULTS

4.3.1 PARAMETER VALUES

Approximate ranges for the ultrastructural parameters involved in the model, are given in Table 4.1. For the "baseline" calculations we used the following values: R_f = 30 nm (Lea et al., 1989) ; W_s (= 2W) = 39.4 nm, L = 5.6 nm, R_B = 3.5 nm and R_C = 5.45 nm (Rodewald and Karnovsky, 1974) (W, L, R_B and R_C are the slit diaphragm parameters shown in Figure 3.1); δ_{bm} = 200 nm, a representative value, halfway between the extreme values given in Table 4.1; and W_{bm} = 360 nm, L_{bm} = 120 nm and N_f = 3, leading to ε_f = 0.20 and ε_s = 0.11, which are consistent with the values given in Table 4.1. Another required model input is the Darcy permeability of the basement membrane. The value used, K_D = 2.7 nm^2, was derived from the recent results of Daniels et al. (1992) [3]. The fluid viscosity in all simulations was that of water at 37°C, μ = 7x10^{-4} Pa·s.

4.3.2 HYDRAULIC PERMEABILITY OF THE ENDOTHELIUM

The main conclusion from the calculations detailed in Appendix A is that, if the fenestrae contain only fluid, the water flow resistance of the endothelium is negligible, that is $k_{en} >> k$. In fact, using the baseline inputs we obtained $k_{en} \cong$ 2.0x10^{-7} m/s/Pa. Estimates of k from micropuncture data yield k ~ 3 - 5x10^{-9} m/s/Pa (see Section 1.1). A comparison between this experimental range for k and the computed value of k_{en} suggests that the resistance of the endothelium is ~2% of the total resistance of the capillary wall.

---

[3] Daniels et al. (1992) measured the hydraulic permeability of films of basement membrane (8.8 μm in thickness) at 25°C. Using an albumin solution at a concentration of 4g/dl, and using a filtration pressure of 50 mm Hg, they obtained a hydraulic permeability of 4.61x10^{-6} cm/s/mm Hg. The product of this value, the film thickness, and the viscosity of a dilute albumin solution at 25°C (0.00089 Pa·s) yielded K_D = 2.7x10^{-18} m^2.

Table 4.1 - Ultrastructural parameters for glomerular capillary wall of normal rat

Quantity (units)	Approximate Range	References
R_f [a] (nm)	20 - 100	Avasthi & Koshy (1988)[g], Kondo (1990), Koriyama et al. (1992), Larsson & Maunsbach (1980), Lea et al. (1989), Levick & Smaje (1987)[g], Maul (1971), Ryan (1986)[g], Takami et al. (1991)
ε_f [b]	0.08 - 0.3	Larsson & Maunsbach (1980), Lea et al. (1989), Levick & Smaje (1987)[g], Webber & Blackbourne (1970)
δ_{bm} (nm)	110 - 280	Abrahamson (1987)[g], Kondo (1990), Larsson & Maunsbach (1980), Ryan (1986)[g], Takami et al. (1991), Webber & Blackbourne (1970)
R_B [c] (nm)	3 - 10	Kondo (1990), Kubosawa & Kondo (1985), Rodewald & Karnovsky (1974)
R_C [d] (nm)	5 - 6	Rodewald & Karnovsky (1974)
L [d] (nm)	5 - 6	Rodewald & Karnovsky (1974)
W_s (nm)	20 - 80	Furukawa et al. (1991), Kondo (1990), Larsson & Maunsbach (1980), Ohno et al. (1992), Rodewald & Karnovsky (1974), Ryan (1986)[g], Webber & Blackbourne (1970)
ε_s [e]	0.09 - 0.2	Furukawa et al. (1991), Larsson & Maunsbach (1980), Rodewald & Karnovsky (1974), Shea & Morrison (1975)
W_{bm} [f] (nm)	280 - 400	Furukawa et al. (1991), Gundersen et al. (1980), Larsson & Maunsbach (1980), Rodewald & Karnovsky (1974)

Table 4.1 (continued)

Notes:

[a] In Lea et al. (1989) R_f correponds to the radius of the fenestra at $z = 0$ (Figure 4.2). The other studies do not mention the curvature of the walls.
[b] The value from Lea et al. (1989) ($\varepsilon_f = 0.2$) is based on the area of the fenestrae at $z = 0$ (Figure 4.2).
[c] The range for R_B was obtained from the mean value ± standard deviation given in Rodewald and Karnovsky (1974), and from the approximate sizes reported in Kondo (1990) and Kubosawa & Kondo (1985).
[d] The ranges for R_C and L were obtained from the mean value ± standard deviation given in Rodewald and Karnovsky (1974).
[e] The values of ε_s from Furukawa et al. (1991) were calculated as W_s/W_{bm}. The estimate of ε_s from the results of Shea and Morrison (1975) was based on the assumption of these authors that $W_s = 39$ nm.
[f] The values of W_{bm} from Rodewald and Karnovsky (1974) were calculated from reported values of W_s and estimates of ε_s.
[g] This reference either is a review or gives value(s) for the quantity of interest which were obtained from other reference(s).

We also addressed the possibility that the fenestrae are filled with a glycocalyx. Because, to our knowledge, the Darcy permeability of the glomerular glycocalyx (K_D') is not known, we performed calculations for various values Darcy permeability, including that used for the basement membrane ($K_D' = K_D = 2.7$ nm^2). In Appendix A we give results for values of K_D' ranging from 2 to 100 nm^2. The result for $K_D' = 2.7$ nm^2 was $k_{en} \cong 1.3\text{x}10^{-8}$ m/s/Pa. Although an order of magnitude smaller than the value of k_{en} calculated for fenestrae filled only by fluid, this estimate of k_{en} is still three to four times larger than experimental values for the overall permeability k. As will be discussed, the true value of K_D' is almost certainly larger than that used here. Thus, even if the fenestrae are filled with glycocalyx, it is likely that the endothelium contributes little to the overall hydraulic resistance of the capillary wall.

4.3.3 HYDRAULIC PERMEABILITY OF THE BASEMENT MEMBRANE

We first examined whether or not the circular shape of the endothelial openings is important in the calculations of k_{bm}. To do so, we compared numerical results for the three-dimensional domain with results for a simpler, two-dimensional domain where each circular fenestra was replaced by a stripe with the same fractional area and with the orientation of the epithelial slit. The fractional area was calculated using the minimum radius of the fenestra, R_f. The two-dimensional domain is shown in Figure 4.3. The width of the transformed endothelial openings, W_f, is such that $N_f W_f / W_{bm} = N_f \pi R_f^2 / (W_{bm} L_{bm}) = \varepsilon_f$. This approximation considerably reduced the computational time. For example, for a 3-D finite element mesh with ~13,000 nodes the CPU time on a Cray X-MP EA/464 was ~3 min, whereas for a 2-D mesh with ~10,000 nodes the CPU time was only ~40 s. For the baseline values of the ultrastructural parameters and constant pressure boundary conditions (equation (4.8)), the 2-D and 3-D values of k_{bm} were equal to two digits ($k_{bm} = 8.6 \times 10^{-9}$ m/s/Pa). This demonstrates that the shape of the fenestrae is not an important factor in assessing the effect of the boundaries on the permeability of the basement membrane, and justifies the use of the 2-D geometry in Figure 4.3.

It is noteworthy that if the part of the basement membrane resistance that is associated with the endothelial openings were a larger fraction of the overall basement membrane resistance, then the 2-D simplification we have employed would not be as accurate. This would occur if ε_f and/or δ_{bm} were significantly smaller than the values reported for rats. For $\varepsilon_f < \sim 0.03$ or $\delta_{bm} < \sim 30$ nm, the error in the 2-D approximation would be > ~10%, if all other parameters remained at their baseline values.

Focusing thereafter on the simpler, 2-D case, we then examined the effect of the type of boundary conditions imposed at the endothelial and slit openings. For the baseline values of the structural parameters, the numerical values of k_{bm} were 8.6×10^{-9} m/s/Pa using constant pressure boundary conditions (equation (4.8)), and 8.3×10^{-9} m/s/Pa

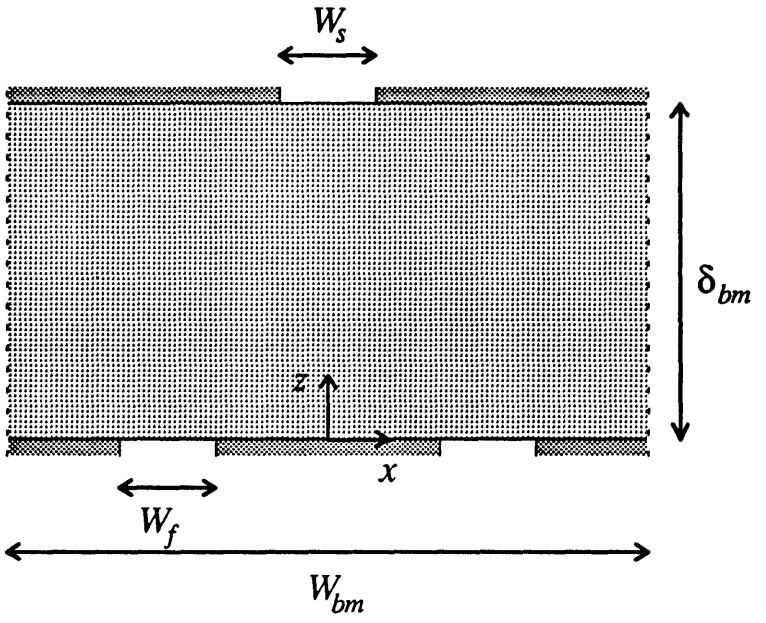

Figure 4.3 - Two-dimensional representation of the basement membrane, in which the circular fenestrae have been replaced by stripes (width = W_f) ocupying the same fractional area. W_s is the width of the slit opening and δ_{bm} is the thickness of the basement membrane.

using constant velocity boundary conditions (equation (4.9)). The difference between these two estimates of k_{bm} is negligible. We preferred the use of constant velocity boundary conditions because an analytical solution of equation (4.7) could be obtained. The 2-D pressure field with constant velocity boundary conditions is given by

$$P^* = D_0 - \frac{\mu \bar{v}^*_{bm} W_{bm}}{K_D}\left[\frac{z}{W_{bm}} + 2\sum_{n=1}^{\infty} \frac{\xi_n \cosh\left(\frac{\lambda_n z}{W_{bm}}\right) - \gamma_n \cosh\left(\frac{\lambda_n (\delta_{bm} - z)}{W_{bm}}\right)}{\lambda_n \sinh\left(\frac{\lambda_n \delta_{bm}}{W_{bm}}\right)} \cos\left(\frac{\lambda_n x}{W_{bm}}\right)\right] \tag{4.16}$$

where

$$\lambda_n = 2n\pi \tag{4.17}$$

$$\xi_n = \frac{\sin n\pi\varepsilon_s}{n\pi\varepsilon_s} \tag{4.18}$$

$$\gamma_n = \frac{\frac{1}{2}\sum_{i=1}^{N_f}\left[\sin\left(\frac{\lambda_n x_{2i}}{W_{bm}}\right) - \sin\left(\frac{\lambda_n x_{2i-1}}{W_{bm}}\right)\right]}{n\pi\varepsilon_f} \tag{4.19}$$

and D_0 is a constant related to $\overline{P}_0^*$. The quantities x_{2i-1} and x_{2i} (i = 1, ... N_f) are the x-coordinates defining the boundaries of the fenestrae in a structural unit. To calculate these coordinates we assumed that the fenestrae are equally spaced and that the structural unit is symmetric relative to $x = 0$. The values of x such that $x_{2i-1} < x < x_{2i}$ correspond to an endothelial opening whereas the values of x such that $x_{2i} < x < x_{2i+1}$ correspond to a covered region. Thus, $\varepsilon_f = \sum_{i=1}^{N_f}(x_{2i} - x_{2i-1})/W_{bm}$.

The velocity field was determined from equations (4.16) and (4.6), yielding

$$\frac{v_x^*}{\overline{v}_{bm}^*} = -2\sum_{n=1}^{\infty}\frac{\xi_n \cosh\left(\frac{\lambda_n z}{W_{bm}}\right) - \gamma_n \cosh\left(\frac{\lambda_n(\delta_{bm} - z)}{W_{bm}}\right)}{\sinh\left(\frac{\lambda_n \delta_{bm}}{W_{bm}}\right)}\sin\left(\frac{\lambda_n x}{W_{bm}}\right) \tag{4.20}$$

$$\frac{v_z^*}{\bar{v}_{bm}^*} = 1 + 2\sum_{n=1}^{\infty} \frac{\xi_n \sinh\left(\frac{\lambda_n z}{W_{bm}}\right) + \gamma_n \sinh\left(\frac{\lambda_n (\delta_{bm} - z)}{W_{bm}}\right)}{\sinh\left(\frac{\lambda_n \delta_{bm}}{W_{bm}}\right)} \cos\left(\frac{\lambda_n x}{W_{bm}}\right). \qquad (4.21)$$

Using either equation (4.20) or (4.21), one can calculate the stream function, ψ (up to an arbitrary additive constant). This yields,

$$\frac{\psi}{W_{bm}\bar{v}_{bm}^*} = \frac{x}{W_{bm}} + 2\sum_{n=1}^{\infty} \frac{\xi_n \sinh\left(\frac{\lambda_n z}{W_{bm}}\right) + \gamma_n \sinh\left(\frac{\lambda_n (\delta_{bm} - z)}{W_{bm}}\right)}{\lambda_n \sinh\left(\frac{\lambda_n \delta_{bm}}{W_{bm}}\right)} \sin\left(\frac{\lambda_n x}{W_{bm}}\right). \qquad (4.22)$$

Figure 4.4 shows isobars calculated using equation (4.16). The close spacing of the isobars near the endothelial and slit openings indicates that a large fraction of the overall pressure drop occurs in those regions. Figure 4.5 shows streamlines calculated using equation (4.22), illustrating the diverging/converging nature of the flow which causes the effective permeability of the basement membrane, k_{bm}, to be smaller than that of "bare" basement membrane.

Using equation (4.16), the average pressures at the endothelial and epithelial openings can be calculated and then substituted into equation (4.12), yielding

$$k_{bm} = \frac{K_D}{\mu \delta_{bm}} \left[1 + 2\frac{W_{bm}}{\delta_{bm}} \sum_{n=1}^{\infty} \left(\frac{\xi_n^2 + \gamma_n^2}{\lambda_n \tanh\left(\frac{\lambda_n \delta_{bm}}{W_{bm}}\right)} - \frac{2\xi_n \gamma_n}{\lambda_n \sinh\left(\frac{\lambda_n \delta_{bm}}{W_{bm}}\right)} \right) \right]^{-1}. \qquad (4.23)$$

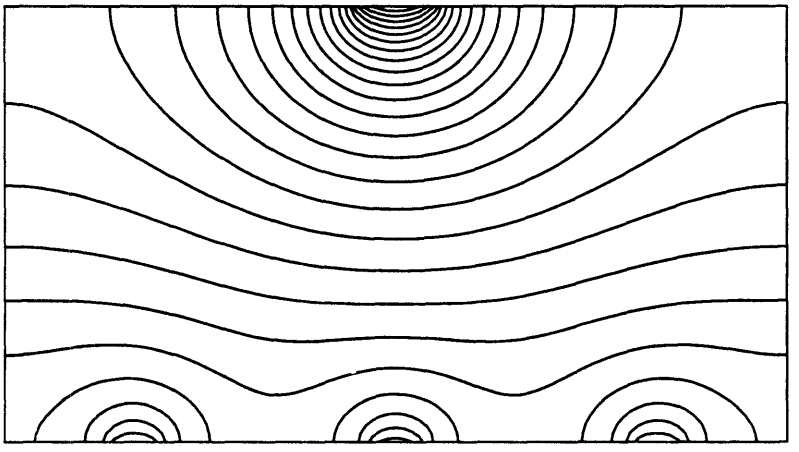

Figure 4.4 - Isobars in the basement membrane for $\varepsilon_s = 0.11$, $\varepsilon_f = 0.20$, $N_f = 3$ and $\delta_{bm}/W_{bm} = 0.56$. There are 25 equally spaced contour levels.

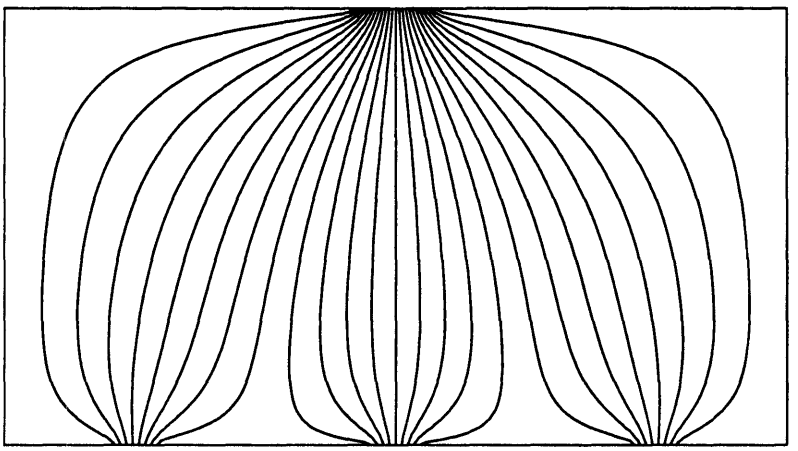

Figure 4.5 - Streamlines in the basement membrane for $\varepsilon_s = 0.11$, $\varepsilon_f = 0.20$, $N_f = 3$ and $\delta_{bm}/W_{bm} = 0.56$. There are 25 equally spaced contour levels.

Using equation (4.23) and the baseline values of the ultrastructural parameters yielded k_{bm} = 8.27x10^{-9} m/s/Pa, which confirms the finite-element result.

Equation (4.23) can be used to analyze the effect of the ultrastructural parameters on k_{bm}, without the need for further finite element computations. Figure 4.6 illustrates the effect of the fractional areas of the endothelial and slit openings on the resistance of the basement membrane. The ordinate is a dimensionless resistance of the basement membrane to filtration of water, obtained by taking the ratio of the permeabilities with (k_{bm}) and without (k°_{bm}) cells,

$$k^{*}_{bm} \equiv \frac{k_{bm}}{K_D/(\mu\delta_{bm})} = \frac{k_{bm}}{k^{\circ}_{bm}}. \qquad (4.24)$$

By definition, k^{*}_{bm} = 1 when there are no cells ($\varepsilon_s = \varepsilon_f = 1$). As cell coverage increases, that is, as ε_s and ε_f decrease, the resistance of the basement membrane increases. For the baseline condition of ε_s = 0.11 and ε_f = 0.20, Figure 4.6 shows that the actual resistance of the basement membrane is 2.3 times the resistance without cells.

Plotted in Figure 4.7 is the dimensionless resistance of the basement membrane as a function of ε_f, for varying numbers of fenestrae per structural unit (N_f). For a given value of ε_f, an increase in N_f causes a decrease in the hydraulic resistance. This is because distributing a given amount of opened area into a larger number of smaller, evenly spaced, openings (while keeping the total opened area constant) causes the flow pattern to approach that for a homogeneous surface. Since each structural unit is based on one slit, N_f may be expected to increase in glomerular diseases characterized by broadening of the foot processes.

For small enough values of ε_f and ε_s and large enough values of δ_{bm}/W_{bm}, equation (4.23) can be considerably simplified. First, we note that for large enough values of

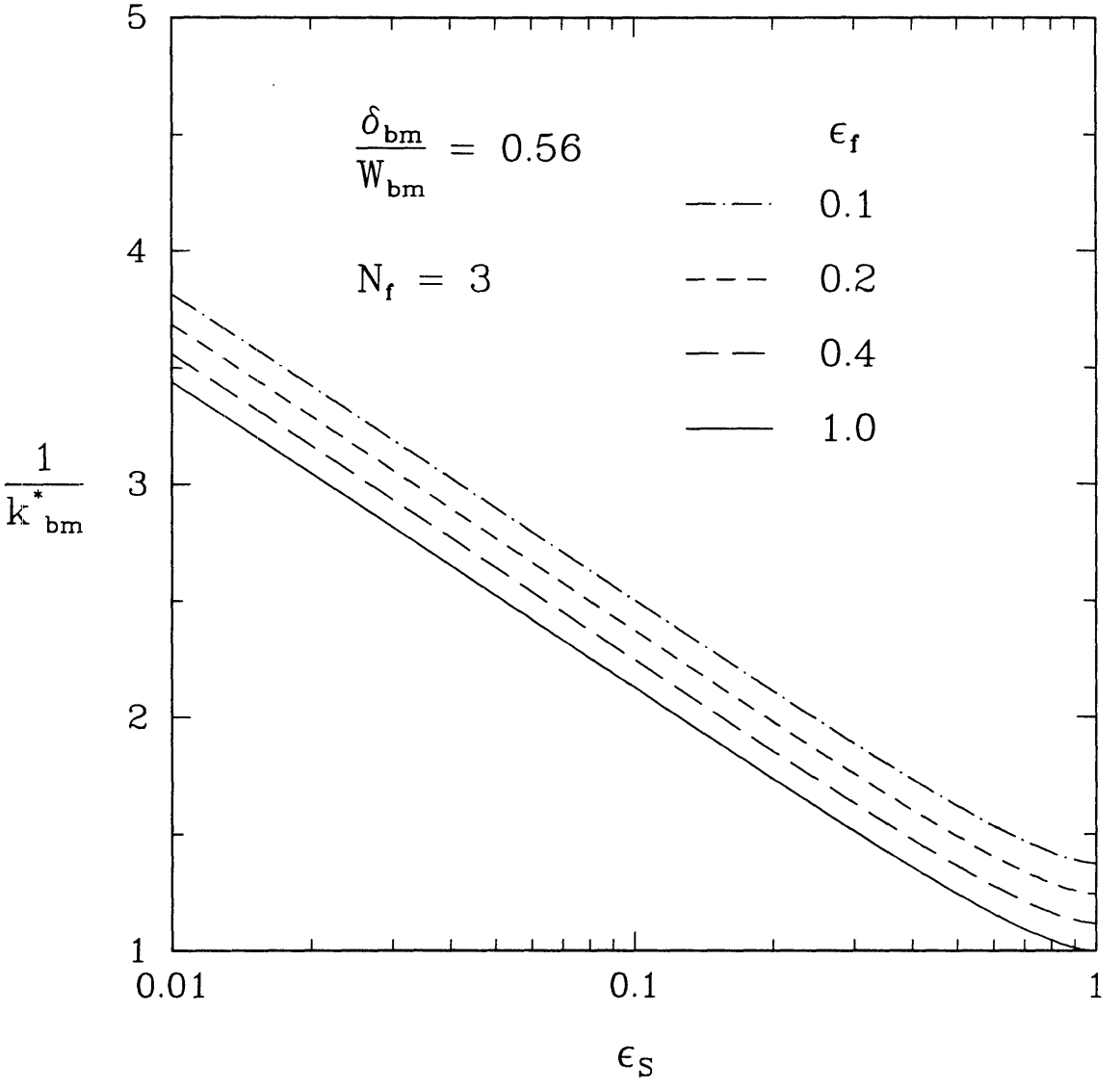

Figure 4.6 - Dimensionless resistance of the basement membrane ($1/k^*_{bm}$) as a function of the fractional area of the slit opening (ε_s) and fractional area of the fenestrae (ε_f), for three fenestrae per structural unit ($N_f = 3$) and $\delta_{bm}/W_{bm} = 0.56$.

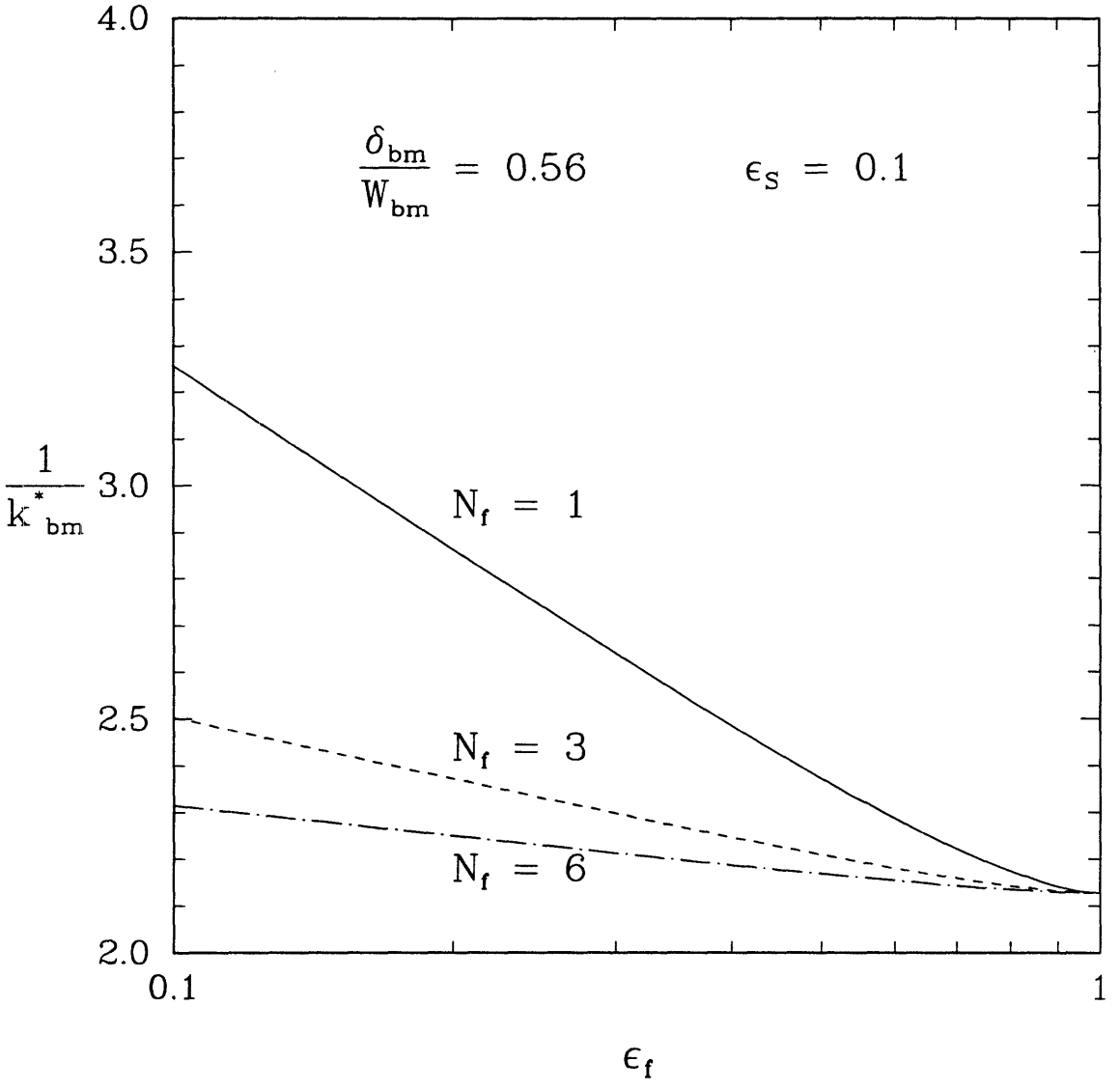

Figure 4.7 - Dimensionless resistance of the basement membrane ($1/k^*_{bm}$) as a function of the fractional area of the fenestrae (ε_f) and the number of fenestrae per structural unit (N_f), for $\varepsilon_s = 0.1$ and $\delta_{bm}/W_{bm} = 0.56$

δ_{bm}/W_{bm}, $\tanh(\lambda_n\delta_{bm}/W_{bm}) \cong 1.0$ and $\sinh(\lambda_n\delta_{bm}/W_{bm}) >> 1.0$ so that equation (4.23) can be written approximately as

$$k_{bm} \cong \frac{K_D}{\mu\delta_{bm}}\left[1+2\frac{W_{bm}}{\delta_{bm}}\sum_{n=1}^{\infty}\left(\frac{\xi_n^2+\gamma_n^2}{\lambda_n}\right)\right]^{-1}. \tag{4.25}$$

It can also be shown that

$$\begin{aligned}\sum_{n=1}^{\infty}\frac{\xi_n^2}{\lambda_n} &= \frac{1}{4\pi^3\varepsilon_s^2}\int_0^u\int_0^{u'}\sum_{n=1}^{\infty}\frac{\cos(nu'')}{n}du''\,du' \\ &= \frac{-1}{4\pi^3\varepsilon_s^2}\int_0^u\int_0^{u'}\ln\left(2\sin\left(\frac{u''}{2}\right)\right)du''\,du'\end{aligned} \tag{4.26}$$

where $u = 2\pi\varepsilon_s$. To obtain the second equality we used equation 1.441.2 of Gradshteyn and Ryzhik (1980). Expanding $\sin(u''/2)$ in a Taylor series for small u'' (i.e., for small ε_s), and retaining only the first non-zero term of the expansion, we evaluated the integrals in equation (4.26), yielding

$$\sum_{n=1}^{\infty}\frac{\xi_n^2}{\lambda_n} \cong \frac{3}{4\pi} - \frac{1}{2\pi}\ln(2\pi\varepsilon_s). \tag{4.27}$$

Similarly, it can be shown that, for small ε_f and evenly spaced fenestrae,

$$\sum_{n=1}^{\infty}\frac{\gamma_n^2}{\lambda_n} \cong \frac{1}{N_f}\left(\frac{3}{4\pi} - \frac{1}{2\pi}\ln(2\pi\varepsilon_f)\right). \tag{4.28}$$

Substituting equations (4.27) and (4.28) into equation (4.25) and using equation (4.24) yields

$$k_{bm}^{*} \cong \left\{1+\frac{W_{bm}}{\pi\delta_{bm}}\left[\frac{1}{N_f}\left(\frac{3}{2}-\ln(2\pi\varepsilon_f)\right)+\left(\frac{3}{2}-\ln(2\pi\varepsilon_s)\right)\right]\right\}^{-1}. \qquad (4.29)$$

Equation (4.29) indicates that there is a linear relationship between the dimensionless resistance, $1/k_{bm}^{*}$, and ln ε_f or ln ε_s, as was observed in Figures 4.6 and 4.7. Moreover, the slopes of the lines in Figure 4.7 are inversely proportional to the number of fenestrae/structural unit. For $N_f \geq 2$, equation (4.29) is accurate to within 2% for $\varepsilon_f \leq 0.3$, $\varepsilon_s \leq 0.3$ and $\delta_{bm}/W_{bm} \geq 0.4$. For the baseline values of the ultrastructural parameters the error is only 0.2%. Equation (4.29) provides the most convenient way to estimate the effects on k_{bm} of changes in the various structural parameters.

In the preceding analysis we assumed that the basement membrane is homogenous. In Appendix B we describe an alternative model which assumes that the basement membrane is formed by three layers of distinct Darcy permeability, corresponding to lamina rara interna, lamina densa and lamina rara externa.

4.3.4 HYDRAULIC PERMEABILITY OF THE EPITHELIUM

Assuming the zipper configuration for the slit diaphragm, and using the mean values of the structural parameters given by Rodewald and Karnovsky (1974), we obtained f = 101 (see Table 3.3). Neglecting the resistance offered by the slit channel alone (f_p), equation (4.14) yielded k_s = 7.9x10^{-8} m/s/Pa, a result also given in Section 3.4.3. We neglected f_p because for reasonable slit lengths, the resistance of the channel is much smaller than that of the slit diaphragm. (The resistance of a straight channel 100

nm long is only ~4% of the resistance of the diaphragm.). For $\varepsilon_s = 0.11$ and $k_s = 7.9\text{x}10^{-8}$ m/s/Pa, equation (4.15) yields $k_{ep} = 8.6\text{x}10^{-9}$ m/s/Pa.

An assumption of the model for the epithelial slits was that the walls of the slit channel are straight. However, electron micrographs of the capillary wall suggest that the width of the channel increases downstream from the diaphragm. In Appendix C we describe an alternative model for the epithelial slits which accounts for increases in channel width.

4.3.5 Comparison with Experimental Results for Rats

The baseline results for fluid-filled fenestrae are given in Table 4.2. The overall hydraulic permeability, calculated from equation (4.3), is $k = 4.1\text{x}10^{-9}$ m/s/Pa. It is predicted that the resistance of the endothelium is negligible and that the basement membrane and epithelium contribute roughly half to the total water flow resistance. If we assume that the fenestrae are filled with a glycocalyx with the same Darcy permeability of the basement membrane, then $k_{en} = 1.3\text{x}10^{-8}$ m/s/Pa (Section 4.3.2) and $k = 3.2\text{x}10^{-9}$ m/s/Pa. In either case, the model predicts values of k which are within the experimental range for normal rats.

The study of Miller et al. (1990) using adriamycin, which included both micropuncture and morphometric measurements, provides an excellent opportunity to apply the model to data for nephrotic rats. In that study all rats received a dose of adriamycin, which causes proteinuria and significant structural changes in the foot processes. The rats were divided into three groups: Group 1 (control) received no further treatment, Group 2 was subjected to 4/5 renal ablation and Group 3 was placed on a low protein diet. Shown in Table 4.3 are ultrastructural parameters derived from measurements reported in that study. The width of the structural unit, W_{bm}, was

Table 4.2 - Predicted and experimental values of hydraulic permeability for normal rat

	Hydraulic Permeability (m/s/Pa)	% Resistance
Endothelium, k_{en}[a]	2.0×10^{-7}	2
Basement Membrane, k_{bm}	8.3×10^{-9}	50
Epithelium, k_{ep}	8.6×10^{-9}	48
Overall, k	4.1×10^{-9}	100
Experimental Range for k	$3\text{-}5 \times 10^{-9}$	

[a] The value of k_{en} shown is for fluid-filled fenestrae.

Table 4.3 - Values of ultrastructural parameters for rats with adriamycin nephrosis

Group	W_{bm} (μm)	δ_{bm} (μm)	g
1	1.5±0.1	0.31±0.08	$(9.8 \pm 3.6) \times 10^{-3}$
2	1.2±0.1	0.50±0.09	$(4.1 \pm 1.3) \times 10^{-2}$
3	1.2±0.1	0.31±0.08	$(1.1 \pm 0.4) \times 10^{-2}$

The values are given as mean ± standard error.

calculated from the measured slit frequency as described in Appendix D, [4] and the basement membrane thickness δ_{bm} was estimated as the volume of basement membrane divided by the surface area of peripheral capillary wall (S). The fraction of the capillary wall from which foot processes had become detached, g, was calculated from the surface area of peripheral capillary wall denuded of epithelial cells divided by S. The errors shown in Table 4.3 were calculated based on the standard errors of the measured quantities. To obtain the other parameters needed, we assumed the baseline values of ε_f (= 0.2), W_s (= 39 nm), and number density of fenestrae (N_f/W_{bm} = 8.33x10^6 m^{-1}). In addition, we assumed that k_{en} = 2.0x10^{-7} m/s/Pa, calculated k_{bm} using equation (4.23) with K_D = 2.7 nm^2, and calculated k_{ep} using equation (4.15) with k_s = 7.9x10^{-8} m/s/Pa.

To account for the fact that some of the filtering surface was denuded of foot processes, we assumed that filtration occurred through two parallel pathways. Path 1, with overall hydraulic permeability k_1, included all three layers of the capillary wall. Path 2, with permeability k_2, represented areas where foot processes were absent (structural unit with ε_s = 1 and $k_{ep} \rightarrow \infty$). The overall hydraulic permeability of the composite barrier was calculated as

$$k = (1-g)k_1 + gk_2. \qquad (4.30)$$

The results of these calculations, as well as the experimental values k_{exp} (derived from the values of K_f and S reported by Miller et al. (1990)) are summarized in Table 4.4. The errors in k_{exp} were calculated based on the standard errors of K_f and S. The errors in k_1, k_2 and k were obtained by an analysis of propagation of errors (see below) based only on the

[4] This is a departure from the analysis described in the paper listed in the Foreword as containing the material of Chapter 4. In that paper, the values of W_{bm} were simply calculated as the inverse of the filtration slit frequency reported by Miller et al. (1990), without any correction to account for the random angle of sectioning (see Appendix D).

Table 4.4 - Experimental and predicted hydraulic permeabilities for rats with adriamycin nephrosis

Group	k_1 (m/s/Pa)	k_2 (m/s/Pa)	k (m/s/Pa)	k_{exp} (m/s/Pa)
1	$(9.7\pm2.0)\times10^{-10}$	$(1.0\pm0.4)\times10^{-8}$	$(1.1\pm0.2)\times10^{-9}$	$(8.7\pm1.4)\times10^{-10}$
2	$(1.2\pm0.2)\times10^{-9}$	$(6.7\pm2.1)\times10^{-9}$	$(1.4\pm0.3)\times10^{-9}$	$(1.3\pm0.2)\times10^{-9}$
3	$(1.2\pm0.2)\times10^{-9}$	$(1.0\pm0.4)\times10^{-8}$	$(1.3\pm0.3)\times10^{-9}$	$(8.7\pm1.5)\times10^{-10}$

The errors shown were obtained as described in the text.

errors of the parameters given in Table 4.3. The model was able to predict reasonably well the trends in k_{exp} (similar k_{exp} in Groups 1 and 3, and a larger value in Group 2). Although k overestimated k_{exp} in all groups, if we account for the errors in k and in k_{exp}, we see that the ranges for k and k_{exp} overlap.

4.4 DISCUSSION

The mathematical model presented here is the first one to predict the hydraulic permeability of the glomerular capillary wall from its morphology. Using only structural information and *in vitro* results obtained with isolated films of basement membrane, the model predictions agreed very well with values derived from micropuncture in normal rats. The model also predicted the trends of k observed in a study with nephrotic rats. The Darcy permeability of the basement membrane (K_D) was the only model parameter not derived from ultrastructural data. However, the value used (K_D = 2.7 nm^2), calculated from the data of Daniels et al. (1992), is consistent with the approximate structural properties of the basement membrane, namely its porosity and fiber radius. Assuming

that the volume fraction occupied by fibers is 0.1 (Robinson and Walton, 1989) and that the fiber radius is that of collagen (~1 nm), one can use the empirical relations given in Jackson and James (1986) to predict K_D. Using the equations for cubic and random arrays of fibers one obtains, respectively, $K_D = 2.1$ nm^2 and $K_D = 2.5$ nm^2, both estimates being close to the value used. Robinson and Walton (1989) have also measured the hydraulic permeability of films of basement membrane. Using their result for an albumin solution at a filtration pressure of 75 mm Hg, one gets $K_D = 1.8$ nm^2. Using this value in equation (4.23) one obtains $k_{bm} = 5.5\text{x}10^{-9}$ m/s/Pa and, from equation (4.3) (with the value of k_{en} for fluid-filled fenestrae), $k = 3.3\text{x}10^{-9}$ m/s/Pa. This is 20% lower than the baseline value of $k = 4.1\text{x}10^{-9}$ m/s/Pa, but still within the experimental range for normal rats.

Because the range of parameters given in Table 4.1 is relatively wide, we used a propagation of errors analysis (Taylor, 1982) to estimate the sensitivity of k to changes in ε_s, ε_f, δ_{bm}, W_{bm}, K_D, k_s and k_f. We assumed uncertainties of ±30% in the baseline values of ε_s, ε_f and δ_{bm}, and an uncertainty of ±20% in the baseline value of W_{bm}. To account for the value of K_D derived from the results of Robinson and Walton (1989), we assumed $K_D \equiv 2.7\pm0.9$ nm^2. We made additional simulations with the zipper configuration of the slit diaphragm to account for the standard errors of the average structural parameters given by Rodewald and Karnovsky (1974), and obtained $k_s \equiv (7.9\pm1.4)\text{x}10^{-8}$ m/s/Pa. Finally, we used the values of k_{en} given in Section 4.3.2 for fluid-filled fenestrae and fenestrae filled with glycocalyx (which were calculated assuming $\varepsilon_f = 0.2$) and estimated k_f using equation (4.5) with $\varepsilon_f = 0.2$. Based on these calculations we assumed $k_f \equiv (1.0\pm0.9)\text{x}10^{-6}$ m/s/Pa. With these assumptions, a propagation of error analysis (Taylor, 1982), where each of the parameters was independently varied, yielded $k \equiv (4.1\pm2.4)\text{x}10^{-9}$ m/s/Pa.

The model predicts that the hydraulic resistance of the endothelium is much smaller than that of the basement membrane or epithelium. As suggested by Lea et al. (1989), we assumed that the fenestrae have a circular cross-section, but some studies

propose other shapes (e.g. octagonal (Maul, 1971) or oval (Kondo, 1990)). The assumed shape of the fenestrae is of little consequence in the model, because the resistance of the endothelium is small.

As was discussed in Chapter 1, there is some evidence that the endothelial cells are covered by an anionic fiber matrix (the glycocalyx) and that this fiber matrix also fills the fenestrae. Podocalyxin (a sialoglycoprotein), heparan sulfate proteoglycans and hyaluronic acid have been identified in the glycocalyx. This fiber matrix is probably much more permeable to water than the basement membrane, whose major component is collagen. Indeed, whereas reported values of Darcy permeability for pure hyaluronic acid matrices range from 18 to 720 nm^2 (for solid volume fractions ranging from 0.01 to 0.0003) the values for collagen range from 0.8 to 6.1 nm^2 (for solid volume fraction ranging from 0.3 to 0.09) (Jackson and James, 1986). Levick and Smaje (1987) used the Carman-Kozeny equation to estimate the hydraulic permeability of the endothelial glycocalyx of various fenestrated capillaries. They assumed a fiber radius of 0.5 nm and a solid volume fraction of 0.05. These values, given in a review by Curry (1984), were estimated by applying the "fiber matrix model" of Curry and Michel (1980) to hydraulic conductivity and protein filtration data obtained in mammalian capillaries, other than the glomerulus. Despite the limitations of this model (see Section 1.3.2) and the fact that the experimental data might not apply to the glomerular glycocalyx, we used their values of fiber radius and solid volume fraction and the Carman-Kozeny equation (with its constant set equal to 5) to calculate the Darcy permeability (K_D'). This yielded $K_D' = 4.3$ nm^2. Using this value for the Darcy permeability of the glycocalyx, we obtained $k_{en} = 2.0 \times 10^{-8}$ m/s/Pa and $k = 3.5 \times 10^{-9}$ m/s/Pa. In this case, the resistance of the endothelium is 17% of the overall resistance of the capillary wall, still a much smaller percentage than those of the basement membrane (42%) or epithelium (41%). In conclusion, the value of $k_{en} \cong 1.3 \times 10^{-8}$ m/s/Pa, that we calculated assuming $K_D' = 2.7$ nm^2, should underestimate

the true permeability of the endothelium, even if the fenestrae are filled with a glycocalyx.

As was mentioned in Chapter 1, some ultrastructural studies report the existence of one or more diaphragms covering each fenestra. Because most evidence seems to indicate that they are not present in the adult rat glomerular capillary wall, we did not attempt to account for such diaphragms in our model.

In calculating the permeability of the basement membrane (k_{bm}), we assumed that the effective radius of the endothelial openings is equal to the minimum radius of the fenestrae (R_f). This choice was partially motivated by the fact that the study of Lea et al. (1989) seems to be the only one suggesting that the radius of the fenestrae changes, becoming twice as large where the fenestrae contact the basement membrane. As seen in Table 4.1, typical values for the fraction of the capillary wall occupied by the fenestrae, ε_f, are smaller than 0.3. If we had assumed that the effective radius of the endothelial openings was $2R_f$, then we would have obtained a much larger area fraction, $\varepsilon_f \equiv 0.8$. Keeping all other parameters the same, equation (4.23) yields $k_{bm} = 9.2\text{x}10^{-9}$ m/s/Pa and equation (4.3) yields $k = 4.3\text{x}10^{-9}$ m/s/Pa for $\varepsilon_f = 0.8$. The value of k is only 5% higher than the baseline result, indicating that the effective radius assumed for the openings is unimportant. In the calculations of k_{bm} we further assumed that the domain is symmetric relative to $x = 0$ (Figure 4.3). This simplification is justified since we verified that, for a given ε_f, the exact location of the fenestrae is not an important parameter when compared with, for example, N_f.

One of the major limitations of Darcy's law is that, for flow in bounded porous media, it is not capable of satisfying the required continuity of velocity and surface stress at the boundary surfaces, because of its reduced order in $\mathbf{v}^*$ as compared with Stokes equations. To circumvent this problem, Brinkman (Brinkman, 1947) proposed the following correction to equation (4.6)

$$\nabla P^* = -\frac{\mu}{K_D}\mathbf{v}^* + \mu\nabla^2\mathbf{v}^* . \qquad (4.31)$$

This equation can be viewed as Darcy's law with an extra term to account for the viscous stresses in the fluid, or as Stokes equation with an additional term to account for the resistance offered by the solid phase. Because P^* and $\mathbf{v}^*$ in equation (4.31) are averaged over a lenght scale (δ_{ave}) representative of the microstructure of the basement membrane, these two variables must change over a distance which is large compared with δ_{ave}. Examination of equation (4.31) shows that velocity gradients can occur in a length scale comparable to $\sqrt{K_D}$. Therefore, using Brinkman's equation to better describe flow near boundaries is expected to be valid only in highly permeable porous media where $\sqrt{K_D}$ >> δ_{ave}. A lower bound estimate of δ_{ave} is the interfiber spacing. Estimates of the interfiber spacing range from ~3 to ~20 nm (Kubosawa and Kondo, 1985, Laurie et al., 1984; Takami et al., 1991). Assuming K_D = 2.7 nm^2 then $\sqrt{K_D}$ < δ_{ave} and the use of equation (4.31) is questionable. Thus, neither Darcy's law nor Brinkman's equation will give an accurate representation of the flow field near the boundaries, in a length scale comparable to $\sqrt{K_D}$ (1.6 nm). Because this distance is much smaller than the dimensions of a structural unit (δ_{bm} = 200 nm), it is expected that the relative magnitude of the global errors will not be very significant. In systems where the macroscopic dimensions are much larger than $\sqrt{K_D}$ the viscous term in equation (4.31) is negligible over most of the domain and, thus, Darcy's law is a good approximation.

The basement membrane apparently consists of three layers of distinct electron density, namely a central, electron dense layer (the lamina densa) and two external, less dense layers (the lamina rarae interna and externa), although it has been suggested that this three-layered structure might be an artifact of the method used to prepare the tissue for electron microscopy (Goldberg and Escaig-Haye, 1986). For simplicity, and because it was possible to derive experimental values for K_D only for the basement membrane as a

whole, all of the foregoing results were obtained by assuming a single layer of basement membrane with uniform properties. We also investigated an alternative model in which the basement membrane has three layers, each with its own K_D. Specifically, we obtained the analytical solution for the two-dimensional domain (Figure 4.3) using constant velocity boundary conditions at the endothelial and slit openings, as detailed in Appendix B. In that appendix we show that if, as suggested by the limited ultrastructural information available, the Darcy permeability of the lamina rarae is much larger than that of the lamina densa, k_{bm} eventually approaches the value obtained when no boundaries are present ($k_{bm} = 1.93 \times 10^{-8}$ m/s/Pa). Using $k_{bm} = 1.9 \times 10^{-8}$ m/s/Pa, $k_{en} = 2.0 \times 10^{-7}$ m/s/Pa and $k_{ep} = 8.6 \times 10^{-9}$ m/s/Pa in equation (4.3) we obtain $k = 5.8 \times 10^{-9}$ m/s/Pa, which is somewhat above the experimental range of $3 - 5 \times 10^{-9}$ m/s/Pa.

In calculating the resistance of the filtration slits we assumed that the channel walls are straight (Figures 3.1 and 4.1). That is, the shape of the foot processes was not taken into account. Most electron micrographs of the glomerular capillary wall suggest that the channel width (distance between adjacent foot processes) increases with increasing distance downstream from the diaphragm. However, the extent of increase and the shape of the cells depend on the method used to prepare the tissue for electron microscopy (Furukawa et al., 1991). As detailed in Appendix C, we performed numerical simulations for tapered channels in order to estimate the hydraulic permeability of the slit diaphragm in these channels. The results showed that the dimensionless additional resistance of the slit diaphragm (f) is virtually the same as that calculated assuming straight walls. Because the resistance of the channel walls (either straight or tapered) is negligible compared with the resistance due to the slit diaphragm, we conclude that the use of straight walls to predict k_s is acceptable.

The approach used to calculate the hydraulic permeability of the capillary wall by independently computing the permeability of each layer is approximate in the sense that the boundary conditions are not matched exactly at the interfaces between fenestrae and

basement membrane and between basement membrane and epithelial slits. However, the error introduced by this approach should be negligible. Regarding the basement membrane, we showed that k_{bm} is approximately the same for constant pressure and constant velocity boundary conditions, suggesting that the results are not very sensitive to the type of boundary conditions. To check this hypothesis, we performed simulations with the 3-D model of the basement membrane where we specified a pressure profile at the endothelial openings (taken here to have radius = $2R_f$) fitted from the profile computed for a single fenestra. The value of k_{bm} was not significantly different from that obtained for the usual endothelial openings of radius R_f with specified constant pressure. Regarding the epithelium, the boundary conditions at the entrance of the slit channel will have some effect on the resistance of the channel but should not significantly affect the resistance of the slit diaphragm. Since the diaphragm is the dominant contribution to the resistance of the epithelium, the effect of boundary conditions on k_{ep} is also expected to be negligible. Accordingly, there seems to be little justification for pursuing a more rigorous approach of computing the flow field simultaneously in the fenestrae, basement membrane, and slits.

The analytical results derived for k_{bm} (equations (4.23) or (4.29)), together with the results for k_{en} and k_{ep}, provide a convenient way to predict the effect on k of changes in such properties as the frequency of filtration slits and the thickness of the basement membrane. The excellent agreement obtained between predicted and measured values of k for normal and nephrotic rats supports the validity of the physical assumptions. These findings encouraged us to apply the model to an experimental study of two human nephropathies. This study is detailed in Chapter 5.

CHAPTER 5

STRUCTURAL BASIS FOR REDUCED GLOMERULAR FILTRATION CAPACITY IN NEPHROTIC HUMANS

5.1 INTRODUCTION

Studies of a variety of human glomerular diseases have demonstrated that the overall ultrafiltration coefficient (K_f) for the two kidneys is reduced relative to that in healthy controls (Austin et al., 1993; Guasch et al., 1991, 1992; Myers et al., 1991; Scandling et al., 1992). Although the inability to measure the glomerular transcapillary hydraulic pressure difference (ΔP) in humans precludes precise calculations of K_f, the reductions in K_f computed for nephrotic (i.e., heavily proteinuric) individuals are typically so large that there is little doubt that glomerular ultrafiltration capacity is severely compromised in such disorders. Because K_f as determined in these human studies is the product of glomerular hydraulic permeability (k) and the total surface available for filtration in the two kidneys, the observed reductions in K_f might be due to decreased k, decreased surface area per glomerulus, a decreased number of functioning glomeruli, or some combination of these factors. Measurements have been reported for some of the key quantities in humans which should influence K_f, including surface area per glomerulus (Austin et al., 1993; Guasch et al., 1991, 1992; Mauer et al., 1992), basement membrane thickness (Guasch et al., 1991, 1992; Myers et al., 1991; Austin et al., 1993; Mauer et al., 1984; Østerby et al., 1983), and filtration slit frequency (Austin et al., 1993; Guasch et al., 1991, 1992; Myers et al., 1991). Reductions in filtration slit frequency reflect broadening and "effacement" of the epithelial foot processes, a uniform finding in virtually all humans with the nephrotic syndrome. The most consistent

inference from morphometric analysis of glomeruli of nephrotic individuals has been a strong correlation between decreases in estimated K_f and reductions in filtration slit frequency (Bohman et al., 1984; Ellis et al., 1987; Guasch and Myers, 1993; Shemesh et al., 1986). Efforts to ascertain whether changes in filtration slit frequency or other factors can account for the observed alterations in K_f have been hampered by an inadequate understanding of the relationship between the various structural quantities and k.

The objective of the following analysis was to apply the model developed in Chapter 4 to membranous nephropathy (MN) and minimal change nephropathy (MCN), two human glomerulopathies in which K_f is estimated to decline markedly, despite preservation of the surface area available for filtration (Guasch et al., 1992, Guasch and Myers, 1993). To elucidate the biophysical basis for reduced glomerular filtration rate (GFR) and K_f in these disorders, we combined an assessment of glomerular filtration dynamics with a morphometric analysis of glomeruli obtained by renal biopsy.

5.2 METHODS

The experimental data for this study were obtained by Dr. Bryan D. Myers and Dr. Batya Kristal at the Stanford University Medical Center.

5.2.1 PATIENT POPULATION

The subjects of this study were 34 consecutive adult patients below 60 years of age, who were referred to Dr. Bryan D. Myers, because of a nephrotic syndrome and a histopathological diagnosis of either membranous nephropathy (Group MN, n = 23) or minimal change nephropathy (Group MCN, n = 11). They were aged between 18 and 59 years and 20 of the 34 were male. Thirty-six healthy volunteers (Group HC), matched

for age (21 - 54) and gender (19 males) served as controls. They were divided into two groups. One group (Group HC1, n = 24) underwent a physiological evaluation of glomerular function; the other group (Group HC2, n = 12) were living kidney transplant donors, who underwent a morphometric analysis of glomeruli obtained by kidney biopsy at the time of transplantation. Each control subject denied a history of renal disease, hypertension or diabetes, and was found to be normotensive and normoglycemic and to have a negative dipstick test for urinary protein at the time of evaluation.

5.2.2 PHYSIOLOGIC EVALUATION

Patients and Group HC1 consented to undergo differential solute clearances according to a protocol which had been approved previously by the Institutional Review Board at the Stanford University School of Medicine. Each was admitted to a Clinical Research Center on the morning of the study. Antihypertensive agents were withdrawn 48 hr prior to admission in all patients receiving such therapy. Urine was voided spontaneously after diuresis had been established with an oral water load (10 - 15 mg/Kg). A priming dose of inulin (50 mg/Kg) and para-aminohippuric acid (PAH, 12 mg/Kg) was then administered. Thereafter, inulin and PAH were given by continuous infusion to maintain plasma levels at 20 and 1.5 mg/dl, respectively.

Sixty minutes after the priming dose, arterial blood pressure was determined and blood was sampled for examination of systemic colloid osmotic pressure (π_A) and plasma concentrations of albumin and IgG. Four timed urine collections were then made, each of which was bracketed by a blood sample drawn from a peripheral vein. The glomerular filtration rate (*GFR*) was expressed as the average value for the four timed inulin clearances. The rate of plasma flow (*RPF*) was estimated by dividing the corresponding clearance of PAH by an estimate of the prevailing renal arteriovenous extraction ratio for PAH. It has been shown previously that reductions of *GFR* and

peritubular capillary protein concentration exert an additive effect to lower the extraction ratio for PAH in patients with glomerular disease (Battilana et al., 1991). Based on the observed relationships, we assigned a value for the extraction ratio of PAH of 0.9 to healthy controls, and 0.8 or 0.7 to the nephrotic patients with either a normal or depressed *GFR*, respectively.

The concentrations of inulin and PAH were determined with an automated assay (Guasch et al., 1993). The concentrations of endogenous albumin and IgG in serum and urine were determined immunochemically and the colloid osmotic pressure of plasma by membrane osmometry, as described elsewhere (Cannan-Kuhl et al., 1993).

The *GFR*, *RPF* and π_A were used together with the model of Deen et al. (1972) to calculate values of the ultrafiltration coefficient (K_f) for each individual, expressed as the total K_f for all nephrons in the two kidneys. Because the glomerular transcapillary hydraulic pressure difference (ΔP) could not be measured, we used assumed values of 35 and 40 mm Hg, which are representative of micropuncture results in rats (Maddox et al., 1992). The fractional clearances of albumin (θ_{alb}) and IgG (θ_{IgG}) were determined by dividing the clearances of albumin and IgG, respectively, by that of inulin. The fractional clarances of albumin and IgG were measured in only 21 of the 24 individuals of Group HC1.

5.2.3 MORPHOMETRIC MEASUREMENTS

LIGHT MICROSCOPY. The biopsies of all nephrotic patients were performed contemporaneously with clearance determinations and before the initiation of specific treatment. Paraffin-embedded tissue was sectioned at 1 μm intervals and stained with periodic-acid Schiff reagent. On average, 19 glomeruli per biopsy were analyzed at the light microscopic level in each nephrotic patient (range 7 - 30). The average number of glomeruli among the 12 control biopsies was also 19 (range 13 - 30). A dedicated

computer system (Southern Micro Instruments, Inc., Atlanta, GA), consisting of a video camera, screen, microscope and digitizing tablet, was used to perform measurements (Guasch et al., 1991, 1992). The outline of each glomerular tuft in the cross-section was traced onto the digitizing tablet at 900x and the cross-sectional area of the tuft (A_G) computed using area perimeter analysis. Glomerular volume (V_G) was calculated from the measured A_G and corrected to account for tissue shrinkage associated with paraffin embedding, using a linear shrinkage factor (f_s) (Weibel, 1979):

$$V_G = \frac{\beta}{d} A_G^{\frac{3}{2}} f_s^{-3} \tag{5.1}$$

where β is a dimensionless "shape coefficient" (β = 1.38 for spheres) and d is a "size distribution coefficient" which is introduced to account for variations in glomerular size (Weibel, 1979). We used d = 1.1 as in previous studies (Austin et al., 1993; Guasch et al., 1991, 1992, Myers et al., 1991), which corresponds to a distribution of glomerular sizes with a standard deviation of ~25% of the mean size (Weibel, 1979). It was determined that, in the experimental procedure for tissue fixation, the value of the shrinkage factor is f_s = 0.86, and we used this value in equation (5.1).

The numbers of patent (N_P) and globally sclerosed (N_S) glomeruli were counted in sections of cortical tissue. The percentage of sclerosed glomeruli (G) was calculated by

$$G = \frac{N_S}{N_S + N_P \frac{D_S}{D_P}} \cdot 100 \tag{5.2}$$

where D_P and D_S are the diameters of patent and sclerosed glomeruli, respectively, which are proportional to the square root of the tuft cross-sectional area. The ratio D_S /D_P

accounts for the differences in size between patent and sclerosed glomeruli, and the consequent difference in the probability of encountering a glomerulus of either type in a random cross-section.

ELECTRON MICROSCOPY. For transmission electron microscopy the tissue was fixed in 2.5% glutaraldehyde and embedded in epon. Toluidine blue-stained sections were then surveyed to locate the two patent glomeruli closest to the center of each section. Ultrathin sections (60 - 70 nm) of the selected glomeruli were next stained with uranyl acetate and lead citrate and photographed. A complete montage of each glomerulus was prepared and point and intercept counting at 2820x used to determine the peripheral capillary surface area (S) which was defined as the interface between the peripheral capillary wall and epithelium, and calculated as

$$S = s_V V_G \tag{5.3}$$

where s_V is the surface density of peripheral capillary wall (expressed as length of peripheral capillary wall per unit cross-sectional area of glomerulus). Six to eight high-power electron photomicrographs (11,280x) were then obtained from each of the two glomerular profiles to evaluate the thickness of the glomerular basement membrane and the frequency of epithelial filtration slits.

The harmonic-mean basement membrane thickness (δ_{bm}) was calculated for each individual from the measured (apparent) harmonic mean thickness (δ'_{bm}) by

$$\delta_{bm} = \frac{8}{3\pi}\delta'_{bm} \tag{5.4}$$

where $8/(3\pi)$ is a correction factor derived by Jensen et al. (1979) to account for the random angle of sectioning. The filtration slit frequency (FSF) was determined by

counting the total number of slits and dividing it by the total length of peripheral capillary wall captured on the electron micrographs (Guasch et al., 1992, Guasch and Myers, 1993).

5.2.4 CALCULATION OF k FROM HEMODYNAMIC AND MORPHOMETRIC DATA

The experimental estimate of k from the hemodynamic data (k_{exp}) was obtained from K_f, the surface area per glomerulus (S), the percent of sclerosed glomeruli (G), and the total number of glomeruli in the two kidneys (N) by

$$k_{exp} = \frac{K_f}{NS(1-G/100)}. \tag{5.5}$$

We assumed $N = 2\text{x}10^6$ (Dunnill and Halley, 1972) for all subjects.

The value of k_{exp} was calculated for each individual with membranous nephropathy (MN) or minimal change nephropathy (MCN). To obtain k_{exp} for healthy controls (HC), we used the individual morphometric data from Group HC2 together with the mean hemodynamic data from Group HC1.

5.2.5 CALCULATION OF k USING THE HYDRODYNAMIC MODEL

Estimates of k independent of those given by equation (5.5), denoted by k_{model}, were obtained from filtration slit frequency (FSF) and basement membrane thickness (δ_{bm}) by employing the hydrodynamic model developed in Chapter 4. The width of a structural unit (W_{bm}) was calculated from FSF by

$$W_{bm} = \frac{2}{\pi} \frac{1}{FSF} \tag{5.6}$$

where $2/\pi$ is a correction factor, derived in Appendix D, which accounts for the random angle of sectioning. Many of the structural parameters needed to calculate k_{model} appear not to have been measured for the human glomerular capillary wall, so that we used certain values derived for rats, as described in Chapter 4. Specifically, we used the baseline results for the hydraulic permeabilities of the endothelium (k_{en}) and epithelial slits (k_s). The permeability of the epithelial layer (k_{ep}) was calculated using equation (4.15) and the fraction of the basement membrane area occupied by filtration slits, ε_s, was calculated as $\varepsilon_s = W_s/W_{bm}$, where W_s is the slit width. To be consistent with the use of rat data to compute k_s, we used W_s = 39 nm as for the rat. This value is not very different from an estimate obtained using the data of Ellis et al. (1987) for healthy humans ($W_s \cong$ 43 nm). The permeability of the basement membrane (k_{bm}) was calculated using equation (4.23) with baseline values of Darcy permeability (K_D), fractional area of fenestrae (ε_f) and number frequency of fenestrae (N_f/W_{bm}). Finally, k_{model} was calculated using equation (4.3). The inputs for the calculations of k_{model} are listed in Table 5.1.

5.2.6 STATISTICAL ANALYSIS

Tabulated results are given as mean ± standard error. Paired student t-tests, and an analysis of variance (ANOVA) between groups, were used to assess the significance of differences in mean values. In all cases, differences between means were judged significant when $p < 0.05$.

5.3 RESULTS

Table 5.1 - Inputs for hydrodynamic model

Quantity	Value
k_{en}	2.0×10^{-7} m/s/Pa
k_s	7.9×10^{-8} m/s/Pa
W_{bm}	Individual data
W_s	39 nm
δ_{bm}	Individual data
K_D	2.7 nm^2
ε_f	0.2
N_f/W_{bm}	8.33×10^6 m^{-1}

The results of the hemodynamic measurements and calculations are shown in Table 5.2. The mean values of *GFR* and K_f are plotted in Figure 5.1. There were no statistically significant differences between the two nephrotic disorders in any of the hemodynamic quantities. In both nephrotic groups the values of the glomerular filtration rate (*GFR*), filtration fraction and π_A were all significantly depressed relative to those in healthy controls. Conversely, mean arterial pressure (*MAP*) was elevated in the nephrotic groups. Differences in *RPF* between nephrotics and controls were not statistically significant. As a consequence of the low *GFR* and the reduced colloid osmotic pressure opposing filtration, K_f was calculated to be much lower in either nephrotic group than in controls. Depending on the assumed value of ΔP, the reductions in K_f were approximately three- to four-fold. The virtually identical values of K_f in MN and MCN are of particular interest, given the marked differences in morphometry between these groups (see below). Also shown in Table 5.2 are fractional clearances of

Table 5.2 - Mean values of functional results

Quantity (units)	Group		
	HC	MN	MCN
GFR (ml/min)	113±3[a]	75±8[b]	88±12[b]
RPF (ml/min)	618±22[a]	736±85[a]	635±70[a]
Filtration fraction	0.185±0.005[a]	0.117±0.009[b]	0.140±0.018[b]
MAP (mm Hg)	88±2[a]	108±3[b]	102±4[b]
π_A (mm Hg)	23.2±0.4[a]	15.0±0.9[b]	12.9±1.3[b]
$K_f^{(35)}$ (ml/min/mm Hg)	18.4±1.6[a]	4.7±0.7[b]	5.1±1.0[b]
$K_f^{(40)}$ (ml/min/mm Hg)	9.3±0.4[a]	3.5±0.4[b]	3.9±0.6[b]
θ_{alb}	(2.8±1.0)x10^{-6} [a]	0.010±0.003[b]	0.017±0.009[b]
θ_{IgG}	(1.2±0.1)x10^{-6} [a]	0.004±0.001[b]	0.011±0.008[b]

a, b: Different letters indicate means that are different by ANOVA ($p < 0.05$)

albumin and IgG, which were three to four orders of magnitude higher in the two nephrotic groups than in healthy controls.

Results for the morphometric quantities are shown in Table 5.3 and Figure 5.2. The percent of globally sclerosed glomeruli (G) was low in all three groups and the numerical differences in the mean values between groups were not significant. Due to a significant increase in glomerular volume (V_G) in MN, the value for the surface area per glomerulus (S) in this disorder was markedly enhanced. The numerical differences between the mean value of S in MCN and that in HC and MN were not significant, while the differences in the mean values of V_G were marginal ($p = 0.044$ for MCN vs. healthy

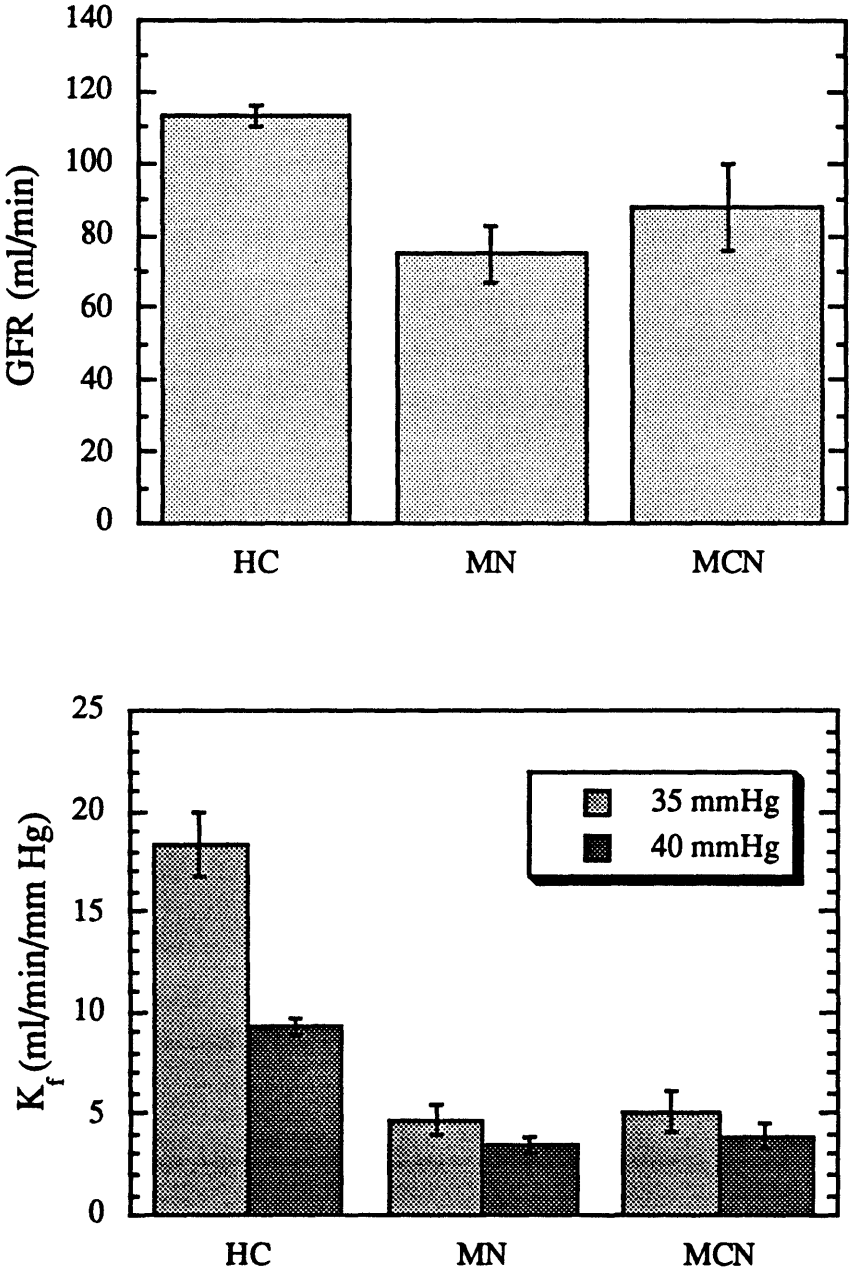

Figure 5.1 - Mean values of glomerular filtration rate (*GFR*) and ultrafiltration coefficient (K_f) in healthy controls (HC) and in membranous (MN) and minimal change (MCN) nephropathies. The error bars represent ± 1 standard error.

Table 5.3 - Mean values of morphometric results

Quantity (units)	Group		
	HC	MN	MCN
G (%)	2.3±1.2[a]	6.2±1.8[a]	0.73±0.73[a]
V_G (10^6 μm^3)	1.98±0.20[a]	4.91±0.34[b]	3.27±0.59[c]
S (10^5 μm^2)	2.97±0.32[a]	5.37±0.46[b]	4.06±0.61[a,b]
FSF (1/mm)	1370±49[a]	384±46[b]	315±60[b]
δ_{bm} (nm)	518±16[a]	1145±106[b]	513±29[a]

a, b, c: Different letters indicate means that are different by ANOVA ($p < 0.05$)

controls and $p = 0.015$ for MCN vs. MN). As clearly illustrated in Figure 5.2, in MN, there was an approximately three-fold reduction in the filtration slit frequency (FSF) relative to controls, accompanied by a doubling of the basement membrane thickness (δ_{bm}). The reduction in FSF measured in MCN was very similar to that seen in MN, but in MCN the value of δ_{bm} remained normal.

The "experimental" estimates (k_{exp}, equation (5.5)) and the predicted values (k_{model}) of hydraulic permeability are compared in Table 5.4 and in Figure 5.3. At either assumed pressure, $\Delta P = 35$ or 40 mm Hg, the mean values of k_{exp} and k_{model} were very similar for MN and MCN, and much smaller in the nephrotic groups than in healthy controls. There was good agreement between k_{exp} and k_{model} for the two nephrotic groups. The differences between k_{exp} and k_{model} were statistically significant only for healthy controls, and then only when k_{exp} was evaluated at the lower assumed pressure, $\Delta P = 35$ mm Hg.

Individual values of k_{exp} (evaluated at $\Delta P = 40$ mm Hg, $k_{exp}^{(40)}$) and k_{model} for MCN and MN are shown in Figure 5.4. There was a significant positive correlation between

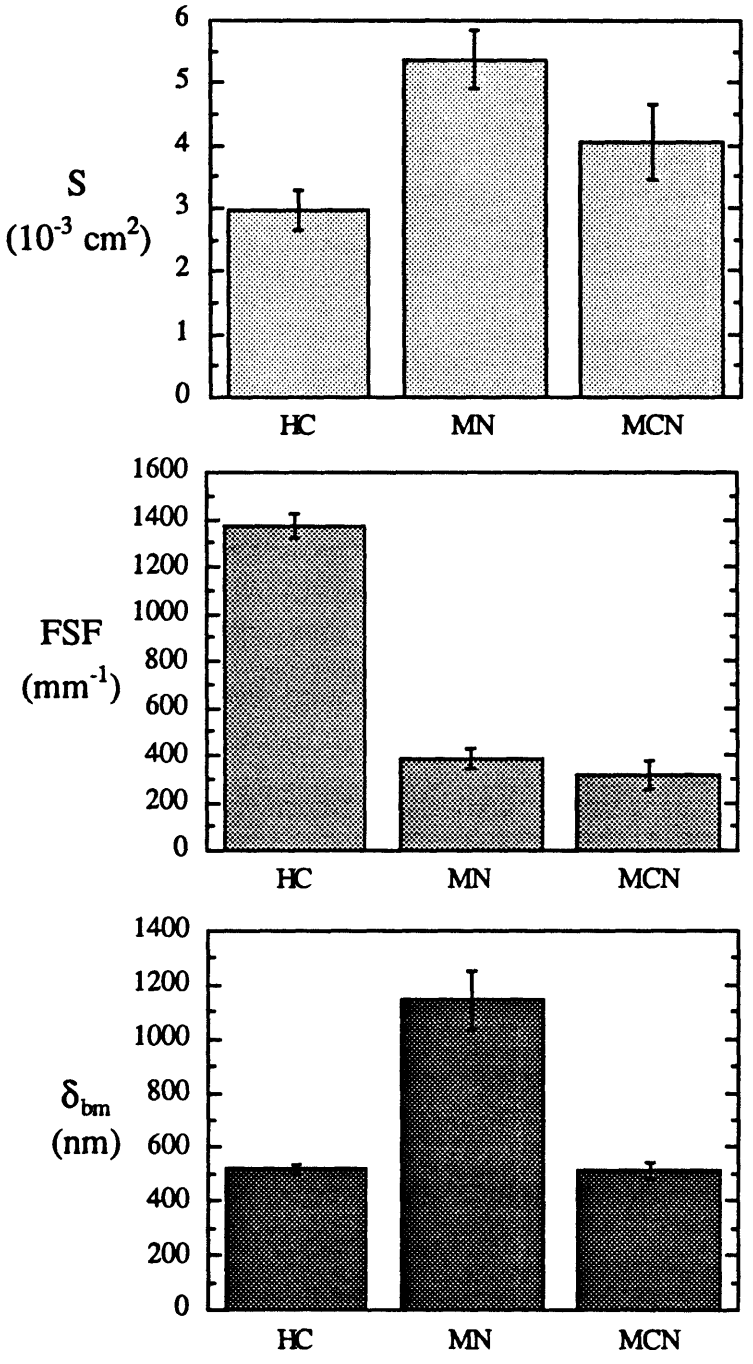

Figure 5.2 - Mean values of filtering surface area (*S*), filtration slit frequency (*FSF*), basement membrane thickness (δ_{bm}) in healthy controls (HC) and in membranous (MN) and minimal change (MCN) nephropathies. The error bars represent ± 1 standard error.

Table 5.4 - Experimental and predicted values of hydraulic permeabilities (units = 10^{-9} m/s/Pa)

	Group		
	HC	MN	MCN
$k_{exp}^{(35)}$	4.54±0.52[a,c]	0.748±0.139[b]	0. 794±0.121[b]
$k_{exp}^{(40)}$	2.31±0.27[*]	0.561±0.100[b]	0.620±0.097[b]
k_{model}	2.58±0.08[*]	0.733±0.081[b]	0.693±0.140[b]

a, b : For comparisons between groups, different letters indicate means that are different by ANOVA ($p < 0.05$)
c : $p < 0.05$ for comparisons of k_{exp} with k_{model} within a given group.

k_{exp} and k_{model} in both groups. The correlation coefficients (r) between k_{model} and $k_{exp}^{(35)}$ and between k_{model} and $k_{exp}^{(40)}$ were, respectively, 0.45 and 0.42 for MN; 0.72 and 0.65 for MCN; and 0.49 and 0.46 for the combined data of MN and MCN. Meaningful correlation coefficients for healthy controls could not be calculated because the functional and morphometric data were obtained in separate groups. Much of the scatter of the points shown in Figure 5.4 is likely due to the assumptions regarding ΔP and N, which significantly affect k_{exp}. Specifically, differences in ΔP between individuals within a given group were not taken into account and N was assumed to be the same for all individuals in all groups. Also contributing to the differences between k_{model} and k_{exp} may have been the assumptions regarding the uniformity of some of the parameters used in the calculation of k_{model}. Thus, it would have been difficult to obtain better quantitative agreement between individual values of k_{exp} and k_{model}.

The fractional clearances of albumin (θ_{alb}) and IgG (θ_{IgG}) for MN and MCN are plotted as functions of k_{model} in Figure 5.5. There were significant negative correlations

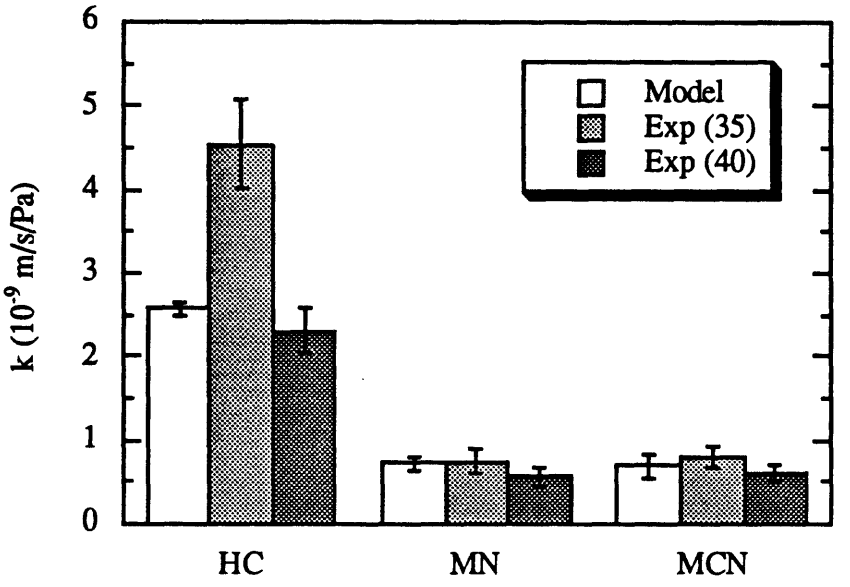

Figure 5.3 - Mean values of experimental estimates (k_{exp}) and model predictions (k_{model}) of the hydraulic permeability of the glomerular capillary wall, in healthy controls (HC) and in membranous (MN) and minimal change (MCN) nephropathies. The error bars represent ± 1 standard error.

between either fractional clearance and k_{model}. The correlation coefficients (r) between log θ_{alb} and k_{model} were r = -0.33 for MN, r = -0.59 for MCN and r = -0.39 for the combined data of MCN and MN. The corresponding relationships between log θ_{IgG} and k_{model} were even stronger (r = -0.47, r = -0.60 and r = -0.51, respectively). Thus, the individuals with the highest fractional clearances of albumin and IgG tended to have the lowest hydraulic permeabilities. The same conclusion is reached if θ_{alb} and θ_{IgG} are plotted vs. k_{exp}.

5.4 DISCUSSION

In both groups of nephrotic individuals, *GFR* was reduced by about 30% relative to an age-matched group of healthy controls. Among the determinants of *GFR*, π_A was

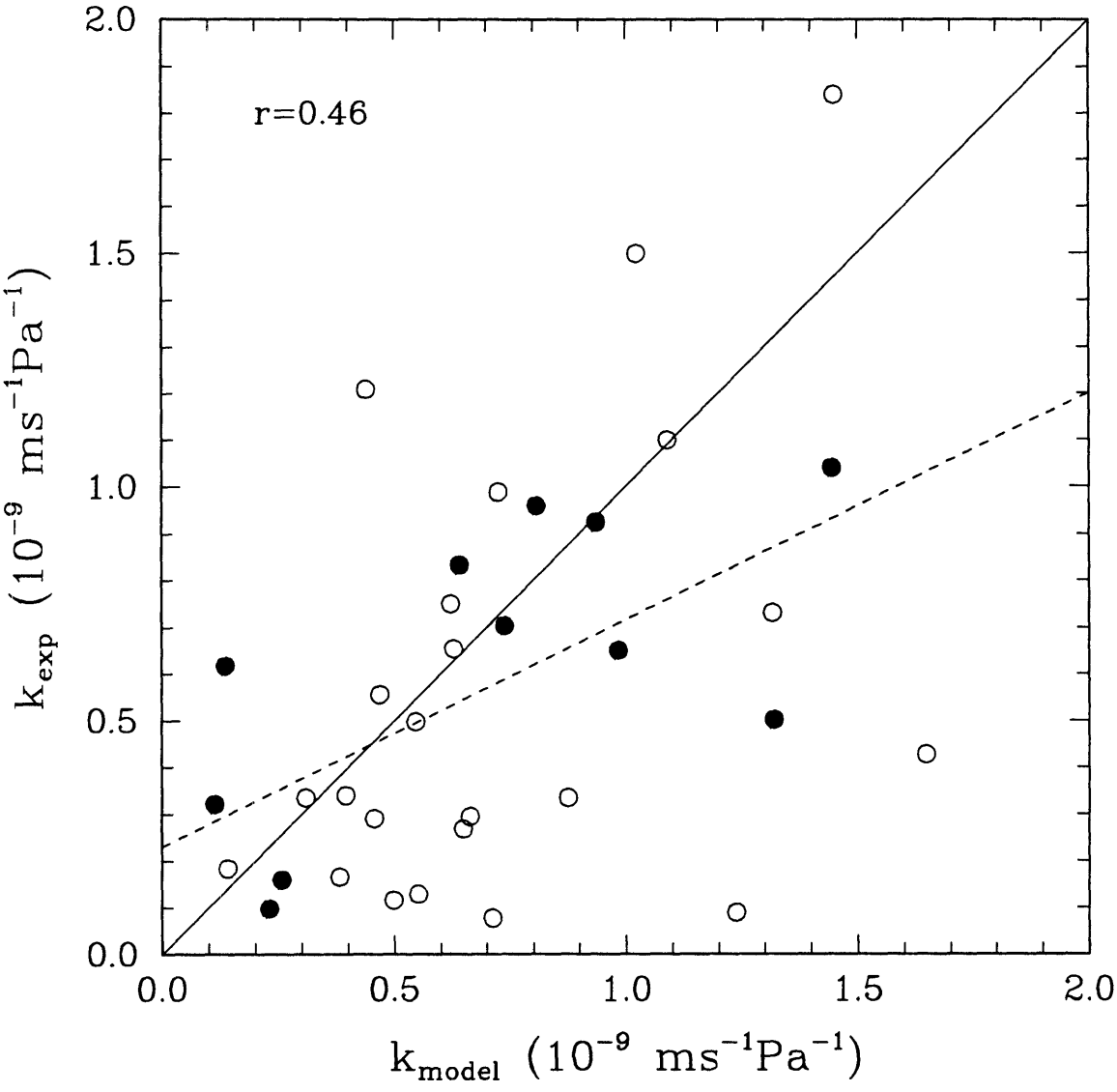

Figure 5.4 - Individual values of k_{model} and k_{exp} in MN (open symbols) and MCN (filled symbols). For each individual, k_{exp} was computed at assumed transcapillary hydraulic pressure difference of 40 mmHg. The solid line is the identity line and the dashed line is the regression line for the two groups. The r value for the two groups is also shown.

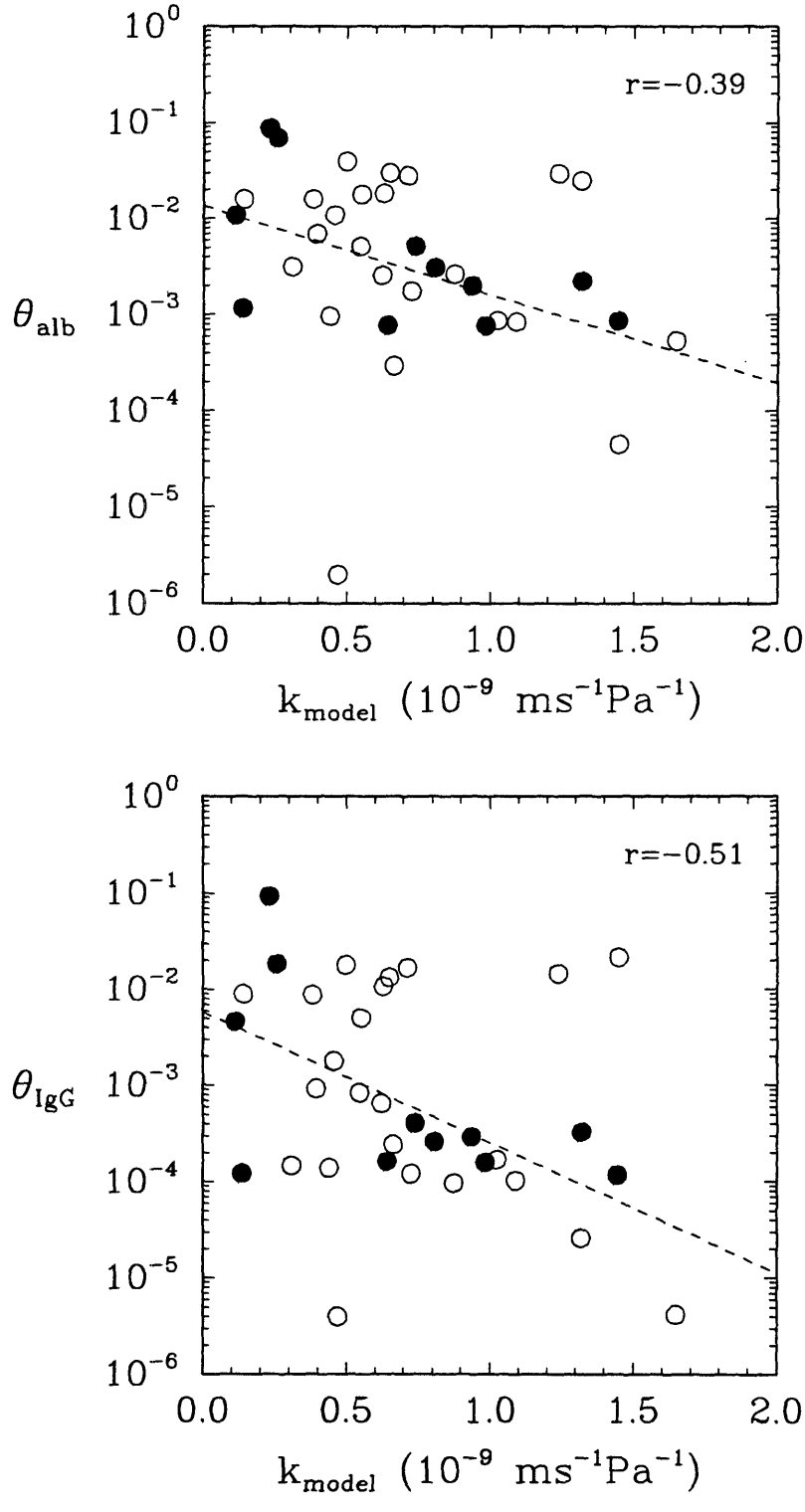

Figure 5.5 - Individual values of θ_{alb} and θ_{IgG} in MN (open symbols) and MCN (filled symbols), plotted as a function of k_{model}. In each plot, the dashed line is the regression line for the two groups. The corresponding r values are also shown.

depressed in the nephrotic patients while *RPF* was not significantly altered. These findings are in keeping with previous observations in membranous and minimal change nephropathies (Guasch et al., 1991, 1992; Guasch and Myers, 1993, Shemesh et al., 1986). Given that mean arterial pressure was higher in each nephrotic group than in controls, it is unlikely that glomerular capillary pressure and hence ΔP was lower in nephrotics than in controls. Thus, the only factor which can explain the reduced *GFR* is a decrease in the overall K_f for the two kidneys. The precise magnitude of the calculated reduction in K_f depends on what is assumed to have happened to ΔP. If ΔP remained constant at either 35 or 40 mm Hg, then K_f was reduced by roughly a factor of three to four, the greater reduction in K_f corresponding to ΔP = 35 mm Hg. If ΔP increased from 35 mm Hg to 40 mm Hg in nephrotics, then there were approximately five-fold reductions in K_f. Modest increases in ΔP in the nephrotic individuals are consistent with micropuncture measurements in rats with Heymann nephritis or with nephropathies induced by puromycin or adriamycin, which are regarded as experimental models for MN and MCN (Anderson et al., 1988; Ichikawa et al., 1982; Scholey et al., 1989; Yoshioka et al., 1987).

Changes in peripheral capillary surface area per glomerulus (S) or in the number of functioning glomeruli are incapable of explaining the three-to-five-fold reductions in K_f. The percentage of globally sclerosed glomeruli measured in nephrotic individuals was similar to that observed in controls, and this sclerosis is likely due to aging. This suggests that there was little or no reduction in the number of functioning glomeruli in the MN and MCN groups. Indeed, $\geq$ 94% of glomerular tufts appeared non-sclerosed and widely patent by light microscopy in all groups studied. There was a tendency toward increased S in both nephrotic groups, although the increase relative to controls reached statistical significance only for MN. Because the changes in the number of functioning glomeruli appeared to be quantitatively insignificant, and because S tended to remain constant or to increase, we infer that the depression of K_f must be attributable

entirely to reductions in the effective hydraulic permeability of the capillary wall (k). Using *GFR* and its determinants to calculate the hydraulic permeability, the resulting values (k_{exp}) were virtually identical in MN and MCN.

The hydrodynamic model developed in Chapter 4 provides estimates of k entirely independent of k_{exp}. The applicability of this model to human data is supported by the finding that k_{model} accurately predicts not only the trends in k_{exp} in the present study, but also the absolute values in each group of subjects.

The similarity of k_{exp} in MCN and MN, despite the two-fold difference in basement membrane thickness (δ_{bm}) is a finding which is not intuitively obvious. To explain this result we consider now the individual factors which contribute to k. First of all, the calculations using the hydrodynamic model suggest that, in healthy controls as well as in subjects with MN and MCN, the hydraulic resistance of the endothelium is negligible, the basement membrane resistance is about 60% of the total, and the epithelial resistance accounts for the remaining 40%.

To examine in more detail the factors which contribute to the basement membrane resistance, we note that a good approximation to k_{bm} under most conditions is given by equation (4.29) [5], that is

$$k_{bm} \cong \frac{K_D}{\mu W_{bm}} \left\{ \frac{\delta_{bm}}{W_{bm}} + \frac{1}{\pi N_f} \left[\frac{3}{2} - \ln(2\pi\varepsilon_f) \right] + \frac{1}{\pi} \left[\frac{3}{2} - \ln(2\pi\varepsilon_s) \right] \right\}^{-1} . \qquad (5.7)$$

The three main contributions to k_{bm} are the terms separated by "+" signs in equation (5.7). The first term represents the resistance of "bare" basement membrane, the second term gives the increased basement membrane resistance due to coverage by endothelial cells,

[5] Except for one subject with MN and four with MCN, equation (4.29) yielded values of k_{bm} within 2% of those obtained from the more rigorous formula (equation (4.23)). For those exceptional cases, in which $\delta_{bm}/W_{bm} \leq 0.08$, the discrepancies were 19 to 37%.

and the third term is the increased resistance due to coverage by podocytes. In healthy controls, the first term was found to be the most important, accounting for ~60% of the basement membrane resistance. By contrast, in nephrotic subjects the *FSF* was reduced enough that the third term became dominant (~60% in MN and ~80% in MCN). Accordingly, k_{bm} in MN and MCN was determined primarily by *FSF* and not by δ_{bm}. This result is clarified by an examination of the streamlines shown in Figure 5.6. Panel A shows streamlines in a structural unit representative of healthy controls and Panel B shows streamlines in a structural unit with a much smaller slit frequency, similar to that of the nephrotic subjects. For this illustration we assumed that δ_{bm} is the same in both cases, but that *FSF* is four times smaller in Panel B than in Panel A. Clearly, the path length for the filtrate tends to be much larger in Panel B than in Panel A, even with identical δ_{bm}. Thus, in the nephrotic groups, where *FSF* is considerably reduced relative to that in controls, the average path length and the resulting pressure drop are determined more by the slit spacing than by δ_{bm}. Assuming no major differences in filtration slit width or slit diaphragm structure, the hydraulic permeability of the epithelial layer (k_{ep}) is governed mainly by *FSF*. With both k_{bm} and k_{ep} in the nephrotic groups being determined primarily by *FSF*, so is the overall value of k. This provides an attractive explanation for the aforementioned fact that reductions in *GFR* and K_f in nephrotic subjects tend to be correlated much more strongly with reductions in *FSF* than with changes in δ_{bm} (Bohman et al., 1984; Ellis et al., 1987; Guasch and Myers, 1993).

For lack of specific data, we assumed that the total number of nephrons (N) was the same in all individuals of the present study, although differences in N are likely to exist. For example, it has been observed that N decreases with age (Dunnill and Halley, 1972; Nyengaard and Bendtsen, 1992). To minimize the effects of age differences on our results, we excluded individuals with age $\geq$ 60 years. If we had excluded all subjects with ages $\geq$ 50 years, the results would not have been significantly changed. Recently, it has been observed that N in diabetic patients with advanced nephropathy is smaller than

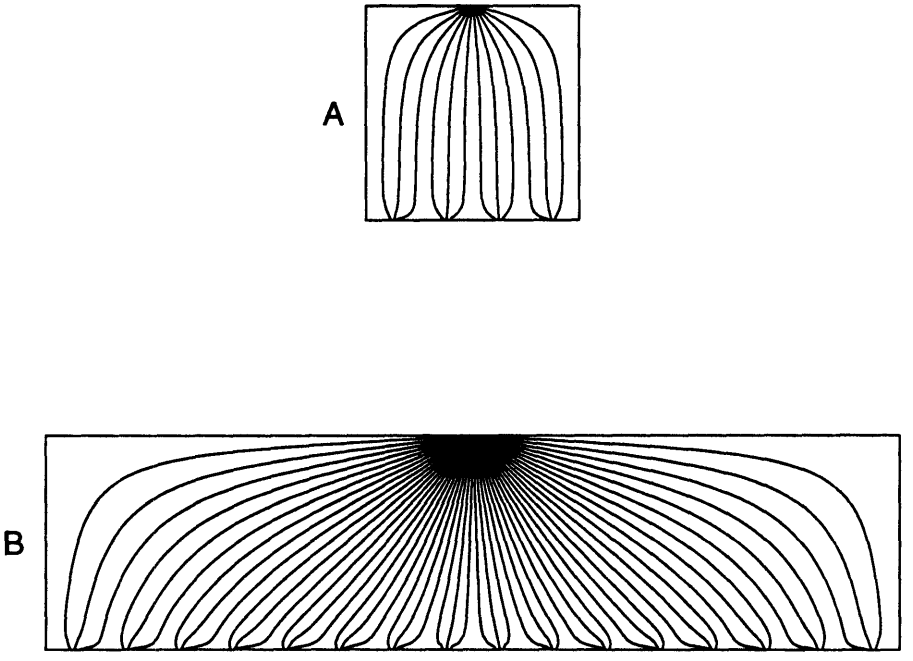

Figure 5.6 - Streamlines in the basement membrane illustrating the effect of changes in filtration slit frequency. Panel A is an example representative of healthy controls. In Panel B the filtration slit frequency is four times smaller than that in Panel A. The basement membrane thickness, the frequency and fractional area of the fenestrae, and the width of the slit opening are the same in both panels.

in healthy controls (Bendtsen and Nyengaard, 1992). If such differences exist in MN and MCN, it is possible that the correction for glomerular sclerosis used in equation (5.5) is not enough to account for the differences in N between groups.

The most widely used method to determine N, as well as V_G, is that proposed by Weibel (Weibel and Gomez, 1962, Weibel, 1979 (p.44)). Using this method, estimates of N in healthy humans have been ~$2x10^6$ (Dunnill and Halley, 1972). Recently, however, this method was criticized as being biased (Bendtsen and Nyendgaard, 1989; Nyengaard and Bendtsen, 1992) and a new method to determine N and glomerular volume proposed. Using this new method, a value of $N = 1.2x10^6$ was obtained (Nyengaard and Bendtsen, 1992). Since the theoretical basis of the relationships involved in the calculations of V_G (which is related to the glomerular filtering surface area, S, by equation (5.3)) and N are the same, and because in this study we used the method of Weibel to determine glomerular volume, we chose to use $N = 2x10^6$ in equation (5.5). In fact, from equations (5.1), (5.3) and equation 2.85 of Weibel (1979), we see that the product NS (which appears in equation (5.5)) does not involve the shape coefficient (β) and distribution coefficient (d), which are sources of bias.

The reductions in k in MN and MCN appear at first to be inconsistent with the finding of considerable proteinuria, as reflected by the values of fractional albumin clearance and fractional IgG clearance. That is, one might expect that any structural changes which retard filtration of water would at least equally retard the transmural passage of proteins. One reasonable hypothesis to explain these findings is that the broadening of the foot processes (decrease of FSF) causes changes in the structure or even entirely disrupts some of the slit diaphragms. Such changes could augment considerably the filtration of albumin and IgG, without significantly affecting the value of k. For example, if 5% of the slit diaphragms are assumed to be disrupted in MN and MCN, and if this causes the resistance of the epithelium to water flow to be negligible in 5% of the capillary wall, the mean values of k_{model} would be $7.57x10^{-10}$ and $7.22x10^{-10}$

m/s/Pa in MN and MCN, respectively. These values are < 4% higher than those given in Table 5.4, not a very noticeable difference. However, given the observation that the cellular component of the capillary wall accounts for much of the overall size-selectivity (Daniels et al., 1993), it is entirely possible that the rupture of this small fraction of the slit diaphragms might allow the filtration of large quantities of albumin and IgG. Another possible explanation is that in MN and MCN there might have been changes in the fixed charge content of the capillary wall which, while not affecting k, could have greatly reduced the resistance to filtration of albumin. Charge-selectivity of the glomerular barrier in healthy humans and its impairment in nephrotic subjects with either MN or MCN has recently been demonstrated (Guasch et al., 1993).

Another potential application of the hydrodynamic model would be to use the values of k_{model} to calculate K_f and, together with the hemodynamic data (GFR, RPF and π_A), to estimate ΔP for each individual. Because of the assumptions involved in the model, as well as in the value of nephron number used to calculate K_f, any such estimates of ΔP at present are highly tentative. Nonetheless, with the present data and assumptions, the mean values of the predicted ΔP were ~39 mm Hg in healthy controls, ~36 mm Hg in MN and ~42 mm Hg in MCN (neglecting the value for one patient with MCN, which was larger than 100 mm Hg). The value of ΔP for healthy controls is quite similar to that calculated for healthy humans by an indirect method (ΔP = 36 mm Hg), one based on curve fitting of the measured sieving coefficients of neutral dextran of discrete and graded size (Myers et al., 1988). Moreover, mean values for ΔP predicted by k_{model} for all three groups are remarkably similar to corresponding values measured directly by micropuncture in normal rats, and in rats with induced glomerular diseases which are analogs of membranous and MCN in humans (Anderson et al., 1988; Ichikawa et al., 1982; Yoshioka et al., 1987; Scholey el al., 1989).

To summarize, our analysis suggests that a reduction of glomerular hydraulic permeability is a major determinant of the impaired ultrafiltration capacity in MN and

MCN. Using the hydrodynamic model developed in Chapter 4 we concluded that, in both disorders, the hydraulic permeability is determined mainly by the slit spacing rather than by the basement membrane thickness. These findings point to an injury to epithelial foot processes, with an ensuing reduction in the frequency of intervening filtration slits, as the predominant cause of hypofiltration during the acute, nephrotic stage of each of these glomerular injuries.

CHAPTER 6

HINDERED TRANSPORT OF MACROMOLECULES THROUGH A SINGLE ROW OF CYLINDERS: APPLICATION TO GLOMERULAR FILTRATION

6.1 INTRODUCTION

An important issue in renal pathophysiology is the role of the various structures in determining the permeability properties of the glomerular capillary wall. Using hydrodynamic models for the three layers in combination with morphometric measurements, we have made some progress in understanding the factors which affect the hydraulic permeability of the glomerular capillary wall in health and disease. The objective of the analysis presented in this chapter was to perform a similar assessment for transport of macromolecules. Because of the large dimensions of the endothelial fenestrae (~300 Å radius), and because studies of isolated rat glomerular basement membrane suggest that basement membrane is much less selective to macromolecules than is the intact capillary wall (Daniels et al., 1993), we focused our attention on the filtration slits and, in particular, the slit diaphragms. The zipper and ladder configurations analyzed in Chapter 3 share the feature that permeating macromolecules must pass through a single layer of fibers in which the smallest dimension of the opening is the distance between adjacent fibers, and in which that dimension is comparable to the diameter of a permeating molecule. There were no existing models for hindered transport of macromolecules through thin structures of this type, so that a major part of our effort was devoted to developing a hydrodynamic model which would be suitable for predicting both diffusional and convective hindrances in this situation. For simplicity, we chose to model the slit diaphragm as a row of infinitely long cylinders (i.e., the ladder

configuration without the wall effects caused by the foot processes). Even with this simplified geometry, a number of hydrodynamic approximations were required, as will be seen.

6.2 MATHEMATICAL MODEL

6.2.1 SOLUTE FLUX IN SLIT

The hindered transport model for the slit diaphragm was based on the arrangement shown in Figure 6.1, in which rigid, non-interacting spherical particles of radius r_s move with velocity **U** through a row of infinitely long cylinders of radius R. The distance between the centers of adjacent cylinders is $2L$. Both R and r_s were assumed to be much larger than the dimensions of the solvent molecules, so that the solvent was treated as a continuum. The local velocity of the solvent is **V**.

The constitutive equation for the solute flux was derived by performing a force balance on one sphere, similar to the approach used by Einstein (1956) to treat diffusion in bulk solution and to that employed in previous hindered transport models for various geometries (Deen, 1987). Neglecting random fluctuations in **U**, there is no net force on the sphere; the effective body force, attributed to a gradient in chemical potential, is balanced by a hydrodynamic force. That is,

$$-kT\nabla \ln C - 6\pi\mu r_s(\mathbf{f}\cdot\mathbf{U} - \mathbf{g}\cdot\mathbf{V}) = \mathbf{0}. \qquad (6.1)$$

The first term of equation (6.1) is the thermodynamic or body force, where k is Boltzmann's constant, T is the absolute temperature and C is the concentration of solute. Implicit in the use of point-wise concentrations is an averaging over many identical particles, so that the concentration at a given point is proportional to the probability of

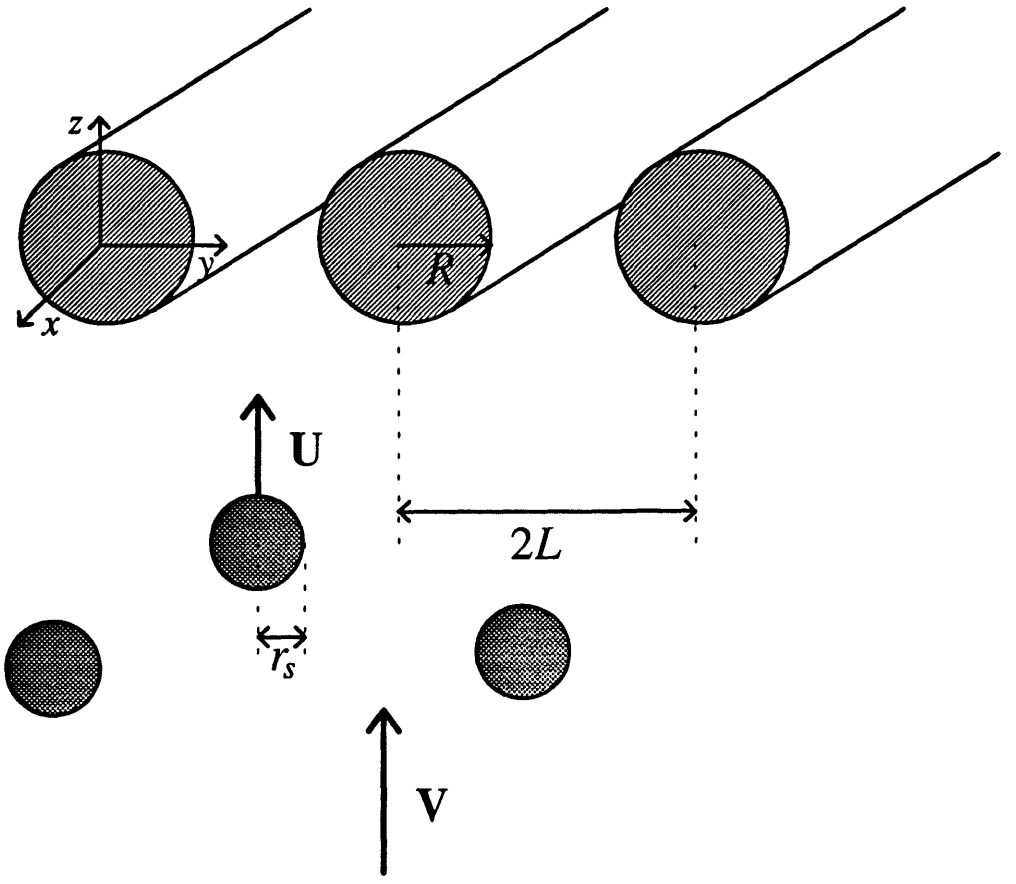

Figure 6.1 - Schematic for transport of spherical macromolecules through a row of infinitely long cylinders.

finding a particle center at that point. The second term of equation (6.1) is the hydrodynamic force, which is expressed as the sum of a force due to translation of the sphere with velocity **U** in a stagnant fluid, and a force due to flow at velocity **V** past a stationary sphere. The tensors **f** and **g** contain force coefficients for translation of the sphere and flow past the sphere, respectively. If there were no cylinders, both **f** and **g** would equal the identity tensor. In the system considered here, **f** and **g** are second-order tensors with position-dependent components determined as described below. In calculating the hydrodynamic force we neglected any coupling between translational and

rotational motions; that is, we have neglected the force acting on the particle due to its rotation. As may be inferred from values of force coefficients given in Yan et al. (1986) this force is expected to be small compared to other contributions to the hydrodynamic force.

The solute flux, **N**, relative to fixed coordinates is defined by

$$\mathbf{N} \equiv \mathbf{U}C. \tag{6.2}$$

Solving equation (6.1) for **U** and substituting the result into equation (6.2), the solute flux is

$$\mathbf{N} = -D_\infty \mathbf{d} \cdot \nabla C + \mathbf{h} \cdot \mathbf{V}C \tag{6.3}$$

where D_∞ is the diffusivity in bulk solution, given by the Stokes-Einstein equation,

$$D_\infty = \frac{kT}{6\pi\mu r_s}. \tag{6.4}$$

The new coefficients are tensors related to **f** and **g** by

$$\mathbf{d} = \mathbf{f}^{-1} \tag{6.5}$$

$$\mathbf{h} = \mathbf{f}^{-1} \cdot \mathbf{g}. \tag{6.6}$$

If there are no cylinders present, then **d** and **h** both equal the identity tensor, and equation (6.3) reduces to the usual form of Fick's law for a dilute solution.

6.2.2 Concentration Field in Slit

To determine the steady-state solute concentration field, equation (6.3) was used together with the solute conservation equation,

$$\nabla \cdot \mathbf{N} = 0. \tag{6.7}$$

The result is

$$\nabla^* \cdot \left(-\mathbf{d} \cdot \nabla^* C + Pe\, \mathbf{h} \cdot \mathbf{V}^* C\right) = 0 \tag{6.8}$$

where $\nabla^* \equiv R\nabla$, $\mathbf{V}^* \equiv \mathbf{V}/V$, V is the undisturbed fluid velocity far from the cylinders and Pe is a Peclet number based on the cylinder radius,

$$Pe \equiv \frac{VR}{D_\infty}. \tag{6.9}$$

In the coordinate system of Figure 6.1, the boundary conditions used with equation (6.8) were

$$N_z = N_0 \text{ at } z = -\delta \tag{6.10a}$$

$$C = C_B = N_0/V \text{ at } z \to \infty \tag{6.10b}$$

$$N_y = 0 \text{ at } y = 0 \text{ and } y = L \tag{6.10c}$$

$$N_r = 0 \text{ at } r \equiv \left(y^2 + z^2\right)^{1/2} = R + r_S. \tag{6.10d}$$

As shown in equation (6.10a), upstream from the cylinders we specified a constant solute flux (N_0) at a distance δ from the center of the cylinders. Far downstream from the cylinders ($z \to \infty$) the concentration was assumed to reach a constant (C_B) (equation

(6.10b)). Because $\nabla C = \mathbf{0}$ at $z = \infty$, $N_z = VC_B$ and, from conservation of mass, $N_0 = VC_B$. Equation (6.10c) expresses symmetry at $y = 0$ and at $y = L$. Finally, because the centers of the spherical particles cannot sample positions closer than r_S from the cylinder surface, the solute flux normal to the cylinder must vanish at a distance r_S from the cylinder surface (equation (6.10d)).

6.2.3 VELOCITY FIELD IN SLIT

The fluid velocity field (**V**) was obtained by solving the Stokes and continuity equations,

$$\nabla P = \mu \nabla^2 \mathbf{V} \tag{6.11}$$

$$\nabla \cdot \mathbf{V} = 0 \tag{6.12}$$

where P is pressure and μ is viscosity. The boundary conditions were constant velocity at $z = -\delta$ and $z \rightarrow \infty$, symmetry at $y = 0$ and at $y = L$, and zero velocity at the cylinder surface. That is,

$$V_z = V\,;\; V_y = 0 \;\text{ at }\; z = -\delta \;\text{ and }\; z \rightarrow \infty \tag{6.13a}$$

$$V_y = 0 \;\text{ at }\; y = 0 \;\text{ and }\; y = L \tag{6.13b}$$

$$\mathbf{V} = \mathbf{0} \;\text{ at }\; r \equiv \left(y^2 + z^2\right)^{1/2} = R. \tag{6.13c}$$

6.2.4 HYDRODYNAMIC APPROXIMATIONS FOR SLIT

To complete the information needed to solve equation (6.8) we require values for the force coefficient tensors **f** and **g**. Because there are no results available for the system

under consideration, we followed an approximate approach similar to those of Keh (1986) and Yan et al. (1986) in their models of transport through short, cylindrical pores. Accordingly, we divided the fluid domain into the hydrodynamic regions shown in Figure 6.2, and used available results to estimate **f** and **g** in each region. In this Section, we describe briefly the approach followed to calculate **f** and **g** in each of the hydrodynamic regions. A more detailed description, with all the equations used, can be found in Appendix E.

In Regions I, we used results for the translation of a sphere in the presence of a planar wall to estimate **f**, and results for flow past a stationary sphere in the presence of a planar wall to estimate **g**. To do this, the "wall" was assumed to be a surface tangent to the surface of the cylinder, the point of tangency being defined by a line connecting the center of the cylinder with the center of the sphere. When the gap between the cylinder and the sphere was small we used the lubrication results of Goldman et al. (1967a, b) and Cox and Brenner (1967). For larger gaps we used Faxen's results (Happel and Brenner, pp. 327 (1983)) and the results of Wakiya (Happel and Brenner, pp. 330 (1983)) and Goldman et al. (1967b), obtained by the method of reflections. The transition between the expressions for small and large gaps was made at the point where both yielded the same value of the force coefficient. This procedure allowed us to estimate force coefficients for translation parallel ($f_{\parallel}$) and perpendicular ($f_{\perp}$) to the fictitious wall, as well as force coefficients for flow parallel to the wall ($g_{\parallel}$). Because there appears to be no solution for flow past a stationary sphere towards an infinite wall, we estimated $g_{\perp}$ from the numerical results of Dagan et al. (1982) for the case of a sphere and a (finite) disk, as follows. We first calculated $h_{\perp}$ (= $g_{\perp}/f_{\perp}$) for their system using the results of their Tables 2 and 3 and equation (5.2); $h_{\perp}$ is a function of b, which is the sphere radius divided by the distance from the center of the sphere to the surface of the disk. Considering only values of $h_{\perp}$ for cases where the radius of the sphere is not larger than the radius of the disk, the results were well approximated by $h_{\perp} = 1 - b^{3.8}$. The components of **f** and **g** in (y,z)

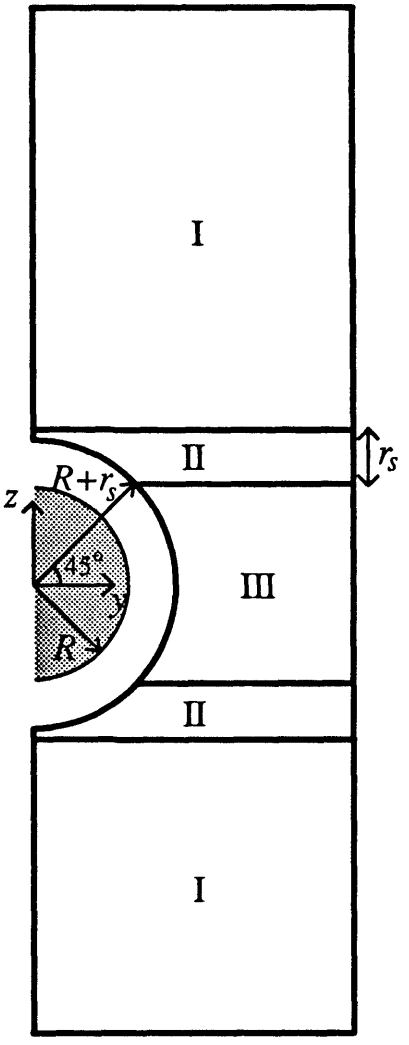

Figure 6.2 - Division of the computational domain into hydrodynamic regions for specification of hindrance coefficients for a row of cylinders.

coordinates were then calculated from $f_{\parallel}$, $f_{\perp}$, $g_{\parallel}$ and $g_{\perp}$ by taking into account the orientation of the wall relative to the (y,z) axis. Finally, **d** and **h** were calculated by equations (6.5) and (6.6), respectively.

In Region III, which is between cylinders, we used the results of Ganatos et al. (1980a, c) for a sphere between walls to estimate $f_{\perp}$, $f_{\parallel}$ and $g_{\parallel}$. The location of the wall closest to the sphere was determined as in Regions I, and the other wall was assumed to

be at a distance of $2(L/\cos\beta - R)$ from the first wall. Because the two-wall results are available only for $b \leq 0.909$, when $b > 0.909$ we followed the approach of Ganatos et al. (1980b) in modifying results for one wall. This was done for any given wall spacing by adding a constant to the original one-wall lubrication results (as used in Regions I). This constant was calculated by matching the two-wall results with the modified one-wall lubrication results, at $b = 0.909$. The coefficient $h_{\perp}$ was estimated as in Regions I and **f**, **g**, **d** and **h** were then calculated as before.

Regions II are transition regions, of width r_s is the z-direction, where the components of **d** and **h** were linearly interpolated between the corresponding values at the boundaries of Regions I and III.

Figure 6.3 shows the diagonal elements of **d** and **h**, namely d_{yy}, d_{zz}, h_{yy} and h_{zz}, as a function of z/L, for $R/L = 0.5$, $r_s/(L - R) = 0.7$, and various values of y/L. All of these coefficients are unity far from the cylinder and all vanish at the point where the sphere touches the cylinder (i.e., at $r = R + r_s$). It can be seen that, despite the piece-wise nature of the approximations, the curves are relatively smooth. The degree of smoothness varied somewhat depending on the values of R/L and $r_s/(L - R)$, but in all cases analyzed the curves were monotonic. As shown in Figure 6.4, the curves for the off-diagonal coefficients were not monotonic nor as smooth as those shown in Figure 6.3, but the magnitude of the coefficients was always much smaller than that of the diagonal elements. When the off-diagonal elements were all set equal to zero, the computed sieving coefficients (see equation (6.16) below) changed by only 1% (root-mean-square difference for 900 values).

6.2.5 Model for Basement Membrane

We used an effective medium approach to model macromolecular transport across the basement membrane, as was done previously in modeling water flow across this part

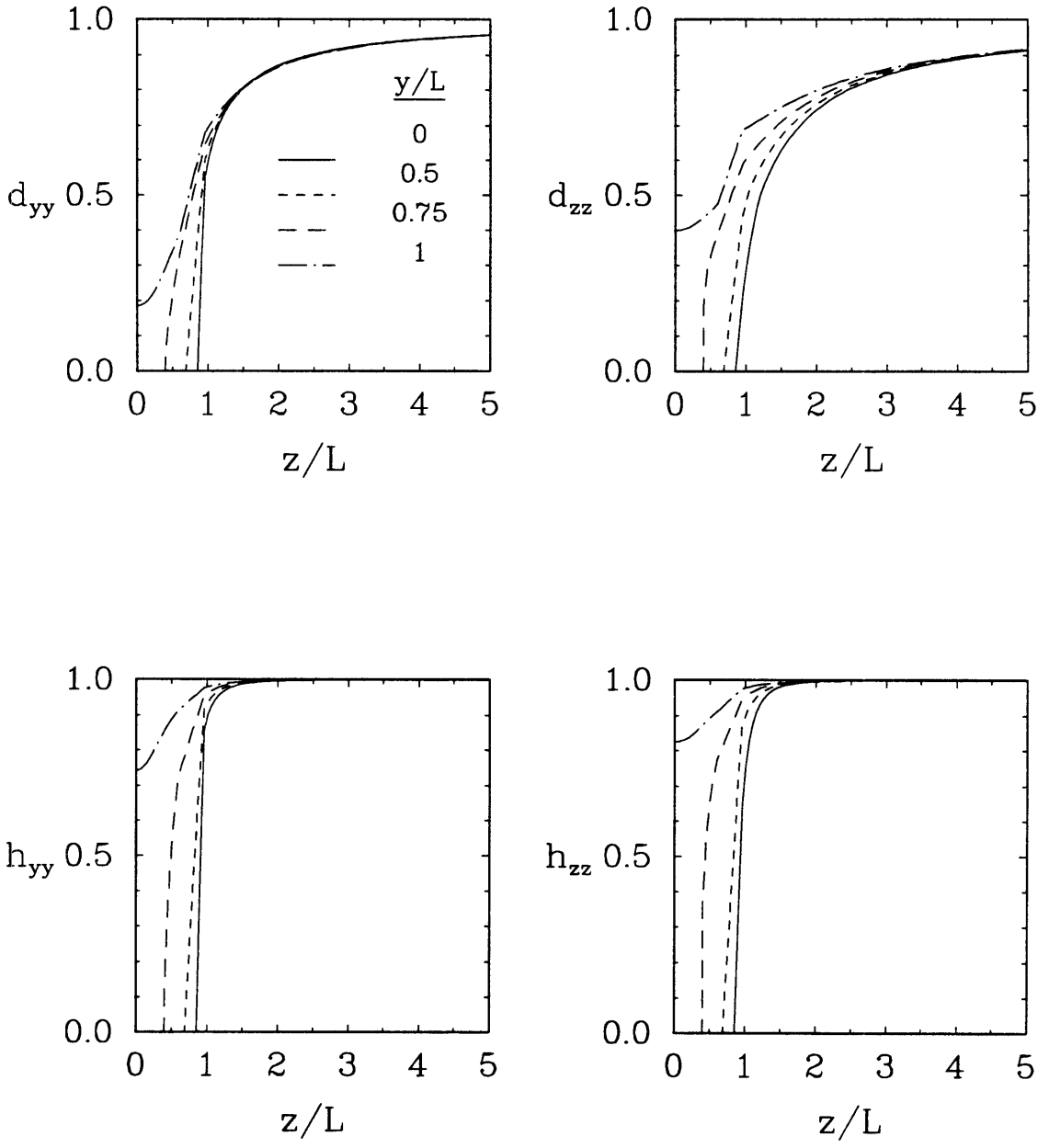

Figure 6.3 - Diagonal elements of the hindrance coefficient tensors **d** and **h** as a function of z/L, for $R/L = 0.5$, $r_s/(L - R) = 0.7$, and four values of y/L.

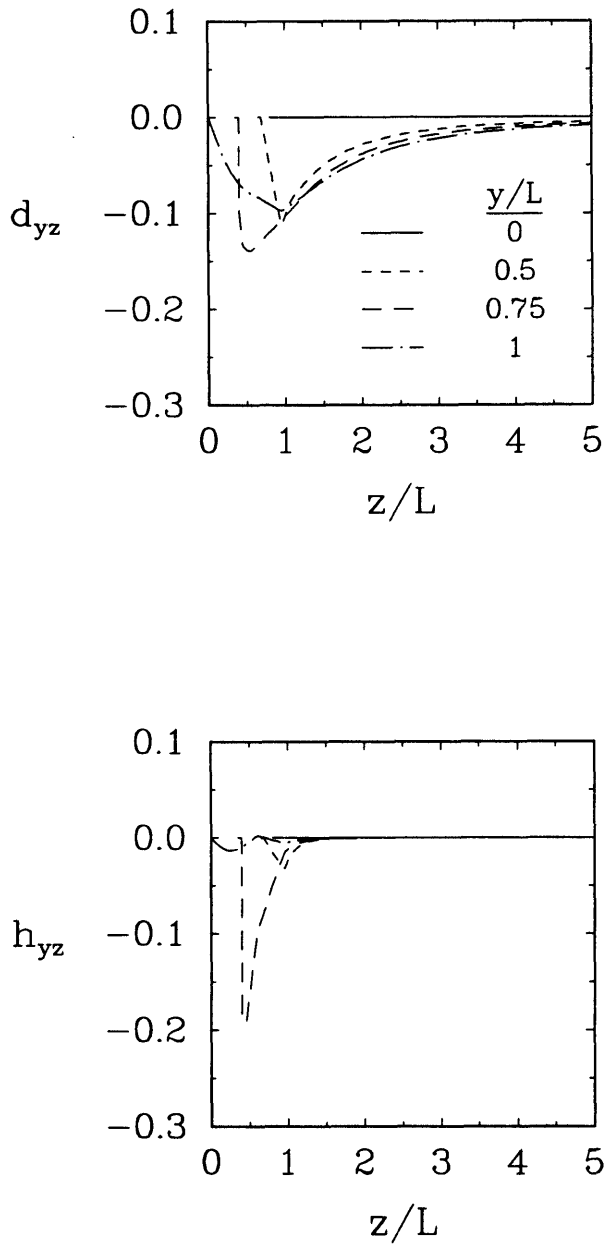

Figure 6.4 - Off-diagonal elements of the hindrance coefficient tensors **d** and **h** as a function of z/L, for $R/L = 0.5$, $r_s/(L - R) = 0.7$, and four values of y/L.

of the glomerular capillary wall (see Chapter 4). With the basement membrane assumed to be isotropic, the conservation equation governing the steady-state concentration field in the basement membrane was

$$\nabla \cdot \left(-d_{bm} D_{\infty} \nabla C^* + h_{bm} \mathbf{V}^* C^* \right) = 0 \tag{6.14}$$

where $\mathbf{V}^*$ and C^* are the filtrate velocity and solute concentration, respectively, both averaged over a length scale which is large compared to that of the microstructure of the fibers of the basement membrane. The hindrance coefficients for diffusion and convection in the basement membrane are d_{bm} and h_{bm}, respectively. Equation (6.14) was solved in a two-dimensional structural unit (see Figure 4.3), with the velocity field $\mathbf{V}^*$ calculated using the analytical solution of Darcy's law given in Section 4.3.3. Because the structural unit was symmetric relative to $x = 0$, only half of the domain was used in the calculations. The boundary conditions for equation (6.14) were constant solute flux at the endothelial openings, constant concentration at the slit opening, zero flux normal to the surfaces covered by endothelium and epithelium, and zero flux normal to the planes of symmetry. That is,

$$N_z^* = \frac{\varepsilon_s N_0}{\varepsilon_f} \text{ at the endothelial openings} \tag{6.15a}$$

$$C^* = C_0^* = \Phi_{bm} C_0 \text{ at the slit opening} \tag{6.15b}$$

$$N_z^* = 0 \text{ at the areas covered by cells} \tag{6.15c}$$

$$N_x^* = 0 \text{ at } x = 0 \text{ and } x = W_{bm}/2 \tag{6.15d}$$

where N_z^* is the z-component of the solute flux in the basement membrane, N_0 is the solute flux in the epithelial slit (see equation (6.10)), ε_f is the fractional area of the

endothelial openings, C_0 is the average concentration in the fluid adjacent to the epithelial slit opening, and Φ_{bm} is the partition coefficient between the basement membrane and the adjacent fluid.

6.2.6 SOLUTION METHODS

Equation (6.8) and equations (6.11) and (6.12), with their respective boundary conditions (equations (6.10) and (6.13)), were solved using Galerkin finite element methods. The Stokes and continuity equations were solved first using the software package FIDAP (Fluid Dynamics International, Evanston, IL) on a Cray X-MP EA/464 supercomputer, following the approach detailed in Section 3.3. The nodal values of **V** computed with FIDAP were then used in equation (6.8). Because the nodes of the domain where equation (6.8) was solved were not all coincident with the nodes used in FIDAP, bilinear interpolation was used to obtain some of the nodal values of **V** needed for equation (6.8). To solve equation (6.8), we employed quadrilateral elements with bilinear basis functions for C. In the finite element meshes used to solve either equation (6.8) or equations (6.11) and (6.12), the number of elements in the y-direction was constant for all z, and the size of the elements in the z-direction was kept approximately constant. The meshes had ~2200 to ~5900 nodes, and the CPU time for solution of equation (6.8) (including interpolation of **V**) on a DECstation 5000/133 was between ~40 and ~130 seconds.

The downstream boundary condition for C was applied at a finite value of z, $z = \delta_1$, chosen large enough so that further increases in δ_1 would not affect the calculated sieving coefficient (see equation (6.16) below). It was verified that the value of δ_1 used previously to compute velocity profiles, $\delta_1 = 5L$ (see Section 3.4.1), was sufficient for all cases.

Equations (6.14) and (6.15) for the basement membrane were solved using the numerical method used to solve equation (6.8). We used a finite element mesh with 1600 elements and the CPU time on a DECstation 5000/133 was ~ 20s.

6.3 RESULTS AND DISCUSSION

6.3.1 PARAMETER VALUES

To our knowledge, there are no reported values for δ, the distance from the basement membrane to the center of the slit diaphragm. We examined electron micrographs from various sources (e.g., Abrahamson, 1987; Furukawa et al., 1991; Kanwar and Venkatachalam, 1992; Kondo, 1990; Rodewald and Karnovsky, 1974) and estimated that δ ranges from ~30 to ~70 nm. To establish an approximate range for R, we used reported sizes of the cylindrical filaments of the zipper configuration (Kondo, 1990; Kubosawa and Kondo, 1990; Rodewald and Karnovsky, 1974) and, in addition, made rough estimates of R based on the electron micrographs of Hora et al. (1990). This yielded a range for R of ~2 to ~10 nm. To obtain the physiological range for Pe we used typical net ultrafiltration pressures at the afferent and efferent ends of the glomerular capillaries (~20 and ~1 mm Hg, respectively (Maddox et al., 1992)), the experimental range for the hydraulic permeability of the glomerular capillary wall (k ~ 3 - 5x10^{-9} m/s/Pa (see Section 1.1)), an approximate range for the fraction of the glomerular capillary wall occupied by the filtration slits (ε_s, ~ 0.05 - 0.2 (Table 4.1)), and values of r_s ranging from 10 to 70 Å. This yielded values of Pe ranging from ~10^{-5} to ~0.1.

Because the net ultrafiltration pressure changes considerably from the afferent to the efferent end of a glomerular capillary (see above), so does the filtrate velocity. In some calculations we used average values of filtrate velocity and net ultrafiltration pressure, which were estimated as follows. Based on typical values for the total filtration

rate per glomerulus (40 nl/min; Maddox et al., 1992) and total glomerular filtration area (0.002 cm^2; Maddox et al., 1992), and using $\varepsilon_s = 0.11$, we estimated an average velocity in the epithelial slits of ~3.0×10^{-5} m/s. Using the previously calculated value for the hydraulic permeability of the epithelial slits, $k_s = 7.9 \times 10^{-8}$ m/s/Pa (see Sections 3.4.3 or 4.3.4), we estimated a pressure drop in the epithelial slits, ΔP_s, of ~3.8×10^2 Pa.

The structural parameters for the basement membrane calculations were as in the baseline calculations of Chapter 4, that is $W_{bm} = 360$ nm; $\delta_{bm} = 200$ nm; $N_f = 3$, where N_f is the number of fenestrae per structural unit; $\varepsilon_f = 0.20$; and $\varepsilon_s = 0.11$. The additional parameters needed to solve equations (6.14) and (6.15) were the hindrance coefficients for diffusion (d_{bm}) and convection (h_{bm}), and the partition coefficient (Φ_{bm}). We calculated d_{bm} and h_{bm} using approximations suggested by Phillips et al. (1989), evaluating d_{bm} from the drag on a sphere in a Brinkman medium and using $h_{bm} = 1/(1-\phi)$, where ϕ is the solid volume fraction of the basement membrane. We calculated Φ_{bm} using Ogston's equation (Ogston, 1958). These relationships required knowledge of the Darcy permeability, K_D, and the fiber radius, r_f, in addition to ϕ. We assumed $K_D = 2.7$ nm^2 (see Section 4.3, footnote 3) and used a semi-empirical equation for a random array of fibers (Jackson and James, 1986) to relate K_D to r_f and ϕ. In addition, we employed the experimental results of Daniels et al. (1993) for diffusion of dextran with $r_s = 6.4$ nm through basement membrane *in vitro*, from which it can be inferred that $\Phi_{bm} d_{bm} = 7.8 \times 10^{-4}$. Using the Brinkman approach to calculate d_{bm} and Ogston's result to calculate Φ_{bm}, this provided the additional relationship needed to calculate r_f and ϕ. The result was $r_f = 1.14$ nm and $\phi = 0.111$.

6.3.2 Sieving Coefficients and Concentration Profiles

The sieving coefficient for the slit diaphragm is defined as

$$\theta_{sd} = \frac{C_B}{C_0} \tag{6.16}$$

where C_0 is the average concentration at $z = -\delta$, adjacent to the basement membrane. The dependence of θ_{sd} on Pe is illustrated in Figure 6.5 for a particular combination of sphere size, cylinder size, and cylinder spacing, at three values of δ/R. For $Pe \rightarrow 0$, there is diffusional equilibration across the slit diaphragm and $\theta_{sd} \rightarrow 1$. As Pe increases, θ_{sd} at first decreases and then eventually returns to unity. As δ/R is increased, the minimum value of θ_{sd} becomes closer to unity and is reached at smaller values of Pe.

The non-monotonic dependence of θ_{sd} on Pe is explained by the concentration profiles shown in Figure 6.6. Representative concentration profiles along the main direction of flow (z) are shown for four values of Pe; note the different concentration scales in the four panels. It can be seen that as Pe increases, two competing effects come into play: there is a larger concentration drop in the immediate vicinity of the cylinders (near $z = 0$) and there is increasing concentration polarization upstream from the cylinders ($z < 0$). The net effect, as was shown in Figure 6.5, is that θ_{sd} at first decreases with increasing Pe, but eventually returns to unity as polarization becomes more prominent.

Figure 6.6 includes concentration profiles for positions aligned with the center of a cylinder ($y/L = 0$) or midway between cylinders ($y/L = 1$). The dashed curves which show the former are interrupted at $|z| = R + r_S$, where the sphere contacts the cylinder. It is noteworthy that although $N_z = 0$ at those points, $\partial C/\partial z \neq 0$. The solute flux vanishes because $\mathbf{d} = \mathbf{h} = \mathbf{0}$ at the point of contact. An advantage of using a finite element formulation to solve equation (6.8) is that concentration gradients next to the cylinder need not be known *a priori*. Instead, the no-flux boundary conditions represented by equations (6.10c) and (6.10d) are automatically incorporated in the development of the discretized finite element equations.

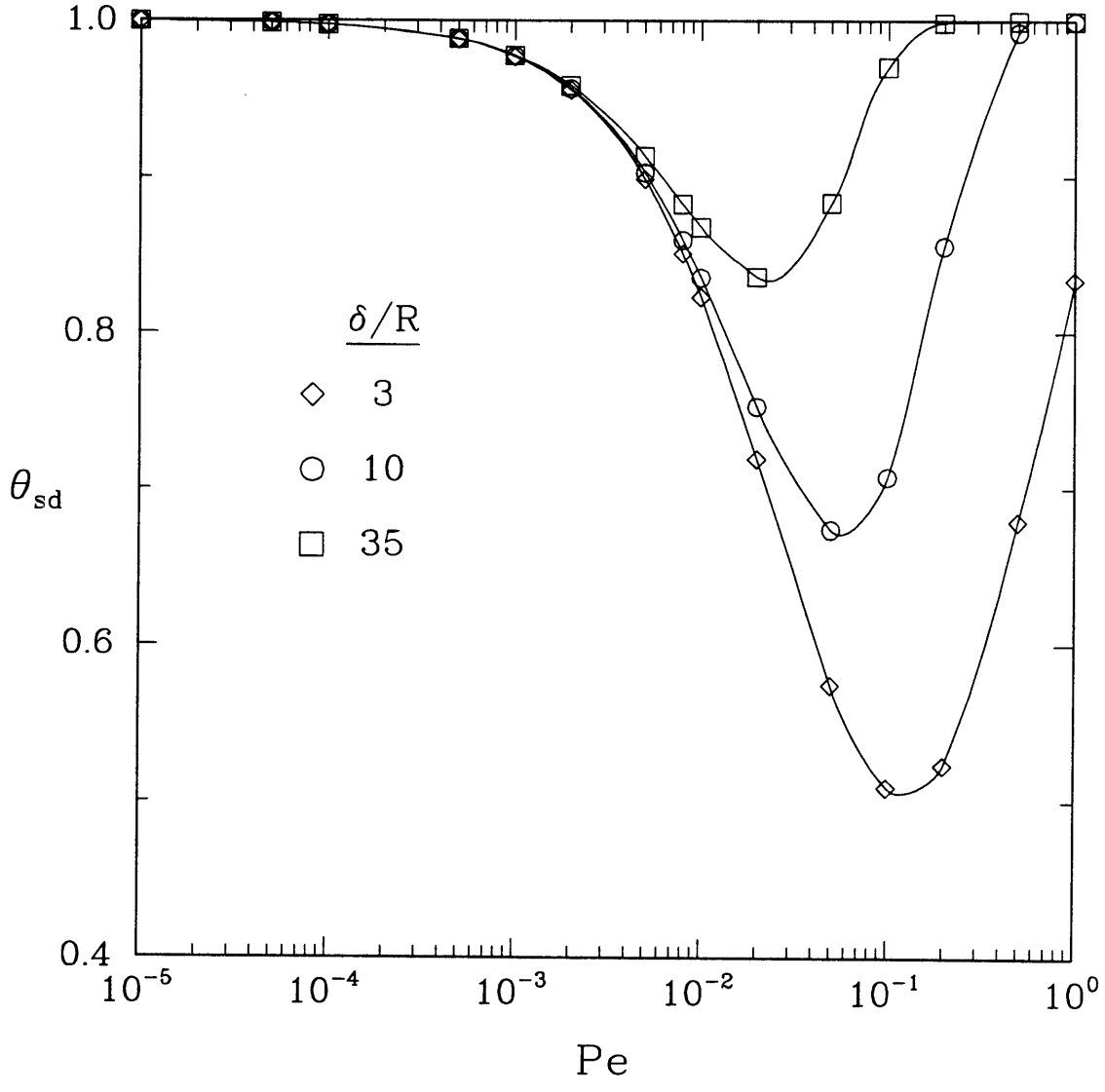

Figure 6.5 - Effect of the Peclet number, *Pe*, on the sieving coefficient, θ_{sd}, for $R/L = 0.5$, $r_s/(L - R) = 0.7$, and three values of δ/R.

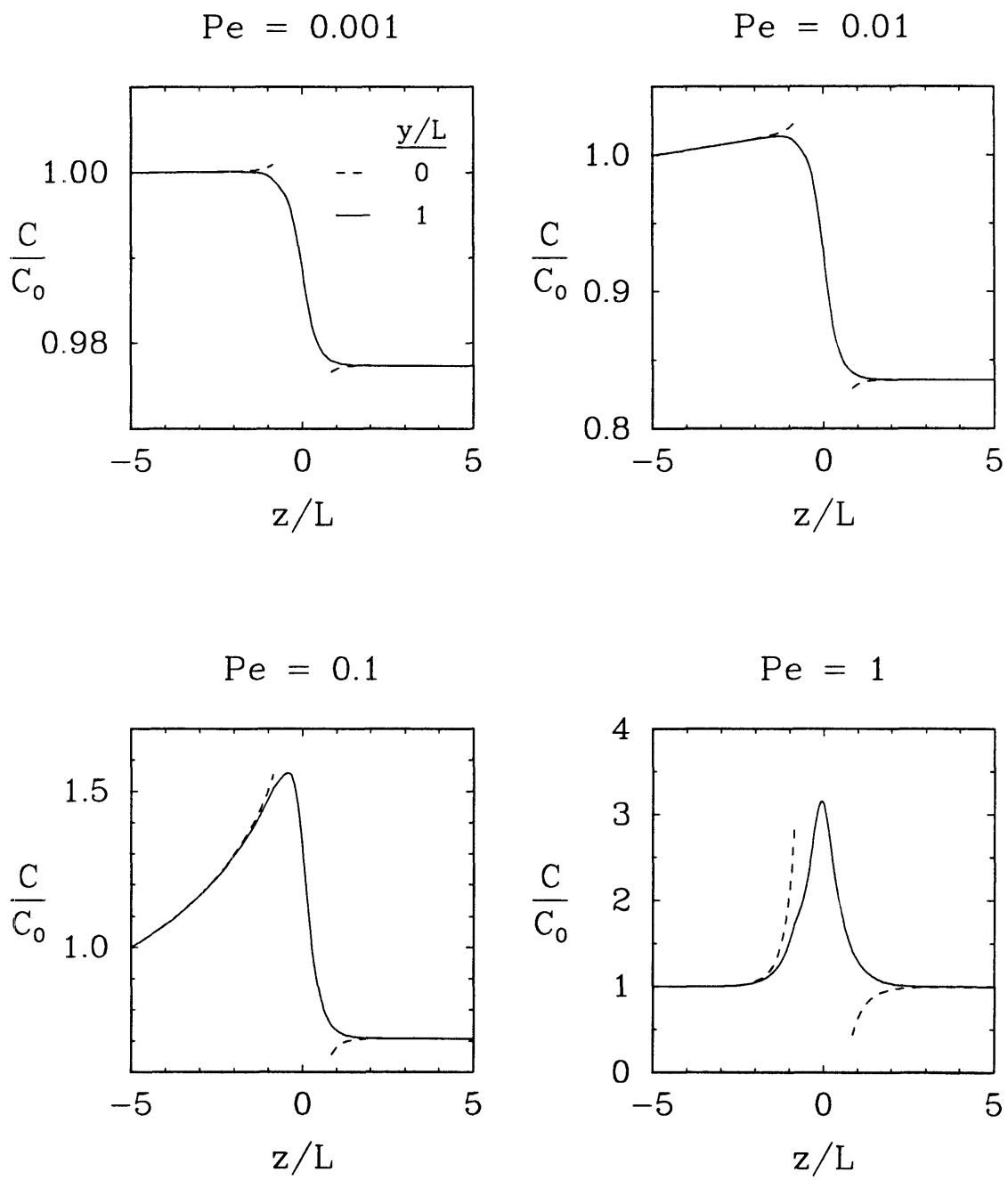

Figure 6.6 - Concentration profiles at $y/L = 0$ (dashed curves) and $y/L = 1$ (solid curves) for $R/L = 0.5$, $r_s/(L - R) = 0.7$, $\delta/R = 10$, and four values of Pe.

Figure 6.7 illustrates the dependence of the sieving coefficient on molecular radius; the abscissa, $\lambda \equiv r_s/(L - R)$, is equivalent to the solute diameter divided by the gap between cylinders. Solute transport is unrestricted for $\lambda \rightarrow 0$ and vanishes for $\lambda \geq 1$. For $Pe \rightarrow 0$, the slow flow rate permits diffusional equilibration of all solutes for which $\lambda < 1$. Accordingly, $\theta_{sd}(\lambda)$ approaches a step function under these conditions, declining from 1 to 0 at $\lambda = 1$. This is roughly the case for $Pe = 0.001$ in Figure 6.7. However, even for $Pe = 0.01$, the fluid velocity is large enough that θ_{sd} declines gradually with increasing λ.

It is convenient to have an analytical relationship between θ_{sd} and its determinants, namely Pe, R/L, δ/L and λ. An expression which worked well was

$$\theta_{sd} = \frac{1-\lambda}{1-\left(1-e^{-Pe\delta/R}\left(1-e^{-APe}\right)\right)\lambda}. \tag{6.17}$$

The parameter A in equation (6.17) was evaluated using

$$A = \frac{A_1}{R/L} + \frac{A_2}{1-R/L} \tag{6.18}$$

where $A_1 = 3.65$ and $A_2 = 0.573$. The form of equation (6.17) is based on that obtained for a simple, one-dimensional model of ultrafiltration across a membrane with a concentration polarization layer. It yields correct limiting values of θ_{sd} for $Pe = 0$ ($\theta_{sd} = 1$), $Pe \rightarrow \infty$ ($\theta_{sd} = 1$), $\lambda = 0$ ($\theta_{sd} = 1$) and $\lambda = 1$ ($\theta_{sd} = 0$). The range of dimensionless parameters used to fit the numerical values of θ_{sd} to equations (6.17) and (6.18) was $10^{-5} \leq Pe \leq 0.1$, $3 \leq \delta/R \leq 35$, $0.1 \leq R/L \leq 0.9$, and $0.1 \leq \lambda \leq 0.95$. Combinations of these parameters which yielded $(R + r_s)/L > 0.99$ were excluded because the finite element method does not provide accurate solutions for very small gaps. Also excluded were

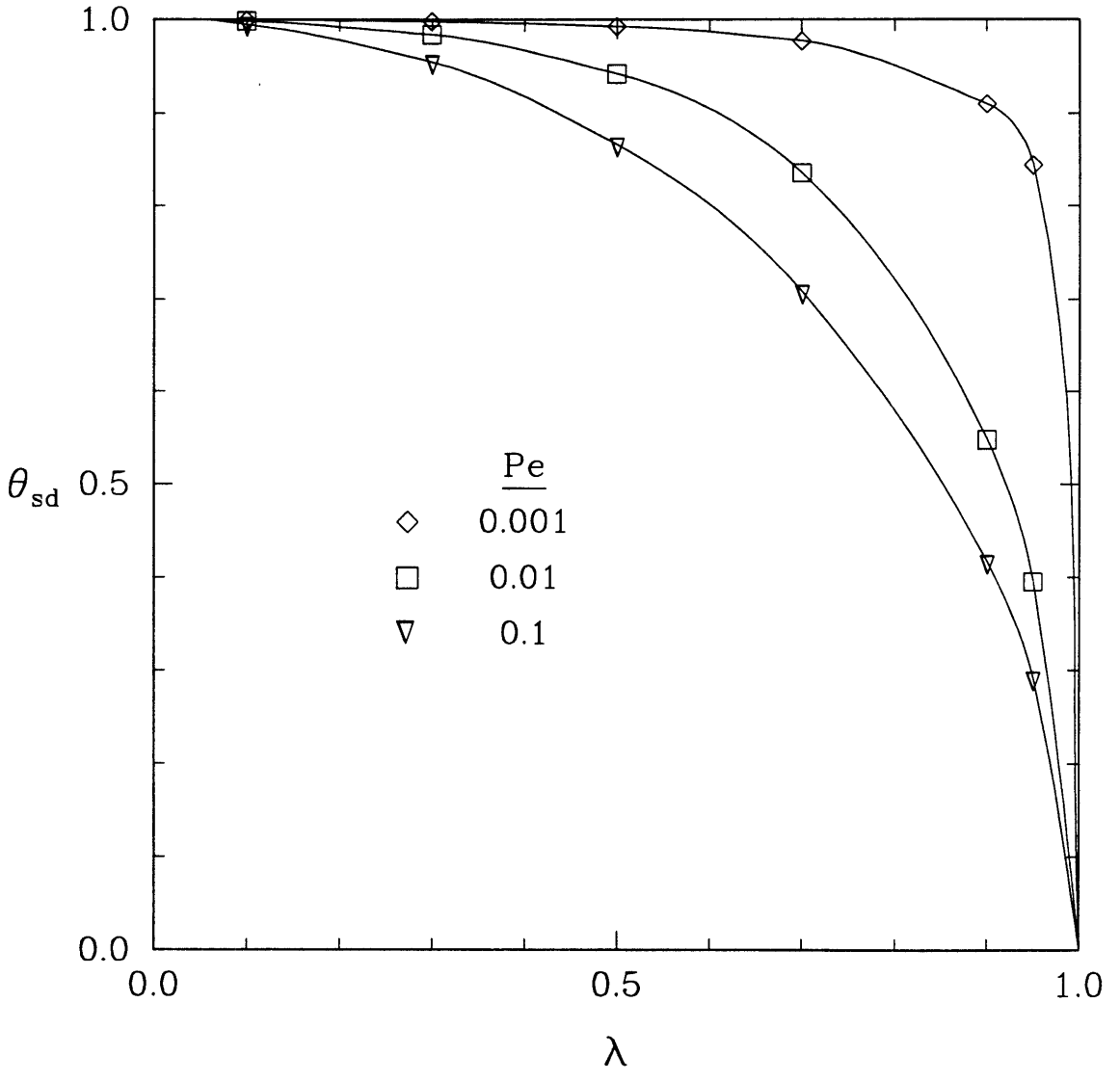

Figure 6.7 - Effect of relative molecular size, λ, on the sieving coefficient, θ_{sd}, for R/L = 0.5, δ/R =10, and three values of Pe.

combinations which yielded $\delta/(R+r_s) < 1.5$, because the distance from z = -δ to the cylindrical boundary was then too small for computational accuracy, as well as being outside the physiological range. Powell's method (Press et al., 1986) was used to obtain the constants A_1 and A_2 from a total of 900 points. The root-mean-square error was 5%.

6.3.3 DISTRIBUTION OF CYLINDER SPACINGS

Using the dimensions given by Rodewald and Karnovsky (1974), the openings in the slit diaphragm are only 40Å by 140Å, so that one would conclude that only molecules with $r_s < 20$ Å can cross the slit diaphragm. However, rigid molecules with r_s as large as 60 - 70 Å cross the capillary wall in limited amounts (Oliver et al., 1992), suggesting that the structure of the slit diaphragm is probably not uniform. This hypothesis is supported by the electron micrographs of Hora et al. (1990). To model the effects of non-uniformities in the structure of the slit diaphragm, we assumed that the spacing between cylinders follows a continuous probability distribution. This is much like assuming a continuous distribution of pore radii, as done in previous models of glomerular filtration (Deen et al., 1985). For a given distribution of spacings, the average sieving coefficient, $\langle \theta_{sd} \rangle$, was calculated as

$$\langle \theta_{sd} \rangle = \int_0^\infty \theta_{sd}(u) G(u) du \tag{6.19}$$

where u is half the gap width between adjacent cylinders (i.e., $u = L - R$) and $G(u)du$ is the fraction of filtrate volume passing through gaps of half-widths between u and $u + du$. In $\langle \theta_{sd} \rangle$ and other quantities, the brackets indicate an average with respect to cylinder spacing. The function $G(u)$ is proportional to the probability distribution function for the gap width, $g(u)$, and to a weighting factor, $q(u)$, which accounts for the fact that, for a

given filtration pressure, the volume flow rate of filtrate through a given gap depends on u. The latter function can be expressed as

$$q(u) = \frac{(u+R)^2}{f_T} \tag{6.20}$$

where f_T is the dimensionless flow resistance defined by equation (3.9). Noting that, by definition, $\int_0^\infty G(u)du = 1$, one obtains

$$G(u) = \frac{(u+R)^2 g(u) f_T^{-1}(u)}{\int_0^\infty (u+R)^2 g(u) f_T^{-1}(u) du}. \tag{6.21}$$

There are at present insufficient data on the structure of the slit diaphragm to define a specific gap-width distribution function, $g(u)$. Two reasonable choices for the form of $g(u)$ are the lognormal and gamma distributions. Both should give qualitatively similar results, in that $g \to 0$ for $u \to 0$ or $u \to \infty$, and $g(u)$ exhibits a single peak at intermediate u. We chose the gamma distribution, which is defined by

$$g(u) = \frac{\gamma_2^{\gamma_1} u^{\gamma_1 - 1} e^{-\gamma_2 u}}{\Gamma(\gamma_1)} \tag{6.22}$$

where Γ is the gamma function and γ_1 and γ_2 are constants. The mean and variance of $g(u)$ are γ_1/γ_2 and γ_1/γ_2^2, respectively, so that $\gamma_1^{-1/2}$ is the standard deviation divided by the mean.

The assumed distribution of gap widths affects not only θ_{sd} but also the hydraulic permeability of the slit diaphragm, k_s. Accordingly, we define an average hydraulic permeability, $\langle k_s \rangle$, given by

$$\langle k_s \rangle \equiv \frac{\langle V_s \rangle}{\Delta P_s} = \frac{\int_0^{\infty} (u+R) g(u) V_s du}{\Delta P_s \int_0^{\infty} (u+R) g(u) du} \tag{6.23}$$

where ΔP_s is the pressure drop due to the slit channel and diaphragm and $\langle V_s \rangle$ is the mean filtrate velocity in the slit channel, averaged over all cylinder spacings. Using equation (3.9) with $V = V_s$ and $\Delta P = \Delta P_s$, equation (6.23) becomes

$$\langle k_s \rangle = \frac{1}{\mu} \frac{\int_0^{\infty} (u+R)^2 f_T^{-1}(u) g(u) du}{\int_0^{\infty} (u+R) g(u) du} = \frac{1}{\mu} \frac{\int_0^{\infty} (u+R)^2 f_T^{-1}(u) g(u) du}{\frac{\gamma_1}{\gamma_2} + R} \tag{6.24}$$

Because the hydraulic permeability of the slit diaphragm previously calculated for the zipper configuration, k_s = 7.9x10^{-8} m/s/Pa, yielded an overall hydraulic permeability which agreed very well with the experimental range from micropuncture data in rats (see Section 4.3), we assumed here that $\langle k_s \rangle$ = 7.9x10^{-8} m/s/Pa. This assumption, together with equations (6.22) and (6.24), provided a relationship between γ_1 and γ_2. Thus, to calculate $\langle \theta_{sd} \rangle$, we first specified γ_1, then calculated γ_2 from equation (6.24) using Newton's method, and finally evaluated $\langle \theta_{sd} \rangle$ using equation (6.19). The values of Pe needed in equation (6.17) were calculated using equation (6.9) with $V = V_s$. The values of V (= V_s) were obtained from equation (3.9), assuming a representative pressure

difference $\Delta P_s = 3.8 \times 10^2$ Pa and calculating f_T as described in Appendix F. The integrals in equations (6.19), (6.21) and (6.24) were evaluated numerically using Romberg's method (Press et al., 1989).

Figure 6.8 illustrates sieving curves obtained for probability distributions $g(u)$ with standard deviations of 0, 30, and 90 % of the mean half-width (i.e., $\gamma_1^{-1/2}$ =0, 0.3, or 0.9). The Peclet number was calculated as described above and the cylinder radius was fixed at R = 5 nm or 10 nm. When the spacing between cylinders is constant, as is the case for standard deviations of 0% in Figure 6.8, the sieving curves exhibit relatively sharp cutoffs, similar to the results for low Pe in Figure 6.7. As the distribution of spacings broadens, the molecular-size cutoffs become less sharp, as shown for standard deviations of 30% and 90%. These trends can be understood by recalling that $\langle k_s \rangle$ is the same for all of the curves in Figure 6.8. As the standard deviation of the spacing increases, there is a tendency for rapid water flow through the larger gaps, and the mean spacing must decrease to keep $\langle k_s \rangle$ constant. For R = 5 nm, the mean half-width between cylinders (γ_1/γ_2, the mean value of L - R) ranged from 2.0 nm at a standard deviation of 0% to 1.4 nm at a standard deviation of 90%. For R = 10 nm, the mean half-width ranged from 2.9 to 2.1 nm. The decrease in mean spacing causes $\langle \theta_{sd} \rangle$ for small molecules to decrease as the standard deviation increases. However, for the larger standard deviations there is a substantial number of very large spacings between cylinders, which allows the passage of large molecules which otherwise would be prevented from crossing the diaphragm. Thus, the sieving coefficient of large molecules increases significantly as the standard deviation of $g(u)$ increases.

One of the assumptions of the model, either for uniform or variable gap widths between cylinders, was that the walls (cell surfaces) which bound the filtration slits have negligible effect on θ_{sd}. To test this assumption, we computed sieving coefficients for the case of ultrafiltration through slit channels of width $2W$ and length δ, in the absence of a diaphragm. In this case, the sieving coefficients are given by

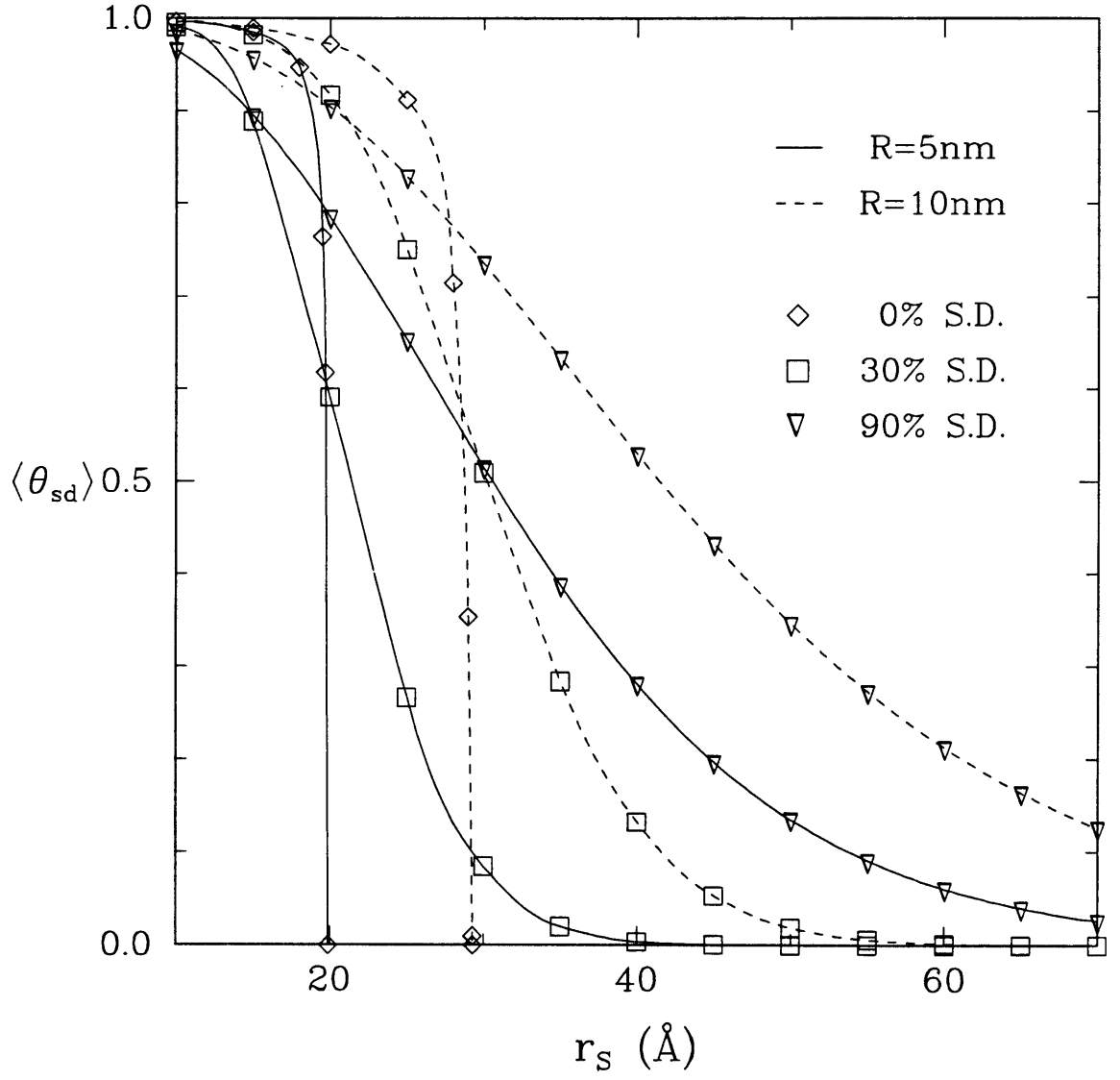

Figure 6.8 - Average sieving coefficient for the slit diaphragm, $\langle\theta_{sd}\rangle$, for various distributions of cylinder spacing. The sieving coefficient is shown as a function of molecular radius, for R = 5 nm (solid curves) and R = 10 nm (dashes curves), δ = 50 nm, and W = 20 nm. The gamma distributions $g(u)$ had standard deviations of 0, 50, and 90% of the mean half-spacing.

$$\theta_{channel} = \frac{\Phi h}{1 - \exp(-hV_s\delta/dD_\infty)(1-\Phi h)} \tag{6.25}$$

where Φ is the steric partition coefficient between the slit channels and the adjacent bulk solution, and d and h are, respectively, hindrance coefficients for diffusion and convection. These three coefficients were evaluated using equations (32) - (34) of Deen (1987). (The coefficients d and h are equivalent to, respectively, H/Φ and W/Φ of Deen (1987).) For $10 \leq r_s \leq 70$ Å and the hydrodynamic conditions of Figure 6.8 we obtained $\theta_{channel} > 0.98$, which suggests that the resistance of the channel is indeed negligible compared to the resistance of the slit diaphragm. The reason the channel resistance is negligible is that the half-width of the gaps tends to be much smaller than the half-width of the channel (W).

6.3.4 Overall Sieving Coefficients for the Glomerular Capillary Wall

In vivo, one can only measure sieving coefficients for the glomerular capillary wall as a whole, and not for the slit diaphragm alone. Thus, the results from the previous section will now be used, together with the approximate model for transport across the glomerular basement membrane, to provide estimates of overall sieving coefficients for the glomerular capillary wall. From the computed concentration profiles in the basement membrane, we calculated sieving coefficients for the basement membrane, θ_{bm}, defined as the concentration at the slit opening divided by that at the endothelial openings. Then, assuming that the sieving coefficient for the fenestrae is unity (i.e., neglecting the resistance of the fenestrae to the filtration of macromolecules), overall sieving coefficients for the glomerular capillary wall, θ, were calculated by

$$\theta = \frac{C_B}{C_L} \cong \langle \theta_{sd} \rangle \theta_{bm}, \tag{6.26}$$

where C_L is the solute concentration in the capillary lumen.

Figure 6.9 shows values of θ calculated for conditions similar to those of Figure 6.8. Some of the results for θ_{sd} in Figure 6.8 are repeated for comparison; the dashed curves include the effects of the basement membrane, whereas the solid curves do not. For small standard deviations of the cylinder spacing (up to ~50% of the mean) the values of θ and $\langle \theta_{sd} \rangle$ are almost identical, implying that the basement membrane has a negligible effect on the overall sieving coefficient under these conditions. For some of the larger solute sizes, where $\langle \theta_{sd} \rangle << 1$, there is predicted to be some concentration polarization in the basement membrane. Accordingly, in these cases, $\theta_{bm} > 1$ and θ slightly exceeds $\langle \theta_{sd} \rangle$. Only for a very broad distribution of cylinder spacings (standard deviation of 90%) is there a significant difference between the corresponding curves for θ and $\langle \theta_{sd} \rangle$. In this case sieving in the basement membrane overcomes polarization, so that $\theta_{bm} < 1$ and $\theta < \langle \theta_{sd} \rangle$. The curve labeled "$\langle \theta_{sd} \rangle = 1$" represents a limiting case in which the slit diaphragm is effectively absent and $\theta = \theta_{bm}$. It can be seen from this that, even if there is no downstream resistance to cause concentration polarization, θ_{bm} tends to greatly exceed $\langle \theta_{sd} \rangle$.

Figure 6.10 provides an approximate comparison of theoretical values of θ with experimental values measured in rats using Ficoll, a polysaccharide which behaves as a neutral, solid sphere (Oliver et al., 1992). The model predictions were calculated using the value of the filtrate velocity already used in Figures 6.9 and 6.10. It can be seen that, for values of r_S < ~40 Å, there is good agreement between the experimental values and the model predictions for R = 2 nm and a standard deviation of 50%. For larger values of r_S, for which $\theta < 0.01$, the model predictions for R = 2 nm underestimate θ. The

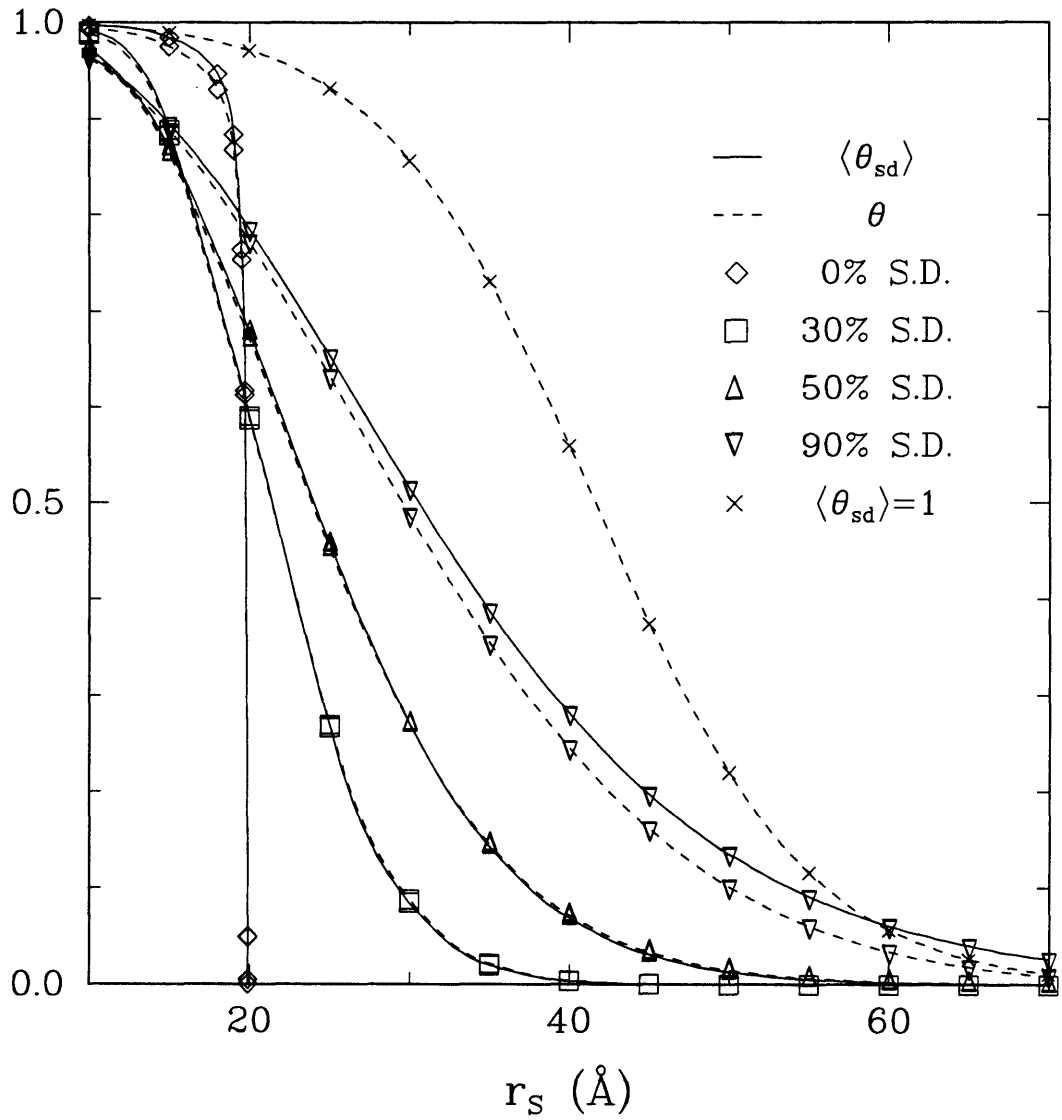

Figure 6.9 - Average sieving coefficient for the slit diaphragm ($\langle\theta_{sd}\rangle$, solid curves) and overall sieving coefficient for the glomerular capillary wall (θ, dashed curves) as a function of molecular radius. The parameter values used included R = 5 nm, δ = 50 nm, and W = 20 nm. The gamma distributions $g(u)$ had standard deviations of 0, 30, 50, and 90% of the mean half-spacing. Also shown are results for θ obtained using $\langle\theta_{sd}\rangle = 1$.

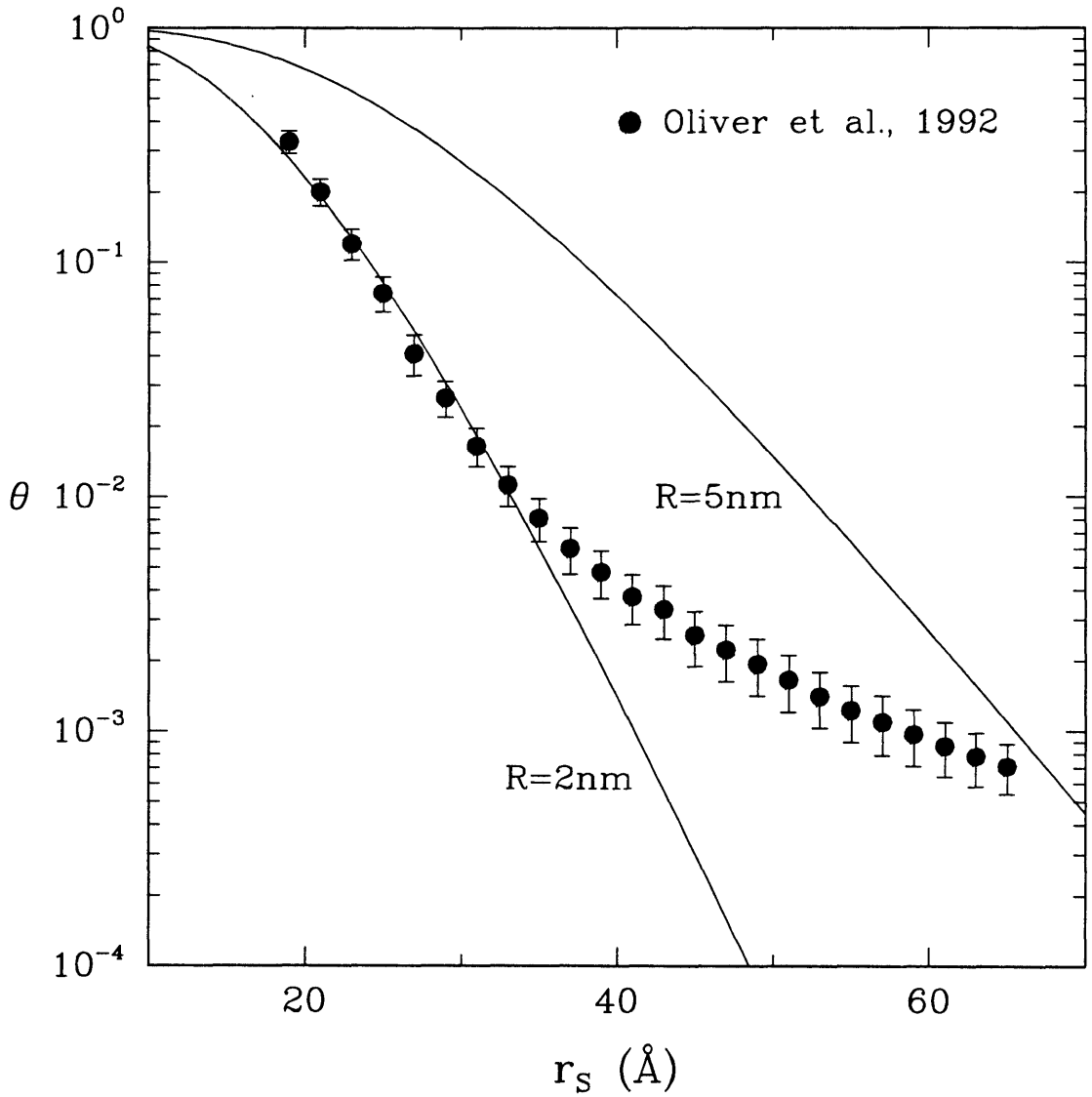

Figure 6.10 - Comparison between theoretical and experimental values of the sieving coefficient (θ). The experimental values (symbols) are based on fractional clearances of Ficoll measured in rats (Oliver et al., 1992) and are shown as mean ± S.E.. The input parameters for the theoretical curves were R = 2 or 5 nm, δ = 50 nm, W = 20 nm, and an assumed standard deviation of $g(u)$ equal to 50% of the mean half-spacing.

reason for the discrepancy in the shape of the theoretical and experimental sieving curves is unclear. Because $\langle \theta_{sd} \rangle$ is significantly affected by the assumed value of R (see Figure 6.8), we tested whether assuming a distribution of R together with a distribution of $u = L - R$ would alter the shape of the sieving curves. These calculations yielded sieving curves qualitatively similar to those calculated for constant R, so that we conclude that a distribution of R cannot explain the differences in shape between the experimental and theoretical curves shown in Figure 6.10. A possible explanation for these differences is that "defects" in a small fraction of the filtering surface area provide a non-selective (shunt) pathway that offers little or no resistance to the passage of macromolecules. The assumption of a shunt pathway in parallel with a highly selective membrane has been used previously in "equivalent-pore" models of glomerular filtration (e.g., Deen et al., 1985; Oliver et al., 1992). Calculations with those models have shown that a shunt will cause a leveling off of the sieving curve for large molecular sizes, as suggested by the data in Figure 6.10. It should be noted that the comparison between theory and experiment in Figure 6.10 is only approximate, because the model predictions are valid for a single location along a glomerular capillary, whereas measurements of θ *in vivo* reflect the changing conditions along a capillary. Specifically, the net ultrafiltration pressure, and thus the filtrate velocity, decrease from the afferent to the efferent end of a glomerular capillary.

6.3.5 SUMMARY AND CONCLUSIONS

We have developed a novel hydrodynamic model to describe hindered transport of spherical macromolecules through single rows of cylindrical fibers of macromolecular dimensions. Applying this model to the glomerular slit diaphragm, we conclude that the sieving characteristics observed in normal animals or healthy humans are consistent with a fairly broad distribution in the spacings between adjacent fibers. A comparison with

results for Ficoll in the rat suggests that the standard deviation is roughly 50% of the mean spacing. Under these conditions, we infer that the glomerular basement membrane makes little or no contribution to the overall sieving coefficient for electrically neutral macromolecules. If the endothelial fenestrae are filled by water, or by a glycocalyx which provides a fibrous barrier no more dense than the basement membrane, then the fenestrae will represent at most a modest extension of a basement-membrane-like barrier. Thus, the fenestrae also will have little effect on the overall size-selectivity of the glomerular capillary wall. We conclude that the overall sieving behavior of neutral macromolecules is determined almost entirely by the slit diaphragm. This conclusion is consistent with that reached in a recent study of dextran transport across isolated glomerular basement membrane or intact glomeruli *in vitro* (Daniels et al., 1993). It was found that glomerular basement membrane was much less selective than the intact capillary wall, which included the cellular components.

Our conclusion that the basement membrane makes little or no contribution to the size-selectivity of the glomerular capillary wall is necessarily tentative, because of the uncertainty in the values of the transport coefficients used in the basement membrane model. These coefficients are d_{bm} and h_{bm} in equation (6.14). The equations used to estimate these parameters are expected to be accurate for fibrous media with lower solid volume fractions than the basement membrane (Phillips et al., 1989). In addition, these equations, as well as Ogston's equation for Φ_{bm}, require values for the fiber radius and solid volume fraction of the basement membrane, neither of which is known precisely. Using the *in vitro* methods referred to above (Daniels et al., 1993), it should be possible to obtain experimental estimates of d_{bm} and h_{bm} as a function of molecular size for test molecules such as Ficoll. Finally, we should note that the glomerular capillary wall restricts passage of macromolecules on the basis of molecular charge as well as molecular size (Maddox et al., 1992). The overall sieving coefficients for anionic macromolecules tend to be much lower than those for uncharged macromolecules of

similar size and chemical structure. The basement membrane may contribute significantly to this charge-selectivity, whether or not it also constitutes an important size-selective barrier.

APPENDIX A

WATER FLOW THROUGH THE ENDOTHELIAL FENESTRAE

A.1 FLUID-FILLED FENESTRAE

If it is assumed that the fenestrae contain only fluid, the governing equations for water flow through the endothelial fenestrae are the Stokes and continuity equations (Equations (3.1) and (3.2)). The axisymmetric geometry of the fenestrae suggests the use of cylindrical coordinates (r,θ,z). The boundary conditions at the surface of the endothelial cells (Ω_c) are

$$v_z = v_r = v_\theta = 0 \text{ at } \Omega_c. \tag{A.1}$$

At the entrance of a fenestra, the boundary condition in the z-direction which could be imposed using FIDAP was

$$\Pi_{zz} = \text{constant at } z = -R_f \tag{A.2}$$

where Π_{zz} is the total normal stress at $z = -R_f$. Because the normal viscous stress is expected to be small compared with the pressure, equation (A.2) can be written approximately as

$$\Pi_{zz} \cong P_G \text{ at } z = -R_f \tag{A.2a}$$

where P_G is the luminal pressure. Because of flow in the capillary lumen, the remaining boundary conditions at $z = -R_f$ are more difficult to determine precisely, and we investigated three alternatives. One was to impose a constant shear stress (τ_{zx}, where x is the direction of blood flow). Based on typical blood velocities and capillary dimensions (Shea, 1981), the shear stress (τ_{zx}) was estimated to be on the order of ~1 Pa. As a second approach, we set v_x equal to various constants at $z = -R_f$, as is sometimes done in modeling flow past fluid-filled cavities. A third approach used, motivated entirely by simplicity, was

$$v_r = v_\theta = 0 \quad \text{at } z = -R_f \; . \tag{A.3}$$

Equation (A.3) yields flow in the fenestra which is axisymmetric and without swirl; that is, for all r and z, the velocity and pressure are independent of θ and $v_\theta = 0$. The three approaches were compared using fenestrae approximated as straight cylinders of radius R_f. The results showed that k_{en} does not depend significantly on the boundary conditions used at $z = -R_f$. There is no reason to believe that this conclusion would be different for fenestrae with tapered walls, so that subsequent calculations were performed using equation (A.3).

Because the pressure at the exit of the fenestra (adjacent to the basement membrane) might depend on r, none of the boundary conditions at $z = R_f$ is known *a priori*. To overcome this problem, we considered the extended domain shown in Figure A.1, which includes a portion of the basement membrane downstream from the fenestra. The value of r_{bm} was chosen such that ε_f (= $(R_f/r_{bm})^2$) had the desired value of 0.2, and z_{bm} was made large enough ($z_{bm} = 4R_f$) so that further increases in this parameter would not affect k_{en}. Brinkman's equation (equation (4.31)) was used to model flow through the basement membrane next to the fenestra. Although, throughout most of the basement membrane, the viscous (Stokes) term is small compared with the Darcy's term, the full

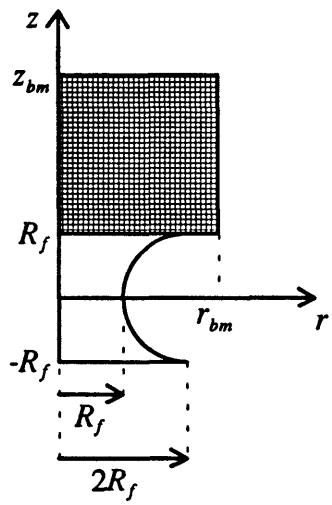

Figure A.1 - Computational domain for calculating the permeability of a single fenestra. It consists of the fenestra (from $z = -R_f$ to $z = R_f$) and part of the basement membrane (from $z = R_f$ to $z = z_{bm}$).

Brinkman equation was used here to allow the matching of the viscous stresses at the interface between basement membrane and fluid in the fenestra.

The boundary conditions for the basement membrane are

$$v_r = 0 \text{ and } \tau_{rz} = 0 \text{ at } r = r_{bm} \tag{A.4}$$

$$v_r = v_z = 0 \text{ at } z = R_f \text{ and } 2R_f \le r \le r_{bm} \tag{A.5}$$

$$v_r = 0 \text{ and } \Pi_{zz} = \Pi_2 \text{ at } z = z_{bm} \tag{A.6}$$

where τ_{rz} is the viscous stress exerted in the z-direction on a surface of constant r, and Π_2 is a constant. At the interface between the fenestra and basement membrane ($z = R_f$, $0 \le r \le 2R_f$) the velocities, pressure and viscous stresses in the basement membrane (*bm*) and fenestra (*f*) were matched

$$
\begin{aligned}
(v_r)_{bm} &= (v_r)_f \\
(v_z)_{bm} &= (v_z)_f \\
(P)_{bm} &= (P)_f \\
(\tau_{rr})_{bm} &= (\tau_{rr})_f \\
(\tau_{zz})_{bm} &= (\tau_{zz})_f \ .
\end{aligned}
\tag{A.7}
$$

Equations (3.1), (3.2), (4.31) and (A1)-(A7) were solved simultaneously using FIDAP on a Cray X-MP EA/464. As shown in Figures A.2 and A.3, the velocity and pressure profiles at $z = R_f$ depended significantly on r. Both v_z and P changed little between $r = 0$ and $r = R_f$, but decreased faster between $r = R_f$ and $r = 2R_f$. Using the computed velocity and pressure profiles at $z = -R_f$ and $z = R_f$, we calculated k_{en} using equations (4.4) and (4.5). For the baseline input we obtained $k_{en} = 2.0\text{x}10^{-7}$ m/s/Pa. This value is smaller than if it had been assumed that the fenestrae are cylindrical pores of radius R_f and length $2R_f$. Performing the calculations detailed above with this simpler geometric model we obtained $k_{en} = 3.9\text{x}10^{-7}$ m/s/Pa. If we had assumed fully developed flow in cylindrical pores, the result (from Poiseuille's equation) would be $k_{en} = \varepsilon_f R_f^2 / (16 \mu R_f) = 5.4\text{x}10^{-7}$ m/s/Pa.

A.2 FENESTRAE FILLED WITH GLYCOCALYX

If it is assumed that the fenestrae are filled with a fiber matrix of Darcy permeability K_D', then Stokes equation (equation (3.1)) must be replaced by Brinkman's equation (equation (4.31) with K_D' instead of K_D). All other equations and boundary conditions are as before. Because K_D' is not known we performed numerical calculations with FIDAP for values of K_D' ranging from 2 to 100 nm^2. In these calculations we used

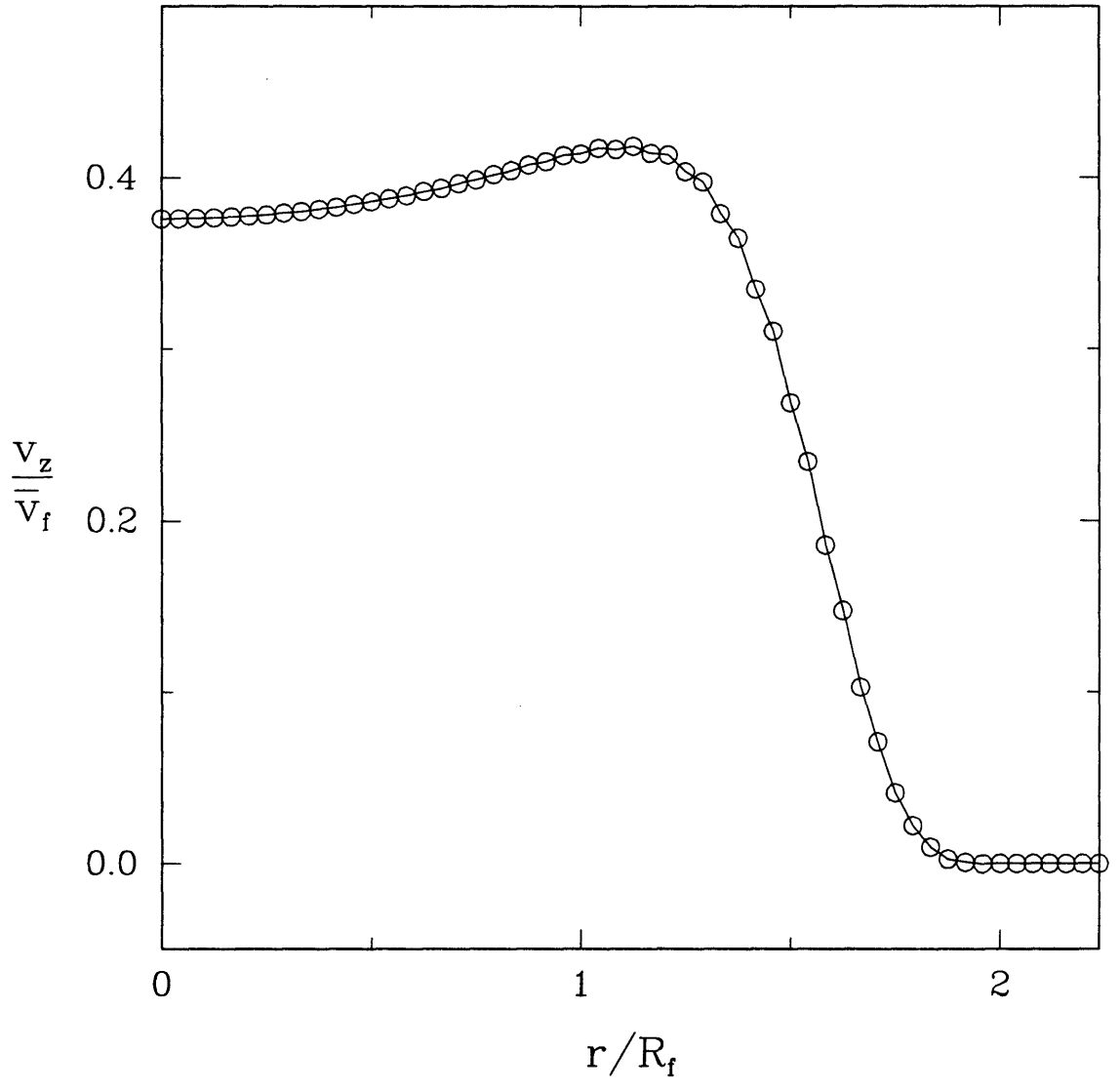

Figure A.2 - Velocity profile at the interface between fenestra and basement membrane ($z = R_f$). $\bar{v}_f$ is an average velocity in the fenestra, based on the cross-sectional area at $z = 0$.

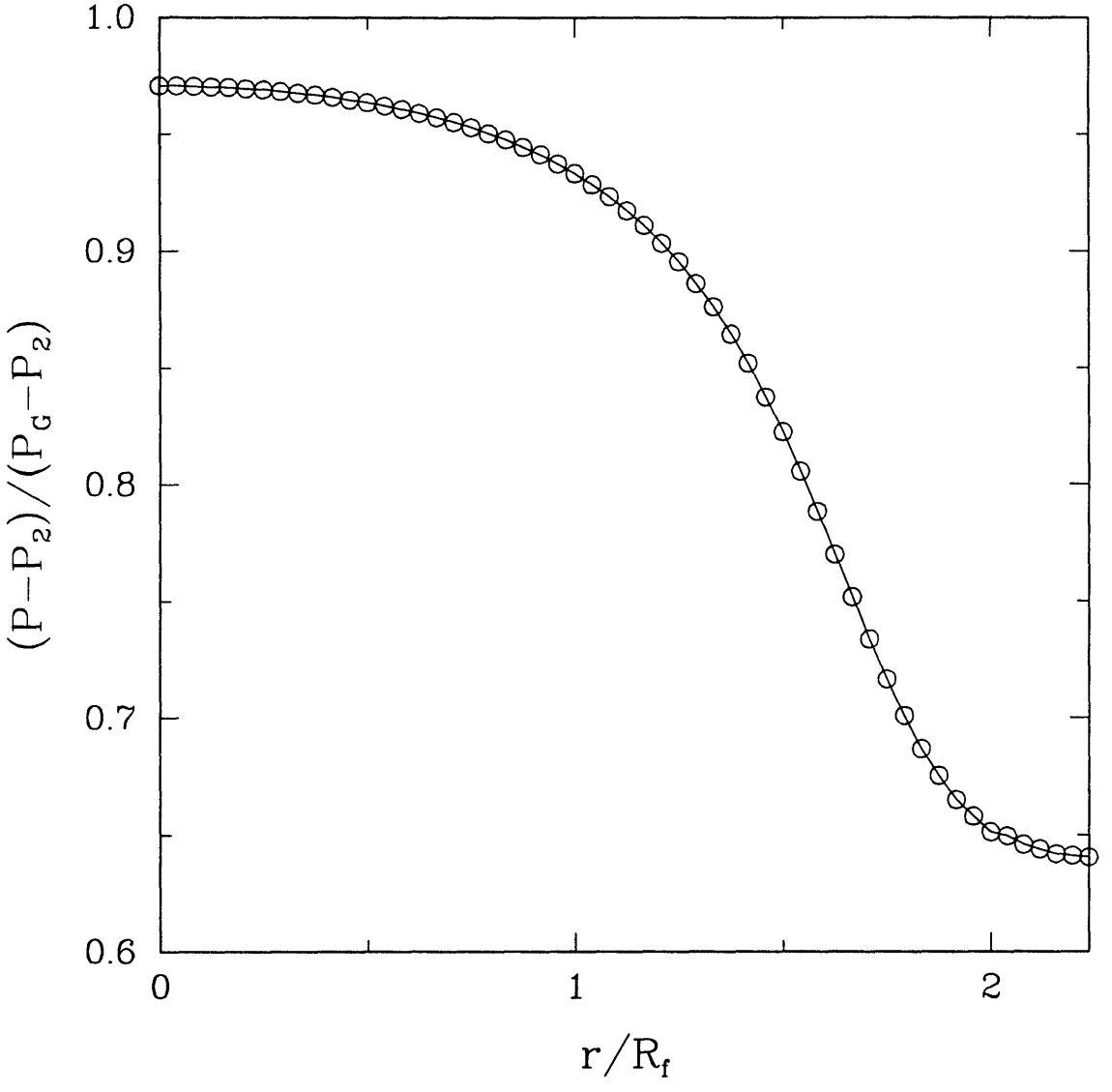

Figure A.3 - Pressure profile at the interface between fenestra and basement membrane ($z = R_f$). P_2 is the average pressure at $z = z_{bm}$ and P_G is the pressure in the capillary lumen.

the same structural parameters as in Section A.1. Calculated values of k_{en} are given in Table A.1. As $K_D^{'}$ increases, k_{en} increases, eventually approaching the value for fluid-filled fenestra. If we assume that the Darcy permeability of the glycocalyx and basement membrane are the same ($K_D^{'} = K_D = 2.7$ nm^2), the result is $k_{en} = 1.3 \times 10^{-8}$ m/s/Pa.

Table A.1 - Calculated values of hydraulic permeability of the endothelium (k_{en}) for various values of Darcy permeability of the glycocalyx ($K_D^{'}$)

$K_D^{'}$ (nm^2)	k_{en} (m/s/Pa)
2	1.0×10^{-8}
5	2.3×10^{-8}
10	4.0×10^{-8}
50	1.1×10^{-7}
100	1.4×10^{-7}

APPENDIX B

WATER FLOW THROUGH THREE-LAYERED BASEMENT MEMBRANE

As was mentioned in Chapter 1, the glomerular basement membrane apparently consists of three layers: the lamina rara interna, the lamina densa and the lamina rara externa. Because the ultrastructure of the fibers seems to change from one layer to the next, the Darcy permeability might also change from one layer to the next. Here we describe a model of water flow through the three layers of the basement membrane.

B.1 MATHEMATICAL MODEL

As for a homogeneous basement membrane, the governing equations are Darcy's law and the continuity equation. However, because the Darcy permeability varies in a step-wise manner with z, we have

$$\begin{aligned} \mathbf{v}^* &= -\frac{K_D K_1}{\mu}\nabla P^* \quad \text{for } 0 \le z \le z_1 \\ \mathbf{v}^* &= -\frac{K_D K_2}{\mu}\nabla P^* \quad \text{for } z_1 \le z \le z_2 \\ \mathbf{v}^* &= -\frac{K_D K_3}{\mu}\nabla P^* \quad \text{for } z_2 \le z \le \delta_{bm}\,. \end{aligned} \tag{B.1}$$

where z_1 corresponds to the interface between lamina rara interna (LRI) and lamina densa (LD) and z_2 corresponds to the interface between lamina densa and lamina rara externa

(LRE). The dimensionless quantities K_i (i = 1, 2, 3) are ratios of Darcy permeabilities, defined as

$$K_1 = \frac{K_D(LRI)}{K_D} \; ; \; K_2 = \frac{K_D(LD)}{K_D} \; ; \; K_3 = \frac{K_D(LRE)}{K_D}. \tag{B.2}$$

The overall Darcy permeability, K_D, is related to the values for the individual layers by

$$\frac{\delta_{LRI}}{K_D(LRI)} + \frac{\delta_{LD}}{K_D(LD)} + \frac{\delta_{LRE}}{K_D(LRE)} = \frac{\delta_{bm}}{K_D} \; . \tag{B.3}$$

Using the continuity equation together with equation (B.1) one obtains, for each layer, a Laplace's equation for P^*. Here we analyze only the case where we specify constant velocity at the endothelial and slit openings. The boundary conditions at $z = 0$ and $z = \delta_{bm}$ for this case are

$$\begin{aligned}
&\frac{\partial P^*}{\partial z} = -\frac{\mu \bar{v}^*_{bm}}{\varepsilon_f K_1 K_D} \text{ at } \Omega_f \\
&\frac{\partial P^*}{\partial z} = -\frac{\mu \bar{v}^*_{bm}}{\varepsilon_s K_3 K_D} \text{ at } \Omega_s \\
&\frac{\partial P^*}{\partial z} = 0 \text{ at } \Omega_{en} \text{ and } \Omega_{ep}.
\end{aligned} \tag{B.4}$$

where Ω_f and Ω_s correspond the endothelial and slit openings, respectively, and Ω_{en} and Ω_{ep} correspond to the surfaces covered by endothelium and epithelium, respectively. At $z = z_1$ and $z = z_2$ the pressures and velocities for the adjacent layers were matched, that is,

$$
\begin{aligned}
&\left(P^*\right)_1 = \left(P^*\right)_2 \quad \text{at } z = z_1 \\
&K_1\left(\frac{\partial P^*}{\partial z}\right)_1 = K_2\left(\frac{\partial P^*}{\partial z}\right)_2 \quad \text{at } z = z_1 \\
&\left(P^*\right)_2 = \left(P^*\right)_3 \quad \text{at } z = z_2 \\
&K_2\left(\frac{\partial P^*}{\partial z}\right)_2 = K_3\left(\frac{\partial P^*}{\partial z}\right)_3 \quad \text{at } z = z_2 \,.
\end{aligned}
\tag{B.5}
$$

The remaining boundary conditions are equations (4.10) and (4.11). Solving Laplace's equation for each layer with these boundary conditions, one obtains for $0 \le z \le z_1$:

$$
P' = D_0' - \left[\frac{z'}{K_1} + 2\sum_{n=1}^{\infty}\left(C_{1n}e^{-\lambda_n z'} + D_{1n}e^{\lambda_n z'}\right)\cos\left(\lambda_n x'\right)\right]. \tag{B.6}
$$

where the primed (dimensionless) variables are defined by

$$
P' \equiv \frac{P^*}{\mu \bar{v}_{bm}^* W_{bm}/K_D} \;;\; x' \equiv \frac{x}{W_{bm}} \;;\; z' \equiv \frac{z}{W_{bm}} \;;\; \delta_{bm}' \equiv \frac{\delta_{bm}}{W_{bm}} \tag{B.7}
$$

and D_0' is a dimensionless constant related to $\overline{P}_0'$. For $z_1 \le z \le z_2$,

$$
P' = D_0' - \left[\frac{z_1'}{K_1} + \frac{z' - z_1'}{K_2} + 2\sum_{n=1}^{\infty}\left(C_{2n}e^{-\lambda_n z'} + D_{2n}e^{\lambda_n z'}\right)\cos\left(\lambda_n x'\right)\right]. \tag{B.8}
$$

For $z_2 \le z \le \delta_{bm}$,

$$P' = D_0' - \left[\frac{z_1'}{K_1} + \frac{z_2' - z_1'}{K_2} + \frac{z' - z_2'}{K_3} + 2\sum_{n=1}^{\infty} \left(C_{3n} e^{-\lambda_n z'} + D_{3n} e^{\lambda_n z'} \right) \cos\left(\lambda_n x'\right) \right] \qquad \text{(B.9)}$$

The constants C_{in} and D_{in} (i = 1, 2, 3) are given by:

$$C_{1n} = \frac{\xi_n^*(1-R_n) - \frac{\gamma_n^*}{2}\left[\left(1+\frac{K_1}{K_2}\right)\left(1-\frac{K_2 R_n}{K_3}\right) + \left(1-\frac{K_1}{K_2}\right)\left(1+\frac{K_2 R_n}{K_3}\right) e^{-2\lambda_n (z_2' - z_1')} \right]}{c_n^*\left(1+\frac{K_2 R_n}{K_3}\right) + a_n\left(1-\frac{K_2 R_n}{K_3}\right)} \qquad \text{(B.10)}$$

$$D_{1n} = \frac{\xi_n^*(1-R_n) + \frac{\gamma_n^*}{2}\left[\left(1-\frac{K_1}{K_2}\right)\left(1-\frac{K_2 R_n}{K_3}\right) e^{-2\lambda_n z_1'} + \left(1+\frac{K_1}{K_2}\right)\left(1+\frac{K_2 R_n}{K_3}\right) e^{-2\lambda_n z_2'} \right]}{c_n^*\left(1+\frac{K_2 R_n}{K_3}\right) + a_n\left(1-\frac{K_2 R_n}{K_3}\right)} \qquad \text{(B.11)}$$

$$C_{2n} = \frac{\xi_n^* c_n^*(1-R_n) e^{2\lambda_n z_2'} - \gamma_n^* \frac{K_1}{K_2}\left(1-\frac{K_2 R_n}{K_3}\right)}{c_n^*\left(1+\frac{K_2 R_n}{K_3}\right) + a_n\left(1-\frac{K_2 R_n}{K_3}\right)} \qquad \text{(B.12)}$$

$$D_{2n} = \frac{\xi_n^* a_n (1 - R_n) + \gamma_n^* \frac{K_1}{K_2}\left(1 + \frac{K_2 R_n}{K_3}\right) e^{-2\lambda_n z_2'}}{c_n^*\left(1 + \frac{K_2 R_n}{K_3}\right) + a_n\left(1 - \frac{K_2 R_n}{K_3}\right)} \tag{B.13}$$

$$C_{3n} = \frac{\xi_n^*\left[c_n^*\left(1 + \frac{K_2}{K_3}\right) + a_n\left(1 - \frac{K_2}{K_3}\right)\right] e^{2\lambda_n z_2'} - \frac{2\gamma_n^* K_1}{K_3}}{\left(1 - e^{-2\lambda_n(\delta_{bm}' - z_2')}\right)\left[c_n^*\left(1 + \frac{K_2}{K_3} R_n\right) + a_n\left(1 - \frac{K_2}{K_3} R_n\right)\right]} \tag{B.14}$$

and

$$D_{3n} = C_{3n} e^{-2\lambda_n \delta_{bm}'} + \xi_n^* \tag{B.15}$$

where

$$a_n = \frac{1}{2}\left[1 + \frac{K_1}{K_2} + \left(1 - \frac{K_1}{K_2}\right) e^{-2\lambda_n z_1'}\right] \tag{B.16}$$

$$c_n^* = \frac{1}{2}\left[\left(1 - \frac{K_1}{K_2}\right) e^{-2\lambda_n (z_2' - z_1')} + \left(1 + \frac{K_1}{K_2}\right) e^{-2\lambda_n z_2'}\right] \tag{B.17}$$

$$R_n = \frac{e^{-2\lambda_n(\delta_{bm}' - z_2')} + 1}{e^{-2\lambda_n(\delta_{bm}' - z_2')} - 1} \tag{B.18}$$

$$\gamma_n^* = \frac{\gamma_n}{\lambda_n K_1} \tag{B.19}$$

$$\xi_n^* = \frac{\xi_n}{\lambda_n K_3} e^{-\lambda_n \delta_{bm}'} \tag{B.20}$$

and λ_n, ξ_n and γ_n are given by equations (4.17) through (4.19).

Using equations (B.6), (B.7) and (B.9) together with equation (4.12), one obtains

$$k_{bm} = \frac{K_D/(\mu W_{bm})}{\frac{\delta_{bm}' - z_2'}{K_3} + \frac{z_2' - z_1'}{K_2} + \frac{z_1'}{K_1} + 2\sum_{n=1}^{\infty}\left[\xi_n\left(C_{3n}e^{-\lambda_n \delta_{bm}'} + D_{3n}e^{\lambda_n \delta_{bm}'}\right) - \gamma_n\left(C_{1n} + D_{1n}\right)\right]} \tag{B.21}$$

For $K_1 = K_2 = K_3 = 1$, equations (B.10) - (B.15) become

$$C_{1n} = C_{2n} = C_{3n} = \frac{\xi_n - \gamma_n e^{\lambda_n \delta_{bm}'}}{\lambda_n\left(e^{\lambda_n \delta_{bm}'} - e^{-\lambda_n \delta_{bm}'}\right)}, \tag{B.22}$$

$$D_{1n} = D_{2n} = D_{3n} = \frac{\xi_n - \gamma_n e^{-\lambda_n \delta_{bm}'}}{\lambda_n\left(e^{\lambda_n \delta_{bm}'} - e^{-\lambda_n \delta_{bm}'}\right)}, \tag{B.23}$$

and equation (B.21) reduces to the result for a homogeneous basement membrane (equation (4.23)).

B.2 RESULTS

The limited ultrastructural information available for the three layers of the basement membrane (Takami et al., 1991) suggests that the Darcy permeability of the lamina densa ($K_D(LD)$) may be much smaller than that of the lamina rarae ($K_D(LR)$). We assumed that $K_D(LRI) = K_D(LRE) \geq K_D(LD)$; based on the observations of Takami et al. (1991), we estimated that $\delta_{LRI} = \delta_{LRE} = 0.14\delta_{LD}$. We assumed that $K_D = 2.7$ nm^2 and δ_{bm} (= $\delta_{LRI}+\delta_{LD}+\delta_{LRE}$) = 200 nm, and that all other structural parameters were equal to the baseline values (see Section 4.3.1).

Figure B.1 shows isobars calculated assuming $K_D(LR)/K_D(LD) = 5$ (Panel A) and $K_D(LR)/K_D(LD) = 20$ (Panel B). A comparison between these two sets of isobars and with the isobars shown in Figure 4.4 for homogeneous basement membrane, shows that as the Darcy permeability of the lamina rarae increases (i.e., as $K_D(LR)/K_D(LD)$ increases), most of the pressure drop occurs in the lamina densa. Figure B.2 shows streamlines calculated for the same parameters of Figure B.1. As $K_D(LR)/K_D(LD)$ increases, the streamlines in the lamina densa approach vertical lines, as if there were no cells.

Table B.1 shows calculated values of k_{bm} for various values of $K_D(LR)/K_D(LD)$, including those used in Figures B.1 and B.2. As $K_D(LR)/K_D(LD)$ increases, k_{bm} increases, eventually approaching the value obtained when no boundaries are present (k_{bm} = $1.93\text{x}10^{-8}$ m/s/Pa). This is because when $K_D(LR)/K_D(LD)$ is large, most of the pressure drop occurs in the middle layer (see Figure B.1), where the converging/diverging effect of the boundaries on the flow is no longer critical.

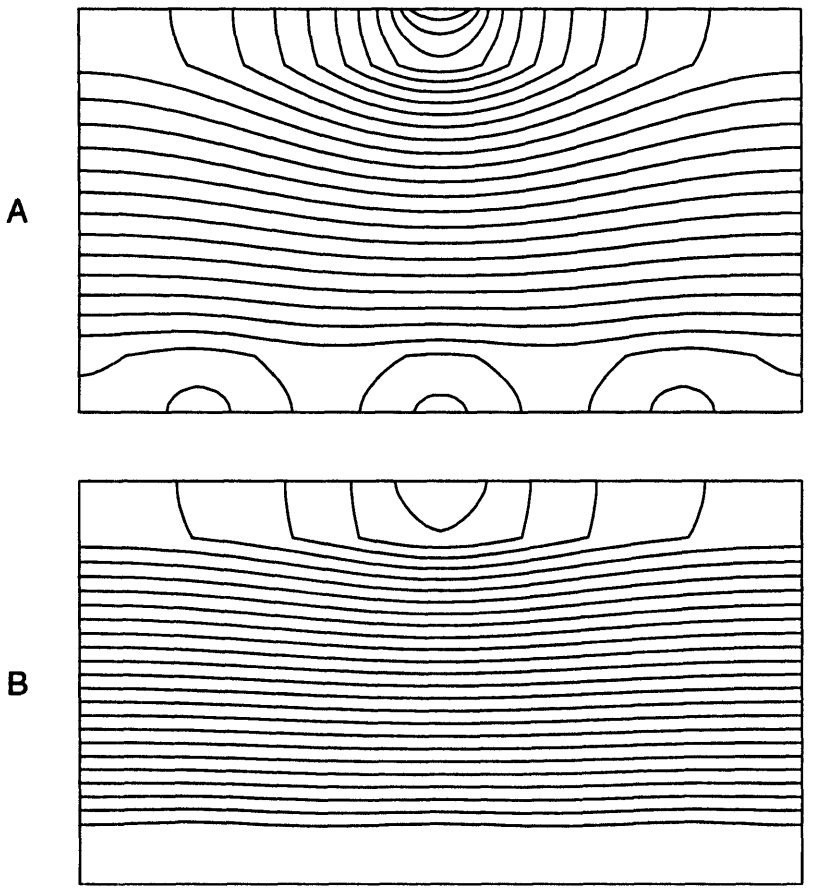

Figure B.1 - Isobars in the basement membrane for $\varepsilon_s = 0.11$, $\varepsilon_f = 0.20$, $N_f = 3$, $\delta_{bm}/W_{bm} = 0.56$, $z_1/\delta_{bm} = 0.14$, $z_2/\delta_{bm} = 0.86$, and $K_D(LR)/K_D(LD) = 5$ (Panel A) and $K_D(LR)/K_D(LD) = 20$ (Panel B).

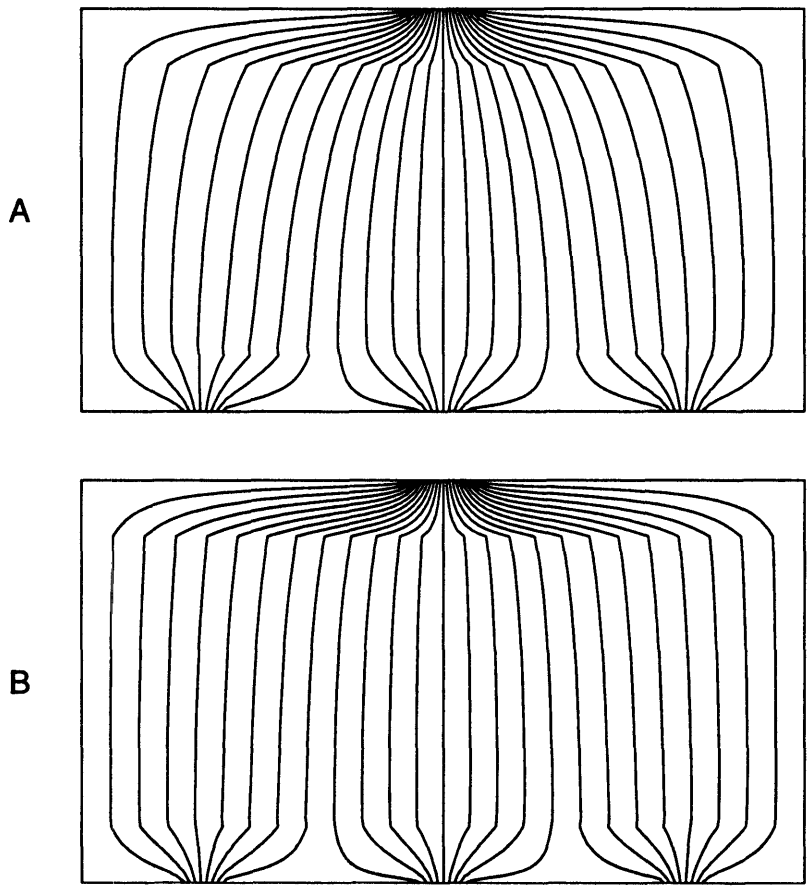

Figure B.2 - Streamlines in the basement membrane for $\varepsilon_s = 0.11$, $\varepsilon_f = 0.20$, $N_f = 3$, $\delta_{bm}/W_{bm} = 0.56$, $z_1/\delta_{bm} = 0.14$, $z_2/\delta_{bm} = 0.86$, and $K_D(LR)/K_D(LD) = 5$ (Panel A) and $K_D(LR)/K_D(LD) = 20$ (Panel B).

Table B.1 - Hydraulic permeability calculated for basement membranes assumed to consist of three distinct layers.

$K_D(LR)/K_D(LD)$	k_{bm} (m/s/Pa)
1	8.27×10^{-9}
2	1.02×10^{-8}
5	1.32×10^{-8}
10	1.54×10^{-8}
20	1.70×10^{-8}
50	1.82×10^{-8}

APPENDIX C

STOKES FLOW IN A TAPERED CHANNEL: APPLICATION TO THE EPITHELIAL SLITS

An assumption of the hydrodynamic models developed in Chapters 3 and 4 was that the width of the epithelial slits is constant. However, as seen in electron micrographs, the width of the slit channel seems to increase with increasing distance downstream from the diaphragm. Such an increase in width causes the hydraulic resistance of the channel to decrease. Thus, the approximation made in Chapters 3 and 4 of neglecting f_P (f_P is a dimensionless hydraulic resistance of the channel alone) in the calculation of the hydraulic permeability of the epithelium (k_{ep}), is even more justifiable. However, because the width of the slit channel increases immediately downstream of the diaphragm, the disturbances in the flow field caused by the diaphragm will be different from those in a parallel wall channel. Because the dimensionless "additional" resistance of the diaphragm, f (f is defined by equation (3.11) as the dimensionless total resistance, f_T, minus f_P), is determined by these disturbances, the values of f for the actual tapered channel can be different from those previously calculated for straight channels (Chapter 3). It is expected that, as long as the increase in channel width is not very pronounced, differences in f will be relatively small. The objective of the analysis presented in this Appendix was to verify this hypothesis. The approach was as follows. After specifying the geometry of the slit channel (Section C.1), we computed values of f_T using FIDAP and used equation (3.11) to calculate f. This equation requires the knowledge of f_P for a tapered channel; In Section C.2 we derive an analytical result for f_P. Finally, in Section C.3 we give results for f and compare them with corresponding results for a parallel wall channel.

C.1 MODEL GEOMETRY

The shape and dimensions of the slit channel, as seen in electron micrographs, depend on the method used to prepare the glomerular tissue for electron microscopy (Furukawa et al., 1991). Based on the limited available information, our approach was to choose a simple geometric model with the most general features of the slit channel, namely a gradual increase in width downstream of the diaphragm. For this purpose, it was convenient to use a coordinate system where the geometry of the channel could be described with only a small number of additional parameters. We chose elliptic cylinder coordinates (ξ,η), which are related to the cartesian coordinates used in Chapter 3 by

$$\begin{cases} x = c\cosh\xi\,\cos\eta \\ z = c\sinh\xi\,\sin\eta \end{cases} \tag{C.1}$$

where c is a constant. Properties of this orthogonal coordinate system are given in Appendix A of Happel and Brenner (1983). Figure C.1 shows curves of constant η or of constant ξ. The curves of constant η suggest that the tapered walls of the slit channel can be described by $\eta = \eta_0 = \text{constant}$. Accordingly, our geometric model for the slit channel was as shown in Figure C.2. We assumed that the distance between foot processes is constant from $z = -(\delta+a)$ to $z = 0$, and that it increases further downstream of the diaphragm ($0 \le z \le \delta_1$) in such a way that the surface of the foot processes is described by $\eta = \text{constant}$. The distance a from the center of the cylinders ($z = -a$) to the point where the tapering of the channel begins ($z = 0$) was chosen such that $R \le a << \delta$. From $z = -(\delta+a)$ to $z = 0$, the distance between the channel walls is $2W$. Thus, the constant c in equation (C.1) is given by

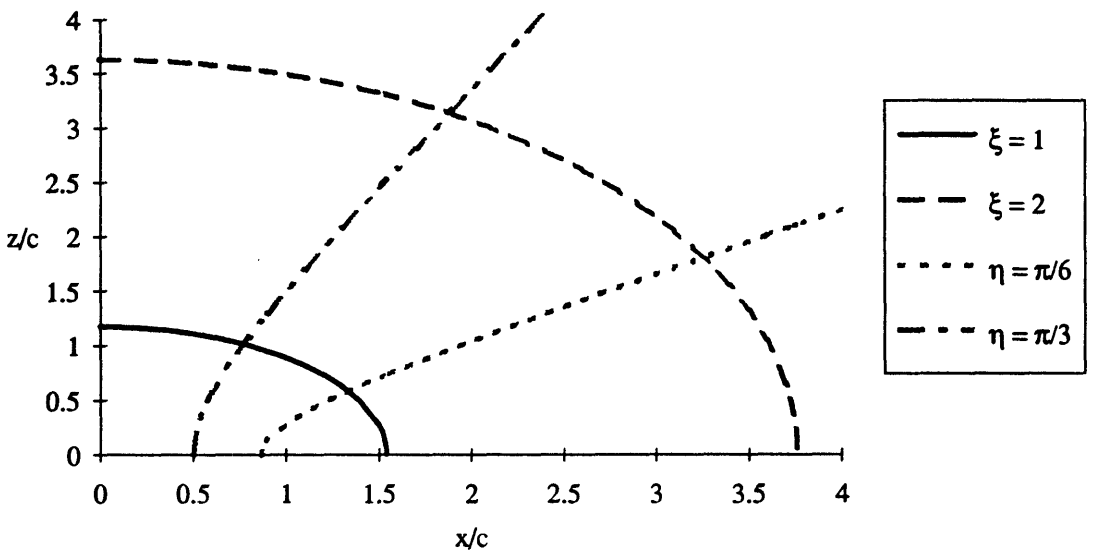

Figure C.1 - Elliptic cylinder coordinates.

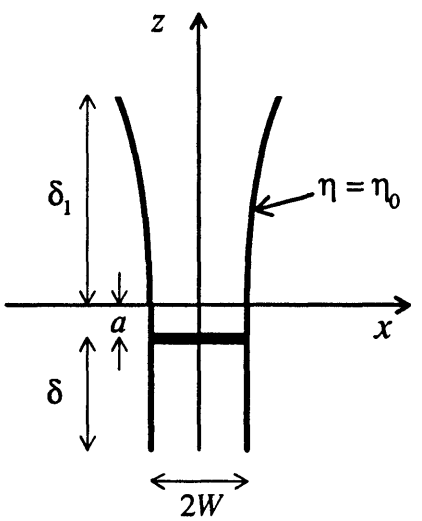

Figure C.2 - Schematic representation of the slit channel. The slit diaphragm is located at $z = -a$. The width of the channel is constant from $z = -(\delta+a)$ to $z = 0$. For $z > 0$, the walls of the slit channel are described by $\eta = \eta_0$ (for $x > 0$) and $\eta = \pi-\eta_0$ (for $x < 0$).

$$c = \frac{W}{\cos \eta_0}. \tag{C.2}$$

C.2 STOKES FLOW IN A TWO-DIMENSIONAL TAPERED CHANNEL

The following derivation closely resembles that of Happel and Brenner (1983) for low Reynolds number flow in a Venturi tube. The Stokes equations, written in terms of the stream function (ψ), are

$$\nabla^4 \psi \equiv \nabla^2 \left(\nabla^2 \psi \right) = 0 \tag{C.3}$$

where ∇^2 is the Laplace operator. In elliptic cylinder coordinates, ∇^2 is given by

$$\nabla^2 = \frac{1}{c^2 \left(\cosh^2 \xi - \cos^2 \eta \right)} \left(\frac{\partial^2}{\partial^2 \xi} + \frac{\partial^2}{\partial^2 \eta} \right). \tag{C.4}$$

The shape of the channel motivates the assumption (subject to verification) that $\psi = \psi(\eta)$. With this assumption, equation (C.3) becomes

$$\nabla^4 \psi = \frac{1}{c^4 (G-H)} \left[\frac{\partial^2}{\partial \eta^2} \left(\frac{F}{G-H} \right) + \frac{\partial^2}{\partial \xi^2} \left(\frac{F}{G-H} \right) \right] = 0 \tag{C.6}$$

where

$$F \equiv \frac{d^2\psi}{d\eta^2} \tag{C.7}$$

$$G \equiv \cosh^2 \xi \tag{C.8}$$

and

$$H \equiv \cos^2 \eta\,. \tag{C.9}$$

After some algebra, equation (C.6) becomes

$$\begin{aligned}\nabla^4\psi = \frac{1}{c^4(G-H)^4}\Big[&G^2\left(F'' + 4F\right) + \\ &G\left(FH'' - 2HF'' + 2F'H' + 4HF - 6F\right) + \\ &\left(F''H^2 - FH''H - 2F'H'H + 2F\left(H'\right)^2 - 2FH\right)\Big] = 0\end{aligned} \tag{C.10}$$

where the superscripts ' and " refer to the first and second derivatives with respect to η, respectively. Since F and H are functions of η only and G is a function of ξ only, equation (C.10) can only be satisfied for all ξ if

$$F'' + 4F = 0 \tag{C.11a}$$

$$FH'' - 2HF'' + 2F'H' + 4HF - 6F = 0 \tag{C.11b}$$

$$F''H^2 - FH''H - 2F'H'H + 2F\left(H'\right)^2 - 2FH = 0. \tag{C.11c}$$

Using equation (C.11a) in equations (C.11b) and (C.11c), it can be shown that the latter two equations reduce to the same relationship. Equations (C.11a) - (C.11c) can then be simplified to

$$F'' = -4F \tag{C.12a}$$

$$F'H' + 4HF - 2F = 0. \tag{C.12b}$$

Integrating equation (C.12a) twice yields

$$F = A\cos(2\eta) + B\sin(2\eta) \tag{C.13}$$

where A and B are integration constants. Using equation (C.13) and the definition of H (equation (C.9)), it can be shown that equation (C.12b) can only be satisfied if $A = 0$. Then, using equations (C.7) and (C.13) (with $A = 0$) and integrating twice yields

$$\psi = -\frac{B}{4}\sin(2\eta) + C\eta + D. \tag{C.14}$$

The three integration constants in equation (C.14) (B, C and D) can be determined as follows. First, because the stream function is defined only up to an arbitrary additive constant, we can specify

$$\psi = 0 \text{ at } \eta = \frac{\pi}{2} \tag{C.15}$$

where $\eta = \pi/2$ corresponds to the centerline of the channel (i.e., $x = 0$). The condition of no-slip at the wall requires that

$$\frac{d\psi}{d\eta} = 0 \text{ at } \eta = \eta_0 \,. \tag{C.16}$$

Finally, the total flow rate per unit depth in the y-direction (q) is given by

$$q = \psi(\eta_0) - \psi(\pi - \eta_0) \,. \tag{C.17}$$

where $\eta = \pi - \eta_0$ corresponds to the wall located at $x < 0$. Using equations (C.15) - (C.17) in equation (C.14), one obtains

$$B = -\frac{2q}{\sin 2\eta_0 + (\pi - 2\eta_0)\cos 2\eta_0} \tag{C.18}$$

$$C = -\frac{q\cos 2\eta_0}{\sin 2\eta_0 + (\pi - 2\eta_0)\cos 2\eta_0} \tag{C.19}$$

$$D = \frac{\pi q \cos 2\eta_0}{2\left(\sin 2\eta_0 + (\pi - 2\eta_0)\cos 2\eta_0\right)} \tag{C.20}$$

and thus,

$$\psi = \frac{q\left[\sin(2\eta) + (\pi - 2\eta)\cos(2\eta_0)\right]}{2\left[\sin(2\eta_0) + (\pi - 2\eta_0)\cos(2\eta_0)\right]} \,. \tag{C.21}$$

It can be noted that $\psi(\eta) = -\psi(\pi-\eta)$, or equivalently, $\psi(x) = -\psi(-x)$. That is, ψ is anti-symmetric relative to $x = 0$. Also, $\psi'(\pi-\eta_0) = 0$ so that the no slip condition at the wall located at $x < 0$ is also satisfied.

The velocity components, in elliptic cylinder coordinates, can be calculated from ψ by

$$v_\xi = -\frac{1}{c\sqrt{\cosh^2\xi - \cos^2\eta}}\frac{\partial\psi}{\partial\eta} \tag{C.22}$$

$$v_\eta = \frac{1}{c\sqrt{\cosh^2\xi - \cos^2\eta}}\frac{\partial\psi}{\partial\xi}. \tag{C.23}$$

Since ψ is a function of η only, equation (C.23) yields $v_\eta = 0$. Using equations (C.21) and (C.22) to obtain v_ξ, and substituting the result into Stokes equations (now written in terms of v_ξ, v_η and P instead of ψ) one obtains

$$\frac{\partial P}{\partial\xi} = -\frac{2B\mu}{c^2}\frac{\left(2\cos^2\eta\cosh^2\xi - \cos^2\eta - \cosh^2\xi\right)}{\left(\cosh^2\xi - \cos^2\eta\right)^2} \tag{C.24}$$

$$\frac{\partial P}{\partial\eta} = -\frac{2B\mu}{c^2}\frac{\sin 2\eta\cosh\xi\sinh\xi}{\left(\cosh^2\xi - \cos^2\eta\right)^2}. \tag{C.25}$$

It can be shown that equations (C.24) and (C.25) are equivalent to

$$\frac{\partial P}{\partial\xi} = \frac{2B\mu}{c^2}\frac{\partial}{\partial\xi}\left[\frac{\cosh\xi\sinh\xi}{\cosh^2\xi - \cos^2\eta}\right] \tag{C.26}$$

$$\frac{\partial P}{\partial \eta} = \frac{2B\mu}{c^2}\frac{\partial}{\partial \eta}\left[\frac{\cosh\xi \sinh\xi}{\cosh^2\xi - \cos^2\eta}\right] \tag{C.27}$$

and thus,

$$dP = \frac{2B\mu}{c^2} d\left[\frac{\cosh\xi \sinh\xi}{\cosh^2\xi - \cos^2\eta}\right]. \tag{C.28}$$

Upon integration, equation (C.28) yields

$$\begin{aligned} P &= P_0 + \frac{2B\mu}{c^2}\frac{\cosh\xi \sinh\xi}{\cosh^2\xi - \cos^2\eta} \\ &= P_0 - \frac{4q\mu}{c^2\left(\sin 2\eta_0 + (\pi - 2\eta_0)\cos 2\eta_0\right)}\frac{\cosh\xi \sinh\xi}{\left(\cosh^2\xi - \cos^2\eta\right)}. \end{aligned} \tag{C.29}$$

where P_0 is the (constant) pressure at the throat of the channel ($z = \xi = 0$). As $\xi \to \infty$, P approaches a constant (P_∞) which is given by

$$P_\infty = P_0 - \frac{4q\mu}{c^2\left(\sin 2\eta_0 + (\pi - 2\eta_0)\cos 2\eta_0\right)}. \tag{C.30}$$

Defining an average fluid velocity based on the cross-sectional area at the throat of the channel, $\bar{v}_s = q/(2W)$, and using equation (C.2), equation (C.30) yields

$$P_0 - P_\infty = \frac{8\cos^2\eta_0 \mu \bar{v}_s}{W\left(\sin 2\eta_0 + (\pi - 2\eta_0)\cos 2\eta_0\right)}. \tag{C.31}$$

The results derived in this section can be applied to the case of flow through a slit opening in a planar wall, for which $\eta_0 = 0$. In this case equation (C.30) simplifies to

$$P_0 - P_{-\infty} = \frac{4q\mu}{\pi c^2} \tag{C.32}$$

and, because the pressure and velocity profiles are symmetric relative to $\xi = 0$,

$$P_{-\infty} - P_{\infty} = \frac{8q\mu}{\pi c^2} \tag{C.33}$$

where $P_{-\infty}$ is the pressure as $\xi \rightarrow -\infty$.

For the channel geometry shown in Figure C.2, we calculated the dimensionless resistance of the channel alone (f_P) as a sum of two terms, one for the straight portion of the channel and the other for the tapered portion. That is,

$$f_P = \frac{3(\delta + a)L}{W^2} + \frac{(P_0 - \overline{P}_1)L}{\mu \overline{v}_s} \tag{C.34}$$

where $\overline{P}_1$ is the pressure at the exit of the slit channel ($z = \delta_1$), averaged in the x and y directions. Unlike at the entrance of the channel ($z = -(\delta+a)$) where, as long as δ is large, the pressure becomes independent of x, the tapering of the channel causes the pressure at $z = \delta_1$ to be a function of x even for large δ_1. In fact, the pressure decreases from the centerline ($x = 0$) to the wall of the channel. As an approximation, we replaced $\overline{P}_1$ in equation (C.34) by the local pressure, P_1, at $x = 0$ (i.e., at $\eta = \pi/2$) and $z = \delta_1$. The value of δ_1 was chosen such that

$$\frac{P_0 - P_1}{P_0 - P_\infty} = \alpha \tag{C.35}$$

where α is an arbitrary parameter ($\alpha < 1$). For values of α close to unity, which correspond to long channels, the difference between the pressures at the centerline and at the wall is small and, thus, the expected error of replacing $\overline{P_1}$ by P_1 in equation (C.34) is also small. In the numerical calculations, δ_1 was made sufficiently large that $\alpha \geq 0.9$. As an example, for $L/W = 1$, $\eta_0 = 1.21$ and $\alpha = 0.9$ (see Table C.1), at $z = \delta_1$, the difference between P_1 and the pressure at the wall is only ~3% of $(P_0 - P_1)$.

Using equation (C.29) with $\eta = \pi/2$, $\xi = \xi_1$ and $P = P_1$, and equation (C.30) in equation (C.35) yields

$$\tanh \xi_1 = \alpha . \tag{C.36}$$

Noting that ξ_1 is the value of ξ at $z = \delta_1$ and $x = 0$, equations (C.1) and (C.2) yield

$$\delta_1 = \frac{W \sinh \xi_1}{\cos \eta_0} . \tag{C.37}$$

Using equation (C.31) in equation (C.35) yields

$$P_0 - P_1 = \frac{8\alpha\mu\bar{v}_s \cos^2 \eta_0}{W\left(\sin 2\eta_0 + (\pi - 2\eta_0)\cos 2\eta_0\right)} . \tag{C.38}$$

Finally, equation (C.34) becomes

$$f_P \equiv \frac{3(\delta + a)L}{W^2} + \frac{8\alpha L \cos^2 \eta_0}{W\left(\sin 2\eta_0 + (\pi - 2\eta_0)\cos 2\eta_0\right)}. \qquad \text{(C.39)}$$

C.3 DIMENSIONLESS ADDITIONAL RESISTANCE OF THE SLIT DIAPHRAGM

Using four different experimental methods to prepare glomerular samples for electron microscopy, Furukawa et al. (1991) measured the distance between adjacent foot processes at the level of the slit diaphragm and at a distance of 50 nm downstream from the diaphragm. We used their results to estimate an approximate range for η_0. We then specified the curvature of the walls by choosing η_0 and, for a given α, calculated the length of the tapered portion of the channel (δ_1) using equations (C.36) and (C.37).

Assuming the ladder configuration of the slit diaphragm, we determined f_T using FIDAP, calculated f_P using equation (C.39), and calculated the dimensionless additional resistance of the diaphragm (f) using equation (3.11). Table C.1 shows values of f obtained in four case studies (we used $a = L$ in all cases). It can be seen that the values of f for a tapered channel are very similar to the corresponding values for a straight channel. In conclusion, one can assume straight channel walls in calculating f for the glomerular slit diaphragm, as was done in Chapter 3.

As a final comment, we note that the geometric model used here represents a limiting case because, as seen in electron micrographs, the width of the slit channel seems to stop increasing somewhere downstream from the diaphragm. Therefore, the actual result should be bounded by the results for a straight channel and those for the type of tapered channel considered here.

Table C.1 - Numerical values of f for tapered and straight channels

L/W	R/L	δ/L	α	η_0	δ_1/L	f	
						Tapered channel	Straight channel
1	0.5	4	0.95	0.72	4.0	35.5	35.6
1	0.5	4	0.9	1.06	4.2	35.6	35.6
1	0.5	4	0.9	1.21	5.9	35.6	35.6
4	0.5	4	0.99	0.88	2.7	99.4	101

APPENDIX D

CALCULATION OF THE WIDTH OF A STRUCTURAL UNIT FROM THE MEASURED FILTRATION SLIT FREQUENCY

In this Appendix we derive equation (5.6), which relates the width of a structural unit (W_{bm}) to measured values of filtration slit frequency (FSF).

Because of the random angle of sectioning the glomerular capillary, the measured apparent width of a structural unit (W'_{bm}) will generally exceed the true width (W_{bm}). As illustrated in Figure D.1, W'_{bm} depends on the angle (ϕ) between the filtration slits and the line of intersection of the sample plane ($\mathcal{P}$) with the outer surface of the capillary wall ($\mathcal{B}$). It can be seen that for $0 \leq \phi \leq \pi$, $W'_{bm} \geq W_{bm}$, the equality holding when $\phi = \pi/2$.

To calculate W_{bm} from the measured mean width of a structural unit ($\overline{W}'_{bm}$) we used principles of geometrical probability. In particular, our problem is closely related to that of calculating the expected length (σ) of the chord formed by the intersection of a plane ($\mathcal{P}$) with a closed convex figure lying in another plane ($\mathcal{B}$). Using results given in Kendall and Moran (1963) we obtained

$$\sigma = \frac{\pi A}{P} \tag{D.1}$$

where A is the area of the closed convex curve and P is its perimeter. This result is equivalent to that derived by Solomon (1978) (p. 32) for the case of a straight line intersecting a closed convex curve in a plane. Equation (D.1) can be directly applied to our problem by defining the closed curve as a rectangle of width W_{bm} and (arbitrary)

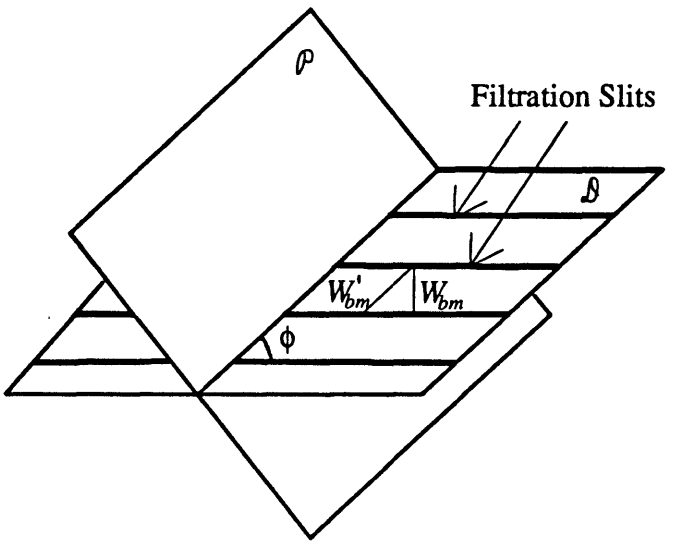

Figure D.1 - Schematic representation of the outer surface of the capillary wall ($\mathcal{B}$) and sample plane ($\mathcal{P}$), showing the relationship between the measured apparent width of a structural unit (W'_{bm}) and the true width (W_{bm}).

length ℓ, corresponding to the area occupied by one foot process and one filtration slit. Then, $\sigma = \overline{W}'_{bm}$. Neglecting edge effects (i.e., assuming $\ell >> W_{bm}$), equation (D.1) yields

$$\overline{W}'_{bm} = \frac{\pi}{2} W_{bm} \tag{D.2}$$

which is the desired relationship between the apparent and true widths of a structural unit. In the experimental studies described in Section 4.3.5 and in Chapter 5, the filtration slit frequency (*FSF*) was determined by dividing the total number of slits captured in the electron micrographs by the total length of peripheral capillary wall. Thus, $1/FSF$ is an estimate of $\overline{W}'_{bm}$. Using this result in equation (D.2) we obtain the relationship between *FSF* and W_{bm} (equation (5.6)).

Equation (D.2) can be derived also as follows. As indicated by Figure D.1, the apparent width $W_{bm}^{'}$ is related to W_{bm} by

$$W_{bm}^{'} = \frac{W_{bm}}{\sin\phi}. \tag{D.3}$$

The arithmetic mean of $W_{bm}^{'}$ is then calculated by

$$\overline{W}_{bm}^{'} = \frac{\int_0^{\pi} W_{bm}^{'} f(\phi) d\phi}{\int_0^{\pi} f(\phi) d\phi} \tag{D.4}$$

where $f(\phi)$ is the probability density of the angle ϕ. As shown by Solomon (1978) (p. 71), the probability density of the angle formed by two random lines that are known to intersect within some finite region in space is given by

$$f(\phi) = \frac{1}{2}\sin\phi. \tag{D.5}$$

Using equations (D.3) and (D.5) in equation (D.4), and performing the required integrations, one obtains again equation (D.2).

Similarly, one can also calculate W_{bm} from the apparent harmonic mean width ($\overline{W}_h^{'}$) which is defined by

$$\frac{1}{\overline{W_h'}} = \frac{\int_0^{\pi} \frac{1}{W_{bm}'} f(\phi) d\phi}{\int_0^{\pi} f(\phi) d\phi}. \qquad \text{(D.6)}$$

The result is

$$\overline{W_h'} = \frac{4}{\pi} W_{bm}. \qquad \text{(D.7)}$$

The derivations presented here to obtain relationships between $\overline{W_{bm}'}$ (or $\overline{W_h'}$) and W_{bm} are different from that of Jensen et al. (1979), who obtained the relationship we have used to calculate the "true" thickness of the basement membrane (δ_{bm}, equation (5.4)). To determine δ_{bm} one measures the distance between two lines obtained by the intersection of the sample plane ($\mathcal{P}$) with two parallel planes ($\mathcal{B}'$ and $\mathcal{B}$) corresponding to the "inner" and "outer" surfaces of the basement membrane. The angle of interest in that case (denoted as θ) is that between $\mathcal{P}$ and $\mathcal{B}$ (or $\mathcal{B}'$), and the probability density for that angle is proportional to $\sin^2\theta$ (Jensen et al., 1979). In contrast, W_{bm}' is the distance between two points in the line of intersection of the sample plane ($\mathcal{P}$) with the plane ($\mathcal{B}$) corresponding to the outer surface of the basement membrane. The angle of interest is now the angle (ϕ) formed by the line of intersection of the two planes with the parallel lines in $\mathcal{B}$ corresponding to the filtration slits. This is why, contrary to the suggestion of Gundersen et al. (1980), we did not use the same correction factors for W_{bm} and δ_{bm}.

APPENDIX E

HYDRODYNAMIC APPROXIMATIONS FOR HINDERED TRANSPORT OF MACROMOLECULES THROUGH A SINGLE ROW OF CYLINDERS

In Chapter 6 we described briefly the hydrodynamic approximations used to estimate the force coefficient tensors **f** and **g**, which appear in the force balance for a sphere moving through a row of infinitely long cylinders (equation (6.1)). Here we give a more detailed description which includes all the equations used to calculate **f** and **g** in each hydrodynamic region shown in Figure 6.2.

E.1 HYDRODYNAMIC APPROXIMATIONS IN REGIONS I

In Regions I, **f** was estimated using results for the translation of a sphere in the presence of a planar wall and **g** was estimated using results for flow past a stationary sphere in the presence of a planar wall. We assumed that the "wall" was tangent to the surface of the cylinder and, for each location of the sphere, the point of tangency was defined as shown in Figure E.1. For simplicity, and because the overall aproach was in itself only approximate, when possible we estimated the force coefficients using asymptotic results for small and large gaps between the sphere and the wall.

FORCE COEFFICIENTS FOR A SPHERE TRANSLATING PARALLEL TO A PLANAR WALL ($f_{\parallel}$). For small gaps between the sphere and the wall, we calculated $f_{\parallel}$ using the "lubrication" result of Goldman et al. (1967a), whereas for larger gaps we used the result obtained by Faxen (Happel and Brenner, 1983, p. 327),

$$f_{\parallel} = -\frac{8}{15}\ln\left(\frac{1}{b}-1\right)+0.9588 \quad \text{for } b \geq 0.967 \tag{E.1a}$$

$$f_{\parallel} = \left(1-\frac{9}{16}b+\frac{1}{8}b^3-\frac{45}{256}b^4-\frac{1}{16}b^5\right)^{-1} \quad \text{for } b < 0.967 \tag{E.1b}$$

where b is the ratio between the sphere radius (r_s) and the distance from the sphere center to the wall. The transition between equations (E.1a) and (E.1b) was made at the value of b where both equations yield the same value of $f_{\parallel}$, which is $b \equiv 0.967$.

FORCE COEFFICIENTS FOR A SPHERE TRANSLATING TOWARDS A PLANAR WALL ($f_{\perp}$). As above, we used asymptotic results for small and large gaps instead of an exact solution, which in this case is given in Brenner (1961). For small gaps, $f_{\perp}$ was calculated using the "lubrication" result of Cox and Brenner (1967), whereas for larger gaps $f_{\perp}$ was calculated using the method of reflections' result of Wakiya (Happel and Brenner, 1983, p. 330),

$$f_{\perp} = \frac{2}{\alpha^2}+\frac{2}{5}\ln\left(\frac{1}{\alpha}\right)+0.943226 \quad \text{for } b \geq 0.508 \tag{E.2a}$$

$$f_{\perp} = \left(1-\frac{9}{8}b+\frac{1}{2}b^3\right)^{-1} \quad \text{for } b < 0.508 \tag{E.2b}$$

where

$$\alpha = \ln\left(\frac{1}{b}+\sqrt{\frac{1}{b^2}-1}\right). \tag{E.3}$$

FORCE COEFFICIENTS FOR SHEAR FLOW PAST A STATIONARY SPHERE ($g_{\parallel}$). We first calculated $h_{\parallel}$ (= $g_{\parallel}/f_{\parallel}$) using the asymptotic results given in Goldman et al. (1967b),

$$h_{\parallel} = \frac{0.7431}{0.6376 - 0.200 \ln\left(\frac{1}{b} - 1\right)} \quad \text{for } b \geq 0.747 \tag{E.4a}$$

$$h_{\parallel} = 1 - \frac{5}{16} b^3 \quad \text{for } b < 0.747 \tag{E4.b}$$

and then calculated $g_{\parallel}$ by

$$g_{\parallel} = h_{\parallel} f_{\parallel} \tag{E.5}$$

with $f_{\parallel}$ calculated by equation (E.1a) or (E.1b), depending on the value of b.

FORCE COEFFICIENTS FOR FLOW PAST A STATIONARY SPHERE TOWARDS A PLANAR WALL ($g_{\perp}$). Because there appears to be no solution for flow past a stationary sphere towards an infinite wall, we used the results of Dagan et al. (1982) for a sphere and a (finite) disk to estimate $g_{\perp}$ as follows. First, $h_{\perp}$ was calculated for the case of a sphere and a disk, using the results of Tables 2 and 3 and equation (5.2) of Dagan et al. (1982). The computed values of $h_{\perp}$ are given in Table E.1, where r_D is the radius of the disk and b is the sphere radius divided by the distance from the center of the sphere to the surface of the disk. As described in Section 6.2.4, for $r_s/r_D \leq 1$, the results given in Table E.1 were well approximated by

$$h_{\perp} = 1 - b^{3.8}. \tag{E.6}$$

Therefore, we calculated $g_{\perp}$ using

Table E.1 - Values of $h_\perp$ for a sphere and a disk, calculated from the results of Dagan et al. (1982)

	r_s/r_D								
b	0.1	0.25	0.5	0.75	1	2.5	5	7.5	10
0.909	0.302	0.307	0.324	0.320	0.291	0.253	0.434	0.608	0.724
0.8	0.570	0.579	0.651	0.573	0.530	0.580	0.812	0.908	0.953
0.667	0.796	0.804	0.808	0.766	0.737	0.864	0.960	0.988	0.997
0.5	0.956	0.959	0.937	0.909	0.909	0.977	0.999	1.002	1.003
0.333	1.015	1.009	0.986	0.984	0.990	1.001	1.002	1.002	1.001
0.25	1.019	1.008	0.997	0.999	1.000	1.002	1.001	1.001	1.001
0.2	1.016	1.005	1.001	1.001	1.001	1.001	1.001	1.000	1.000
0.167	1.012	1.004	1.001	1.001	1.001	1.001	1.000	1.000	1.000
0.125	1.007	1.002	1.001	1.003	1.001	1.000	1.000	1.000	1.000
0.1	1.004	1.001	1.001	1.001	1.000	0.990	1.000	1.000	1.000

$$g_\perp = h_\perp f_\perp \tag{E.7}$$

with $h_\perp$ given by equation (E.6) and $f_\perp$ given by equation (E.2a) or (E.2b), depending on the value of b.

COMPONENTS OF **f**, **g**, **d** AND **h** IN (y,z) COORDINATES. Having calculated the force coefficients for motion parallel and perpendicular to the planar wall ($f_\parallel$, $f_\perp$, $g_\parallel$ and $g_\perp$), the components of **f** and **g** in (y,z) coordinates were determined by taking into account the orientation of the wall. This yielded,

$$
\begin{aligned}
f_{yy} &= f_{\parallel}\sin^2\beta + f_{\perp}\cos^2\beta \\
f_{zz} &= f_{\parallel}\cos^2\beta + f_{\perp}\sin^2\beta \\
f_{yz} &= f_{zy} = (f_{\perp} - f_{\parallel})\sin\beta\cos\beta \\
g_{yy} &= g_{\parallel}\sin^2\beta + g_{\perp}\cos^2\beta \\
g_{zz} &= g_{\parallel}\cos^2\beta + g_{\perp}\sin^2\beta \\
g_{yz} &= g_{zy} = (g_{\perp} - g_{\parallel})\sin\beta\cos\beta
\end{aligned}
\qquad \text{(E.8)}
$$

where β is the angle between the y-axis and the line connecting the center of the cylinder (0,0) with the center of the sphere (y,z), i.e. $\beta = \tan^{-1}(z/y)$ (see Figure E.1). Then, the components of the tensors **d** and **h**, used in equation (6.3), were calculated using equations (6.5) and (6.6), respectively. That is,

$$
\begin{aligned}
d_{yy} &= f_{zz}/\det(\mathbf{f}) \\
d_{zz} &= f_{yy}/\det(\mathbf{f}) \\
d_{yz} &= d_{zy} = -f_{yz}/\det(\mathbf{f})
\end{aligned}
\qquad \text{(E.9)}
$$

and

$$
\begin{aligned}
h_{yy} &= (f_{zz}g_{yy} - f_{yz}g_{zy})/\det(\mathbf{f}) \\
h_{zz} &= (f_{yy}g_{zz} - f_{zy}g_{yz})/\det(\mathbf{f}) \\
h_{yz} &= (f_{zz}g_{yz} - f_{yz}g_{zz})/\det(\mathbf{f}) \\
h_{zy} &= (f_{yy}g_{zy} - f_{zy}g_{yy})/\det(\mathbf{f})
\end{aligned}
\qquad \text{(E.10)}
$$

where

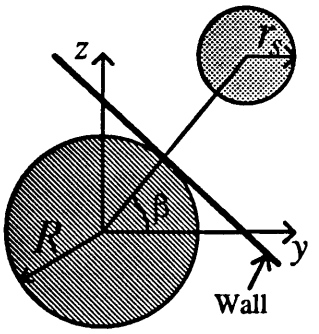

Figure E.1 - Diagram illustrating the location of the planar wall.

$$\det(\mathbf{f}) = f_{yy} f_{zz} - f_{zy} f_{yz}. \tag{E.11}$$

Using equation (E.8) in equation (E.10) one can show that **h** is symmetric,

$$h_{zy} = h_{yz} = \frac{(f_{\parallel} g_{\perp} - f_{\perp} g_{\parallel}) \sin\beta \cos\beta}{\det(\mathbf{f})}. \tag{E.12}$$

E.2 HYDRODYNAMIC APPROXIMATIONS IN REGION III

In Region III we estimated $f_{\parallel}$, $f_{\perp}$ and $g_{\parallel}$ using the results of Ganatos et al. (1980a, c) for a sphere between parallel walls. Tables E.2 through E.4 give the values of these coefficients, which were estimated from Figures 3a and 6a of Ganatos et al. (1980a) and Figure 3 of Ganatos et al. (1980c). The new parameter s is the distance from the center of the sphere to the closest wall divided by the distance between the two walls. (Note that $0 \le s \le 0.5$.) The values of $g_{\parallel}$ were calculated from the values of F_y^P plotted in Figure 6a of Ganatos et al. (1980a) using

Table E.2 - Values of $f_{\parallel}$ for a sphere between parallel walls, obtained from Figure 3a of Ganatos et al. (1980a)

	s					
b	0	0.1	0.2	0.3	0.4	0.5
0.1	1.06	1.06	1.06	1.07	1.09	1.11
0.2	1.12	1.12	1.14	1.16	1.19	1.24
0.333	1.22	1.23	1.25	1.29	1.36	1.46
0.5	1.38	1.40	1.43	1.51	1.64	1.85
0.667	1.59	1.61	1.67	1.79	2.02	2.37
0.8	1.85	1.88	1.95	2.13	2.45	3.00
0.909	2.25	2.29	2.39	2.62	3.00	3.92

Table E.3 - Values of $f_{\perp}$ for a sphere between parallel walls, obtained from Figure 3 of Ganatos et al. (1980c)

	s					
b	0	0.1	0.2	0.3	0.4	0.5
0.1	1.12	1.12	1.12	1.14	1.15	1.16
0.2	1.28	1.28	1.28	1.30	1.34	1.39
0.333	1.57	1.57	1.57	1.60	1.69	1.85
0.5	2.14	2.14	2.14	2.18	2.34	2.75
0.667	3.24	3.24	3.24	3.30	3.65	4.77
0.8	5.32	5.32	5.38	5.48	6.06	8.83
0.909	11.5	11.5	11.5	11.7	12.6	20.9

Table E.4 - Values of $g_{\parallel}$ for a sphere between parallel walls, obtained from Figure 6c of Ganatos et al. (1980a) and equation (E.13)

	s					
b	0	0.1	0.2	0.3	0.4	0.5
0.1	1.06	1.04	1.05	1.06	1.08	1.11
0.2	1.12	1.13	1.14	1.15	1.19	1.23
0.333	1.21	1.22	1.20	1.28	1.35	1.42
0.5	1.32	1.32	1.35	1.43	1.54	1.69
0.667	1.45	1.45	1.48	1.59	1.78	2.00
0.8	1.54	1.54	1.60	1.77	1.98	2.26
0.909	1.62	1.67	1.73	1.89	2.15	2.50

$$g_{\parallel} = \frac{F_y^P}{4s(1-s)}. \qquad \text{(E.13)}$$

The denominator in equation (E.13) accounts for the fact that we defined $g_{\parallel}$ relative to the *local* undisturbed fluid velocity whereas Ganatos et al. (1980a) defined F_y^P relative to the undisturbed velocity at the *centerline* of the planar wall channel.

To calculate s and b in Region III, the location of the wall closest to the sphere was determined as in Regions I and the distance between walls was assumed to be $2(L/\cos\beta - R)$. For $b \le 0.909$, $f_{\parallel}$, $f_{\perp}$ and $g_{\parallel}$ were calculated by linearly interpolating $1/f_{\parallel}$, $1/f_{\perp}$ and $h_{\parallel}$ (= $g_{\parallel}/f_{\parallel}$) using the values given in Tables E.2 - E.4. When $b < 0.1$ the interpolations were done between $b = 0.1$ and $b = 0$ for which case all force coefficients equal 1.

For $b > 0.909$, we calculated $f_{\parallel}$, $f_{\perp}$ and $g_{\parallel}$ using an approach similar to that of Ganatos et al. (1980b) who modified one-wall lubrication results to account, in an approximate way, for the effect of the second wall. Specifically, the modified lubrication results, based on equations (E.1a), (E.2a) and (E.4a), were

$$f_{\parallel} = -\frac{8}{15}\ln\left(\frac{1}{b}-1\right)+C_{\parallel}(s) \tag{E.14}$$

$$f_{\perp} = \frac{2}{\alpha^2}+\frac{2}{5}\ln\left(\frac{1}{\alpha}\right)+C_{\perp}(s) \tag{E.15}$$

$$g_{\parallel} = \frac{0.7431\left(-\frac{8}{15}\ln\left(\frac{1}{b}-1\right)+0.9588\right)}{0.6376-0.200\ln\left(\frac{1}{b}-1\right)}\frac{D_{\parallel}(s)}{b}. \tag{E.16}$$

The new parameters $C_{\parallel}(s)$, $C_{\perp}(s)$ and $D_{\parallel}(s)$, which depend only on s, were obtained by matching the estimates of equations (E.14) - (E.16) with the values given in Tables E.2 - E.4, at $b = 0.909$. That is,

$$C_{\parallel}(s) = (f_{\parallel})_{0.909}+\frac{8}{15}\ln(0.1) \tag{E.17}$$

$$C_{\perp}(s) = (f_{\perp})_{0.909}-\left(\frac{2}{\alpha_{0.909}{}^2}+0.4\ln\left(\frac{1}{\alpha_{0.909}}\right)\right) \tag{E.18}$$

$$D_{\parallel}(s) = \frac{(g_{\parallel})_{0.909}}{1.1} \frac{0.6376 - 0.200\ln(0.1)}{0.7431\left(-\frac{8}{15}\ln(0.1) + 0.9588\right)} \tag{E.19}$$

where $(f_{\parallel})_{0.909}$, $(f_{\perp})_{0.909}$ and $(g_{\parallel})_{0.909}$ are the values of $f_{\parallel}$, $f_{\perp}$ and $g_{\parallel}$, respectively, given in Tables E.2 - E.4 for $b = 0.909$, and $\alpha_{0.909}$ is the value of α calculated using equation (E.3) with $b = 0.909$. We then determined $C_{\parallel}(s)$, $C_{\perp}(s)$ and $D_{\parallel}(s)$ for each value of s given in Tables E.2 - E.4, and used the calculated values in equations (E.14) - (E.16) to calculate $f_{\parallel}$, $f_{\perp}$ and $g_{\parallel}$ when $b > 0.909$. For values of s not included in Tables E.2 - E.4, we linearly interpolated $1/f_{\parallel}$, $1/f_{\perp}$ and $g_{\parallel}/f_{\parallel}$.

The remaining force coefficient, $h_{\perp}$, was estimated as in Region I (Section E.1) and then **f**, **g**, **d** and **h** were calculated using equations (E.8) - (E.11).

E.3 HYDRODYNAMIC APPROXIMATIONS IN REGIONS II

Regions II are transition regions where the components of **d** and **h** were interpolated linearly from the corresponding values at the boundaries of Regions I and III. In the points of Region II for which $0 \le y \le (R + r_s)\cos(\pi/4)$, we assumed that the boundary of Region III corresponds to $r \equiv \left(y^2 + z^2\right)^{1/2} = R + r_s$, where $\mathbf{d} = \mathbf{h} = \mathbf{0}$.

E.4 RESULTS

In Figures 6.3 and 6.4 we plotted the diagonal and off-diagonal elements of **d** and **h** as a function of z/L, for $R/L = 0.5$, $r_s/(L - R) = 0.7$, and various values of y/L. Tables E.5 and E.6 give values of those coefficients for the same parameter values.

Table E.5 - Calculated values of the diagonal elements of **d** and **h** for $R/L = 0.5$ and $r_s/(L - R) = 0.7$

z/L	d_{yy} for y/L =			d_{zz} for y/L =			h_{yy} for y/L =			h_{zz} for y/L =		
	0	0.5	1	0	0.5	1	0	0.5	1	0	0.5	1
0	-	-	.185	-	-	.400	-	-	.742	-	-	.826
0.5	-	-	.341	-	-	.455	-	-	.887	-	-	.893
1	.596	.631	.692	.287	.478	.692	.893	.932	.978	.742	.896	.978
2	.870	.868	.865	.744	.761	.799	.996	.996	.997	.996	.997	.998
3	.922	.921	.919	.844	.848	.861	.999	.999	.999	.999	.999	1.00
4	.944	.943	.943	.888	.890	.895	1.00	1.00	1.00	1.00	1.00	1.00
5	.956	.956	.956	.913	.914	.916	1.00	1.00	1.00	1.00	1.00	1.00

Table E.6 - Calculated values of the off-diagonal elements of **d** and **h** for $R/L = 0.5$ and $r_s/(L - R) = 0.7$

z/L	d_{yz} for y/L =			h_{yz} for y/L =		
	0	0.5	1	0	0.5	1
0	-	-	0	-	-	0
0.5	-	-	-7.6×10^{-2}	-	-	-3.9×10^{-3}
1	0	-1.0×10^{-1}	-9.5×10^{-2}	0	-2.3×10^{-2}	-4.2×10^{-3}
2	0	-2.9×10^{-2}	-4.4×10^{-2}	0	$\cong 0$	$\cong 0$
3	0	-1.2×10^{-2}	-2.2×10^{-2}	0	$\cong 0$	$\cong 0$
4	0	-6.8×10^{-3}	-1.3×10^{-2}	0	$\cong 0$	$\cong 0$
5	0	-4.3×10^{-3}	-8.2×10^{-3}	0	$\cong 0$	$\cong 0$

Entries shown as "$\cong 0$" had absolute values $\leq 1\times10^{-4}$.

APPENDIX F

ESTIMATE OF THE DIMENSIONLESS FLOW RESISTANCE FOR LARGE CYLINDER SPACINGS

In this appendix we summarize the procedure followed to calculate the dimensionless flow resistance, f_T, needed in equation (6.20). This quantity, defined by equation (3.9), can be expressed as the sum of the dimensionless Poiseuille flow resistance, f_P (= $3\delta_T L/W^2$, where δ_T is the total length of the slit channel) and a dimensionless "additional" flow resistance, f. For flow through a row of infinitely long cylinders, $f_P = 0$. For flow through the slit channel and diaphragm we saw in Chapter 4 that f_P is expected to be much smaller than f. It should be noted, however, that if we assume a distribution of cylinder spacings, as we did in Section 6.3.3, we need to account for the existence of a small fraction of very large spacings, for which f_P will be non-negligible.

To calculate θ_{sd} in Chapter 6 we neglected the effect of the walls. However, we can incorporate wall effects on $q(u)$ by calculating f using the interpolation formulas derived for the ladder configuration (equations (3.15) - (3.20)). Because these formulas only apply for $R/L \geq 0.1$ and $L/W \leq 4$, when $R/L < 0.1$ or $L/W > 4$ we estimated f_T as follows. For $L/W >> 1$ and $R/L << 1$, $v_x \equiv 0$ and $v_y \equiv 0$ in most of the domain and v_z can be estimated by a modified Poiseuille flow result where, because of continuity, the average velocity V_z is a function of z in the region between cylinders. Under these assumptions, it can be shown that

$$f = 3\left(\frac{L}{W}\right)^2\left(\frac{1}{\sqrt{1-(R/L)^2}}\left(\pi + 2\tan^{-1}\left(\frac{R/L}{\sqrt{1-(R/L)^2}}\right)\right) - \pi\right) - \frac{6LR}{W^2}. \qquad \text{(F.1)}$$

Thus, to calculate f_T when $R/L < 0.1$ or $L/W > 4$ we linearly interpolated f between the results for $R/L = 0.1$ or $W/L = 0.25$ and the estimate of equation (F.1), which corresponds to $R/L = 0$ or $W/L = 0$. Regarding f_P, we verified that, for reasonable channel lengths (δ_T < ~100 nm) the assumed value of δ_T did not significantly affect $\langle \theta_{sd} \rangle$. Thus, we used $\delta_T = \delta$ in the calculations of $\langle \theta_{sd} \rangle$; that is, we neglected the hydraulic resistance of the channel downstream of the diaphragm.

BIBLIOGRAPHY

Abrahamson, D.R. Structure and development of the glomerular capillary wall and basement membrane. *Am. J. Physiol.* 253 (*Renal Fluid Electrolyte Physiol.* 22): F783-F794, 1987.

Anderson, S., J.R. Diamond, M.J. Karnovsky, and B.M. Brenner. Mechanisms underlying transition from acute glomerular injury to late glomerular sclerosis in a rat model of nephrotic syndrome. *J. Clin. Invest.* 82: 1757-1768, 1988.

Austin, S.M., J.S. Lieberman, L.D. Newton, M. Mejia, W.A. Peters, and B.D. Myers. Slope of serial GFR and the progression of diabetic glomerular disease. *J. Am. Soc. Nephrol.* 3: 1358-1370, 1993.

Avasthi, P.S., and V. Koshy. The anionic matrix at the rat glomerular endothelial surface. *Anat. Rec.* 220: 258-266, 1988.

Battilana, C., H. Zhang, R. Olshen, L. Wexler, and B.D. Myers. PAH extraction and the estimation of plasma flow in the diseased human kidney. *Am. J. Physiol.* 261 (*Renal Fluid Electrolyte Physiol.* 30): F726-F733, 1991.

Bendtsen, T.F., and J.R. Nyengaard. The number of glomeruli in Type 1 (insulin-dependent) and Type 2 (non-insulin-dependent) diabetic patients. *Diabetologia* 35: 844-850, 1992.

Bendtsen, T.F., and J.R. Nyengaard. Unbiased estimation of particle number using sections - an historical perspective with special reference to the stereology of glomeruli. *J. Microsc.* 153: 93-102, 1989.

Bohman, S.O., G. Jaremko, A.B. Bohlin, and U. Berg. Foot process fusion and glomerular filtration rate in minimal change nephrotic syndrome. *Kidney Int.* 25: 696-700, 1984.

Brenner, B.M., J.L. Troy, and T.M. Daugharty. The dynamics of glomerular ultrafiltration in the rat. *J. Clin. Invest.* 50: 1776-1780, 1971.

Brenner, B.M., J.L. Troy, T.M. Daugharty, W.M. Deen, and C.R. Robertson. Dynamics of glomerular ultrafiltration in the rat. II. Plasma-flow dependence of GFR. *Am. J. Physiol.* 223: 1184-1190, 1972.

Brenner, H. The slow motion of a sphere through a viscous fluid towards a plane surface. *Chem. Eng. Sci.* 16: 242-251, 1961.

Bridges, C.R., H.G. Rennke, W.M. Deen, J.L. Troy, and B.M. Brenner. Reversible hexadimethrine-induced alterations in glomerular structure and permeability. *J. Am. Soc. Nephrol.* 1: 1095-1108, 1991.

Brinkman, H.C. A calculation of the viscous force exerted by a flowing fluid on a dense swarm of particles. *Appl. Sci. Res. A* 1: 27-34, 1947.

Bugliarello, G., and J. Sevilla. Velocity distribution and other characteristics of steady and pulsatile blood flow in fine glass tubes. *Biorheology* 7: 85-107, 1970.

Cannan-Kuhl, S., E.S. Venkatraman, S.I.B. Ernst, R.A. Olshen, and B.D. Myers. Relationships among protein and albumin concentrations and oncotic pressure in nephrotic plasma. *Am. J. Physiol.* 264 (*Renal Fluid Electrolyte Physiol.* 33): F1052-F1059, 1993.

Chang, R.L.S. A model of capillary solutes and fluid exchange. *Chem. Eng. Commun.* 4: 189-206, 1980.

Chang, R.L.S., C.R. Robertson, W.M. Deen, and B.M. Brenner. Permselectivity of the glomerular capillary wall to macromolecules. I. Theoretical considerations. *Biophys. J.* 15: 861-886, 1975.

Cox, R.G., and H. Brenner. The slow motion of a sphere through a viscous fluid toward a plane surface - II. Small gap widths, including inertial effects. *Chem. Eng. Sci.* 22: 1753-1777, 1967.

Curry, F.E. Mechanisms and thermodynamics of transcapillary exchange. In *Handbook of Physiology: The cardiovascular system*, Vol. IV. Microcirculation, Part 1 (Renkin, E.M., and C.C. Michel, eds), American Physiological Society, Bethesda, Maryland, 1984, pp. 309-374.

Curry, F.E., and C.C. Michel. A fiber matrix model of capillary permeability. *Microvasc. Res.* 20: 96-99, 1980.

Dagan, Z., R. Pfeffer, and S. Weinbaum. Axisymmetric stagnation flow of a spherical particle near a finite planar surface at zero Reynolds number. *J. Fluid Mech.* 122: 273-294, 1982.

Daniels, B.S., E.B. Hauser, W.M. Deen, and T.H. Hostetter. Glomerular basement membrane: in vitro studies of water and protein permeability. *Am. J. Physiol.* 262 (*Renal Fluid Electrolyte Physiol.* 31): F919-F926, 1992.

Daniels, B.S., W.M. Deen, G. Mayer, T. Meyer, and T.H. Hostetter. Glomerular permeability barrier in the rat: Functional assessment by in vitro methods. *J. Clin. Invest.* 92: 929-936, 1993.

Deen, W.M. Hindered transport of large molecules in liquid-filled pores. *AIChE J.* 33: 1409-1425, 1987.

Deen, W.M., C.R. Bridges, B.M. Brenner, and B.D. Myers. Heteroporous model of glomerular size-selectivity: application to normal and nephrotic humans. *Am. J. Physiol.* 249 (*Renal Fluid Electrolyte Physiol.* 18): F374-F389, 1985.

Deen, W.M., C.R. Robertson, and B.M. Brenner. A model of glomerular ultrafiltration in the rat. *Am. J. Physiol.* 223: 1178-1183, 1972.

Deen, W.M., C.R. Robertson, and B.M. Brenner. Concentration polarization in an untrafiltering capillary. *Biophys. J.* 14: 412-431, 1974.

Deen, W.M., and B. Satvat. Determinants of the glomerular filtration of proteins. *Am. J. Physiol.* 241 (*Renal Fluid Electrolyte Physiol.* 10): F162-F170, 1981.

Deen, W.M., B. Satvat, and J.M. Jamieson. Theoretical model for glomerular filtration of charged solutes. *Am J. Physiol.* 238 (*Renal Fluid Electrolyte Physiol.* 7): F126-F139, 1980.

Deen, W.M., J.L. Troy, C.R. Robertson, and B.M. Brenner. Dynamics of glomerular ultrafiltration in the rat. IV - Determination of the ultrafiltration coefficient. *J. Clin. Invest.* 52: 1500-1508, 1973.

Du Bois, R., P. Decoodt, J.P. Gassée, A. Verniory, and P.P. Lambert. Determination of glomerular intracapillary and transcapillary pressure gradients from sieving data. I. A mathematical model. *Pflügers Arch.* 356: 299-316, 1975.

Dunnill, M.S., and W. Halley. Some observations on the quantitative anatomy of the kidney. *J. Pathol.* 110: 113-121, 1973.

Edwards, D.A., M. Shapiro, P. Bar-Yoseph, M. Shapira. The influence of Reynolds number upon the apparent permeability of periodic arrays of cylinders. *Phys. Fluids A* 2: 45-55, 1990.

Einstein, A., *Investigations on the Theory of Brownian Motion*, Dover, New York, 1956.

Ellis, E.N., M.W. Steffes, B. Chavers, and S.M. Mauer. Observations of glomerular epithelial cell structure in patients with type I diabetes mellitus. *Kidney Int.* 32: 736-741, 1987.

Farquhar, M.G. The glomerular basement membrane: A selective macromolecular filter. In *Cell Biology of Extracellular Matrix*, (Hay, E.D., ed.), Plenum Press, New York, 1981, pp. 335-378.

Flory, P.J. *Principles of Polymer Chemistry*. Cornell University Press, Ithaca, 1953.

Fries, J.W.U., D.J. Sandstrom, T.W. Meyer, and H.G. Rennke. Glomerular hypertrophy and epithelial cell injury modulate progressive glomerulosclerosis in the rat. *Lab. Invest.* 60: 205-218, 1989.

Furukawa, T., S. Ohno, H. Oguchi, K. Hora, S. Tokunaga, and S. Furuta. Morphometric study of glomerular slit diaphragms fixed by rapid-freezing and freeze-substitution. *Kidney Int.* 40: 621-624, 1991.

Ganatos, P., R. Pfeffer, and S. Weinbaum. A strong interaction theory for the creeping motion of a sphere between plane parallel boundaries. Part 2. Parallel motion, *J. Fluid Mech.* 99: 755-783, 1980a.

Ganatos, P., S. Weinbaum, J. Fischbarg, and L. Liebovitch. A hydrodynamic theory for determining the membrane coefficients for the passage of spherical molecules through an intercellular cleft. In *Advances in Bioeng.*, Amer. Soc. Mech. Eng., New York, 1980b, pp. 193-196.

Ganatos, P., S. Weinbaum, and R. Pfeffer. A strong interaction theory for the creeping motion of a sphere between plane parallel boundaries. Part 1. Perpendicular motion. *J. Fluid Mech.* 99: 739-753, 1980c.

Goldberg, M., and F. Escaig-Haye. Is the lamina lucida of the basement membrane a fixation artifact? *Eur. J. Cell Biol.* 42: 365-368, 1986.

Goldman, A.J., R.G. Cox, H. Brenner. Slow viscous motion of a sphere parallel to a plane wall - I. Motion through a quiescent fluid. *Chem. Eng. Sci.* 22: 637-651, 1967a.

Goldman, A.J., R.G. Cox, H. Brenner. Slow viscous motion of a sphere parallel to a plane wall - II. Couette flow. *Chem. Eng. Sci.* 22: 653-660, 1967b.

Gradshteyn, I.S., and I.M. Ryzhik. *Table of Integrals, Series, and Products.* Academic Press, San Diego, 1980.

Guasch, A., W.M. Deen, and B.D. Myers. Charge-selectivity of the glomerular filtration barrier in healthy and nephrotic humans. *J. Clin. Invest.* 92: 2274-2282, 1993.

Guasch, A., H. Hashimoto, R.K. Sibley, W.M. Deen, and B.D. Myers. Glomerular dysfunction in nephrotic humans with minimal changes or focal glomerulosclerosis. *Am. J. Physiol.* 260 (*Renal Fluid Electrolyte Physiol.* 29): F728-F737, 1991.

Guasch, A., and B.D. Myers. Determinants of glomerular hypofiltration in nephrotic patients with minimal change nephropathy. *J. Am. Soc. Nephrol.* (In press), 1993.

Guasch, A., R.K. Sibley, P. Huie, and B.D. Myers. Extent and course of glomerular injury in human membranous glomerulopathy. *Am. J. Physiol.* 263 (*Renal Fluid Electrolyte Physiol.* 32): F1034-F1043, 1992.

Gundersen, H.J.G., T. Seefeldt, and R. Østerby. Glomerular epithelial foot processes in normal man and rats. *Cell Tissue Res.* 205: 147-155, 1980.

Happel, J. and H. Brenner. *Low Reynolds Number Hydrodynamics.* Martinus Nijhoff, Dordrecht, 1983.

Hele-Shaw, H.S. Investigation of the nature of surface resistance of water and of streamline motion under certain experimental conditions. *Trans. Institution Naval Architects* 40: 21-40, 1898.

Hora, K., S. Ohno, H. Oguchi, T. Furukawa, and S. Furuta. Three-dimensional study of glomerular slit diaphragm by quick-freezing and deep-etching replica method. *Eur. J. Cell Biol.* 53: 402-406, 1990.

Horvat, R., A. Hovorka, G. Dekan, H. Poczewski, and D. Kerjaschki. Endothelial cell membranes contain podocalyxin - the major sialoprotein of visceral glomerular epithelial cells. *J. Cell Biol.* 102: 484-491, 1986.

Huss, R.E., D.J. Marsh, and R.E. Kalaba. Two models of glomerular filtration rate and renal blood flow in the rat. *Ann. Biomed. Engr.* 3: 72-99, 1975.

Ichikawa, I., J.R. Hoyer, W.M. Seiler, and B.M. Brenner. Mechanism of glomerulotubular balance in the setting of heterogeneous glomerular injury. *J. Clin. Invest.* 69: 185-198, 1982.

Ionue, S. Ultrastructure of basement membranes. *International Review of Cytology* 117: 57-98, 1989.

Jackson, G.W., and D.F. James. The permeability of fibrous porous media. *Can. J. Chem. Eng.* 64: 364-374, 1986.

Jensen, E.B., H.J.G. Gundersen, and R. Østerby. Determination of membrane thickness distribution from orthogonal intercepts. *J. Microsc.* 115: 19-33, 1979.

Johnson, M., A. Shapiro, C.R. Ethier, and R.D. Kamm. Modulation of outflow resistance by the pores of the inner wall endothelium. *Invest. Ophthalmol. Vis. Sci.* 33: 1670-1675, 1992.

Kanwar, Y.S., and M.G. Farquhar. Presence of heparan sulfate in the glomerular basement membrane. *Proc. Natl. Acad. Sci.* USA 76: 1303-1307, 1979.

Kanwar, Y.S., and M.A. Venkatachlam. Ultrastructure of glomerulus and juxtaglomerular apparatus. In *Handbook of Physiology: Renal Physiology*, Vol I (Windhager, E. E., ed.), American Physiological Society, Oxford University Press, New York, 1992, pp. 3-40.

Katz, M.A., T. Barrette, and M. Krasovich. Hydraulic conductivity of basement membrane with computed values for fiber radius and void volume ratio. *Am. J. Physiol.* 263 (*Heart Circ. Physiol.* 32): H1417-H1421, 1992.

Kedem, O., and A. Katchalsky. Thermodynamic analysis of the permeability of biological membranes to non-electrolytes. *Biochim. Biophys. Acta* 27: 229-246, 1958.

Keh, H.J. Diffusion of rigid Brownian spheres through pores of finite length. *Physico Chem. Hydrodynam.* 7: 281-295, 1986.

Kendall, M.G., and P.A.P. Moran, *Geometrical Probability*. Charles Griffin & Co., London, 1963.

Kerjaschki, D., D.J. Sharkey, and M.G. Farquhar. Identification and characterization of podocalyxin - the major sialoprotein of the renal glomerular epithelial cell. *J. Cell Biol.* 98: 1591-1596, 1984.

Kheshgi, H.S., and L.E. Scriven. Finite element analysis of incompressible viscous flow by a variable penalty function method. In *Penalty Finite Element Methods in Mechanics*, (Reddy, J.N., ed.), ASME Winter Annual Meeting, 1982, pp. 67-73.

Kondo, H. Rat kidney glomerular basement membrane visualized in situ by embedment-free sectioning and subsequent platinum-carbon replication. *J. Electron Microsc. Tech.* 14: 63-69, 1990.

Koriyama, Y., E. Yamada, and I.-S. Watanabe. "Pored-domes" of the fenestrated endotheliocyte of the glomerular and peritubular capillares in the rodent kidney. *J. Electron Microsc.* 41: 30-36, 1992.

Kubosawa, H., and Y. Kondo. Ultrastructural organization of the glomerular basement membrane as revealed by a deep-etch replica method. *Cell Tissue Res.* 242: 33-39, 1985.

Lamb, H. *Hydrodynamics*. 6th edition, Dover, New York, 1945. (p. 582)

Lambert, P.P., B. Aeikens, A. Bohle, F. Hanus, S. Pegoff, and M. Van Damme. A network model of glomerular function. *Microvasc. Res.* 23: 99-128, 1982.

Larsson, L., and A.B. Maunsbach. The ultrastructural development of the glomerular filtration barrier in the rat kidney: A morphometric analysis. *J. Ultrastruct. Res.* 72: 392-406, 1980.

Latta, H., W.H. Johnson, and T.M. Stanley. Sialoglycoproteins and filtration barriers in the glomerular capillary wall. *J. Ultrastruct. Res.* 51: 354-376, 1975.

Laurie, G.W., C.P. Leblond, S. Ionue, G.R. Martin, and A. Chung. Fine structure of the glomerular basement membrane and immunolocalization of five basement membrane components to the lamina densa (basal lamina) and its extensions in both glomeruli and tubules of the rat kidney. *Am. J. Anat.* 169: 463-481, 1984.

Lea, P.J., M. Silverman, R. Hegele, M.J. Hollenberg. Tridimensional ultrastructure of glomerular capillary endothelium revealed by high-resolution scanning electron microscopy. *Microvasc. Res.* 38: 296-308, 1989.

Lee, J.S. Slow viscous flow in a lung alveoli model. *J. Biomech.* 2: 187-198, 1969.

Lee, J.S., and Y.C. Fung. Stokes flow around a circular cylindrical post confined between two parallel plates. *J. Fluid Mech.* 37: 657-670, 1969.

Levick, J.R., and L.H. Smaje. An analysis of the permeability of a fenestra. *Microvasc. Res.* 33, 233-256, 1987.

Maddox, D.A., W.M. Deen, and B.M. Brenner. Glomerular Filtration. In *Handbook of Physiology: Renal Physiology*, Vol I, (Windhager, E.E., ed.), American Physiological Society, Oxford University Press, New York, 1992, pp. 545-638.

Mauer, S.M., M.W. Steffes, E.N. Ellis, D.E.R. Sutherland, D.M. Brown, and F.C. Goetz. Structural-functional relationships in diabetic nephropathy. *J. Clin. Invest.* 74: 1143-1155, 1984.

Maul, G.G. Structure and formation of pores in fenestrated capillaries. *J. Ultrastruct. Res.* 36: 768-782, 1971.

Messina, A., D.J. Davies, P.C. Dillane, and G.B. Ryan. Glomerular epithelial abnormalities associated with the onset of proteinuria in aminonucleoside nephrosis. *Am. J. Pathol.* 126: 220-229, 1987.

Miller, P.L., J.W. Scholey, H.G. Rennke, and T.W. Meyer. Glomerular hypertrophy aggravates epithelial cell injury in nephrotic rats. *J. Clin. Invest.* 85: 1119-1126, 1990.

Mills, C.J., I.T. Gabe, J.H. Gault, D.T. Mason, J. Ross, E. Braunwald, and J.P. Shillingford. Pressure-flow relationships and vascular impedance in man. *Cardiovasc. Res.* 4: 405-417, 1970.

Myers, B.D., T.B. Okarma, S. Friedman, C. Bridges, J. Ross, S. Asseff, and W. M. Deen. Mechanisms of proteinuria in human glomerulonephritis. *J. Clin. Invest.* 70: 732-746, 1982.

Myers, B.D., A. Chagnac, H. Golbetz, L. Newton, S. Strober, and R.K. Sibley. Extent of glomerular injury in active and resolving lupus nephritis: A theoretical analysis. *Am. J. Physiol.* 260 (*Renal Fluid Electrolyte Physiol.* 29): F717-F727, 1991.

Myers, B.D., C. Peterson, C.R. Molina, S.J. Tomlanovich, L.D. Newton, R. Nitkin, H. Snadler and F. Murad. Role of cardiac atria in the human renal response to changing plasma volume. *Am. J. Physiol.* 254 (*Renal Fluid Electrolyte Physiol.* 23): F562-F573, 1988.

Nakamura, Y., and B.D. Myers. Charge selectivity of proteinuria in diabetic glomerulopathy. *Diabetes* 37: 1202-1211, 1988.

Nyengaard, J.R., and T.F. Bendtsen. Glomerular number and size in relation to age, kidney weight, and body surface in normal man. *Anat. Rec.* 232: 194-201, 1992.

Oden, J.T. Penalty method and reduced integration for the analysis of fluids. *Penalty Finite Element Methods in Mechanics*, (Reddy, J.N., ed.), ASME Winter Annual Meeting, 1982, pp. 21-32.

Ogston, A.G. The spaces in a uniform random suspension of fibers, *Trans. Farad. Soc.* 54: 1754-1757, 1958.

Ogston, A.G., B.N. Preston, and J.D. Wells. On the transport of compact particles through solutions of chain-polymers. *Proc. R. Soc. Lond. A* 333: 297-316, 1973.

Ohno, S., K. Hora, T. Furukawa, and H. Oguchi. Ultrastructural study of the glomerular slit diaphragm in fresh unfixed kidneys by a quick-freezing method. *Virchows Archiv B - Cell Pathol.* 61: 351-358, 1992.

Oliver III, J.D., S. Anderson, J.L. Troy, B.M. Brenner, and W.M. Deen. Determination of glomerular size-selectivity in the normal rat with Ficoll. *J. Am. Soc. Nephrol.* 3: 214-228, 1992.

Olson, J.L., H.G. Rennke, and M.A. Venkatachalam. Alterations in the charge and size selectivity barrier of the glomerular filter in aminonucleoside nephrosis in rats. *Lab. Invest.* 44: 271-279, 1981.

Østerby, R. H.J.G. Gundersen, A. Hørlyck, J.P. Koustrup, G. Nyberg, G. Westberg. Diabetic glomerulopathy: structural characteristics of the early and advanced stages. *Diabetes* 32 (Suppl. 2): 79-82, 1983.

Phillips, R.J., W.M. Deen, and J.F. Brady. Hindered transport of spherical macromolecules in fibrous membranes and gels. *AIChE J.* 35: 1761-1769, 1989.

Pinnick, R.V. and V.J. Savin. Filtration by superficial and deep glomeruli of norvolemic and volume-depleted rats. *Am. J. Physiol.* 250 (*Renal Fluid Electrolyte Physiol.* 19): F86-F91, 1986.

Press, W.H., B.P. Flannery, S.A. Teukolsky, and W.T. Vetterling. *Numerical Recipes: The Art of Scientific Computing*, Cambridge University Press, Cambridge, UK, 1986.

Remuzzi, A., and W.M. Deen. Theoretical effects of a distribution of capillary dimensions on glomerular ultrafiltration. *Microvasc. Res.* 32: 131-144, 1986.

Remuzzi, A., and W.M. Deen. Theoretical effects of network structure on glomerular filtration of macromolecules. *Am. J. Physiol.* 257 (*Renal Fluid Electrolyte Physiol.* 26): F152-F158, 1989.

Rhodin, J.A.G. The diaphragm of capillary endothelial fenestrations. *J. Ultrastruct. Res.* 6: 171-185, 1962.

Robinson, G.B., and T.G. Cotter. Studies on the filtration properties of isolated renal basement membranes. *Biochim. Biophys. Acta* 551: 85-94, 1979.

Robinson, G.B., and H.A. Walton. Ultrafiltration through basement membrane. In *Basement Membranes in Health and Disease*, (Price, R.G., and B.G. Hudson, eds.), Academic Press, New York/London, 1987, pp. 147-161.

Robinson, G.B., and H.A. Walton. Glomerular basement membrane as a compressible ultrafilter. *Microvasc. Res.* 38: 36-48, 1989.

Rodewald, R., and M.J. Karnovsky. Porous substructure of the glomerular slit diaphragm in the rat and mouse. *J. Cell Biol.* 60: 423-433, 1974.

Rosenzweig, L.J., and Y.S. Kanwar. Removal of sulfated (heparan sulfate) or nonsulfated (hyaluronic acid) glycosaminoglycans results in increased permeability of the glomerular basement membrane to ^{125}I-bovine serum albumin. *Lab. Invest.* 47: 177-184, 1982.

Ryan, G.B. The glomerular filtration barrier. In *Advances in Renal Physiology*, (Lote, C.J., ed.), Alan R. Liss, New York, 1986, p. 1-32.

Ryan, G.B., R. Rodewald, and M.J. Karnovsky. An ultrastructural study of the glomerular slit diaphragm in aminonucleoside nephrosis. *Lab. Invest.* 33: 461-468, 1975.

Sangani, A.S., and A. Acrivos. Slow flow past periodic arrays of cylinders with application to heat transfer. *Int. J. Multiphase Flow* 8: 193-206, 1982.

Scandling, J.D., V.M. Black, W.M. Deen, and B.D. Myers. Glomerular permselectivity in healthy and nephrotic humans. Necker's Seminar in Nephrology. *Advances in Nephrology* (Mosby-Yearbook Inc.) 21: 159-176, 1992.

Schnabel, E., J.M. Anderson, and M.G. Farquhar. The tight junction protein ZO-1 is concentrated along slit diaphragms of the glomerular epithelium. *J. Cell Biol.* 111: 1255-1263, 1990.

Schnabel, E., G. Dekan, A. Miettinen, and M.G. Farquhar. Biogenesis of podocalyxin - the major sialoglycoprotein - in the newborn rat kidney. *Eur. J. Cell Biol.* 48: 313-326, 1989.

Scholey, J.W., P.L. Miller, H.G. Rennke, and T.W. Meyer. Effect of converting enzyme inhibition on the course of adriamycin-induced nephropathy. *Kidney Int.* 36: 816-822, 1989.

Shea, S.M. The relation between structure and function in the glomerular capillary bed. *Acta Endocrinol. Suppl.* 242: 47-50, 1981.

Shea, S.M., and A.B. Morrison. A stereological study of the glomerular filter in the rat: Morphometry of the slit diaphragm and basement membrane. *J. Cell Biol.* 67: 436-443, 1975.

Shemesh, O., J.C. Ross, W.M. Deen, G.W. Grant, and B.D. Myers. Nature of the glomerular capillary injury in human membranous glomerulopathy. *J. Clin. Invest.* 77: 868-877, 1986.

Solomon, H. *Geometric Probability*. Soc. Ind. Appl. Math., Philadelphia, 1978.

Takami, H., A. Naramoto, H. Shigematsu, and S. Ohno. Ultrastructure of glomerular basement membrane by quick-freeze and deep-etch methods. *Kidney Int.* 39: 659-664, 1991.

Tamada, K., and H. Fujikawa. The steady two-dimensional flow of viscous fluid at low Reynolds numbers passing through an infinite row of equal parallel circular cylinders. *Quart. J. Mech. Applied Math.* 10: 425-432, 1957.

Taylor, J.R. *An Introduction to Error Analysis: The Study of Uncertainties in Physical Measurements*. University Science Books, Oxford University Press, Mill Valley, CA, 1982.

Thompson, B.W. Secondary flow in a Hele-Shaw cell. *J. Fluid Mech.* 31: 379-395, 1968.

Tsay, R.-Y. and S. Weinbaum. Viscous flow in a channel with periodic cross-bridging fibers: Exact solutions and Brinkman approximation. *J. Fluid Mech.* 226: 125-148, 1991.

Van Damme, M., and M. Prevost. Transport of charged macromolecules across a biological charged membrane. *Comp. Progr. Biomed.* 19: 107-117, 1985.

Vrahopoulou, E.P. Flow distortions around particles between parallel walls with application to streak formation in slide-coating methods. *Chem. Eng. Sci.* 47: 1027-1037, 1992.

Webber, W.A., and J. Blackbourn. The permeability of the immature glomerulus to large molecules. *Lab. Invest.* 23: 1-7, 1970.

Weibel, E.R. *Stereological Methods. Vol. 1: Practical Methods for Biological Morphometry.* Academic Press, London, 1979.

Weibel, E.R. and D.M. Gomez. A principle for counting tissue structures on random sections. *J. Appl. Physiol.* 17: 343-348, 1962.

Welling, L.W., and J.J. Grantham. Physical ¡ roperties of isolated perfused renal tubules and tubular basement membranes. *J. Clin. Invest.* 51: 1063-1075, 1972.

Wolgast, M., and G. Ötjeg. Electrophysiology of renal capillary membranes: Gel concept applied and Starling model challenged. *Am. J. Physiol.* 254: F364-F373, 1988.

Yan, Z.-Y., S. Weinbaum, and R. Pfeffer, On the fine structure of osmosis including three-dimensional pore entrance and exit behavior, *J. Fluid Mech.* 162: 415-438, 1986.

Yoshioka, T., H.G. Rennke, D.J. Salant, W.M. Deen, and I. Ichikawa. Role of abnormally high transmural pressure in the permselectivity deffect of glomerular capillary wall: a study in early passive Heymann nephritis. *Circ. Res.* 61: 531-538, 1987.

Yurchenco, P.D., and J.C. Schittny. Molecular architecture of basement membranes. *FASEB J.* 4: 1577-1590, 1990.